THE UNIVERSITY
of EDINBURGH

Response of Saline Reservoir to Different phaseCO$_2$-Brine: Experimental Tests and Image-based Modelling

Daniel, Peter Ameh

This dissertation is submitted for the degree of
Doctor of Philosophy

THE UNIVERSITY *of* EDINBURGH

August, 2021

Dedication

To the loving memory of my mum, and very understanding, supportive dad.

Acknowledgement

It feels really good to have reached this point, there have been numerous heights of joy and valleys of despair. Lots of perseverance, courage, mental agility and good health kept me going, and for those, I am very grateful to God.

I wish to express my gratitude to my major supervisor, Dr. Dongmin Yang, for his support, guidance and encouragement throughout my research. I enjoyed his friendliness, promptness and flexibility. We had a lot of brainstorming sessions that ultimately led to the success of my research. Thank you.

I also wish to thank my second supervisor, Prof. Xianfeng Fan for his contribution to the success of this work. I wish to thank Prof. Yong Sheng, with whom I started my Ph.D. research as my major Supervisor at the University of Leeds until he moved to another role. Thank you for laying the foundation and for all the other times you answered our calls. I also thank Dr. Kenneth Ishiet of the University of Wolverhampton for his time, criticisms and advice.

I enjoyed tremendous support from the guys at the Wolfson multiphase laboratory at the school of Earth and Environment, University of Leeds- Dr. John Martin, Dr. Carlos Grattoni. Thank you for the helpful advice and discussions during the experiments. I also thank Harri Williams for granting access to thin section workshop and for help during thin-sectioning. I thank Dr. Glen Thomas of the University of Edinburgh for access to Avizo software, and Dr. Sarawuth Wantha of Avizo for discussions and useful advice. Appreciation is reserved for Avizo and COMSOL technical support teams.

Friends and colleagues in Leeds and Edinburgh, the list is too numerous to mention, for all the outings, drinks and banters that provided a needed buffer, I am grateful and will hold the memories. For friends in Holborn Church Leeds, CCE and the refinery small group, Thank you for care, friendliness and community. I will fondly remember you guys.

To all those that have been instrumental along the journey to this point, the list is too numerous to mention, but here, I refer to all my teachers in the past in all capacities. Notably, Prof. A.I. Haruna, Prof. Igwe Ogbonnaya, Prof. P. O Osadebe, Prof. N.K Samaila, Dr. Timothy Bata. I say a big thank you.

To all friends and family back in Nigeria, a very big thank you for holding forth, for the support, understanding and love. It was a great help. To Mabel, thank you for your uncommon patience and understanding.

Know that I have only come this far only with your support. You are all valued!

Declaration

I hereby declare that this thesis has been composed by me. The work contained herein is mine. The work has not been submitted for any other degree or professional qualification, and any included publications are my own work, except where indicated throughout this thesis.

----------------------·
Ameh Peter

Abstract

Geological CO_2 storage in saline rocks is a promising method for meeting the target of net zero emission and minimizing the anthropogenic CO_2 emitted into the earth's atmosphere. Storage of CO_2 in saline rocks triggers CO_2-brine-rock interaction that alters the properties of the rock. Properties of rocks are very crucial for the integrity and efficiency of the storage process. Changes in properties of the reservoir rocks due to CO_2-brine-rock interaction must be well predicted, as some changes can reduce the storage integrity of the reservoir. Considering the thermodynamics, phase behavior, solubility of CO_2 in brine and the variable pressure-temperature conditions of the reservoir, there will be undissolved CO_2 in a CO_2 storage reservoir alongside the brine for a long time, and there is a potential for phase evolution of the undissolved CO_2. The phase of CO_2 influence the CO_2-brine-rock interaction, different phaseCO_2-brine have a unique effect on the properties of the reservoir rocks, Therefore, this study evaluates the effect of four different phaseCO_2-brine reservoir states on the properties of reservoir rocks using experimental and image-based approach. Samples were saturated with the different phaseCO_2-brine, then subjected to reservoir conditions in a triaxial compression test. The representative element volume (REV)/representative element area (REA) for the rock samples were determined from processed digital images, and rock properties were evaluated using digital rock physics and rock image analysis techniques. This research has evaluated the effect of different phaseCO_2-brine on deformation rate and deformation behavior, bulk modulus and compressibility, strength and stiffness as well as porosity and permeability of sample reservoir rocks. Changes in pore geometry properties, porosity and permeability of the rocks in CO_2 storage conditions with different phaseCO_2-brine have been evaluated using digital rock physics techniques. Microscopic rock image analysis has been applied to provide evidence of changes in micro-fabric, topology of minerals and elemental composition of minerals in saline rocks resulting from different phaseCO_2-br that can exist in a saline CO_2 storage reservoir. It was seen that the properties of the reservoir that are most affected by the scCO_2-br state of the reservoir include secondary fatigue rate, bulk modulus, shear strength, change in topology of minerals after saturation as well as change in shape and flatness of pore surfaces. The properties of the reservoir that is most affected by the gCO_2-br state of the reservoir include primary fatigue rate, change in permeability due to stress, change in porosity due to stress, and change topology of minerals due to stress. For all samples, roundness and smoothness of grains as well as smoothness of pores increased after compression while the roundness of pores decreased. Change in elemental composition in rock minerals in CO_2-brine-rock interaction was seen to depend on the reactivity of the mineral with CO_2 and/or brine and the

presence of brine accelerates such change. Carbon, oxygen and silicon can be used as index minerals for elemental changes in a CO_2-brine-rock system. The result of this work can be applied to predicting the effect the different possible phases of CO_2 will have on the deformation, geomechanic indices and storage integrity of giant CO_2 storage fields such as Sleipner, In Salah etc.

Lay Summary

Anthropogenic CO_2 is the major gas responsible for global warming. CO_2 is emitted into the atmosphere by industries, power stations and daily human activities, etc. The Intergovernmental Panel on Climate Change (IPCC) have fixed a target of keeping the increase in temperature to below 1.5 $^{\circ}$C by 2050. This implies that the atmospheric concentration of CO_2 must be less than 450 ppm. Some industries, governments and institutions have committed to the ambitious goals of net zero and net negative CO_2 emissions to achieve the target.

Since industrial and human activities must continue, geological storage of CO_2 in deep saline porous rocks is a great method for meeting the target of net zero emission and minimizing the anthropogenic CO_2 emitted into the earth's atmosphere. In this process, the CO_2 emitted from industrial sources is captured, compressed and pumped into favorable saline rocks. This method has been demonstrated to be feasible. It is very important that the integrity of the rocks in which CO_2 is stored is not compromised throughout the storage process, otherwise, there would be disastrous leakage of the CO_2. The CO_2 will be present in the reservoir for multiple hundreds of years and the CO_2-brine-rock interaction will be continuous the whole time. This interaction alters the properties of the reservoir rocks and the alteration of the properties have consequences on the storage integrity of the reservoir rocks. Therefore, it is necessary to understand the effect of the CO_2-brine-rock interaction on the properties of the rocks before the storage of CO_2 in any reservoir rock. The nature of the alteration is seen to depend on the mineralogy of the rock, the physical condition of the reservoir and the phase of the CO_2 among other factors.

The effect of the phase of CO_2 on the CO_2-brine-rock interaction has not been well studied. Understanding the effect of the phase of CO_2 in the CO_2-brine-rock interaction in a CO_2 storage reservoir is very important considering the thermodynamic and phase behavior of CO_2, there will be evolution of the phase of the undissolved mobile CO_2 according to the prevailing temperature and pressure conditions. Each phase will have a unique effect on the CO_2-brine-rock interaction and consequently, the reservoir properties.

Therefore, this study evaluates the effect of four different phaseCO_2-brine reservoir states on the properties of reservoir rocks using an experimental and image-based approach. It was seen that the properties of the reservoir that are most affected by the scCO_2-br state of the reservoir include the secondary fatigue rate, bulk modulus, shear strength, change in the topology of minerals after saturation as well as change in shape and flatness of pore surfaces.

The properties of the reservoir that is most affected by the gCO$_2$-br state of the reservoir include the primary fatigue rate, change in permeability due to stress, change in porosity due to stress, and change in the topology of minerals due to stress. For all the samples, the roundness and smoothness of grains as well as smoothness of pores increased after compression while the roundness of pores decreased. Change in elemental composition of the rock minerals due to the CO$_2$-brine-rock interaction was seen to depend on the reactivity of the mineral with CO$_2$ and/or brine and the presence of brine accelerates such change. Carbon, Oxygen and Silicon can be used as index minerals for elemental changes in a CO$_2$-brine-rock system.

This research has evaluated the effect of different phaseCO$_2$-brine on deformation rate and deformation behavior, bulk modulus and compressibility, strength and stiffness, changes in pore geometry properties, porosity and permeability, as well as changes in micro-fabric, topology of minerals and elemental composition of minerals in saline rocks, and the result of this work can be applied to predicting the effect the different possible phases of CO$_2$ will have on the deformation, geomechanic indices and storage integrity of giant CO$_2$ storage fields such as Sleipner.

Table of Content

List of Figures

List of Tables

List of Appendices

Nomenclature

Mathematical symbols

π	Pi
μ	Dynamic viscosity
Q	Flow rate (cm^3 /s)
A	Area of the sample (cm^2)
d_c	Diameter of the core sample
M_{sat}	Mass of a saturated sample
M_{sub}	Mass of a submerged sample
M_{dry}	Mass of the dry sample
ρ	Bulk density of rock (g/cm^3)
L	Length of the disc shaped core sample in the direction of flow (cm)
Δ	Change
ΔP	Differential pressure in the direction of flow (atm/cm)
k	Permeability (Darcy)
Ψ	Sphericity of pore
V	Volume of a pore (mm^3)
a	Surface area of a pore (mm^2)
R	Equivalent radius of a pore (mm)
D	Equivalent diameter of a pore (mm)
τ	Tortuosity
Φ	Porosity measured from the digital rock (%)
$\varnothing$	Initial connected porosity (%)
$\varnothing_T$	Initial total porosity (%)
d	Diameter of the grain
ρ_p	Particle density taken as the average density of the minerals in the rock i.e. 2.58g/cm^3.
ΔL	Axial displacement
Δd	Lateral displacement
ε_a	Axial strain
ε_L	Lateral strain
ε_{vol}	Volumetric strain
$\Delta\varepsilon_{vol}$	Change in volumetric strain
$\Delta\varepsilon_a$	Change in axial strain
$\Delta\varepsilon_L$	Change in lateral strain
σ_{dev}	Deviatoric stress
σ_m	Mean effective stress
σ_3	Confining stress
σ_2	Intermediate stress
σ_1	Axial stress
σ_2	Peak stress
$\Delta\sigma_1$	Change in the axial stress
σ_f	Failure stress
q	Deviatoric shear stress
p	Mean effective stress
τ_{max}	Maximum shear stress
f_r	Fatigue rate

f_t	Fatigue duration
K	Bulk modulus
B	Compressibility
E	Stiffness
E_{t50}	Tangent modulus at 50% peak stress
C*'	End of shear enhanced compaction or the onset of dilation
V_2	Viscosity of CO_2-brine fluid at room temperature
V_1	Viscosity of distilled water at room temperature
ρ_1	Density of distilled water
ρ_2	Density of CO_2-brine fluid
t_1	Mean time for flow of distilled water
t_2	Mean time for flow of the CO_2-brine fluid

Acronyms/Abbreviation

2D	2-Dimension
3D	3-Dimension
BET	Brunauer-Emmett-Teller
br	Brine saturated sample
CCS	Carbon capture and storage
DIA	Digital image analysis
EDS	Energy dispersive spectroscopy
FIB SEM	Focused ion beam–scanning electron microscopy
FSI	Fluid structure interaction
GCCSI	Global carbon capture and storage institute
gCO_2	Gaseous CO_2 saturated sample
$scCO_2$-br	Supercritical CO_2-brine saturated sample
gCO_2-br	Gaseous CO_2-brine saturated sample
ICP-AES	Inductively coupled plasma-atomic emission spectroscopy
LVDT	Lateral variable differential transducers
M_{sat}	Mass of the saturated sample
M_{dry}	Mass of the dry sample
M_{sub}	Mass of a submerged sample
NLM	Non- local means
PPM	Part per million
PVD	Pore volume distribution
p-q curve	Deviatoric shear stress vs the mean effective stress curve
P-T	Pressure-Temperature
REA	Representative element area
REV	Representative element volume
ROI	Region of interest
SESI	Secondary electron secondary ion detector
SEM	Scanning electron microscopy
SEM-EDS	Scanning electron microscopy-Energy dispersive spectroscopy
XRD	X-ray diffraction
μ-CT	Micro-computerised tomography

Chapter 1: Introduction

1.1   Background on Geological CO_2 Storage

Climate change, global warming and sustainable energy are problems confronting the world today. Concerted efforts are in place by institutions, governments and industries to control climate change and its effects on the earth. The emission of CO_2 into the atmosphere is currently the main known cause of climate change and global warming. CO_2 is emitted through domestic and industrial activities that humanity depends on. Given this reality, it is imperative to keep a very healthy balance in the amount of CO_2 emitted into the atmosphere by human activities.

According to the Inter-Governmental Panel on Climate Change (IPCC) as cited in Allen et al. (2018), the earth's temperature has increased by about $1^{\circ}C$ since the pre-industrial time. This increase in temperature correlates with the increase in the rate of emission of CO_2, occasioned by the industrial revolution in the last century. At the present rate of emission, it is predicted that the earth's temperature is expected to rise by $2\text{-}5^{\circ}C$ by 2050. A target to limit the global warming to $1.5^{\circ}C$ by 2050 has been set by the IPCC. This target translates to keeping the atmospheric concentration of CO_2 at less than 450ppm, this means that deliberate policies and actions must be pursued to ensure that the present rate of emission of CO_2 is halved by 2050. To achieve this target, there is a call to action at national, institutional, industrial and individual levels. levels. The Ambitious goals of net zero and net negative CO_2 emissions are been pursued by institutions, industries and governments to make this target achievable.

CO_2 storage in deep porous rock formations, also known as geological CO_2 storage or geosequestration is a promising method for meeting the net zero target and minimize the anthropogenic CO_2 emitted into the earth's atmosphere. Despite the effort and progress towards clean and safe energy utilization, geological CO_2 storage is a field that needs further attention and development. This is because for a long time to come, fossil-fuel will still remain the main driver of most domestic and industrial process as can be seen in Figure 1.
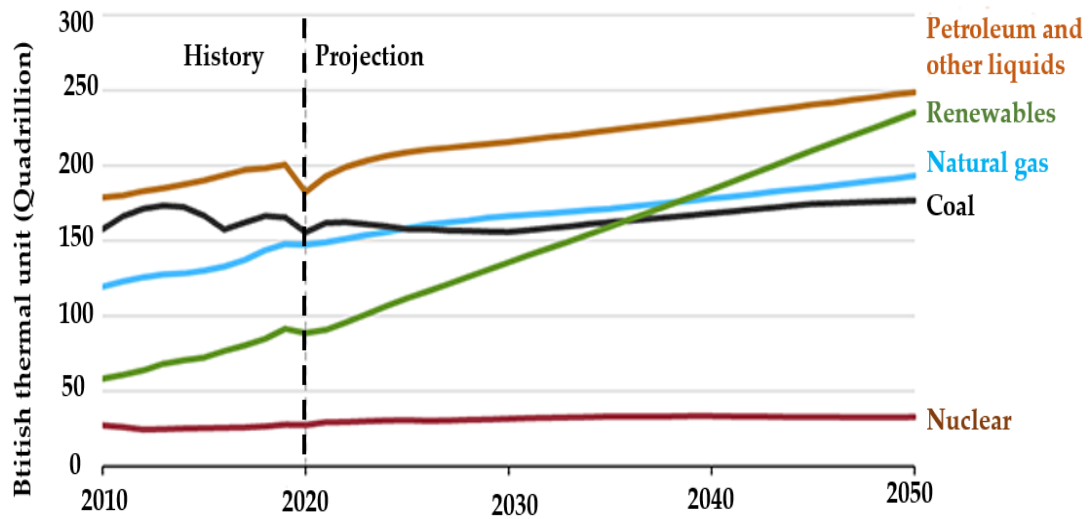
Figure 1: World energy consumption by source in quadrillion BTU. Collected from U.S Energy Information Administration, International Energy Outlook 2021.

In fact, the dependence of humans on fossil fuel is so intricate, that only a systematic and gradual change from the use of fossil fuel can be remotely feasible. Geological CO_2 storage has an additional incentive of providing CO_2 -enhanced oil recovery (CO_2-EOR). Another potential benefit of this process is the possibility of the reaction between the stored CO_2-brine-rock to result in useful mineral products.

Geological CO_2 storage is the last stage of a Carbon Capture and Storage (CCS) process. The precursor stages involve CO_2 capture (i.e the removal of CO_2 from the flux of gases emitted from sources such as power plants, steeland chemical industries, and gas stations etc.), followed by transportation of the captured CO_2 (i.e pressurization and transporting the treated gases via dedicated pipelines or other channels into favorable porous underground reservoirs). The entire process of CCS is illustrated in Figure 2. The porous underground reservoir could be a saline reservoir (Sandstone and Carbonates), depleted oil and gas fields, un-mineable coal seams or ocean sinks.
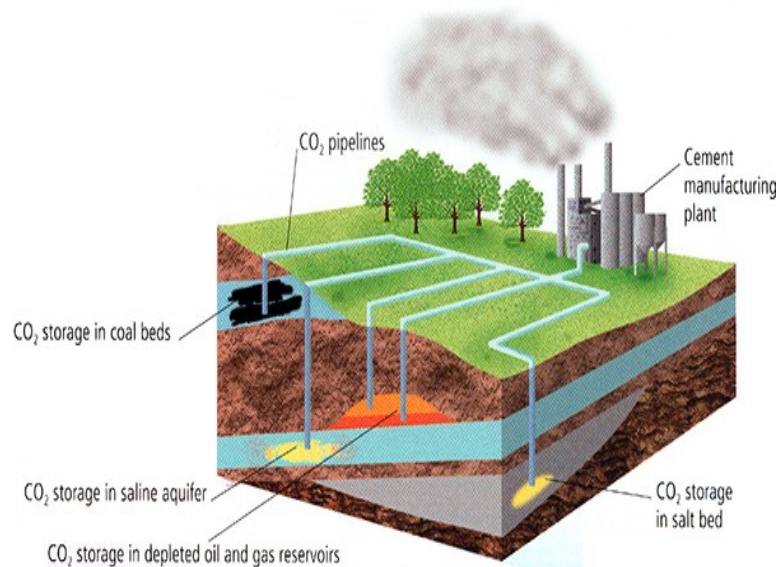
Figure 2: Schematic of carbon storage (Mann & Kump 2015).

Compared to the other types of storage reservoirs, the saline reservoir offers the greatest storage potential in terms of capacity (Li et al., 2009; Sun et al., 2016), and injectivity, as well as proximity to CO_2 sources. Estimates of the storage capacities of the various geologic reservoirs in the world are presented in Table 1. Estimate for saline fields is mostly from offshore environments because the onshore fields are considered too small and are of competing interest.

Over 200 million tonnes of anthropogenic CO_2 have been successfully injected and stored in geologic reservoir over several decades around the world; over 40 sites are presently and/or have in the past safely injected anthropogenic CO_2 into geologic reservoirs for enhanced oil recovery or for geological storage (GCCSI, 2018). Examples of such sites include In-Salah. Sleipner, Snohit and Otway amongst others. This show that geological CO_2 storage is a feasible technology for reducing the amount of CO_2 released into the atmosphere. However, there are concerns about the long term integrity of the storage reservoir considering the several changes that occur in the reservoir properties due to the CO_2-brine-rock interaction. The CO_2-brine-rock interaction has been shown to cause changes that could be constructive or deleterious to the ability of the reservoir to safely store the CO_2. There is a need to understand the effect the different phases of CO_2 will have on the time-dependent deformation and geomechanical properties of the reservoir rocks.

Geomechanical properties of reservoir rocks are affected when CO_2 is stored in them (Rutqvist, 2012). The injection and storage of CO_2 in reservoir rocks increases the volume of pore fluid and leads to a commensurate increase in pore pressure (Al-Zaidi et al., 2018). This increase in pore pressure changes the effective stresses on the rock (Rutqvist, 2012; Zhang, 2017). Effective stress depends on the change in pore pressure while the confining stress remains constant. The magnitude of change in pore pressure depends on the volume of pore fluid. In geosequestration, the volume of CO_2 in the pore reduces with time following dissolution and mineralization, therefore the effective stress on the rock increases as the volume of CO_2 in the pore and the pore pressure reduces. Change in the effective stress regime triggers geomechanical changes in the rock's framework.

The strength of a rock is very important for the integrity of CO_2 storage. The strength of the rock is controlled by the mineralogy, porosity, and grain geometry of the rock amongst other factors. These factors are affected by CO_2-brine, therefore the strength of the rock will be affected by the CO_2-brine. The influence will vary according to the phaseCO_2-brine because the change in stress due to CO_2 storage is dependent on the phase of the CO_2 (Al-Zaidi et al., 2018). To ensure the integrity of the reservoir, knowledge of how the different phaseCO_2-brine affects the strength and related geomechanical properties of reservoir rocks is important.

Mechanism of change in geomechanical properties in CO_2 storage rocks has been extensively studied (Bemer & Lombard, 2010; Delle & Sarout, 2016; Espinoza et al., 2018; Grombacher et al., 2012; Hangx et al., 2013; Lamy-Chappuis et al., 2016; Lei & Xue, 2009; Liu et al., 2016; Makhnenko et al., 2017; Marbler et al., 2013; Mikhaltsevitch et al., 2014; Rinehart et al., 2016; Vialle & Vanorio, 2011b; Xie et al., 2014). They reported changes in geomechanical properties and strength of rocks due to CO_2 activity. Researchers such as Alemu et al., 2011; Fuchs et al., 2019; Olabode & Radonjic, 2017; Pang et al., 2012; Pimienta et al., 2017 and Sun et al., 2016 observed that CO_2-br-rock interaction leads to change in the composition of the rocks, pore fluid and surrounding hydrogeology, while Han et al. (2020) and Rutqvist and Tsang (2002) reported a change in porosity due to CO_2-brine-rock interaction.

4

Dissolution, residual and capillary trappings are methods of trapping CO_2 in a saline reservoir. The rate of dissolution of CO_2 is therefore a critical parameter for effective CO_2 storage. Yan et al., (2011) Ratnakar et al.,(2020) and Mohammadian et al. (2015) provided solubility data of CO_2 in brine. It was seen that the solubility of CO_2 in brine depends on the temperature, pressure and molality of the brine. The solubility is very low at low pressure, high temperature and high brine molality. Therefore, in a geosequestration site, there will be undissolved CO_2 for a few thousand of years (Blunt et al. 2013). The phase of CO_2 depends on the pressure and temperature (P-T) conditions of the reservoir. Variability in P-T conditions results in a change of phase of CO_2. The P-T condition of reservoirs are variable (KGS, 2003; Wang et al. 2014). This means that the undissolved CO_2 will be present in different phases with the brine (Acevedo and Chopra 2017; Zhang et al. 2019). The undissolved CO_2 is contained in the pores with the brine and will change the shape, radius, sphericity and flatness of the pores, as well as the porosity. These changes are induced by the pressure of the pore fluid and the associated geochemical reactions. Al-Zaidi et al. (2018) showed that the pore pressure due to CO_2 depends on the phase of the CO_2 and Vanorio et al. (2011) opined that compositional changes control the change in the rock's fabric as well as other changes in rock's properties. So, different phaseCO_2-brine present in a reservoir will trigger unique changes. Therefore, there is the need to understand the effect of the different phaseCO_2-brine on rock properties in a CO_2-brine-rock interaction. This study looks at the effect of different phaseCO_2-brine on the pore geometry properties of saline reservoir rocks. Pore geometry properties are important because they control the transport, petrophysical and geomechanical properties of the rock (Akbar et al. 2019). Change in pore geometry leads to change in the transport properties, strength, and stiffness of porous rocks. This has been reported by Delle Piane and Sarout (2016); Griffiths et al. (2017), Sun et al. (2017), Islam et al. (2019), Fuchs et al. (2019), Foroutan et al. (2020), Seyyedi et al. (2020), Luo (2020), Han et al. (2020), Li et al. (2020), Rigby et al. (2020) and Tan et al. (2020). The type of rocks used in these researches reflects the variety of porous saline rocks that can be used as reservoirs for CO_2. They range from heterogeneous carbonate rocks and sandstones, to shale rocks that serve as a caprock. Berg et al. (2017), Sun et al. (2019) and Islam et al. (2019) characterized sandstones and carbonate rocks from digital rock physics. Digital rock

physics involve evaluating the properties of rocks using digital images from micro-CT using suitable software (Andrä et al., 2013; Faisal et al., 2019; Lesueur et al., 2017; Li & Iskander, 2021; Madonna et al., 2012; Voorn et al., 2015; Walls & Sinclair, 2011).

Saline rocks contain minerals and pores of different shapes and sizes in the form of grains and voids. The pores normally contain fluid that exerts pressure on the grains. The pressure leads to alteration in the rock's fabric, mineral topology, mineral composition and consequently, the bulk and transport properties of the rock (Pearce et al., 2019; Rathnaweera et al., 2016; Vanorio et al., 2011). The magnitude of this pore pressure, and the consequent alteration in the fabric, the topology and the composition of the rock depends on the nature of the pore fluid amongst other factors. Al-Zaidi et al. (2018) showed that the pore pressure due to CO_2 injection into porous rock depends on the phase of the CO_2. Given the variation in pressure-temperature (P-T) conditions of reservoirs as shown by KGS,(2003), the thermodynamics and phase behavior (Ricketts, 2016), as well as the solubility of CO_2 in brine. There will be undissolved CO_2 and the undissolved CO_2 will exist in different phases alongside brine in the reservoir for a long time (Peter et al., 2020; Xie et al., 2016). Blunt et al. (2013) predicted this time to be in thousands of years.

The mechanism by which pore fluid and pore pressure influences the micro-fabric, the topology of minerals, the composition and other properties of the rock is by stress corrosion (Suppe, 2014; Wu et al., 2018). Stress corrosion is a progressive chemo-mechanical reduction in the surface energy and strength of the saline rocks (Kvashnin et al., 2019). The reduction in surface energy and strength of saline rocks have been explained as a consequence of the absorption of pore fluids at the grain surface, causing breakage in the crystal boundaries (Azadi Tabar & Ghazanfari, 2019), this has been called Rehbinder effect in literature. The exposed bond in contact with the fluid breaks and accepts a new atom into the bridging bond. This is followed by bond lengthening and weakening, then newer surfaces are exposed and the crack grows deeper. As shown by Vanorio et al. (2011), compositional changes are thought to control the change in fabric and strength, as well as other changes in rock's properties.

6

Sub-surface CO_2-brine-rock reaction results in a change in chemical composition. This leads to change in other properties of rocks. Vanorio et al. (2011) explained that change in chemical composition controls the change in fabric and strength as well as other changes in rock's properties. This is true for both the reservoir rock that contains the CO_2 and the Caprock that seals the reservoir rock and prevent the CO_2 from escaping. The sealing integrity of the Caprock is a critical parameter during CO_2 storage as much as the integrity of the reservoir rocks. The Caprock should be devoid of any fault or fracture that can allow leakage. It should be dense, intact and thick, relatively impermeable, be composed of minerals with proven sealing capability, as well as should possess high compressive strength. Olabode and Radonjic (2013) explained that Caprock with a smaller pore throat size makes a better seal. It, therefore, means that any reaction or process that increase the pore throat size of the caprock will be detrimental to the sealing integrity of the caprock. Similarly, any reaction that leads to a reduction in the strength of the Caprock, the formation of new micropores or fractures, an increase in permeability, and degradation of the mineral composition of the Caprock will be detrimental to sealing integrity of the Caprock and the CO_2 storage, and vice versa.

Most researches that have studied the effect of CO_2-brine interaction on the properties of rocks in the context of CO_2 storage have used supercritical CO_2 because most CO_2 storage sites inject CO_2 at supercritical state (Delle & Sarout, 2016; Fuchs et al., 2019; Liu et al, 2020 and Pimienta et al., 2017). There is an assumption that the CO_2 remains in a single phase throughout the storage history, but this is not always true. However, based on the thermodynamics and phase behavior of CO_2, the phase of undissolved CO_2 in the storage reservoir will evolve with time. Lu and Connell (2014) explained that the density and phase of the supercritical CO_2 injected into wells, change over time in response to the variation in P-T condition. The change in the phase of CO_2 in the reservoir and its consequences have been reported by Paterson et al. (2008), Denney (2009) and Lu and Connell (2014). Researches have shown that CO_2 storage in saline rocks lead to change in the transport, petrophysical and geomechanical properties of the rocks. For example, Saeedi et al.,(2011) observed that the multiphase flow characteristics of CO_2-brine reservoir change due to chemical reactions, and change in stress in reservoir conditions associated with flooding cycles.

7

Similarly, Reynolds and Krevor (2015) reported changes in relative permeability of saline rocks due to CO_2 flow. Vanorio et al. (2011) has shown that injecting CO_2 into brine-rock system induced chemo-mechanical processes that permanently alters the rock's framework, and Griffiths et al., (2017) showed that change in pore aspect ratio influences the strength and stiffness of porous rocks. Reduction in the strength of the rocks due to CO_2-brine-rock reaction has been reported in Delle and Sarout (2016), Pimienta et al. (2017), Meredith et al., (2017), Espinoza et al. (2018), Keshavarz et al. (2019), Fuchs et al. 2019 and Zhang et al., (2020). The change in the strength of rocks is seen to vary from slight to high depending on the mineralogy and the reservior conditions. The types of rock used in these researches range from carbonate rocks, sandstones and shale rocks. It is clear that research on the effect of different phaseCO_2-brine on the pore geometry properties of reservoir rocks is lacking. Therefore, this research sets out to evaluate the changes to the pore geometry of a saline rock due to the different phaseCO_2-brine using digital rock physics. Digital rock physics involve evaluating the properties of rocks fromdigital images from micro-CT using suitable software. Applications of digital rock physics in studying rock properties are rapidly growing and examples can be found in Andrä et al. (2013); Lesueur et al. (2017); Berg et al. (2017) and Sun et al. (2019).

In the light of the finding by Al-Zaidi et al. (2018) that the change in pore pressure (and thus effective stress) due to CO_2 injection depends also on the phase of the CO_2, it is necessary to understand how the change in stress from the different phases of CO_2 that could be present in a CO_2 storage reservoir affects the deformation and geomechanical properties of the reservoir. This will enable a better understanding and prediction of the behaviour of the reservoir and provide better information with which to constrain CO_2 storage modelling studies.

As this research seeks to evaluate the effect of different phaseCO_2-brine on deformation rate and geomechanical properties of the rocks, it is necessary to determine the exposure time needed for the different phaseCO_2-brine to have a marked impact on the rock's properties. In a prior experiment where CO_2 was flooded into a brine saturated sample immersed in excess brine, it was observed that for the first five days of CO_2 flooding, there was a gradual drop in CO_2 pressure until the sixth day

when the CO_2 pressure stabilized. This indicates that the CO_2 was actively dissolving into the excess and pore brine and forming an acidic solution for the first five days until the sixth day when all the brine became saturated with CO_2. Also, Li et al. (2019) reported that the effect of CO_2 on the properties of rocks increases with a longer exposure time. Therefore the effect of CO_2-brine on the properties of rocks is exposure-time dependent. Results from Peter et al. (2020); Pimienta et al. (2017); Zou et al. (2018) and Olabode and Radonjic (2013) showed that the impact of CO_2 on the properties of rock starts vigorously almost immediately. Therefore, it was decided that for this experiment, more than 5 days would be good enough for the phaseCO_2 saturated-brine to have an effect on the properties of the rocks. The samples were flooded in the different phaseCO_2-brine for 7 days.

Table 1: World-wide CO_2 storage capacities in different reservoirs

Storage option	Capacity	Source	Resource estimate level
Oil and gas fields	675-900 Gt-C	(Doherty et al., 2017; Klass & Wilson, 2008)	Theoretical
Un-mineable coal seams	3-200 Gt-C	(Klass & Wilson, 2008; Yamasaki, 2003)	Theoretical
Deep saline fields	>1000 Gt-C	(Klass & Wilson, 2008)	Theoretical

There has been little interest in CO_2 storage in coal seams because of the historical competing interest on coal, and the peculiar issues associated with coal storage. Such issues include high reduction of strength otherwise known as outburst (Mehic et al., 2006), excessive induced fracturing which could result in a costly increase in the permeability of coal in ground conditions (Viete & Ranjith, 2006), matrix-swelling (Shukla et al.,2010), and low porosity and permeability (Bickle, 2009; Garg & Shukla, 2009; Viete & Ranjith, 2006). Ocean sinks are also rarely considered as geosequestration sites because of the high environmental risk it portend for the oceanic ecosystem (Shukla et al., 2010).

1.2   Behavior and timescale of CO$_2$ in geological storage

When CO$_2$ is injected into a reservoir for storage, it becomes subject to the temperature and pressure conditions in the reservoir. At depth, it undergoes a relative change in density depending on the geothermal gradient. Figure 3 shows the change in density of CO$_2$ according to different geothermal gradients. Under the pressure-temperature conditions commonly found in the subsurface, both gaseous and supercritical CO$_2$ can be present, and both are less dense than the water or brine contained in the pore spaces of the reservoir, this allows for buoyant rise relative to the water or brine (Figure 4). This buoyant rise facilitates mixing with saline water, firstly by diffusion, and later by convection current, followed by dissolution. The buoyant nature of CO$_2$ makes the presence of an efficient trapping mechanism very necessary.
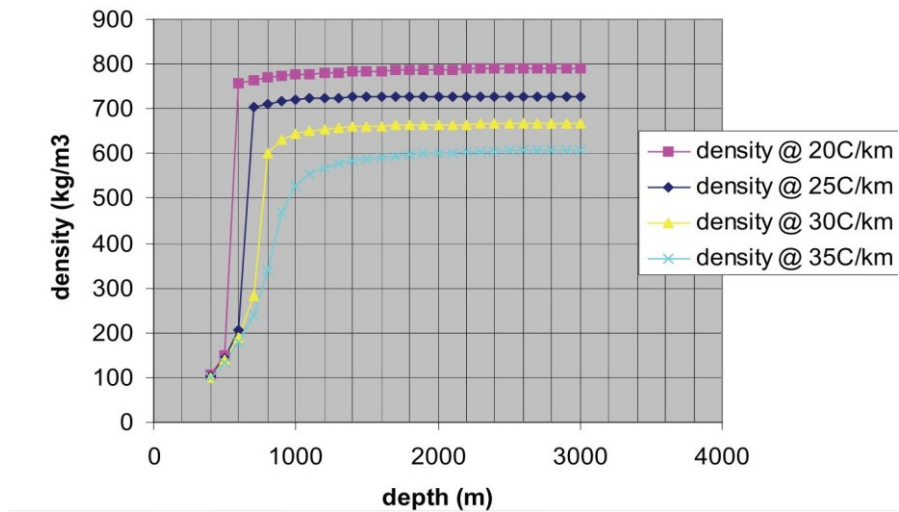
Figure 3: Density variation with depths at different geothermal gradients (Holloway et al., 2006a). Geothermal gradient and pressure conditions in the storage reservoir causes CO$_2$ to undergo a relative change in density at depths between about 600 and 1000m.
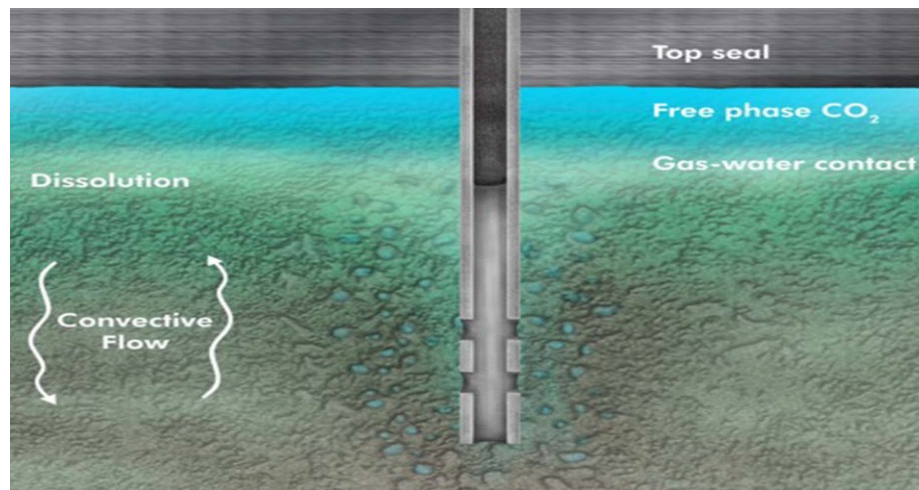
Figure 4: Schematic of CO_2-brine mixing in a deep saline reservoir (CO2CRC, 2015)

CO_2 injected for storage into a reservoir combines with the pre-existing brine in the reservoir. If the interface between the injected CO_2 and the brine is perfectly stable, mixing of the brine and CO_2 would be by diffusion and would be very slow. Diffusion-mixing will be faster if the reservoir is thin and if the CO_2-brine interface is wide and has a high surface area to volume ratio. Mixing continues for a few thousands of years for typical injection scenarios (Blunt et al., 2013; Ennis-King & Paterson, 2001).

Mixing by fluid convection also occurs within the reservoir. Mixing by convection is an active process in most CO_2 storage reservoirs, because the density of CO_2-saturated brine is approximately 10 kg/m³, two times greater than pure brine. Molecular diffusion of CO_2 into the brine sets up an unstable hydrodynamic layer at the CO_2/brine interface. This creates convection currents within the brine as the CO_2-rich brine descends toward the base of the reservoir formation and the pure brine rises to the top of the reservoir rock. Convection mixing is predicted to be more rapid in thick, relatively homogeneous reservoirs than in thin low permeability reservoirs (Lindeberg & Bergmo, 2003). Ajibola et al., (2016) explained that understanding whether the dominant mixing mechanism is convective mixing rather than pure diffusion is important as this affects the timescale over which free undissolved CO_2 would be present in the reservoir while the carbon dioxide-saturated brine mixes with the unsaturated brine.

Until the CO_2 dissolves completely into the brine, the resident undissolved CO_2 will be mobile and migrate within the reservoir both vertically and horizontally. The rate of dissolution of the CO_2 in brine is dependent on the solubility of the CO_2 in the brine or the CO_2 saturated brine, the temperature, pressure as well as the salinity of the brine. The preferred direction of migration is determined by factors including the geometry of the reservoir, the permeability (Oldenburg, 2006) and the fracture orientation, stress and pressure conditions as well as density, buoyancy and interface as well as the viscosity of the CO_2. This migration could be slow or fast, depending on similar factors, as well as the density and CO_2-brine mixing pattern. Slow mobility of the CO_2 allows for more reaction between CO_2-brine where an acidic solution which reacts with rock minerals to precipitate new minerals is formed. If this happens, less un-reacted mobile CO_2 will be available in the reservoir and there would be less buoyancy pressure on the top part of the reservoir rock and the caprock. Conversely, if the rate of migration is fast, there would be less CO_2-brine-rock reaction (dissolution and precipitation), more buoyancy pressure is then exerted on the top part of the reservoir rock and caprock as a result of the higher volume of un-reacted mobile CO_2.

The mobility and reactivity of CO_2 go on for a few thousand years until all the CO_2 is dissolved/mineralized (Blunt et al., 2013; Holloway et al., 2006; Peter et al., 2020; Plug & Bruining, 2007). Because of the thermodynamic and phase behavior of CO_2, and the fact that the temperature and pressure conditions of the reservoir are variable (Figure 5), more so that injection of CO_2 is done at temperature and pressure conditions around the critical point where phase transition is highly likely (Figure 6), the mobile undissolved CO_2 in the reservoir will exist in different phases (Buscheck et al., 2019). Hence, there will be different phaseCO_2-brine states in the reservoir at different depths and times, depending on the phase of the mobile CO_2. Al-Zaidi et al., (2018) showed that the pore pressure and effective stress due to CO_2 in a porous rock depend on the phase of the CO_2. The pore pressure and effective stress affect the properties of rocks.
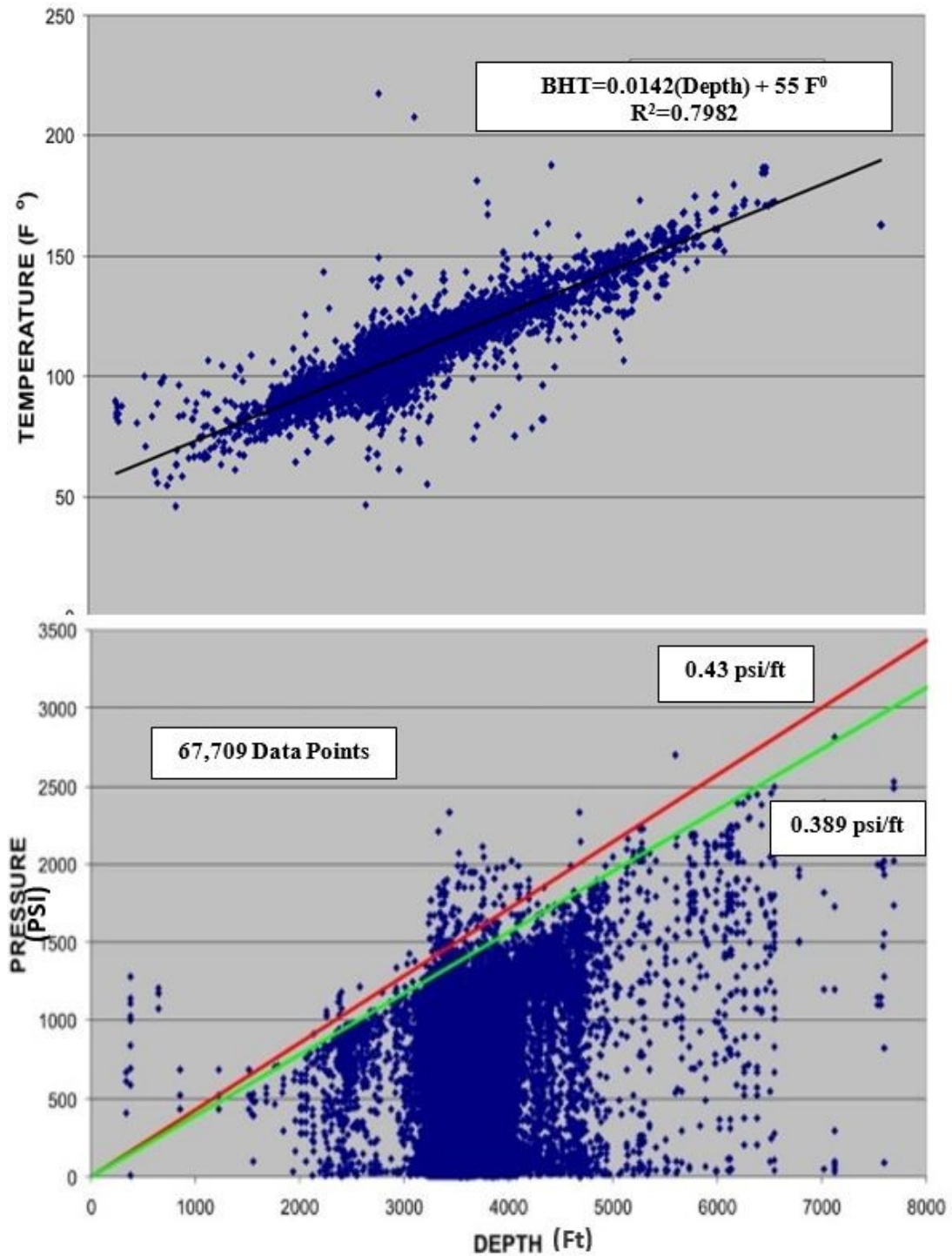
Figure 5:Corrected bottom hole temperature from 19161 well bores (top) and bottom hole pressures from 57,709 well bores (bottom) both showing a steady increase in temperature and pressure with depth (geothermal gradient) and great variation in tempera temperature and pressure measured from different wellbores at the same depth (KGS, 2003).
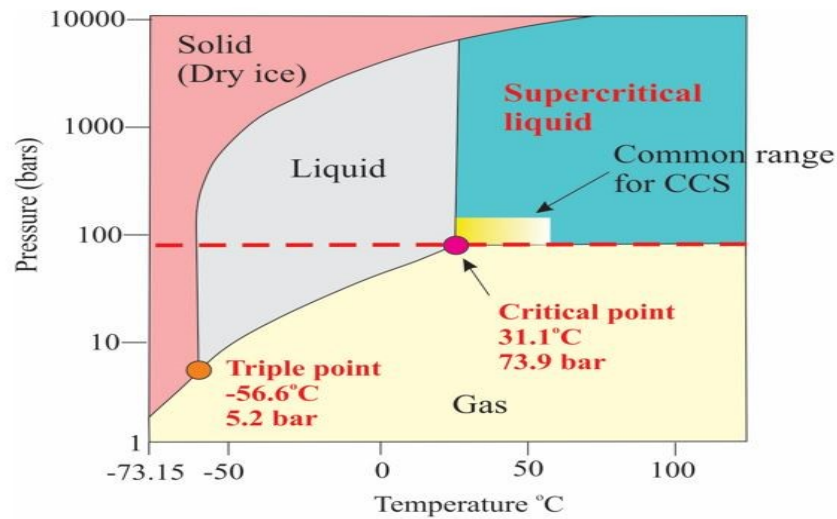
Figure 6: The phase diagram showing temperature and pressure conditions for the different phases of carbon dioxide (Ricketts, 2016).

1.3 Non-geological CO_2 storage methods

There are other non-geological methods of storing CO_2. These methods include a range of biological CO_2 sequestration and CO_2 utilization methods. Biological CO_2 sequestration involves the storage of atmospheric CO_2 in biomass (vegetation) and aquatic environment (oceanic water). Storing CO_2 in biomass involves planting trees (biomass) that extract CO_2 from the atmosphere as it grows. Compared to geological CO_2 storage, this method may have a higher monetary cost and land use implication per unit of CO_2 stored. Unlike geological sequestration, the amount of CO_2 that can be removed per unit of biomass is not exactly known, so it may be difficult to rely on this method to effectively remove atmospheric CO_2. Also, compared to geological CO_2 storage, there is the challenge of permanence in this method, as CO_2 may be released into the atmosphere when the biomass is burnt to release energy except Bioenergy with Carbon Capture and Storage (BECCS) is in place, in BECCS, bioenergy is extracted from biomass that has been extracting CO_2 from the atmosphere. The energy is extracted in useful forms such as electricity, heat or biofuels through combustion, pyrolysis or fermentation. The remnant of the energy extraction process often referred to as biochar contains CO_2, and is stored away by geologic sequestration. BECCS is believed to be a negative emission process, but only if it ends with geological sequestration of the biochar.

14

Storage of CO_2 in the aquatic environment is another option. It utilizes the ability CO_2 to dissolve in water. This method has a limitation of volume, as it can only be achieved in a marine environment, provided the pressure, temperature and solubility conditions are met. This process acidifies the aquatic environment and harms the aquatic ecosystem, therefore, this method is discouraged.

Storage of CO_2 by CO_2 utilization is another option. This applies the circular economy model in handling CO_2 such that CO_2 is used in making concrete, land and water remediation and other useful products. The principle is that the CO_2 is utilized and permanently locked up in the product through carbonation, redox and precipitation reactions. The amount of CO_2 that can be taken out of circulation depends on the product in which the CO_2 is been locked up. Also, the use of CO_2 in these products must not reduce the desirable qualities of the product, rather it should improve the desirable qualities of the product if this method will be economically viable. While this method may be effective, unlike geological CO_2 storage, this method still needs a lot of research and development, especially to optimize the reaction process for the products.

This research focuses on geological CO_2 storage. This method has been shown to be safe, feasible, effective and considerably well-developed compared to the others. Over 200 million tonnes of anthropogenic CO_2 has been successfully injected and stored in geologic reservoir over several decades around the world, plus there are surplus of porous saline reservoirs in both onshore and offshore environments that make it the most popular option. The scope of this thesis is limited to the effect of different phaseCO_2-brine on the physical, geomechanical, mineralogical and petrophysical properties of the reservoir rocks, and the implication for CO_2 storage integrity.

1.4   Background of this research

The petrophysical, mineralogical and geomechanical properties, as well as micro-fabric and topology of rocks, are affected by the effective stress, pore fluid, pore pressure as well as pore and grain geometry of the rocks. When CO_2 is injected and stored in a reservoir, it is contained in the pore spaces and affect the effective stress, pore fluid, pore pressure, pore and grain geometry of the rocks by dissolution and/or

15

precipitation, which consequently affect these properties of the rock.(Olabode & Radonjic, 2013).

Considering the solubility of CO_2 in brine, resident undissolved CO_2 will exist in the reservoir for a long time, studies have indicated that resident undissolved CO_2 in the subsurface exist for thousands of years (Holloway et al., 2006; Peter et al., 2020; Plug & Bruining, 2007). The phase of CO_2 is controlled by the temperature and pressure conditions. The temperature and pressure conditions of the reservoirs are variable as shown in borehole's temperature and pressure in Figure 5. Studies have also indicated that due to the variability in temperature and pressure conditions, the undissolved CO_2 will not remain in a single state throughout the storage history as there will be change of phase over time (Buscheck et al., 2019; Holloway et al., 2006; Peter et al., 2020; Plug & Bruining, 2007). Previous studies by Delle and Sarout (2016), Al-Zaidi et al. (2018) and Jin et al., (2020) suggest that the change in effective stress, pore pressure and properties of rocks in a CO_2-brine-rock interaction is sensitive to the phase of the CO_2. Therefore, the different phaseCO_2-brine in saline reservoir can trigger unique kind of alteration in the geomechanic, petrophysical and mineralogical properties, as well as micro-fabric and topology of the rock. It is necessary to understand how the different phaseCO_2-brine affect the properties of the reservoir rocks. Therefore, this research sets out to investigate the effect of different phaseCO_2-brine on properties of reservoir rock.

The states of the samples used in this experiment include dry sample, br saturated sample, gCO_2-br saturated sample, scCO_2-br saturated sample, and gCO_2 saturated sample. These various states represent the different phaseCO_2-br states that could exist in CO_2 storage. A sample was tested in dry conditions to represent the property of the dry natural reservoir rock. The gCO_2-br and the scCO_2-br reservoir conditions represent a scenario where gaseous and supercritical CO_2 exist with the brine respectively. The gCO_2 saturated reservoir represents when gaseousCO_2 migrates into a dry reservoir, while the brine saturated reservoir represents the normal saline reservoir before saturation with CO_2.

1.5   Definition of the problem

Studies evaluating the effect of CO_2-brine-rock interaction on the properties of reservoir rocks have treated CO_2 as if the injected CO_2 remains in a single phase throughout the storage history. Most researches concerning the effect of stored CO_2 on reservoir rocks have considered CO_2 in supercritical phase with or without brine. Because reservoir condition is variable, and given that the phase of the undissolved resident CO_2 changes with time according to the reservoir conditions, there is a need to understand how different phaseCO_2-brine affect the properties of the reservoir rocks. However, the effect of the different phases of CO_2 in a CO_2-brine-rock interaction on rock properties has not been investigated explicitly. Therefore, this study sets out to investigate the effect of the different phaseCO_2–brine on the properties of the rock. This will enable a better understanding and prediction of the changes in reservoir properties in a geosequestration site and provide better information for CO_2 storage modelling studies.

1.6   Aim and Objectives

The aim of this research is to evaluate the impact of the different phaseCO_2-brine on the geomechanical, mineralogical, petrophysical properties as well as the micro-fabric, and the mineral topology of the CO_2 storage reservoir rocks. This will provide a better understanding and prediction of the response of the reservoir rocks to CO_2 storage, and provide better insights with which to design and constrain future CO_2 storage modelling and experimental studies.

To achieve the aim, core flooding-triaxial compression laboratory experiments and image-based pore-scale models will be used to evaluate the petro-physical, mineralogical, geomechanical, micro-fabric, and topological responses of reservoir rocks. The objectives include:

- Characterize the Captain Sandstone sample in a dry natural state i.e petro-physical, mineralogical, micro-fabric, topological, and geomechanical characterisation.
- Prepare core samples to represent all the phaseCO_2-brine states in this study. Characterize the samples after saturation with the different phaseCO_2-brine to

evaluate the effect of saturation with the different phaseCO_2-brine on the petro-physical, mineralogical, micro-fabric, and topological properties.

- Conduct triaxial compression test on the saturated samples with the triaxial test conditions simulating the reservoir condition at depth, and characterize the compressed samples to evaluate the effect of compression on the petrophysical, geomechanical, micro-fabric, and topological properties of the saturated samples.

- Create a digital rock model from micro-CT and SEM images of the samples from (2 and 3 above) and determine the representative element volume (REV)/representative element area (REA) of the digital rock.

- Use the REV/REA size of the digital rock model to characterize the pore and grain geometry, mineralogical, and the topological properties of the rocks using digital rock physics and rock image analysis techniques.

- Conduct finite element analysis showing the distribution of strains in the digital rock model under the reservoir's confining pressure condition.

1.7   Scope and limitation

This research is designed to study the effect of the phase of CO_2 in CO_2-brine-rock interaction on the properties of reservoir rocks. It is assumed that the effect of a different brine state is independent and not passed on to another phaseCO_2-brine state. The result applies to core and pore-scale.

1.8   Contribution of this research to knowledge

This research extends the understanding of CO_2-brine-rock interaction, including contributing new knowledge on the effect of the phase of CO_2 in a CO_2-brine-rock interaction in geosequestration sites. The understanding and knowledge generated by this research will be valuable in improving the prediction of the effects of CO_2-brine-rock interaction on the physical, geomechanical, chemical and petrophysical properties of reservoir rocks, and contribute to ensuring CO_2 storage integrity in geosequestration towards meeting the target of net zero.

1.9   Outline of the thesis

This thesis is composed of 9 chapters. Chapter 1 discusses the motivation and the concept of geological CO_2 storage explains the background of this research and defines the problem this research sets out to address as well as the aim. The scope and limitation, as well as the outline of the thesis are also considered in this chapter.

Chapter 2 presents a systematic review of relevant scientific literature as well as technical issues concerning geological CO_2 storage.

Chapter 3 presents a detailed description of the samples, procedures and methodology used in this research.

Chapter 4 contains the results and discussion of the initial characterization of the samples before the commencement of the experiments.

Chapter 5 shows the results and discussion of the static fatigue test in terms of evaluated geomechanical indices for all the different phaseCO_2-saturated samples. This chapter has been published as a journal article. See section 9.3 for details.

Chapter 6 shows the results and discussion of the multiple failure triaxial compression test in terms of the strength and related geomechanical indices for all the different phaseCO_2-brine saturated samples.

Chapter 7 explains the procedure employed for the determination of the representative element volume (REV). It contains the result and discussion of 3D analysis of the REV size of the digital rock model in terms of pore geometry properties, and discusses the effect of the different phaseCO_2 brine on the 3D pore geometry properties of the rocks. This chapter is under review as a journal paper. See section 9.3 for details.

Chapter 8 explains the procedure employed for the determination of the representative element area (REA), contains the results and discussion of the effect of the different phaseCO_2-brine on the mineral topology, micro-fabric of pore and grain, and composition of rocks from 2D rock image analysis. It also presents the results of image-based finite element analysis (FEA) on the digital rock model. Parts of this chapter is under review as a journal paper. See section 9.3 for details.

Chapter 9 presents the conclusions drawn from the entire work as well as recommendations for future work.

Chapter 2: Literature Review

Safe injection and storage of the captured CO_2 in a favourable geologic reservoir is the ultimate goal of CO_2 storage. Identifying a favourable geologic reservoir is very important to successful storage. The formation has to have good transport, petro-physical, mineralogical and geomechanical properties. Models are often used to simulate the containment, injectivity and capacity of reservoirs. Around the world, over 200 million tonnes of anthropogenic CO_2 has been successfully injected and stored in geologic reservoir over several decades. Over 40 sites are presently and/or have in the past, safely injected anthropogenic CO_2 underground for enhanced oil recovery or explicitly for geological storage (GCCSI, 2018). This proves that this technology is feasible.

2.1   Types of CO_2 geologic reservoirs

Reservoirs, where CO_2 can be stored, include the saline reservoirs, depleted oil and gas fields, un-mineable coal seams and ocean sinks. This research focuses on saline reservoirs. Hence in this section, the capacity of the saline reservoir will be compared to the other geologic reservoirs. However, the storage capacity of other forms of the reservoir will be discussed briefly.

2.1.1 CO_2 storage in saline reservoir

Saline reservoirs are deep, porous and permeable geological formations. The worldwide storage capacity of saline reservoir is over 1000Gt-C (Klass & Wilson, 2008), included in the estimate are onshore saline fields which are sometimes considered too small and usually of competing interest. Saline reservoirs offer the greatest storage potential in terms of capacity (Li et al., 2009; Sun et al., 2016). Presently, about 90% of storage sites are in deep saline. For instance, Sleipner project was in an offshore deep saline environment, the In Salah CCS project was hosted by an onshore deep saline reservoir, so also is the Otway CCS site. About 99% of possible storage sites identified in china are in the deep saline (Li et al., 2009). In the UK, the offshore saline reservoir theoretical storage estimate is put at 78 Gt-C (Bentham et al., 2014).

The drawback of the saline reservoir compared to the depleted oil and gas field is the need to build infrastructure from the scratch and the possibility of over pressurization especially if the pore pressure due to injection rises too high. While Kim et al., (2013) identified saline reservoirs as the most promising for safe, and effective CO_2 storage, Holloway et al., (2006), pointed that the capacity of saline reservoir must be filtered through the following considerations: (a). Parts of saline reservoir are sources of potable water for human population. (b). Reservoirs where leakage of the injected CO_2 could lead to contamination of potable water must be avoided. (c). Target depth for CO_2 storage must be greater than 800m except where there are particularly large structural or stratigraphic traps above this depth. The lower depth limit of 800m stated above is because it is assumed that at a depth greater than 800m, thedepth, temperature and pressure of most reservoir are such that the CO_2 will be in the supercritical phase (Zulqarnain et al., 2017). Supercritical CO_2 gives an operational advantage to CO_2 storage because the liquid-like density allows for more volume of CO_2 to be stored per unit pore volume and also reduces the buoyancy drive. This depth also allows enough clearance for human activities, extraction of potable water, and allows for intervention in the event of leakage (d). Over-pressured reservoirs must be avoided. (e). Reservoirs with no viable trapping mechanism and/or seal are considered unsuitable.

Shukla et al. (2010) noted that for storage in a saline aquifer to be sustainable, the reservoir must be large and isolated and must have good reservoir properties i.e adequate porosity, permeability, depth, thickness, and poro-elastic properties. It must have an adjoining caprock with a good sealing capacity. Also, the mineralogy of the reservoir must be such that the ensuing reactive process does not degrade the reservoir.

2.1.2 CO_2 storage in depleted oil and gas reservoirs

Oil and gas reservoirs are first saline reservoirs before they become oil and gas reservoirs. This is so because a saline reservoir only needs to go through the window of generation and migration of oil and gas to be transformed into an oil and gas reservoir. Oil and gas are generated at great depth and are normally associated with displacement of saline fluids (Cao et al., 2016). Depleted oil and gas fields hold good prospects for CO_2 storage both in offshore and onshore environments, with an estimated worldwide storage capacity of 675-900 Gt-C (Doherty et al., 2017; Klass &

Wilson, 2008). The operating principle for CO_2 storage in depleted oil and gas reservoir is the replacement of the pores previously occupied by oil and gas with CO_2. According to Shukla et al. (2010), depleted gas reservoirs are great for CO_2 storage because they have proven capacity to hold gas for geologic time. This storage option holds the added benefit of enhanced oil recovery, if needed. However, CO_2 injection for storage poses unique challenges compared to injection for enhanced oil recovery, because of the potential to generate low temperature due to CO_2 expansion into vapour phase during the injection. Storage in depleting and depleted oil and gas field has a comparative cost advantage over saline storage in terms of experience and infrastructure, i. e the facilities used during the production of oil and gas could be employed during CO_2 injection for storage, there is already a considerable body of knowledge on the behaviour and characteristics of the reservoir which could be applied in the CO_2 storage project, and there is a slim chance of over- pressure provided the storage capacity is not exceeded. On the other hand, the drawbacks in this reservoir type include limitation in storage capacity, as its capacity is limited to the depleted zones, and the high probability of leakage through existing well (abandoned or producing). However, the capacity for CO_2 storage in depleted oil and gas field will increase as more oil and gas fields are depleted (Shukla et al., 2010). At present, it is the storage option that is most popular because of the cost advantage it has over other storage types. However, every CO_2 injection well requires a design specific to the reservoir conditions, injection rates and injection stream characteristics. (Acevedo & Chopra, 2017).

2.1.3 CO_2 storage in un-mineable coal seams

Coal becomes un-mineable when the calorific value of the coal is not enough to generate good heat, or when a mine has been worked exhaustively at the present level of technology, or when the geologic disposition of the mine is such that it cannot be worked at a profit. This kind of coal provides another opportunity to store CO_2 (Connell et al., 2011; Jessen et al., 2007). Yamasaki (2003) puts the amount of worldwide CO_2 storage capacity in un-mineable coal at 11Gt-C. Storage in coal releases methane gas in the process. The mechanism of storage is in the micropores of the coal as free gas or as pore fluid, or by adsorption at the surface of the coal. The

former requires that the coal seam has enough micropore spaces that should be interconnected, while the latter requires that the pressure condition of the seam is below the desorption pressure.

Overall, coal is less preferred for CO_2 storage, largely because of the peculiar issues associated with coal and the fact that coal has other competing use. The major issues with CO_2 storage in coal include (a). Reduction in strength as a result of influx of CO_2 in coal, has been referred to as "outburst" in the literature. (b). Low permeability and porosity of coal (Bickle, 2009; Garg & Shukla, 2009; Viete & Ranjith, 2006). (c).The possibility of fracturing and increased permeability resulting from loss of strength due to CO_2 saturation. (d). Matrix swelling that affects the storage capacity of coal especially when the mechanism of storage is adsorption. Consequently, there is a high chance of leakage from un-mineable coal. This has costly economic, environmental and health implications. Mehic et al. (2006) conducted a study on the geomechanical behaviour of the Australian black coal under the CO_2 saturation, they reported a great reduction of the strength of the black coal under uniaxial compression test conditions. A similar study by Viete and Ranjith (2006) on the Australian brown coal agreed with the former, and suggested that such a trend may induce fracturing which could result in a costly increase in permeability of coal in ground conditions. The matrix-swelling effect of coal, when exposed to CO2 and water, was reported by Shukla et al. (2010), and this could reduce the permeability of the coal. The empirical evidence shows that coal is not a good candidate reservoir for CO_2 storage.

2.1.4 CO_2 storage in ocean sinks

This storage option is the least developed and the least favourable for CO_2 storage. The tendency of CO_2 to dissolve in oceanic waters is the principle that is used in this storage option. However, the great environmental risk it poses to the marine ecosystem is a major drawback.

2.2 Technical aspects of CO_2 storage

2.2.1 CO_2 behavior and mobility in the reservoir

Uncontrolled migration of CO_2 poses a risk to reservoir and caprock integrity. The density of CO_2 increases with pressure and decreases with temperature. The density of CO_2 is less than the water or brine contained in the pore spaces of the reservoir. Hence, there is buoyant rise of the CO_2 relative to the water or brine. This buoyant rise facilitates mixing with saline water by diffusion and later by convection current and dissolution. Ennis-King and Paterson (2003) reported that the CO_2 remains in the state of buoyant rise and dissolution for thousands of years. Over time, plumes of CO_2 saturated-brine gradually sink to the bottom of the reservoir. The resident undissolved CO_2 will gradually diminish and all the CO_2 is predicted to be completely dissolved after about 5000 years. This indicates that dissolution has a dominant influence on the lateral spread or migration of free CO_2 in all storage reservoir types.

The rate of migration of the CO_2 plume in the reservoir is important. Al-Khdheeawi et al., (2017) researched the influence of rock wettability on CO_2 plume migration and showed that rock wettability significantly affects the spatio-temporal evolution of the migrating CO_2 plume in the storage reservoir. They observed that the CO_2 plume reached the top of the reservoir after 3 and 10 years in a strongly CO_2-wet and a weakly CO_2-wet reservoir respectively. The CO_2 plume migration rate was seen to be higher in the strongly CO_2-wet reservoir and was lowest in the strongly water-wet reservoir. The CO_2 plume appeared like rain-drops in a strongly water-wet reservoir but appeared candle-like in a CO_2-wet reservoir.

As have been explained before, numerous studies have shown that resident undissolved CO_2 will be in the storage reservoir for a few thousand years or more. It is therefore likely that for a long time in the storage history, different phaseCO_2 and brine will exist in the reservoir and thus, different phaseCO_2-brine will affect the properties of the reservoir. Chadwick et al. (2008b) reported that CO_2 injection and storage is a dynamic process with a time-dependent pressure build-up. They opined that after injection, there will be a period of further expansion of the CO_2 phase, pressure relapse, and dissolution in brine. In unconfined reservoirs, pressure relapse is fast due to the rapid displacement of the brine. But in the confined reservoir, pressure relapse is slow. Also, CO_2 trapped at the top of the reservoir is likely to cause a significant difference in the pressure gradient for a long term, it is likely that this will

have a significant geochemical impact. Chadwick et al. (2008b) showed that there will be variation in the behavior of the CO_2 with time according to the type of reservoir.

2.2.2 Density, solubility, and viscosity of CO_2

In a CO_2 storage system, the density, solubility and viscosity of CO_2 depend on the temperature and pressure of the reservoir. It is necessary to understand the change in the density and viscosity, because such changes affect the CO_2-brine-rock interaction. A summary of some relevant researches on CO_2 density, solubility and viscosity is presented in Table 2.

Table 2: Researches on the density, solubility and viscosity of CO_2

Research	Contribution
Yan etal., (2011)	Presented solubility data of CO_2 in brine and water under different temperature, pressure and molality conditions.
Ali Ahmadi & Ahmadi (2016)	Studied the solubility of CO_2 in brine and concluded that the solubility of CO_2 increases linearly with decreasing water temperature.
Amar et al., (2020)	Presented viscosity data of CO_2 under different temperature and pressure conditions.
Mohammadian et al. (2015).	Provided solubility data of CO_2 in brine for low salinity (0-15000ppm), at a temperature range of 60-100^oC and pressure up to 25MPa.
Lamy-Chappuis (2015).	Provided an estimate of the changes in the density, and viscosity of CO_2 at depths >800m. The density and viscosity of CO_2 were seen to reduce with distance from the well. This implies that the mobility and tendency of CO_2 to change phase and density increases as the CO_2 moves further away from the injection well.
Jacob and Saylor (2016); Ratnakar et al.,(2020).	Argued that the ionic composition of the brine affects the solubility of CO_2. Concluded that the solubility of CO_2 decreases with increased salt content in single ion brines, the solubility of CO_2 depends on the salts present in multi-ion brines, and that the solubility is less affected by changes in pressure above 6 MPa. These findings have implications for geochemical modeling.

Jamshidi et al.,(2019).	Measured the solubility of CO_2 in brine and heavy oil under low-medium temperature and pressure, and found that the solubility of CO_2 in heavy oil increased as the pressure increased and as the temperature decreased. This shows that aside, the ionic composition, pressure and temperature (P-T) conditions, the solubility varies according to the media.
Song et al. (2020).	Argued that the solubility of CO_2 in brine affect the timescale, efficiency and integrity of CO_2 storage and also agreed that the solubility of CO_2 varies with the temperature, pressure and the nature of solvent or brine composition
Li et al., (2021).	Found that an increase in the salinity reduces the solubility of CO_2 in brine in nanopores. This agrees with earlier researches and also implies that the solubility of CO_2 is not sensitive to pore size.

2.2.3 Density and viscosity of brine

Convection current and fingering are the major mechanisms that promote the dissolution of CO_2 in brine. Convection current in a CO_2 storage system arises due to differences in the density and viscosity of the fluids i.e brine and CO_2. Therefore, it is necessary to understand how the density and viscosity of brine affect the CO_2-brine system. The density and viscosity of brine are controlled by the temperature, pressure and salinity of the brine. For instance, the addition of salt to 1M NaCl brine led to a 10% increase in density and an 80% increase in viscosity (Lamy-Chappuis, 2015). The change in viscosity and density will in turn affect the convection current and the rate of CO_2 dissolution in the system. Mao and Duan (2008) presented a model for calculating the density and viscosity of brine under varying temperature, pressure and salinity conditions while, Tatar et al., (2015a) proposed the radial basis function neural networks assisted with a genetic algorithm to predict the density of brine. The prediction from these models was compared with predictions from previously known models and was found to be better. The density and viscosity of brine have been seen to be affected by the composition of the brine (Jacob and Saylor (2016); Ratnakar et al. (2020).

27

2.2.4 Solubility, density and viscosity of CO_2-saturated brine

Once CO_2 mixes with and dissolves into the brine, there is a change in the solubility, density, viscosity, and chemical composition of the individual fluids and the resulting fluid. Chemically, the brine becomes weakly acidified and the pH increases. The change in pH of the brine is an indication of the solubility of CO_2 in the brine. Correct estimation of the solubility of CO_2 in brine at any point in time is needed to predict the integrity and efficiency of storage. A summary of some relevant researches on the solubility, density and viscosity of CO_2-saturated brine is presented in Table 3. However, data on the viscosity of CO_2-saturated brine are scarce.

Table 3: Researches on the Solubility, density and viscosity of CO_2-saturated brine

Researches	Contribution
Mao et al., (2010); Ahmad et al. (2016).	Reported an increase in the density of CO_2 when it dissolves in brine, and the increase in density reduced the upward movement and possibility of leakage of the hitherto buoyantsupercritical/gaseous CO_2.
Mosavat and Torabi (2014); Liu et al., 2011).	Presented that an increase in thepressure leads to an increase in the solubility of CO_2 while the increase in temperature leads to a decrease in the solubility of CO_2 in a CO_2-brine system. An increase in the molality of salt also leadsto a decrease in the solubility and pH for CO_2 saturated NaCl due to salting out.
Islam et al., (2016).	Argued that convection current is a hydrodynamic process that promotes the mixing and dissolution of CO_2 in brine.
Mahmoodpour et al., (2019).	Investigated the effect of brine composition on the onset of convection in a CO_2-saturated brine and found that the diffusion coefficient controls the onset of convection. This implies that diffusion is the precursor to the onset of convection.
Teng et al. (2020).	Showed that anincrease in the viscosity contrast between the CO_2 and brine results in an increase in the viscosity of the transition zone and this retards the gravity-driven convection current.

Li et al. (2021).	Investigated the impact of pH on solubility of CO_2 in brine, and found that ions from brines have a higher affinity for silica pore surfaces as the pH increases. Therefore, the solubility of CO_2 in brine reduces as the pH increases.
Jeon and Lee (2021).	Reported that the solubility of CO_2 in a CO_2-saturated brine is different from the solubility of CO_2 in pure brine. This implies that the solubility of CO_2 in a CO_2 storage reservoir is constantly evolving. It also agrees with the fact that the solubility of CO_2 is affected by the nature of the media.

2.2.5 Relative permeability, capillary pressure and fingering

Because a CO_2 reservoir may contain all or some of brine, water, oil, and CO_2, the relative permeability of the different fluids is an important factor that affects the multiphase flow behavior, efficiency of CO_2 storage, and reservoir properties. Relative permeability is the ratio of effective permeability to absolute permeability. It is an expression of the phase/residual saturation usually between 0 and 1. Relative permeability of CO_2-brine mostly shows a low endpoint for CO_2 permeability and high residual brine.

Unlike channeling, fingering is the unstable migration of the CO_2 dissolved in brine irrespective of the heterogeneities in the porous media. Channeling is controlled by heterogeneities in the media. Fingering enhances CO_2-brine mixing and dissolution. They appear as finger-like projections and are an indicator of dynamic instabilities in a fluid-fluid interface when a less viscous fluid displaces a high viscous resident fluid (Rabbani et al., 2018). Fingering occurs in CO_2 storage fields due to differences in the density, viscosity of the fluids, capillary pressure and gravity forces in the reservoir. Fingering is defined by the dominant force that enables it. Hence there are capillary fingering and viscous fingering etc. Capillary fingering is dominant in a steady state injection while viscous fingering is dominant near an injection well and during injection. Some relevant researches are summarized in Table 4.

Table 4: Researches on the relative permeability, capillary pressure and fingering.

Research	Contribution
Al-Menhali et al.,(2015); Jung and Hu (2016).	Showed the impact of reservoir conditions such as pressure, temperature and salinity on the capillary pressure curves.
Reynolds and Krevor (2015).	Presented that the relative permeability in a CO_2-brine system is sensitive to changes in the capillary pressure and is invariant to the changing reservoir conditions. They argued that changes in the relative permeability seen in other researches is due to theCO_2 flow in heterogeneous pores under capillary limited conditions and not necessarily due to the changing reservoir conditions.
Ajibola et al. (2016).	Investigated the effects of the difference in density, permeability anisotropy, and diffusion on fingering behaviour, and found that the difference in density and vertical permeability had the most control on fingering. They noted that injected CO_2 is initially lighter than the resident brine and forms a gas cap above the brine. Over time, the CO_2 dissolves in the brine, creating a density inversion which induces a gravitational instability in the form of fingering.
Shukla and De Wit (2016).	Presented that aside from differences in viscosity and density of two fluids, fingering can also be caused by the change in mobility due to precipitation reaction decreasing the permeability of the medium. They presented that similar to viscous fingering, precipitation fingering is a result of a difference in the initial concentration of the two reactants.
Sidiq et al., (2017).	Used longer cores to measure relative permeability, since the measurement depends on the drop in pressure across the core. This minimized the capillarity end effect.

Basirat et al., (2017).	Presented that water-wet rocks significantly reduce the relative permeability of CO_2 and affects the saturation and CO_2 breakthrough time.
Hu et al., (2017).	Similar to Basirat et al. (2017), pointed that reduced water wetting increases thr $scCO_2$ relative permeability and saturation.
Jeong et al., (2017).	Furthermore, reported that the relative permeability is a function of viscous force and injection rates.
Abdoulghafour et al., (2020).	Reported that a low capillary pressure promotes high residual CO_2 saturation and a high residual saturation leads to improved capillary trapping.
Jeong et al., (2021).	Investigated the effect of the flowrate and residual saturation on the relative permeability of CO_2-brine system, and found that the endpoint permeability of CO_2 increases as the residual brine saturation decreases and as the flow rate increases. This implies that high flowrates improve the brine displacement and CO_2 storage efficiency.

2.2.6   Multiphase flow of CO_2-brine

Cyclic flooding pattern occurs in CO_2-brine reservoir, and this affects the multiphase flow. Cyclic flooding is caused by changes in the temperature and pressure conditions of the reservoir, alternating CO_2-brine injection, or seasonal CO_2 injection. Some relevant researches on the multiphase behavior of CO_2-brine are summarized in Table 5.

Table 5: Researches on the multiphase flow of CO_2-brine

Researches	Contribution
Saeedi et al.,(2011).	Observed that the multiphase flow characteristics of the fluid-rock system in a CO_2-brine reservoir changes over flooding cycles, and that these changes

	are brought about by the changes in capillary hysteresis, chemical reactions, stress and change in the reservoir conditions associated with the flooding cycles. They concluded that the effect of cyclic CO_2-brine flooding on saturation profiles is minimal but strongly influences the differential pressure. Capillary hysteresis was found to be the most influencing factor among all the factors investigated.
Kuo et al., (2011).	Presented that when the injection rate is high, the multiphase flow characteristics are dominated by viscous forces. While, when the injection rate is low, the multiphase flow is dominated by capillary forces.
Krevor et al., (2016).	Studied the impact of capillary pressure, relative permeability and residual trapping on the multiphase flow of CO_2-brine over a range of temperature, pressure and salinities. Their result showed that reservoir heterogeneity has little impact on the multiphase flow of the CO_2-brine in the reservoir. This agrees with an earlier finding by Reynolds and Krevor (2015) that the relative permeability in a CO_2-brine system is sensitive to capillary forces and not reservoir heterogeneity.
Seyyedi et al. (2020)	Explained that the multiphase flow of CO_2-brine in carbonate rocks result in increased grain roughness, increase in the population of micro and macro pores, and decrease in pore volume of medium size pores. These changes affect the sweep efficiency, relative permeability and residual trapping.

2.2.7 CO_2 injection and long term evolution

The CO_2 captured from sources are compressed or pressurized and transported via pipelines or other channels into favorable reservoir rocks. Injection of the CO_2 into the

reservoir is mostly done as a dense supercritical fluid. This is because the density allows for more volume of CO_2 to be stored per unit pore volume and also reduces the buoyancy drive. Once the CO_2 is in the reservoir, it is under the influence of the reservoir conditions such as pressure, temperature and brine salinity. These factors are highly variable in the reservoir. As have been stated earlier, undissolved mobile CO_2 would be in the reservoir for thousands of years while the CO_2 dissolves gradually into the brine. The phase of the CO_2 would evolve according to the prevailing temperature, pressure and brine composition at a given time. The evolution includes but not limited to the phase, pore pressure, density, flowrates, composition etc. Researches concerning evolution of phaseCO_2-brine are summarised in Table 6.

Table 6: Researches on CO_2 injection and long term evolution

Researches	Contribution
Xu et al., (2010); Whittaker et al. (2011)	Studied the changes in brine and CO_2 chemistry in a CO_2 injection site (Frio-I Brine Pilot). They found that brine samples showed a significant drop in the pH, increase in HCO_3^-, aqueous Fe, and a shift in the isotopic composition of the dissolved inorganic carbon. They observed that the CO_2 plume expands gradually due to capillary forces, and the gas saturation gradually decreased due to its dissolution and precipitation incarbonates. The gas phase was predicted to disappear after 500 years. However, there were high aqueous CO_2 concentrations for a longer time, but eventually decreased due to carbonate precipitation.
Pruess and Nordbotten (2011).	Studied the long term evolution of CO_2 plume in a saline reservoir and reported that the process of plume advancement differs from that of forced immiscible displacement. The CO_2 plume became thinner as it advanced over a distance of 80 km. They also reported an increase in density, and molecular diffusion, but with no convection.
Vilarrasa et al., (2017).	Observed that CO_2 reach the bottom of injection wells at a colder temperature

and cause a cooling of the rocks. This cooling and overpressure tend to enhance injectivity by increasing the effective stress and induced fracturing.

2.2.8 Geomechanics of CO_2 reservoir rocks

Dissolution and precipitation brought about by CO_2-brine interaction in a porous rock affect the pore structure, pore and grain geometry, and the mineral composition of the rocks. The CO_2-brine and the resultant pore pressure causes alteration in the pore geometry by chemo-mechanical processes (Pearce et al., 2019; Rathnaweera et al., 2016; Vanorio et al., 2011). Alteration in the pore structure and composition lead to changes in the geomechanical properties of the reservoir rocks. Vanorio et al. (2011) noted that the compositional changes control the change in fabric, strength and other properties in rocks. This indicates that the change in composition leads to change in the transport properties and strength of the rocks. Some researches on the effect of CO_2 on the geomechanical properties of rocks are highlighted in Table 7.

Table 7: Researches on the geomechanics of CO_2 reservoir rocks

Research	Contribution
Vanorio et al. (2011).	Showed that injecting CO_2 into a brine-rock system induced chemo-mechanical processes that permanently alters the rock's framework.
Delle and Sarout (2016) and Pimienta et al. (2017); Espinoza et al. (2018); Heap (2009); Keshavarz et al. (2019); Meredith et al., (2017); Zhang et al., (2020); Zhang et al., 2019; Zheng et al., 2015).	Studied the effect of CO_2-brine on the strength of rocks and reported a reduction of strength.
Griffiths et al., (2017).	Showed that the pore aspect ratio influences the strength and stiffness of porous rocks as the rock's stiffness and strength is reduced when the pore angle is rotated through 90°. The influence of pore angle decreases as the aspect ratio approaches unity.
Grgic (2011); Olabode and Radonjic (2013); Luo (2020); Jiang and Tsuji	Reported changes in the transport and mechanical properties of porous rocks

(2014); Delle Piane and Sarout (2016);
Srodon et al. (2018); Han et al. (2020);
Li et al. (2020); Rigby et al. (2020); Tan
et al. (2020); Islam et al. (2019) and
Rutqvist (2012).

flooded with CO_2. The changes are seen to vary from slight to high, depending on the mineralogy and the reservoir conditions.

2.3 CO_2-brine-rock interaction

Reservoirs contain brine of varying proportions in the pore and it is in equilibrium at any point in time. Injection and storage of CO_2 in the brine-containing reservoir disturbs the equilibrium between the brine and the reservoir rocks. This triggers changes in the reservoir (Suppe, 2014; Wu et al., 2018), and can potentially have constructive or deleterious consequences on the integrity and capacity of the reservoir to contain CO_2. The effect of CO_2-brine-rock interaction on the reservoir can be either chemical, geomechanical or petrophysical. Most times, these effects are coupled and interdependent as shown in Figure 7.
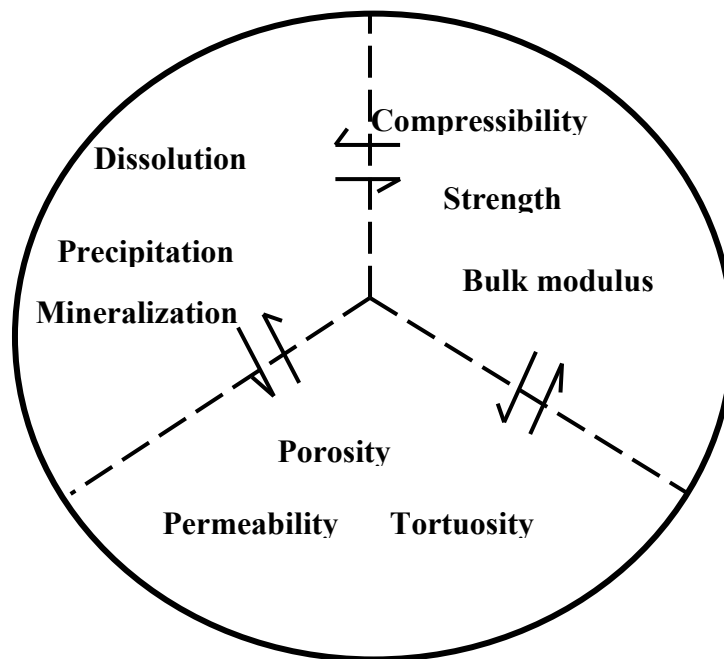
Figure 7: Illustration of the effect of CO_2-brine-rock interaction on reservoir rocks. The effects are most times coupled and dependent.

2.3.1   Effect of CO_2-brine-rock interaction on the composition of the reservoir rocks

When CO_2 is injected into porous and permeable rocks for the purpose of storage, there will be an interaction between the CO_2, rock minerals and brine (Sun et al., 2016).

Usually, the CO_2 dissolves into the brine to form a weak acid which is capable of dissolving rock minerals and precipitating other minerals or ions. Alternatively, the injected CO_2 reacts with rock minerals. Either way, CO_2 is been sequestered as a solution or as a mineral (Pang et al., 2012). The reaction usually leads to changes in the composition of rocks, pore fluid and surrounding hydrogeology. Attention must be paid to these changes so that the effect of this process will be understood before storage (Liu et al., 2014; Xie et al., 2014). Some relevant researches are summarised in Table 8.

Table 8: Researches on the effect of CO_2-brine-rock interaction on the chemical composition of the reservoir rocks

Researches	Contribution
Alemu etal., (2011).	Saturated clay-rich and carbonate rocks with CO_2-brine and brine and found that there was a dissolution of metals into the fluids for all the samples that contain brine and CO_2-brine. But the samples with CO_2-saturated brine released more Fe and SiO_2 into its fluid compared to the samples saturated with brine. The carbonate rock released metals at a much higher rate at temperatures above 250^0C. The clay-rich sample with CO_2-saturated brine showed significant chemical changes. These showed the effect of rock chemistry and brine composition on the CO_2-brine-rock reaction.
Olabode and Radonjic (2013).	Investigated the changes in the microstructural and chemical properties of shales flooded with CO_2-brine. They reported chemical changes, as well as changes in internal surface area and pore size distribution. There were substantial changes in pH of effluent from shale flooded with CO_2-brine after 3 days.
Pimienta et al. (2017).	Used carbonate rocks and supercritical CO_2 to study the effect of residence time on CO_2-brine-rock interaction. They observed that the dissolution of minerals in CO_2-brine increased with residence time.

Fuchs et al., (2019); Nguyen (2020); Valle et al., (2020); Xiao et al. (2020).	Showed that the reactive processes between CO_2-brine-rock affect the geochemical and geomechanical properties either through CO_2 induced mineral dissolution/precipitation reactions or stress corrosion and stress evolution.

2.3.2   Effect of CO_2-brine-rock interaction on the petro-physical properties

The petrophysical properties of rock is defined by the porosity, pore geometry, and permeability. CO_2 plume induces mineral dissolution and precipitation in rocks. These dissolution and/or precipitation affect the porosity, pore geometry and permeability of the rock. A prediction of the effect of the reactive dissolution/precipitation on rock's petro physical properties should therefore be an integral part of the assessment of the CO_2 storage site. The dependence of the petrophysical properties on pore geometry has been shown by Olabode and Radonjic (2013) and Akbar et al., (2019). The porosity of a rock is dependent on the pore volume (Armitage et al., 2010), while permeability of a rock is dependent on the pore geometry, pore volume and pore throat diameter (Olabode & Radonjic, 2013; Schwartz et al., 2019; Yasmaniar et al., 2019). Also, the capillary pressure is a function of the pore throat size. A summary of some related researches is presented in Table 9.

Table 9: Researches on the effect of CO_2-brine-rock interaction on the petro-physical properties of reservoir rocks

Researches	Contribution
Lei & Xue, 2009.	Reported that the P-velocity from sandstone samples saturated with gaseous, liquid and supercritical CO_2 respectively decreased by 7.5, 12, and 14.5% while the attenuation coefficient increased by 3.3, 2.7, and 3.7 %. The decrease in the P-velocity relates to the decrease in strength, and this implies that supercritical CO_2 caused the greatest reduction in strength.
Vialle and Vanorio (2011a).	Evaluated the effect of a reactive CO_2-saturated water on the elastic properties of carbonate rocks in a laboratory experiment. They observed the damping of S and P-wave velocities, and

	concluded that the reduction in velocities was connected to an increase in the porosity and permeability of the rock and deformation of micro-fabric.
Grombacher et al., (2012).	Also showed a reduction in the elastic moduli of carbonate rocks exposed to CO_2-rich brine. But the reduction was lower compared to Vialle and Vanorio (2011a). The reduction in the elastic moduli also resulted in an increase inpermeability.
Lamy-Chappuis et al., 2016).	Reported that a 10% increase in the porosity resulted in a 10% decrease in sonic velocity of calcite-rich Cayton bay sandstone saturated with gaseous CO_2-brine.
Han et al. (2020)	Reported a significant change in a range of properties such as the reduction in permeability, increase in the non-connected pores and increase in irreducible oil saturation as well as capillary entry pressure of carbonate rock reservoir. They concluded that CO_2 flooding in carbonate reservoirs can significantly alter the pore network.

2.3.3 Effect of CO_2-brine-rock interaction on the geomechanical properties

Geomechanical properties of rocks are affected when CO_2 is injected and stored (Rutqvist, 2012). Injection of CO_2 into reservoirs increase the volume of pore fluid and leads to a commensurate increase in pore pressure (Al-Zaidi et al., 2018), and a decrease in temperature (Vilarrasa et al., 2017). This increase in pore pressure and decrease in temperature increases the stresses on the rock (Ilgen et al., 2019; Rutqvist, 2012), and the new stress regime triggers geomechanical changes in the rock's framework.

There have been extensive studies on the effect CO_2 storage on time dependent deformation and geomechanics of reservoir rocks (Grgic, 2011; Hangx et al., 2015; Hangx et al., 2013; Heap, 2009; Liteanu et al., 2012; Peter et al., 2020;). They all agreed that the effect of CO_2 on time-dependent deformation varies from slight to

significant depending on the pore fluid, mineralogy and effective pressure. The mechanism for such effects include pressure solution creep, matrix solubility, micro-cracking, and stress corrosion.

Strong to weak reduction in geomechanical properties of rocks have been reported by (Bemer & Lombard, 2010; Grombacher et al., 2012; Lamy-Chappuis et al., 2016; Lei & Xue, 2009; Makhnenko et al., 2017; Mikhaltsevitch et al., 2014; Rice-Birchall, 2018; Vanorio et al., 2011; Zhang et al., 2020; Zhang et al., 2019). However, studies such as (Hangx et al., 2013; Marbler et al, 2013; Rinehart et al., 2016) reported unclear changes in geomechanical properties. The difference in effect is seen to be due to a difference in mineralogy.

2.4   Criteria for CO_2 storage fields

2.4.1   Trapping mechanism

A viable CO_2 trapping mechanism is very important for CO_2 storage. Trapping mechanism serves to control the migration of the CO_2 plume from the reservoir both vertically and horizontally (Pimienta et al., 2017). It includes but is not limited to an impermeable caprock. Mechanism of trapping includes (i). Solution or dissolution trapping in the brine. (ii). Residual trapping of CO_2 in pores of rocks (iii). Chemical trappings or mineralization as a result of a reaction between CO_2-brine-rock leads to the synthesis of a new mineral. (iv). Structural/stratigraphic trapping by the presence of an impermeable layer or by the presence of structures such as sealed fault or fold, and (v). Hydrodynamic trapping utilizes the tension and capillary properties of the fluid to trap CO_2.

Dissolution trapping of CO_2 in brine commence immediately the CO_2 comes in contact with the brine, provided the solubility conditions are met (Li, 2010; Pang et al., 2012; Shukla et al., 2010). Here, CO_2 is trapped as a solution in the pores. Solution trapping reduces the pore pressure by reducing the free mobile CO_2. Residual trapping in sandstone permanently immobilizes 13-92% of injected CO_2 as residual fluid trapped in pores (Burnside & Naylor, 2014). Trapping by mineralization occurs in the long term as a result of the reaction between CO_2-rock-brine (Jia et al 2017). The reaction is slow and happens over geologic time depending on the CO_2-brine-rock reaction

kinetics (Tsai et al., 2013). It is the safest mode of trapping CO_2. Structural/stratigraphic trapping is the most widespread kind of trap but it is the least efficient form of trapping as any structural or diagenetic change could lead to leakage (Akbarabadi & Piri, 2013; Bolster, 2014; Wang et al., 2015). Hydrodynamic trapping utilizes the tension and capillary properties of the fluid to trap CO_2, such trappings are easily broken by pressure or stress. Figures 8 and 9 illustrate the various forms of trappings discussed above.

In an open reservoir, solution and residual trappings are the dominant mechanisms, while in a closed reservoir, structural or stratigraphic trap is the dominant mechanism. A closed reservoir is one whose volume and extents are confined by non-permeable layer of rock, while an open reservoir is one that is not confined by non-permeable layer of rock, especially at the top.
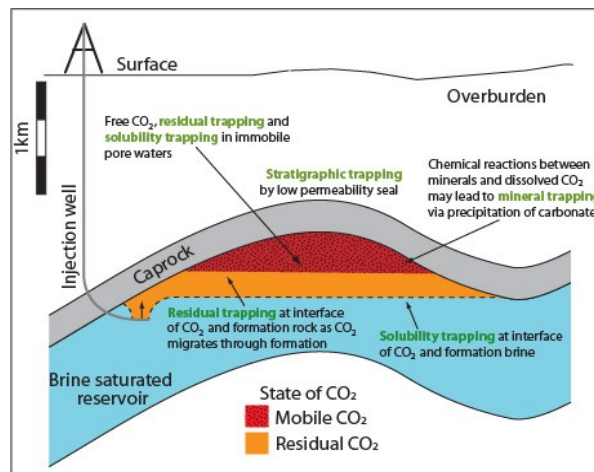
Figure 8: Illustration of various trapping mechanisms (Burnside & Naylor, 2011)
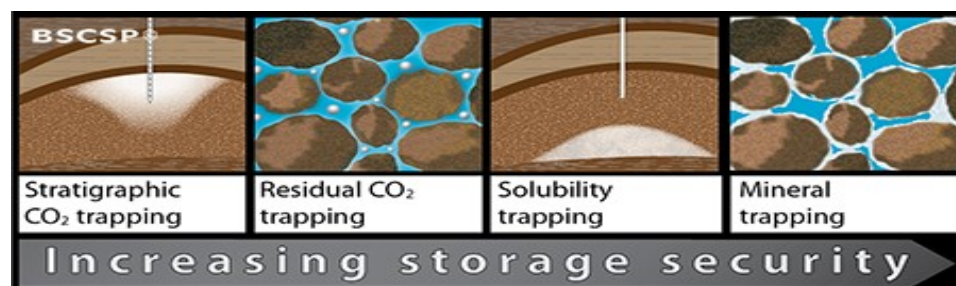
Figure 9: Graphic illustration of different trapping mechanisms. Accessed from https://www.bigskyco2.org/node/127 on 02/05/2020.

2.4.2 Containment capacity

Containment capacity refers to the ability of the caprock and reservoir rock to contain the stored CO_2 within the reservoir at all times without leakage. Containment is a function of both the caprock and reservoir rock. Containment in the reservoir and caprock is mostly achieved by trapping as have been discussed in section 2.4.1. According to Shukla et al. (2010), the caprock integrity is central to the success of CO_2 storage. The caprock should be devoid of any fault or fracture that can allow leakage. It should be dense and intact, have low permeability and should possess high compressive strength. Also, Ramírez et al., (2010) identified caprock thickness, composition, and proven sealing capabilities as necessary parameters for evaluating caprock integrity. Furthermore, Busch et al.,(2010) presented that the ability of the caprock to trap CO_2 depends on the capillary entry and upward buoyancy pressure. Olabode and Radonjic (2013) added that the capillary pressure of a caprock depends on the pore size, while buoyancy pressure depend on the density of the fluid and the column height. Therefore, a smaller pore throat size makes better caprock. It therefore means that any reaction or process that increase the pore throat size of the caprock will be detrimental to CO_2 storage.

Mechanisms that lead to CO_2 leakage through caprock include propagation and reactivation of faults and fractures, and leakage from weak zones. Shukla et al. (2010) added that seismic and stress field may reduce the integrity of caprock and consequently cause leakage. Busch et al. (2010) and Olabode and Radonjic (2013) reported that leakage could occur through the unplugged wellbore, capillary breakthrough and diffusive loss.

Given that leakage is a potential issue with CO_2 storage, Wu et al. (2021) evaluated the potential for faulting and leakage and found that the alpha structures have low fault containment risk compared to the beta structures. This implies that new fault and leakage zones have more propensity to leakage than pre-existing faults and leakage zones.

Considering that salinity varies largely in a CO_2 storage reservoir, Al-Khdheeawi et al. (2018) studied the effect of brine salinity on the containment capacity of reservoir

and found that lower salinity decreases CO_2 mobility and enhance residual and solution trapping. The study showed that brine salinity significantly affects the containment capacity of a reservoir. Furthermore, Al-Khdheeawi et al., (2019) studied the effect of alternating CO_2 injection cycles on containment capacity and found that a higher number of cycles decreased the vertical CO_2 leakage, increased residual trapping and reduced solubility trapping.

2.4.3   Injectivity

Injectivity refers to the interconnectedness of the pores in a reservoir to facilitate the movement of fluid and gases. Such movement could be through the pores or through the micro and macro-structures such as fractures and faults. Prieditis et al., (1991) from laboratory and field injectivity study reported that the injectivity of an unsaturated brine in porous reservoir is much higher than the injectivity of a CO_2-saturated brine because of the dissolution of the CO_2 in brine. This makes sense given that the CO_2-brine is denser than pure brine and would be less mobile than pure brine.

Cui et al. (2018) presented that injection rates, salinity, capillary force and permeability affect CO_2 injectivity, and that geochemical reaction and the volume of salt precipitated from CO_2-rock-water interaction severely reduces the injectivity of storage reservoirs by clogging the pore spaces. Similarly, Sokama-Neuyam and Ursin (2018) argued that good injectivity is required to inject large volumes of CO_2 into reservoirs and also agreed that geochemical CO_2-brine-rock reactions affect the injectivity of reservoirs. From an experiment, it was reported that salt precipitation reduces CO_2 injectivity, reduce permeability and increase brine salinity by the precipitation and re-mobilization of fines. Brine saturation and pore size distribution were seen to control salt precipitation in the experiment. Yang et al. (2019) presented a model to evaluate the variation in the injectivity and noted that the injectivity is different for the different flooding stages due to similar factors investigated by Cui et al. (2018).

It is thought that flowrate can be used to improve the injectivity. Therefore, Giwelli et al. (2019) conducted a $scCO_2$ flooding experiment on core samples using incremental flowrates of 2-14ml/min. There was no significant change in the storage injectivity at

the flow rates. It is thought that the critical flow rate may be higher than the maximum flow rate applied. Moreso Valle et al., (2020) observed that the injection of scCO$_2$-enriched brine increased the effective porosity of storage and consequently, the injectivity.

Also, Yusof et al., (2020) investigated the effect of flow rate, permeability as well as brine type and concentration on CO$_2$ injectivity. The results showed that CO$_2$ flowrate, brine concentration and initial rock permeability significantly affect the porosity and permeability of the core samples, and hence the injectivity. Minerals were observed to be dissolved and precipitated, resulting in detachment of silica particles and formation of new secondary minerals that clogged the pores and reduced the permeability. These observations have implications for the long term injectivity and capacity of the reservoir, and implies that there is a need to make effort to maintain or improve the injectivity of the reservoir during CO$_2$ injection and storage. Huerta et al., (2020) presented that storage injectivity is an important aspect of CO$_2$ storage project and argued that hydraulic fracturing improves the storage injectivity significantly by 13-71%.

2.4.4 Capacity

Capacity is the volume of CO$_2$ that can be contained in a reservoir. It is a function of the porosity of the reservoir rock and solubility of the CO$_2$ in the brine. A lot of researches have reported the estimated capacity of the different storage types to store CO$_2$. These estimates are given at different levels of confidence. Such researches include Platform 2007; Li *et al.* 2009; BP, 2010; CCICED, 2009; Cook, 2014; DOE, 2017; Doherty et al., 2017; Fang & Li, 2013; Godec et al., 2011). However, these estimated storage capacities are limited by site-specific factors. For example, Zulqarnain et al. (2017) provided a storage capacity estimate for a potential storage site in Louisiana USA. The result of the storage capacity showed that boundary type, end-point saturation, and injection rate affect the estimated storage capacity. These factors caused about a 30% change in the estimated storage capacity.

Also, Anderson and Jahediesfanjani (2017) argued that only about 4% of the theoretical 94 billion metric tons of CO$_2$ can be safely stored in Mount Simon Sandstone if resultant pressure build-up is considered. Similarly, Agada et al. (2017)

modeled the storage capacity of the Bunter Sandstone and found that 32 Gt of CO_2 can be stored in the Bunter Sandstone if pressure build-up is neglected. However, if pressure build-up is considered, only half of that amount would be possible.

Aside from the pressure, Al-Khdheeawi et al., (2017) researched the influence of rock wettability on storage capacity, and showed that rock wettability significantly affects the storage capacity of the storage reservoir by affecting the rate of migration of the CO_2 plume. CO_2 plume migrated faster in the strongly CO_2-wet reservoir compared to the strongly water-wet reservoir. This implies that the strongly water wet reservoir has a better storage capacity. Furthermore, Tooseh et al., (2018) argued that injection flowrate affects the storage capacity even more than pressure. They reported that a higher injection flow rate favours higher storage capacity and thus, concluded that the injection pressure can be used to optimise storage capacity. Santibanez-Borda et al., (2019) advised that pressure constraints and brine production are limiting factors to maximizing CO_2 storage capacity and not geological heterogeneity.

2.5   Effect of CO_2 on storage fields

Effect of CO_2 on storage fields includes pressure build-up, stress propagation, leakage, seismicity and fault reactivation, as well as ground deformation and the ecosystem and environment. A summary of some researchers on the effect of CO_2 on the storage field is presented in Table 10.

Table 10: Researches on effect of CO_2 on storage fields

Researches	Contribution
Rubin and De Coninck (2005).	Reported that the annual leakage rates from an average storage site should be less than about 0.01% of the injected CO_2. This rate is only an estimate that is safe enough for controlling the amount of atmospheric CO_2 causing global warming.
Pierce and Sjögersten (2009).	Investigated the effect of increased soil CO_2 level on vegetation and microbial community, and CO_2 utilization in temperate grassland. Their findings showed that the increased concentration resulted in reduced vegetation above and below the ground over time. No

	significant changes in microbial biomass or carbon utilization were observed, but a trend towards reduced microbial respiration was noted.
Bachu and Celia (2009).	Identified prominent leakage paths of CO_2 from the reservoir to include connected faults, fractures and natural discontinuities in strata, as well as leakage through abandoned injection and producing wells amongst others.
Onuma and Ohkawa (2009).	Used Differential Interferometric Synthetic Aperture Radar (DInSAR) data, and reported 7mm/year ground deformation for In Salah.
Kharaka et al. (2010); Apps et al.,(2009); Rempel et al.,(2011); Fischer, et al (2015); Fischer et al., (2016); Lu et al., (2010).	An increase in the pH of the water led to the release of hazardous heavy metals that are soluble in acidic environments and the redox conditions are altered. Further reaction of the carbonic acid may lead to the precipitation of potentially harmful substances in the environment and may trigger certain microbial activity.
Rutqvist et al., (2010); Yang et al. (2015); Shi et al. (2019).	Showed the ground deformation fromdifferent CO_2 storage sites from analysis of Interferometric Synthetic Aperture Radar (InSAR) data.
Espinoza et al., (2011); Stenhouse et al., (2009).	The first effect of CO_2 in water is the dissolution of CO_2 in the water which increase the pH of the water.
Morris et al., (2011).	Modelled the ground deformation around In- Salah's KB-502 CO_2 injection well and compared the output of the model with measurement of ground deformation from InSAR. Results of the model were compared well but even better when connected faults were added.
Jung et al.,(2013); Yang et al. (2019); Buscheck et al. (2019); Ko et al., (2020).	Proposed different methods for detecting CO_2 leakage from reservoir

Zoback and Gorelick (2012);Vilarrasa et al (2019); Orlic (2016); Mazzoldi et al., (2012).	Argued that CO_2 injection induces seismicity. Seismicity is induced by the related pore pressure, non-isothermal effects, rock contraction, change in thermal stress as well as stress redistribution, change in local stress due to change in permeability, seismic and aseismic slip and geochemical effects.
Al-Traboulsi et al., (2013).	Examined seedling emergence and growth of bean plants grown in soils with an elevated CO_2 for 39 days after planting. Observation in the experiment showed that no seed exposed to soil with $CO_2 > 50\%$ emerged even after injection was discontinued. Some seeds exposed to soil $CO_2 < 50\%$ produced seedlings, but many did not survive. Seedling emergence and survival in the experiment was greatest at CO_2 of 5–20%, but root and shoot growth was stunted relative to control plants.
Wiegers and Schäfer (2015).	Presented that the ratio of leakage to the rate of groundwater flow determines the effect of the leakage on groundwater.
Vilarrasa and Carrera (2015).	Observed and reported that the build-up of pressure was stronger in saline reservoirs compared to depleted oil and gas field.
Rinaldi et al., (2015).	Investigated the effect of well geometry on seismic rupture. Found that for vertical well, faultspropagate/reactivate faster but in a small area resulting in an intense seismic event and leakage rate. For the horizontal well, the pressure build-up is distributed over a wider area along the fault and propagates slower resulting in a low seismic event and leakage rate that affects a large area.
Yang et al. (2015).	Reported a pressure build-up of 10 MPa in a CO_2-EOR site after four years of injection and production.

Samsonov et al., (2015); Yang et al.,(2019).	Used Multidimensional Small Baseline-Differential Interferometric Synthetic Aperture Radar (MSBAS-DInSAR) to model ground deformation.
Anderson and Jahediesfanjani (2017).	Agreed that injection of CO_2 into geologic formation leads to a build-up of pressure
Agada et al. (2017).	Pointed that an excessive build-up of pressure can be detrimental to the integrity and safety of the storage project.
Hitchon and Bachu (2017).	Pressure build-up affects tens to hundreds of kilometres from the injection site.
Fu et al.,(2017).	Showed that pressure build-up could lead to hydraulic fracturing.
Jeanne et al., 2017; Gheibi et al., (2018).	Showed that pressure build-up reactivates faults and induces seismicity.
Hunter et al. (2017).	Argued that build-up of pressure increases the cost of CO_2 injection and induces seismicity.
Hu et al. (2017).	Studied the effect of the rate of injection on storage area, and found that the effect of the rate of injection on stress perturbation is comparable to the effect of pressure rise and temperature gradient.
Vilarrasa et al. (2017).	Agreed that CO_2 reaches the bottom of injection wells at a colder temperature. This causes a cooling of the rocks and the temperature gradient induces stress.
Doherty et al. (2017); White et al. (2020); Wang et al. (2020).	Identified leakage paths and potential for leakage.
Vilarrasa et al., (2017).	Agrees that injection of CO_2 into closed reservoirs will induce a large pressure build-up that may reactivate faults while large open reservoirs are safer.

Ji et al., (2018).	Presented that the major impact of CO_2 leakage to the plant community is the degradation of plant cover.
Roy et al., (2018).	Evaluated the impacts of temperature difference between the injected CO_2 and reservoir. The study found that the impact of temperature difference on stress propagation is seriously reduced by effective in-situ horizontal stresses.
Gheibi et al. (2018).	Extracting brine with Enhanced Water Recovery (EWR) from the CO_2 storage reservoir could manage and reduce pressure in the formation.
Wang et al., (2018).	A numerical simulation found that brine leakage rates increased directly with excess pore pressure and inversely with the salinity when excess pore pressure ranged from 0.5 to 1.5 MPa.
Postma et al., (2019).	Argued that leakage through abandoned wells does not pose a great threat to CO_2 storage integrity.
Li et al., (2019).	Geochemical reaction decreases the leakage level. This is because geochemical reaction promotes mineralisation or chemical trapping, which is the safest CO_2 trapping mechanism.
Gupta and Yadav (2020).	Argued that the first effect of CO_2-brine leakage is its impact on pore dynamics of the hydrological regimes. Found that the geochemical reaction between rocks and leaked CO_2 may significantly affect soil microbial dynamics and vegetation in and around CO_2 leakage sites. They presented a comprehensive review of the impact of leakage of CO_2 on fresh water and soil.
Li et al., (2019).	Proposed a triggered gelation method for controlling the leakage of CO_2 during storage. This method allows the reactive process to form gel that can be absorbed

	more easily near the injection or leakage points.
Borrero-Santiago et al. (2020).	Reported that marine bacteria population was altered after 3 weeks of CO_2 leakage, and the marine bacteria did not show potential for recovery when CO_2 leakage was stopped.
Khan et al., (2020).	Investigated the effect of reservoir size, boundary conditions and a number of injection wells on pressure build-up and reactivation of faults. They found that smaller reservoirs with close boundaries have relatively higher pressure build-up while, large reservoir with open boundaries have lower pore-pressure build-up. This agrees with the findings of Vilarrasa et al., (2017). Injecting CO_2 into multiple injection wells cause higher pore-pressure build-up.
Roberts and Stalker (2020).	Presented a comprehensive review of the effect of various reservoir conditions on leakage.

2.6 Approaches to pore scale modelling of porous rocks

Numerical simulation experiments and its influence in the scientific community is growing widely. It is complementary to the rigorous and expensive laboratory and field data collection process, and can be accepted once such numerical models are validated. Piller et al., (2014) argued that the scientific relevance of pore-scale model is in the possibility of upscaling the pore-level data to yield volume-averaged quantities that are useful for practical purposes.

Pore scale models are divided into two categories: Direct pore model and pore network models. Pore network models were first introduced in the 1950s by Fatt (Aghaei & Piri, 2015) who used a network to calculate relative permeability and capillary pressure for a drainage process. It has since evolved greatly. A review of researches on dynamic and quasi-static network pore models has been presented in Aghaei and Piri (2015),

and a comprehensive review of dynamic pore network models of two-phase flow in porous media can be found in Joekar-Niasar and Hassanizadeh (2012).

Direct models are simulated directly in the geometry of digital rocks. The geometry of the rock processed from digital images is referred to as a digital rock. Notable methods for direct modeling include the Lattice Boltzmann method (LBM), Computational fluid dynamics (CFD) and Smooth particle hydrodynamics (SPH). They are computationally expensive. Direct pore modelling has become popular especially with developments in the hardware for imaging and the software for image processing. Bultreys et al. (2016) submitted that pore microstructures control transport processes, and understanding the pore microstructure is a difficult problem which requires three-dimensional pore space characterization. In the same vein, Bogdanov etal., (2011) presented that pore-scale modelling of multiphase fluids flow through real natural porous media is pertinent for scientific and engineering application, stressing that understanding flow at the pore-scale is a fundamental approach in hydrodynamics. Naveed et al. (2016) posted that the rapid development of CT-imaging, image processing software and computational fluid dynamics provide a promising future to simulating flow and transport directly on CT-derived pore geometry. Mehmani et al., (2020a) presented a review outlining the various approaches used in simulating fluid/solute behaviour in the models.

2.7   Trend in pore scale modelling of transport process in rocks

Performing direct numerical experiments at pore scale requires that the geometry of the real porous material (digital rock) obtained from imaging, and image processing is used for the simulation. However, computational resources needed to handle the complex geometry of the material are very high. This implies that there is a limitation of scale and size on direct modeling (Scheibe et al., 2015). The geometry of porous material is tortuous, complex, and heterogeneous and would be difficult to replicate by any Computer-aided design (CAD) function for an effective pore model. Microstructures span centimetre to the nanometre scales in nature and are heterogeneous. Therefore, their characterization requires measurements beyond their porosity and permeability. There has been an increasing need to characterize pore size

distribution, pore geometry properties, and grain geometry properties. These can also be achieved from direct pore models.

In an attempt to systematically assess pore-scale heterogeneity based on a statistical analysis of parameters of pore-structure, Xu et al., (2020) developed a pore-scale-heterogeneity-synthetic index to quantitatively characterize the pore-scale heterogeneity of unconsolidated porous media from a pore network model. In another attempt to describe the throat geometry of pores more accurately, Zhao et al., (2020) performed simulation of pore scale quasi-static drainage displacement by coupling lattice Boltzmann and pore network model. This provided an improved pore network model.

Blunt et al. (2013) demonstrated how to make a digital rock and run simulations on the digital rocks. They focused on applying direct pore modeling in tracing and quantifying the residual supercritical CO_2 trapped in a brine-saturated rock under reservoir conditions. They found that the quality of the digital rock depends on the resolution of the image, and the de-noising and the segmentation. They opined that pore scale modeling will have huge application in dispersion tracing, contaminant transport and CO_2 sequestration. Piller et al. (2014) presented a complete workflow for setting up pore scale simulation using a micro-CT image of samples.

Pore-scale petrophysical and multiphase flow properties computed from direct pore scale models can be up-scaled to core scales using a multi-scale upscaling technique (Long et al., 2013). This approach has been successfully applied on clastic and carbonate rocks and it produced experimentally validated outcomes (Lopez et al. (2010);(2012). Furthermore, Long et al. (2013) explained that this kind of image-based pore scale model is best achieved by integrating 2D and 3D image data obtained at multiple scale using a combination of any of Micro-Computed Tomography (micro-CT), 2-Dimensional Scanning electron microscopy (2D-SEM), automated 2-Dimensional Scanning Electron Microscopy-Energy Dispersive Spectroscopy (2D SEM-EDS) or Focused Ion Beam Scanning Electron Microscopy (FIB-SEM). The goal of integrating the 2D and 3D images is to characterize the different pore types and textures at different scales.

Addressing the need to characterize the changes in the rock properties in a dynamic system, Wu et al. (2020) presented a novel dynamic 3D modeling technique considering pore-system variation with respect to changes in thermal maturation in shale samples. Through characterizing shale models dynamically, it was verified that the proposed technique can generate shale models with distinct properties depending on the pore types, shale component and thermal maturation.

Mesh size and discretization affect the result of pore scale models, Lamy-Chappuis (2015) presented that mesh size affects the output of pore scale models in order of magnitude. However, in their research, regular resolution meshes were used because the emphasis in their research was on changes in permeability and not absolute permeability. Furthermore, pore scale discretization is normally done using the upwind scheme. It is known that the upwind discretization method introduces some errors. Therefore, Sadeghi et al., (2020) proposed the mixed-cell method of pore scale discretization and compared its accuracy with the commonly used upwind scheme. Mehmani et al. (2020) presented a review of the current methods and challenges in constructing porescale models of rocks.

Instruments and software that facilitate imaging of materials have also undergone progressive change over time. A review of the developments of optical imaging instruments has been presented by Bultreys et al., (2016). Each of these devices and modifications, as well as software, has its advantages as well as limitations.

2.8   Challenge with image-based pore scale modeling

A major challenge with direct modeling using an image-based pore model (digital rock) is the size and scale of the image that can be used in the model. The constraint of computational resources limits the size and scale of the image that can be used for the model. It is desirable that the image used and the output of the simulation be representative of the core. Representative Element Volume (REV) is used to circumvent this challenge. Also, multi-scale imaging is imperative especially for highly heterogeneous rocks as the smallest pores determine the resolution to be used for optimal imaging (Goral et al., 2020). Other challenges include the resolution of the image, the filtering, and the segmentation/thresholding process (Blunt et al., 2013). At

the moment, image-based pore scale modelling is a visually-controlled process, as there are no completely automatic processing workflows (Mehmani et al., 2020). Image filtering and segmentation process are user controlled (Iassonov et al., 2009). Goral et al. (2020) had used machine learning to segment and measure minerals and pores in rocks. However, there was a challenge in capturing all the phases in the rock.

2.9 Representative Element Volume (REV)

In continuum mechanics, a major assumption is that the behaviour of many physical elements is continuous. Thus, physical quantities such as mass, density, grain and pore geometry, and pore volume etc. contained in a large volume or mass of a material can be represented by a chosen Representative Element Volume (REV) in a 3D object or Representative Element Area (REA) in a 2D object. This assumption provides a way of effectively predicting the behaviour of many elements from a few of them. Therefore, the macroscopic variable of the entire volume is taken as an average of the variable over the REV or REA. Using a REV or REA as the case may be, is necessary because modeling and analysis of images require huge computational resources. Consequently, it may not be possible to analyze and model the entire image of the core sample.

 REV is the minimum domain size where material properties are continuous and representative of heterogeneous material. It could also be said to be the smallest size in which further increase in size will not cause a significant change in the measured properties. REV can be found for an entire rock type or for a phase of the rock. A phase is a mineral or textural component of the rock matrix. REV for a porous material has been found to be different for different properties or phases (Mehmani et al., 2020). It is a concept used as a tradeoff between computational efficiency and model size. This implies that REV is the size of the digital rock that is big enough to represent the property of the sample and small enough to allow for successful computation (Fernandes, 2012).

REV was used by Borges et al., 2012 to show the variation in the porosity of a sample as the volume progressively increased. The original REV curve has three regions. The first region is the domain of microscopic effect where there is a great variation in the

measured porosity with volume. The second region is the domain of the porous medium where the volume of the material becomes inconsequential to the measured porosity. The third region is the domain of macroscopic effect where there is a variation in the measured porosity. The second region represents the region of homogeneity and is therefore the ideal size that can be taken to adequately represent the material. If any of the volume sizes that falls in region (II) is used, it is the REV.

Researchers such as Fernandes et al. (2012); Al Hattamleh et al., (2009); Razavi et al., (2006); Wang et al., (2015) and Costanza-Robinson et al. (2011) have used the concept of REV. Mehmani et al. (2020) presented a review of the current status of establishing a REV, and upscaling techniques for image-based model in an unconventional reservoir. Unconventional reservoir, in this case, refers to rocks whose pore space can be completely rendered such that all boundary conditions and features such as pore throats are captured with a single micro-CT image e.g. the Berea and Fontainebleau sandstones.

2.10 Previous laboratory and field studies on CO_2 storage

Laboratory core flooding experiments are normally performed on either synthetic or natural core samples in the laboratory. Such experiments are performed at in situ temperature, pressure and brine conditions representing underground CO_2 storage. The laboratory core flooding experiments is the most effective way to study CO_2-brine-rock interaction, and the knowledge gotten from these experiments have proven to be very useful in understanding geological CO_2 storage. The temperature and pressure conditions that have been used in laboratory core flooding researches range from $10^{\circ}C$-$70^{\circ}C$ and 3 MPa-150 MPa respectively. A summary of laboratory core flooding experiments performed by different researchers has been presented by Sun et al., (2016). Other important parameters necessary for the core flooding experiment include the core diameter, core length, temperature, and pressure as well as brine concentration. Sun et al. (2016), from a review of core flooding experiments around the world, presented that statistically, the optimum core diameter used in most core flooding experiments is 20-60mm (79.3%), core length of 50-150mm (83.3%), the injection pressure of 10-30 MPa (95%) and temperature of $40^{\circ}C$-$60^{\circ}C$ (69.6%). Most

CO_2 core flooding experiments have been done with supercritical CO_2 as pressure and temperature used was >7.1 MPa and >31.1ºC.

2.11 Experimental procedure from previous researches

Different experimental procedures have been used in past researches. Some researchers directly injected CO_2-saturated acidic brine into rocks (Alemu et al., 2011; Luquot & Gouze, 2009; Vialle & Vanorio, 2011a). On the other hand, Bemer et al. (2016) used thermally activated acid instead of brine, because CO_2 dissolution in water ultimately produced acid. Meanwhile, Pimienta et al. (2017) injected supercritical CO_2 into brine saturated rocks. Irrespective of the procedure adopted, it is very important that CO_2 and brine or a product of the reaction between CO_2 and brine is in the reservoir.

A lot of apparatus are used for laboratory core flooding. Materials needed include either porous/permeable rock sample (Krevor et al., 2012) or synthetic rocks (e.g.) packed glass beads to represent the rock (Eshiet & Sheng, 2017), CO_2 and/or brine, optical visualization and analysis tools/software, imaging equipment like Computed Tomography (CT) or Scanning Electron Microscopy (SEM), X-ray Diffraction (XRD), Scanning Electron Microscopy (SEM-EDS), for analysis of the chemical composition, Brunauer-Emmett-Teller (BET), and Helium-porosimetry. The injection of the CO_2 is done using flow pipes in a flooding chamber. Where samples are to be saturated with CO_2/brine, this is done in pressure vessels under appropriate conditions. The reservoir pressure and temperature conditions are simulated using a high triaxial compression machine, pressure vessels and heating system.

Luquot and Gouze (2009) experimentally determined the porosity and permeability changes induced by the injection of CO_2 into carbonate rocks from a set of experiments using X-ray CT, SEM and XRD. Their first experiment was designed to quantify reactions occurring near the CO_2 injection zone, where the fluid is saturated with CO_2. The other three experiments correspond to increasing distances from the injection point, where the fluid is expected to contain progressively less CO_2 and more divalent cations resulting from rock dissolution along the fluid pathway.

Berrezueta et al., (2013) conducted studies on the pore changes during experimental CO_2 storage using rock samples from a potential storage basin in Spain. Their approach comprised qualitative and quantitative determination of the mineralogical and textural changes in selected sedimentary rock samples after the injection of supercritical CO_2 at P ≈ 75 bar, T ≈ 35 °C for 12–97 hours under dry condition only. The mineralogy and texture were studied before and after the injection using optical microscopy, scanning electron microscopy and Digital Image Analysis (DIA) using Aphelion 3.2 and Image Pro plus 7.0 software.

Zheng et al. (2015) conducted an experimental investigation on sandstone to study the impact of CO_2–NaCl on the strength, hydraulic, and chemical properties of the quartz-feldspar–detrital sandstone reservoir. In their experiment, the brine composition was 0.1 mol/L sodium chloride. CO_2-rich brine was prepared by dissolving CO_2 into the brine at 1 MPa. The experiments were performed at a temperature of 25°C, confining pressures of 10, 20, and 30 MPa in triaxial compression tests, and a differential pressure of 1 MPa in the creep test. Their result showed that the mineral dissolution did not affect the rock mechanical properties. This was attributed to the fact that the rock is rich in quartz and quartz is rarely reactive to CO_2-rich brine.

Aside from flooding experiment, the percolation experiment is also used to study CO_2 geologic storage in the laboratory. Luquot et al.,(2016) used percolation experiment to investigate the effect of flow rate and brine composition on CO_2 storage using CO_2-rich brine on Heletz reservoir rock samples. As there is an interaction between the CO_2-brine and the rock, the same aim is achieved except that the flow rate differs.

Most experiments that studied changes in rock properties as a result of progressive chemo-mechanical action of pore fluid in rocks have used water, supercritical CO_2 and /or brine as the pore fluid. The frequent use of water as pore fluid in researches is due to the assumption that pores contain mostly water. However, it is known that brine and hydrocarbon (when present) are contained in pores. With CO_2 sequestration, the stored CO_2 will also be contained in pores and will form a more complex mix (Chen et al., 2020). Some researchers have studied the effect of CO_2 on different properties of

rocks. However, majority of such studies have used supercritical CO_2 and/or brine as pore fluid. This is because CO_2 is injected as a dense supercritical fluid.

It is necessary to determine the resident time needed for the different phaseCO_2-brine to have a marked impact on the properties of the rocks. Peter et al. (2020) saturated samples of rocks with different phaseCO_2-brine for 7 days and concluded that the impact of the resulting CO_2-brine on the properties of the rock started gradually from the first day and increased as the concentration of the acidic brine increased. Pimienta et al. (2017) studied the effect of residence time on the dissolution and integrity of rocks flooded with CO_2 and found that the pore brine acidifies just after 2 hours of exposure leading to calcite dissolution and a significant increase in the calcium ions of the brine concentration, as well as a commensurate change in rocks' physical properties such as porosity and permeability. In a scCO_2 fracturing experiment, Zou et al. (2018) observed that the CO_2-brine-rock reaction occurs rapidly (less than 0.5 hour). Olabode and Radonjic (2013) had reported a substantial change in the pH of effluent from shale flooded with CO_2-brine only after 3 days of flooding, and that the change in pH of the effluent was higher in the earlier days. Results from Peter et al. (2020); Pimienta et al. (2017); Zou et al. (2018) and Olabode and Radonjic (2013) showed that the impact of CO_2 on the properties of rock starts vigorously almost immediately.

2.12   Research trends highlighting the gaps in CO_2 storage research

It has been seen from previous studies presented above that effect of CO_2-brine on strength, transport properties and chemical composition of reservoir has been fairly well investigated. However, less attention has been given to the effect of CO_2-brine on pore and grain geometry properties of the rocks. Petrophysical, geomechanical and transport properties of the rocks are controlled by the pore and grain geometry. It is, therefore, necessary to understand how CO_2-brine affects the pore and grain geometry properties, as this will enable a better understanding, prediction and modeling of changes in geomechanical, petrophysical and transport properties of reservoir rocks in a CO_2 storage reservoir.

Secondly, there has not been an attempt to evaluate changes in the properties of reservoir rocks with the different phaseCO_2-brine states. Researches have used CO_2 in the supercritical phase with/without brine. This implies that only the effect of supercritical CO_2-brine is known. Given that reservoir conditions are variable, and considering the fact that the solubility of CO_2 in brine implies that there will be resident undissolved CO_2 in the reservoir for a long time (Buscheck et al., 2019; Chadwick et al., 2008a; Peter et al., 2020), the resident undissolved CO_2 in a reservoir can undergo a change in phase during the storage history, it is, therefore, necessary to understand the changes in the reservoir properties due to the different phaseCO_2-brine.

Chapter 3: Methodology

Natural Captain Sandstone samples were used for this research to replicate the real reservoir rock. The sample was collected from well 13/24a-6 that cuts through the Captain Sandstone. This well falls within Ekofisk 2 CO_2 storage unit according to the CO_2stored database. Ekofisk 2 storage unit is one of the sedimentary units that has been marked for CO_2 storage. Captain Sandstone was used for this research because it has been identified as a suitable geologic formation for the storage of CO_2. This research combines experimental and image based-digital rock physics and rock image analysis to evaluate the impact of the different phaseCO_2-brine states on the geomechanical, mineralogical, petrophysical, as well as pore and grain geometry properties of the rocks. In this research, the phaseCO_2-brine states of the reservoir that are investigated include: (i) br reservoir, i.e. sample saturated with brine; (ii) gCO_2-br reservoir, i.e. sample saturated with brine and gaseous CO_2; (iii) scCO_2-br reservoir, i.e. sample saturated with brine and supercritical CO_2; and (iv) gCO_2 reservoir, i.e. sample saturated with gaseous CO_2. A sample was also tested in dry state.

3.1   Sample Collection

They were recovered from well 13/24a-6 at a depth between 1638.48m-1640.21m in the Central North Sea, UK. The well location is 58.177195, -1.357408. The samples were collected from the British Geological Survey (BGS) core store at Keyworth Nottingham. Description of the core samples are contained in Table 11.

Table 11: Showing core sample data

BGS core ID	Depth (Ft)
SSK105172	5381.4
SSK105173	5379.7
SSK105177	5378.2
SSK105178	5377.2
SSK105176	5376.2
SSK105179	5375.2

✳SSK=BGS code for samples

From the physical examination of the samples, they are weak, structureless, stained whitish, sub-rounded, interlocking-medium grained sandstone. There were no discontinuities. They are well-sorted and mature sandstone (Figures 10 and 11). The

well from which the sample was collected is in the area marked by red dots in Figure 12.

Figure 10: A view of the collected samples
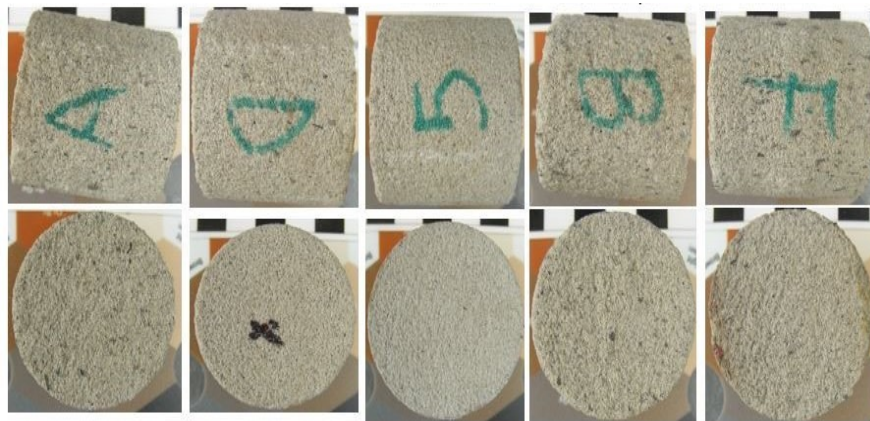
Figure 11: Photograph of the dry core samples
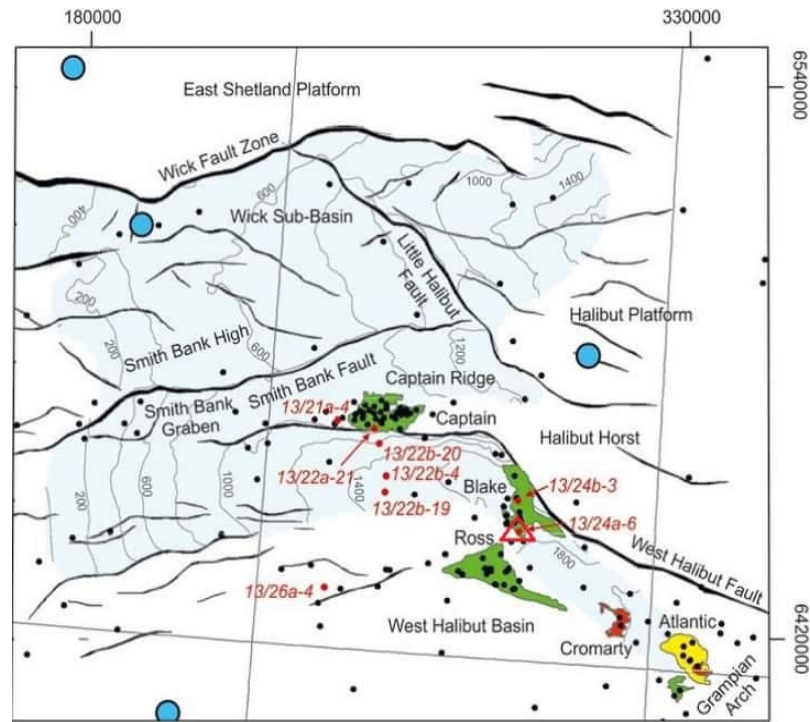
Figure 12: Location map showing well 13/24a-6 (triangulated) where core samples were collected (adapted from Williams et al. (2016)).

3.2 Sample Preparation

3.2.1 Cutting and trimming of samples

Because the samples had uneven edges, they were trimmed with a motorized diamond-blade saw to make the surface square and even. The triaxial compression requires that the surfaces of samples be evenly flat for equal distribution of stresses.

3.2.2 Dimensions and weight of the samples

Dimension and weight of all the samples were taken after cutting and trimming. Hence, the bulk volume and densities were also determined. Table 12 shows the measurements.

Table 12: Dimensions and weight of samples before the experiment

Sample ID	Weight (g)	Diameter (mm)	Length (mm)	Bulk volume (mm^3)	Bulk density (g/mm^3)
Sample to be used as dry	72.05	38.1	35.7	40593.11	1.77e-3
Sample to saturated with br	71.35	38.2	35.2	40472.64	1.76e-3
Sample to be saturated with gCO$_2$	73.44	38.1	36.3	41296.34	1.78e-3
Sample to be saturated with gCO$_2$-br.	71.60	37.9	35.2	39833.52	1.78e-3
Sample to be saturated with scCO$_2$-br.	70.22	37.9	34.5	38932.59	1.78e-3

3.2.3   De-salinating the samples

The samples were recovered from deep saline formation and would contain some salt. This was confirmed by the high conductivity of distilled water in which the sample was soaked initially. It is expected that the sample would have varying amount of the salt. It is necessary that the samples are identical in terms of brine composition. Therefore, the original brine was dissolved and flushed out so that the samples only contain brine prepared for this experiment, and for correct measurement of the dry weight, density and porosity.

The samples were soaked in distilled water for a total of 405.4 hours. During this time, the conductivity of the water was monitored and the water was changed at time intervals. The conductivity curve is presented in Figure 13. Notice that this process got the conductivity down to 5.1 µS from 1215 µS as seen in Figure 3. Compared with the conductivity of tap water measured to be 36 µS, this is an acceptable value to conclude that the original brine has been flushed out. The core samples were then flushed with distilled water under pressure of 3 MPa with 1 litre of distilled water. To further confirm that the samples were free from the original brine content, a few drops of silver nitrate (Ag$_2$NO$_3$) was added to the effluent solution, and there was no cloudy precipitation. This shows that the fluid is now devoid of brine. As expected, the mass of the samples decreased after de-salining. The new masses are recorded in Table 13.
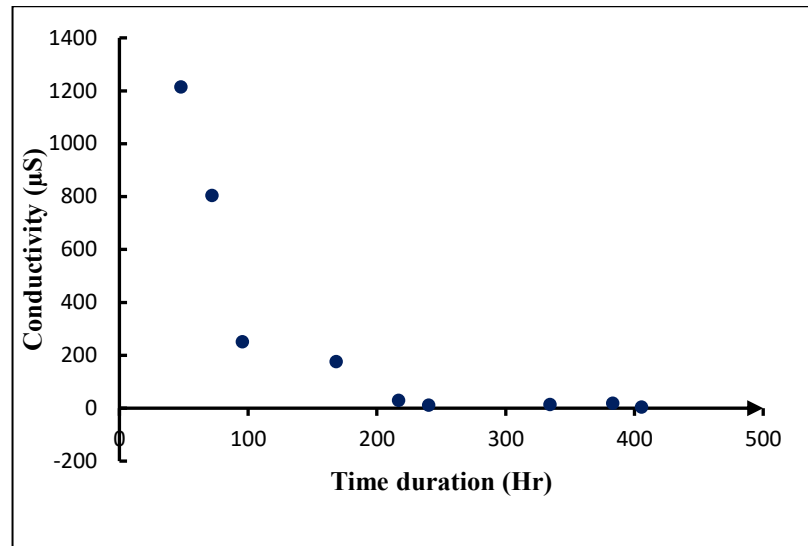
Figure 13: Conductivity curve with time. This shows that salt dissolved out of the rock into the distilled water.

Table 13: Mass of samples after de-salining

Sample ID	dry	br	gCO_2	gCO_2-br	$scCO_2$-br
Mass (g)	69.02	70.61	70.43	69.61	67.49

3.2.4 Preparation of brine

NaCl brine was prepared to be used as brine for this experiment. 121.2g of 99.9% pure NaCl was dissolved in 2 litres of distilled water. This made a standard solution of 60600ppm. Given that the samples have been de-saline of their original salt to ensure that no unknown species was present, the rock sample only contains 60600ppm NaCl solution as brine. 60600ppm is the concentration of brine in the Captain Sandstone formation where the samples were recovered according to CO_2stored.

3.2.5 Preparation and saturation of rock samples in respective phaseCO_2-brine states

The core samples were initially characterised to understand the properties of the samples before saturating the samples with the different phaseCO_2-brine, followed by triaxial compression. The samples were also re-characterized after saturation, and after triaxial compression.

The different states of the rock samples in this research are:

1. Dry sample

2. Rock sample saturated with brine
3. Rock sample saturated with brine and gaseous CO_2
4. Rock sample saturated with brine and supercritical CO_2
5. Rock sample saturated with gaseous *CO_2*

3.2.5.1   Preparation of dry sample

This core sample required no saturation as this sample is to be tested in a dry state. The properties and behaviours obtained from this sample state represent the properties and behaviour of the dry rock at the condition.

3.2.5.2   Preparation of sample saturated with brine

The core sample was vacuum-saturated in brine for 7 days. The properties and behaviours obtained from this sample represent the properties and behaviour of the brine saturated rocks at the condition.

3.2.5.3   Preparation of sample saturated with brine and gaseous CO_2

The core sample was vacuum-saturated in brine for 7 days. The brine saturated sample was put into a Paar pressure vessel (model 4790). Brine was poured into the pressure vessel till the sample is covered with brine. CO_2 is pumped into the pressure vessel until the pressure in the pressure vessel is 50 bars and stays constant. With time, dissolution of the gaseous CO_2 into the brine and entrance of the CO_2 into pore spaces occurred, and the gas pressure reduced gradually. More CO_2 was pumped into the vessel to keep the pressure constant. While the gas pressure was set at 50 bars, the pressure vessel was at a temperature of 27°C. Under this temperature and pressure condition, the CO_2 was kept in a gaseous state. This setup was allowed to stand for 7 days and more CO_2 was pumped in if needed to keep the pressure at 50 bar.

It was observed that CO_2 dissolution in the brine continued for 5 days. This was indicated by the drop in pressure. On the sixth day, the pressure did not drop. This shows that the brine was already saturated with the dissolved CO_2. The properties and behaviour obtained from this sample represent the response of reservoir rocks to storage when gaseous CO_2 is present and dissolves into the brine.

3.2.5.4 Preparation of sample saturated with brine and supercritical CO_2

The setup for the sample in this state is similar to the setup in section 3.2.5.3 except that higher pressure and temperature was used. A Paar pressure vessel (model 4760) was used. The brine saturated sample was placed in the pressure vessel. Brine was poured into the pressure vessel till the sample is covered with brine. CO_2 is pumped into the pressure vessel until the pressure in the pressure vessel is 100 bars and stays constant. With time, dissolution of the CO_2 into the brine and entrance of the CO_2 into pore spaces occurred and the pressure reduced gradually. More CO_2 was pumped into the vessel to keep the pressure constant. While the CO_2 pressure was set at 100 bar, the pressure vessel was at a temperature of $36^{\circ}C$. Under this temperature and pressure condition, the CO_2 was in a supercritical state. This setup was allowed to stand for 7 days and more CO_2 was pumped in if needed to keep the pressure at 100 bar. A similar drop in the pressure as seen in section 3.2.5.3 was also observed in this sample following the dissolution of CO_2 into the brine. Properties and behaviours obtained from this sample represent the response of reservoir rocks to storage when supercritical CO_2 is present and dissolves into the brine.

3.2.5.5 Preparation of sample saturated with gaseous CO_2

The setup for the sample in this state is similar to the setup in sections 3.2.5.3 and 3.2.5.4 except that the sample was not initially saturated with brine. The sample was placed in the pressure vessel. CO_2 is pumped into the pressure vessel until the pressure in the pressure vessel is at 50 bars and stays constant. While the gas pressure was set at 50 bars, the pressure vessel was at a temperature of $27\ ^{\circ}C$. This setup was allowed to stand for 7 days. Contrary to the previous samples, there was no significant reduction in the pressure with time. This is due to the fact that there was no brine and there was no CO_2 dissolution. However, the entrance of CO_2 gas into the pores resulted in a slight drop in the pressure with time and more CO_2 was pumped in if needed to keep the pressure at 50 bar. The properties and behaviour seen in this sample represent the behavior of rocks saturated with only gaseous CO_2. For instance, when CO_2 rises to the top of a reservoir where the rock is dry.

3.3   Sub-sampling and thin sectioning

Three sets of sub-samples from the same core were vacuum-saturated in each phaseCO$_2$-brine. The main sub-sample with a length of 36mm and a diameter of 38mm (Figures 10 and 11) was used for the triaxial experiments. A smaller cylindrical sub-sample with a diameter of 4.5mm and a length of 7.5mm (Figure 14) was prepared for micro-CT imaging and Scanning Electron Microscopy (SEM), and the last sub-sample was used to prepare a thin section slide for petrographic microscopy. The dry natural sample was imaged and scanned before triaxial compression. After the triaxial compression test, another set of 4.5mm by 7.5mm cylindrical sub-samples were collected from the center of all the compressed samples for micro-CT imaging and SEM, and another thin section slide was also made from the compressed samples. Before imaging and scanning, the saturated samples were allowed to dry undisturbed. The thin section was prepared following the standard procedure at the thin section laboratory of the school of Earth and Environment at the University of Leeds.

Figure 14: Sub-samples of the different samples before compression used for micro-CT, SEM and XRD.

3.4   Triaxial compression testing

The experiments consist of saturating the different core samples with the different phaseCO$_2$-brine, and then subjecting the saturated samples to reservoir pressure conditions through the multiple triaxial tests. Dissolution of CO$_2$ in brine produces an acidic solution. Results from Peter et al. (2020), Pimienta et al. (2017) and Zou et al. (2018) showed that the impact of CO$_2$ on the properties of rock starts vigorously almost immediately. It was hence decided that for this experiment, more than 5 days would be good enough for the phaseCO$_2$ saturated-brine to have an effect on the properties of the rocks. The samples were saturated in the different phaseCO$_2$-brine for 7 days.

Triaxial compression was used to simulate the reservoir stress conditions on the prepared samples. The geomechanical and deformational behaviour of each sample under the reservoir conditions was evaluated from the triaxial test data. The sketch of the entire experimental process (including saturation and triaxial compression) is shown in Figure 15.
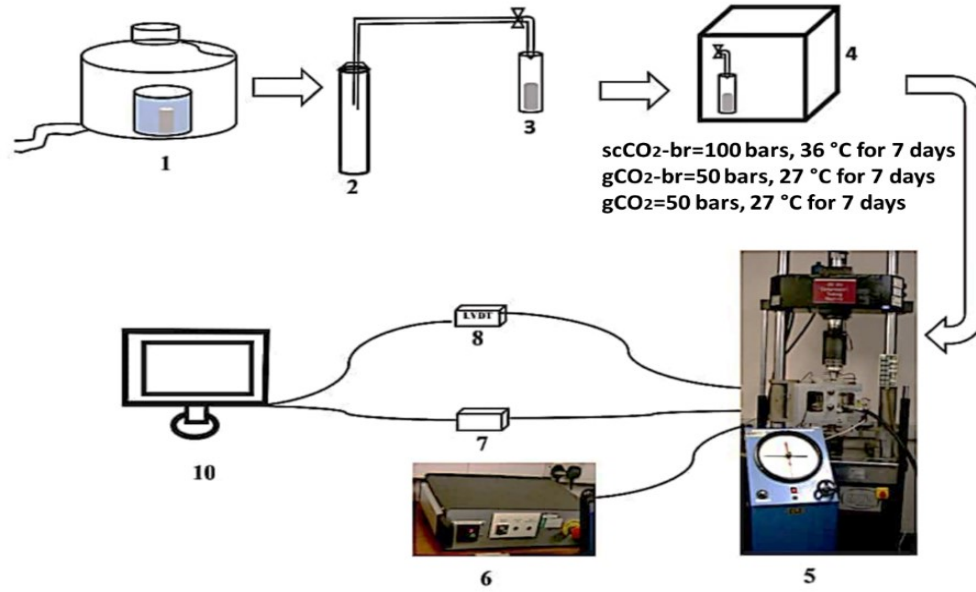
Figure 15: The experimental setup from saturation to triaxial compression testing (1. Vacuum pump for saturating the sample with brine, 2. CO_2 gas cylinder, 3. Pressure vessel with control valve and brine saturated sample being flooded with CO2, 4. Pressure vessel with control valve and CO_2-flooded-brine saturated sample in oven, 5. Triaxial machine and compressor, 6. Temperature regulator, 7. Pressure transducer, 8. Displacement transducer, 9. Desktop computer).

The schematic of the experimental setup as shown in Figure 15 consist of a vacuum pump (model MZ 2D NT) for removing trapped gases in the samples to ensure saturation of brine in the samples, two pressure vessels (Parr instruments, USA) with pressure range of 0-69 bar and 0-200 bar and temperature limit of 350 °C for holding the sample, brine and CO_2 in the desired pressure conditions, an oven to maintain the temperature condition for the sample, brine and CO_2, a 250KN triaxial machine (MAND testing machines Ltd.) for the triaxial compression test, a 3-70 MPa confining pressure pump (ELE) using silicon oil to supply confining pressure, a temperature regulator (custom built in University of Leeds with temperature controller and a K-type thermocouple with a precision of 0.2% and a resolution of ±1 °C) to keep the temperature of the sample and sample holder at the desired temperature during triaxial

test, pressure transducer (gems sensors and controls, range 0-100MPa and precision of 0.25%) to measure and log the real-time pressure impacted on the sample and a microlink 751 multifunction data acquisition and control (set at 15 bits per channel, with each channel limited to ±10 Vdc and a resolution of 0.8 mV over the ±10 V range with a precision of ±0.05%) to record the displacement data from the Lateral Variable Differential Transducers (LVDT), and displayed on a computer using windmill software.

A sample is inserted into the sample holder of the triaxial machine that had been lined with an elastic vuitton sleeve. Triaxial compression stress was applied to each sample. Two Lateral Variable Differential Transducers (LVDT) were clamped via a flexible metal cantilever to the middle of the sample to measure the lateral displacement. Axial displacement was measured by two magnetically-attached displacement transducers that touch the top and bottom of the sample. Both the lateral and axial displacement transducers were connected to a microlink 751 multifunction data acquisition and control box for recording and display. The pressure transducer connected to the computer delivers load/stress to the sample. Before each test, the sample and the sample holder compartment of the triaxial machine were heated to the desired temperature. This was then left for about 30 minutes to ensure that the temperature equilibrated across the sample. The confining pressure and axial stresses were then increased hydrostatically up till 16 MPa. This is the prevailing pressure at depth from which the samples were recovered.

At this point, the sample has been brought to the reservoir stress and temperature condition. For each sample, a triaxial test was first conducted in creep mode. The axial stress was then increased from 16 MPa to 16.75, 17.5, 19.0 and 22.0 MPa and the fatigue was observed for each increase in the axial stress. With confining pressure held constant at 16 MPa, the deviatoric stresses correspond to 0, 0.5,1.0, 2.0 and 4.0 MPa respectively. After this, multiple failure compressive test was then conducted. Again, the confining and axial stress were increased hydrostatically until 16 MPa. The axial stress was continuously increased until shear enhanced compaction ends at 16 MPa confining stress. This is repeated with confining stresses of 26, 36 and 46 MPa until failure in each case. The axial and lateral displacements (Δl and Δd) from both

transducers, confining pressure and axial load/stresses were recorded per second during the entire test and displayed on the screen through the windmill software. The data was processed to yield the axial (ε_a) and lateral (ε_L) strain, volumetric strain (ε_{vol}), fatigue rates (f_r) and fatigue duration (f_t) as well as bulk modulus (K) and compressibility (β).

The triaxial compression test was carried out in two stages. In the first stage, the core samples were initially vacuum-saturated and soaked in brine (60600ppm NaCl solution) for seven days in a vacuum (except the samples to be used as dry and gCO_2 saturated samples). The samples to be used as $scCO_2$-br and gCO_2-br saturated samples were then flooded with the respective phaseCO_2 for a further seven days while still soaked in limited brine. The sample to be used as gCO_2 sample was flooded with gCO_2 for 7 days. To maintain the CO_2 in their desired phases during the CO_2 flooding stage, the pressure and temperature condition were held at 50 bars and 27°C for the gCO_2 samples, while the pressure and temperature condition was held at 100 bars and 36°C for the $scCO_2$ bearing sample. The brine saturated sample was kept at room temperature and 1 atm. By doing these, each rock sample was prepared to represent a phaseCO_2-brine states of the reservoir that has been described in section 1.4.

In the second stage, all the samples were subjected to the reservoir's pressure and temperature conditions using the creep test mode and then, the multiple triaxial compression mode. For creep mode, the axial stress was increased from 16 MPa to 16.75, 17.5, 19.0 and 22.0 MPa and the fatigue was observed for each increase in axial stress. With confining pressure held constant at 16 MPa. For the multiple failure test, confining pressures of 16, 26, 36, and 46 MPa were applied successively to each sample at a constant strain rate of 10^{-5} S^{-1}. The values of the confining pressure ranging from 16-46 MPa were chosen to represent the confining pressure at the site where the samples were collected, starting from the shallowest depth suitable for storage i.e 800m up till greater depths where the confining stress is 46 MPa. It is known that the confining stress in a reservoir increases with depth. According to NERC, the confining pressure at the shallowest depth suitable for CO_2 storage in the Ekofisk storage unit where the samples were collected is 15-16 MPa and the temperature at the shallowest depth is 34-44°C. The shallowest depth suitable for CO_2 storage is 800 m (Holloway

et al. 2006). Also, the minimum confining pressure is 15 MPa (Hangx et al. 2013). Therefore the triaxial test condition was designed to simulate the reservoir conditions ≥ 800 m. For each confining pressure, the axial stress was increased until shear-enhanced compaction ends.

Finally, the samples were removed from the triaxial machine, and sub-samples were collected for micro-CT, and SEM examination. Thin sections were also prepared from the samples for SEM-EDS and SEM examination as explained in section 3.3.

3.5   Digital rock physics and rock image analysis

The reconstructed 3D micro-CT imageswere processed intodigital rocks, and the pore and grain geometry properties were characterized and evaluated using Avizo. Also, the 2D SEM images were processed, and the pore and grain geometry properties were characterized and evaluated using Image J software.

3.6   Characterization

3.6.1   Measurement of Viscosity

The viscosity of the different effluent collected after the different phaseCO_2 dissolved in brine was measured with an Oswald U-tube viscometer at room temperature. This was to see how the different CO_2 phases affect the viscosity of the resulting phaseCO_2-brine fluid. This would be an important parameter for modelling as the viscosity of the resulting fluid is affected by the phase of the CO_2 that dissolved into the brine, aside from temperature and pressure as have been indicated in researches. To do this, the time it takes for a fixed volume of the phaseCO_2-brine fluid and distilled water to flow through the bore in the viscometer is recorded. The experiment was repeated four times for both distilled water and the phaseCO_2-brine fluid and the average time is taken. The mass of a known volume of water and phaseCO_2-brine fluid was also measured to determine their densities. The result of all the measurements taken in relation to the viscosities of all the fluid is presented in **Error! Reference source not found.** 14. The viscosity of the phaseCO_2-brine fluid was calculated using the formula in equation 1 below..

$$V_2 = \frac{\rho_2 t_2}{\rho_1 t_1} V_1 \qquad\qquad (1)$$

Where V_2=The viscosity of the phaseCO$_2$-brine fluid at room temperature, V_1= The viscosity of distilled water at room temperature, ρ_1= The density of distilled water, ρ_2= The density of phaseCO$_2$-brine fluid, t_1=The mean time for the flow of distilled water, t_2=The mean time for the flow of the phaseCO$_2$-brine fluid.

Table 14: Showing measured viscosity of the effluent solution

Effluent	Mean flow time of H$_2$0 (s)	Mean flow time of fluid (s)	Density of H$_2$O (g/dm^3)	Density of fluid (g/dm^3)	Visc. of H$_2$O (cP)	Visc. of brine (cP)
brine	37.16	37.83	0.9950	1.0374	0.9544	1.0128
gCO$_2$ - brine	31.94	33.39	0.9950	1.0418	0.9321	1.0203
scCO$_2$- brine	33.91	33.33	0.9950	1.0378	0.9321	0.9549

*Temperature is 22-23^{0}C, * Viscosity of distilled water sourced from paar.com

3.6.2 Measurement of permeability

The absolute permeability of the samples was measured using a modification of the methods proposed by Lenormand et al. (2010) and Al-Zaidi et al. (2018) as shown in Figure 16. Small chips of the samples embedded in viscous acrylic resin disc were used for this measurements. A confining pressure of 20 bars was used for sealing purposes. For measurement of the original permeability of the rock, flowrates of 0.5, 1 and 1.5 cm^3/sec were used. The permeability was calculated from Darcy's law illustrating the relationship between the flowrates and differential pressure.

$$Q = -\frac{k}{\mu} \cdot \frac{A\Delta p}{L} \qquad\qquad (2)$$

$$k = \frac{Q\mu L}{A(\Delta P)} \qquad\qquad (3)$$

Where Q represents the flow rate (cm^3 /s), μ is the dynamic viscosity (cP) of water at 20° C (1.0020 cP), A is the area (cm^2) of the sample embedded in resin disc, ΔP is the

differential pressure in the direction of flow (atm/cm), L is the length of the sample in the flow direction in cm and k is the permeability (Darcy).
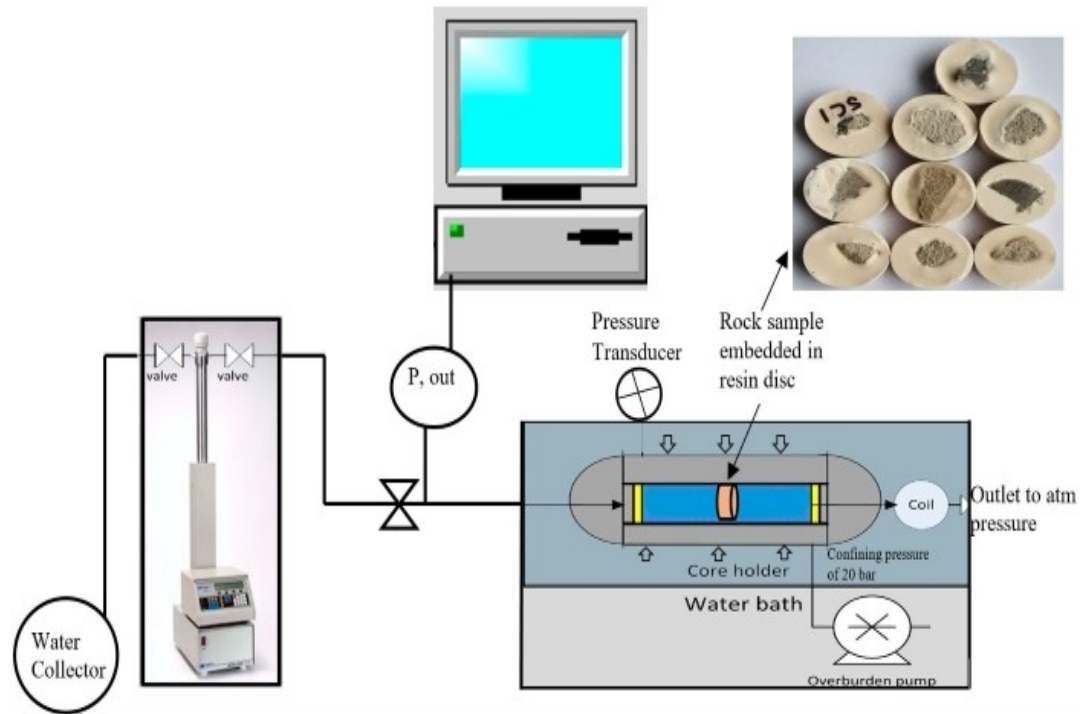
Figure 16: Experimental setup for measuring permeability modified from Al-Zaidi et al. (2018) and Lenormand et al. (2010) with inset of samples embedded in resin disc.

The experimental set-up shown in Figure 16 consists of a high-pressure syringe pump (Teledyne ISCO, Lincoln, NE, USA) for pumping water across the sample, a water bath (Grant Instruments GD 100) with a precision of ±0.02 ∘C for controlling the temperature, a core holder, a pressure transducer for measuring the confining pressure, an overburden pressure pump (CM400) for loading the confining pressure, pressure transducers (UNIK, 0–100 bar with a precision of ±0.1% of BSL) for recording the pressure within the core holder, and LabVIEW software (2015, National Instruments Cooperation, London, UK) for recording the pressure differential across the core holder (the outlet is at atmospheric pressure).

3.6.3 Measurement of porosity

The porosity of the samples was determined as the ratio of the pore volume to the bulk volume [Porosity = pore volume/ Bulk volume ×100]. The weight of the samples in dry, water-saturated and submerged states was measured. The grain volume and pore

volume were determined from the dry, saturated and submerged weights. The bulk volume was determined by measuring the dimensions of the samples. This was repeated four times for each sample. Therefore, the porosity is the average porosities calculated from four repeated measurements. The pore volume, grain volume and bulk density of the samples were also derived from this method using the formulae (equation 4 & 5). Furthermore, the porosity of the samples was evaluated from the 3D digital rock and 2D rock image analysis.

$$\text{Pore volume} = \frac{M_{sat} - M_{sub}}{\rho} \qquad (4)$$

$$\text{Grain volume} = \frac{M_{dry} - M_{sub}}{\rho} \qquad (5)$$

Where M_{sat}= The mass of saturated sample, M_{dry} =Thw mass of dry sample, M_{sub} = The mass of sample when submerged and ρ = The bulk density of the rock sample.

3.6.4   X-Ray Diffractiometry (XRD)

X-ray diffraction (XRD) was used for identification of mineral phases in the dry natural sample and in all the samples after saturation and compression. A thin section photomicrograph was also used to identify minerals in the rocks.

3.6.5   Micro-CT imaging

A Zeiss Xradia 410 micro-CT was used to scan the sub-samples collected before and after compression. Zeiss Xradia 410 micro-computed tomography (μ-CT) housed in the school of Civil Engineering at theUniversity of Leeds, UK was used. The workflow is presented in Figure 17. Avizo was used to process and analyse the CT images. Micro-CT scanning was done using beam energy of 80 keV and power of 7W. 3D image of the rock was reconstructed from the 996 slices. The image was taken at a resolution of 3.39μm and the size of the image was bounded by 988 x 1015 x 997 voxels. Non-local means filter (NLM) was applied to the image to remove the noise. NLM was chosen because of its robustness and the need to preserve edges. No smoothing was applied so as to preserve the structures. The filtered image was

segmented into pore materials using the thresholding algorithm and watershed function.
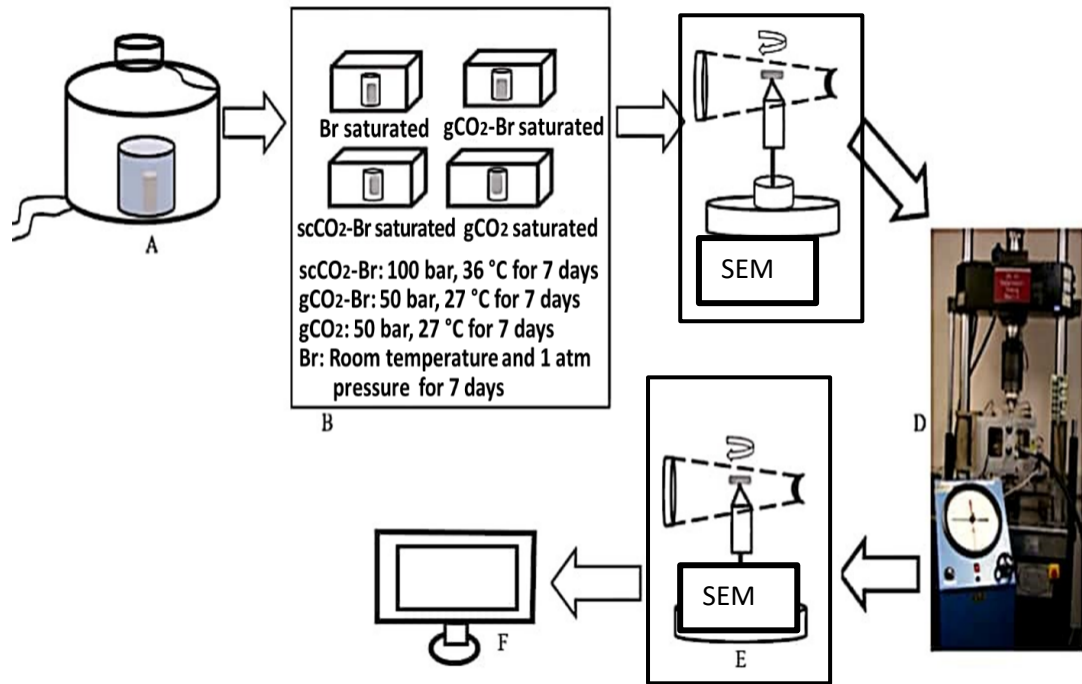
Figure 17: Detailed experimental setup from saturation to CT-scanning and microscopy: (A) Vacuum pump for brine saturation; (B) Sample saturation; (C) Pre-compression CT scanning and SEM; (D) Triaxial compression rig and compressor; (E) Post-compression CT scanning and SEM; (F) Digital image processing.

3.6.6 Electromicroscopy

Scanning electron microscopy (SEM) was done to produce a 2D image of the samples for use in evaluating the mineral topology, pore and grain geometry, and elemental composition of the samples after saturation and after compression. To examine the topology of the minerals, the bulk samples were coated with 40nm gold to reduce the charging effect (Figure 18), and examined with Jeol IT-100 SEM. A beam voltage of 8kv and probe current of 30pA was applied and the image was displayed using the InTouchScope software. To get information on the elemental composition of the minerals in the rock after saturation, polished thin sections slides were prepared off the bulk samples collected after saturation using the standard procedure as stated in section 3.3 above, and SEM-EDS examination was conducted using the Zeiss Gemini crossbeam 550 FIB-SEM. The slides for SEM-EDS were not coated, a secondary electron secondary ion (SESI) detector was used. A beam voltage of 8kv, beam current at 500pA and 100% charge compensation was applied. All these settings is to allow

high detection sensitivity but without adulteration. The image was pixel averaged and displayed using the Aztec software and the entire image was mapped for elements. To get information on the pore and grain geometry property (micro-fabric), the thin-section slides were gold-coated and examined with the Jeol IT-100 SEM.

Figure 18: Gold coated bulk samples for SEM

The workflow of this research is summarised in Figure 19. The core samples collected to be used are characterised, then flooded with the different phaseCO_2-brine and then subjected to triaxial compression. The flooded and compressed samples are re-characterized. Finally, digital rocks are made from the micro-CT image of the cores samples taken before and after compression, the REA and the REV of the digital rocks are determined, and the REA and REV model was used for the analysis of the grain and pore properties and FEA.

```
                    ┌─────────────────┐
                    │   Core sample   │
                    └─────────────────┘
                             │
                             ▼
                    ┌─────────────────┐
                    │   Core plugs    │
                    └─────────────────┘
                             │
                             ▼
        ┌────────────────────────────────────────────┐
        │  Initial XRD, thin section petrography,     │
        │  Porosity and permeability measurement      │
        └────────────────────────────────────────────┘
                             │
                             ▼
                    ┌─────────────────┐
                    │  Core flooding  │
                    └─────────────────┘
```

Dry sample	br saturated sample	gCO_2-br saturated sample	$scCO_2$-br saturated sample	gCO_2 saturated sample

```
                    ┌─────────────────┐
                    │ Multiple triaxial│
                    │   compression    │
                    └─────────────────┘
```

Post-compression XRD and Permeability measurement.	Pre and post compression thin section petrography, SEM and CT imaging

```
                    ┌─────────────────┐
                    │  Digital rocks  │
                    └─────────────────┘
                             │
                             ▼
```

Determination of REA's and REV for digital rock of the samples, Digital rock models

Characterization of grain and pore properties from the rock images and3D digital rock model. FEA on 3D digital rock model
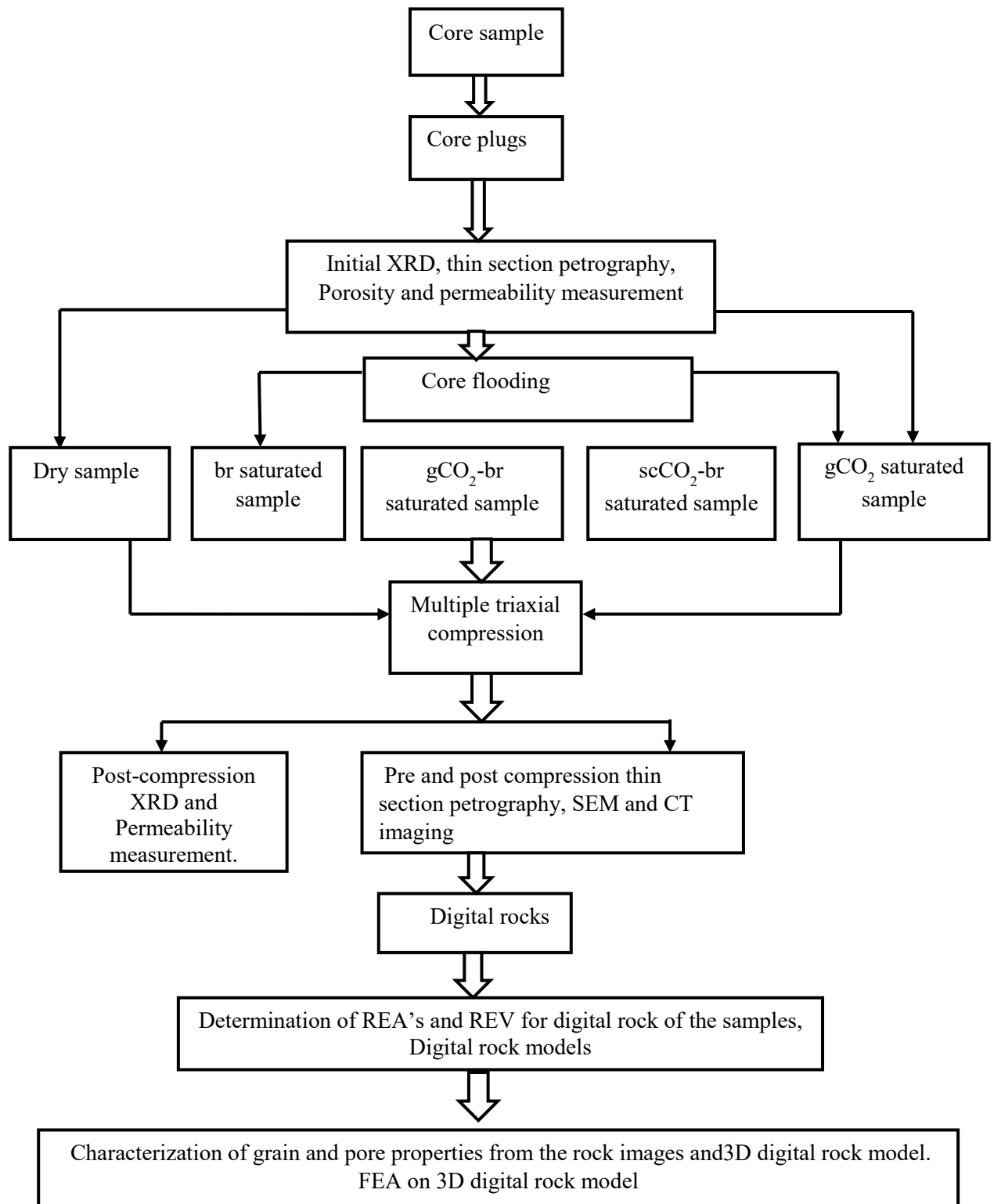
Figure 19: Workflow of the research.

Chapter 4: Initial Characterization of the Rock Samples

4.1   Introduction

It is important to initially characterize the rocks to understand the original properties and be able to track the changes in the properties of the rocks. The characterization of the rock samples involved measurement of the density, porosity, permeability, geomechanic indices, mineralogical composition as well as evaluation of topology of minerals, pore and grain geometry. The core samples were collected from the same core run and the samples were seen to be homogenous. This chapter shows the results of the initial characterization of the samples in a dry state before commencement of the experiment. The same range of characterization was done on the core samples after saturation with the different phaseCO_2-brine and after the triaxial compression. A comparison of the properties evaluated after saturation with the initial properties of the dry sample show the change in properties due to saturation. Also, a comparison of the properties evaluated after saturation, with the properties evaluated after compression show the effectsof stress on the phaseCO_2-brine-saturated samples. The initial properties from the dry sample are presented in Tables 15-19. It is seen that the petrophysical properties (Table15) are similar for all the samples. Therefore, the permeability, mineralogy, geomechanic, mineral topology and pore and grain geometry properties of the dry sample is taken to represent the original properties of all samples before the commencement of the experiments.

4.2   Petro-physical Properties

Table 15 presents a summary of the initial petrophysical properties of all the samples used in this research. The mass of the samples vary slightly from 70.22-73.44g because of slight differences in sizes as can be seen from the diameters and lengths. It is seen that the bulk density of the samples are similar within ± 0.02 (1.78 -1.80 g/cm^3). The porosity, grain volume and pore volume of the samples are also similar. The permeability of the dry sample is 1.14 Darcy, and this is taken to represent the permeability of all the other samples. The samples are of the same lithology i.e weak, sub-rounded, medium grained quartz-arenite.

Table 15: Petro-physical properties.

Sample ID	dry	br	gCO$_2$-br	scCO$_2$-br	gCO$_2$
Mass before desalinating (g)	72.05	71.35	71.60	70.22	73.44
Mass after desalinating (g)	70.35	68.77	69.25	67.24	71.12
Diameter (D) (mm)	38.06	38.21	37.98	37.89	38.08
Length (L) (mm)	35.68	35.24	35.16	34.51	36.26
Bulk volume (cm^3)	39.27	38.64	38.43	37.79	39.73
Grain volume (cm^3)	28.66	27.87	28.07	27.26	28.74
Pore volume (cm^3)	10.30	10.48	10.05	10.24	10.67
Bulk density (ρ) (g/cm^3)	1.79	1.78	1.80	1.78	1.79
Porosity (%)	26.23	27.11	26.17	27.10	26.87
Permeability (Darcy)	1.14				
Lithology	weak, sub-rounded, medium grained quartz- arenite				

4.3 Pore and Grain geometry properties (micro-fabric)

Table 16 is the pore and grain geometry properties of the dry sample. The pore and grain geometry properties of the dry sample before compression represents the initial pore and grain geometry properties of the samples, while the pore and grain geometry properties after compression represent the changes in the pore and grain geometry properties of the samples due to saturation with different phaseCO$_2$-brine and compression.

Table 16: Pore and grain geometry properties

Property description	Before compression	After compression
2D average area of pore (mm^2)	0.073	0.026
Percentage total pore area (%)	42.78	27.93
2D average grain size (μm)	~223	~102
Porosity from 3D model (%)	34	19

The 2D properties were measured from rock image analysis of the 2D SEM images of the rock's thin section using Image J software. From Table 16, it is seen that the average 2D grain size decreased by about 54% after compression, while the average pore size decreased by 64%. The porosity measured from the 3D model using Avizo software decreased from 34% to 19% after compression. These are all impacts of compression on the grains and pores on the dry sample. The processed CT image of the dry sample is shown in Figure 20. Samples of the SEM images of the dry sample used for evaluating the pore and grain geometry properties are shown in Figures 21.
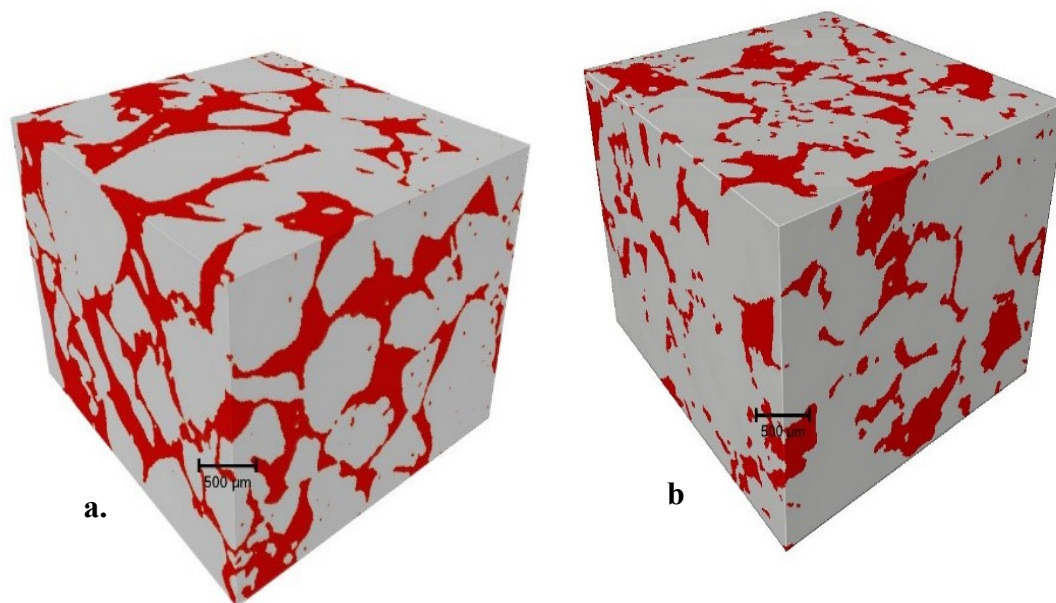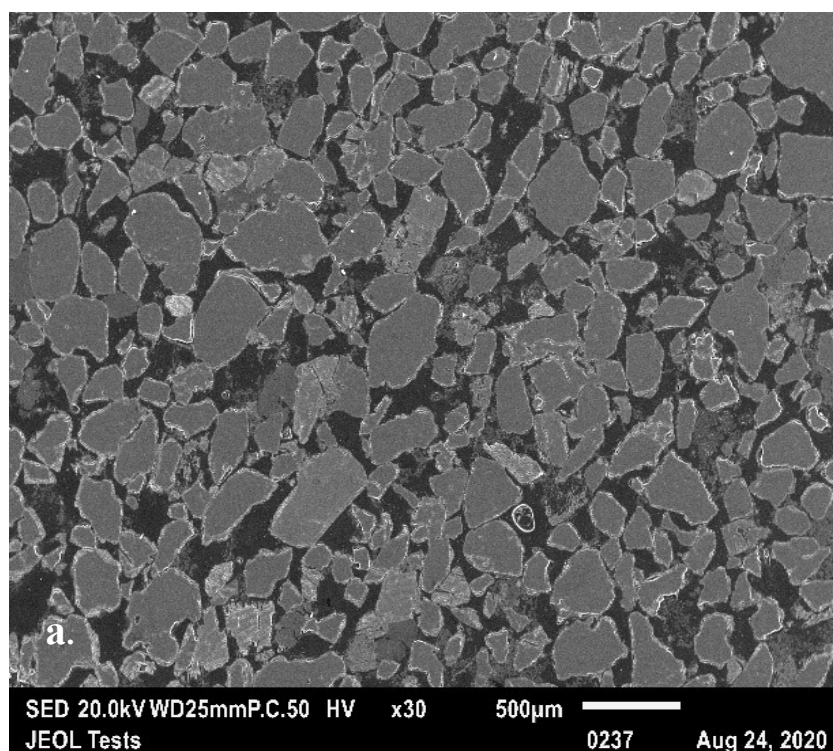
Figure 20: 3D digital rock model of dry sample (a) before compression and (b) after compression. The pore are in red while the grains are grey. The porosity of the sample reduced from 34% to 19% after compression. It is also seen that the geometry of the pores and grains changed markedly after compression.
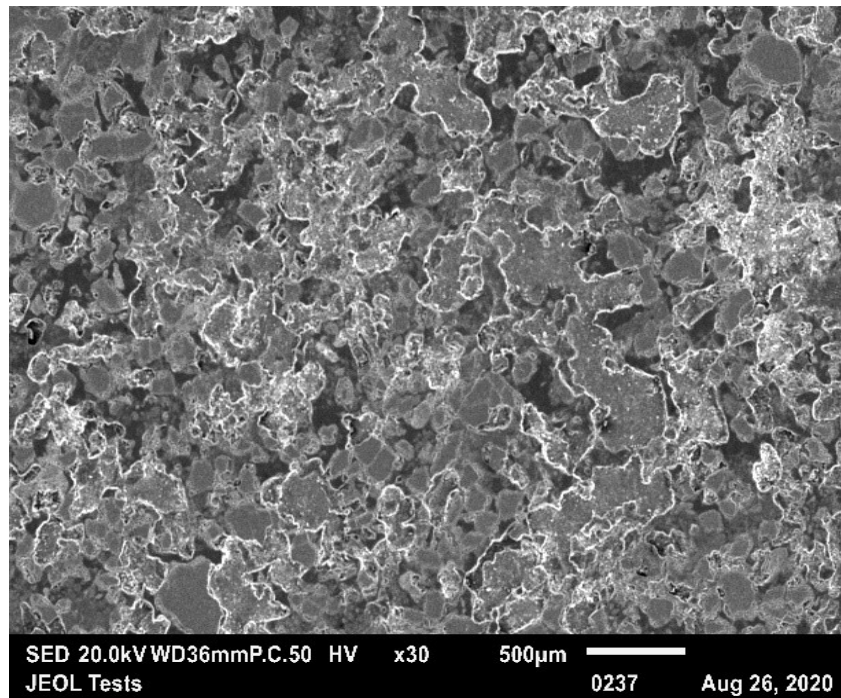
Figure 21: SEM image of dry rock (a) before compression (b) after compression. After compression, the pore area (i.e, dark areas) is seen to be reduced. See more images in Appendix 1a-b.

4.4 Topology of minerals

Figure 22 shows the topology of the minerals and pores in the dry sample. Topology of minerals describes the spatial relationship between the grains of minerals that make up the rock such as overlap, adjacent, disjoint, inside, covered, equal, meets or contains (Thiele et al., 2016). The topology was obtained from SEM images of bulk samples. The topology of the mineral grains before compression is shown in Figures 22a-c. In Figures 22a-b, the grains are globular in shape with intergranular pores. The globular grains are covered with fine materials on their surface. The grains are mostly sub-rounded, disjointed and sometimes, overlapping. The higher resolution image of the dry sample (Figure 22c and f) shows that the surface of the dry sample has ridge and furrows. The image of the topology of minerals (Figure 22d-e) flattened out and became smoother after compression. This is the effect of stress on the minerals. More images showing the topology of the minerals at higher resolution are shown in Appendix 1c-d.

Figure 22: Topology of the minerals in the dry sample. (a-c) Topology of minerals before compression and, (d-f) Topology of minerals after compression. Note that c and f are at 10um resolution while a-d is at 100um resolution.
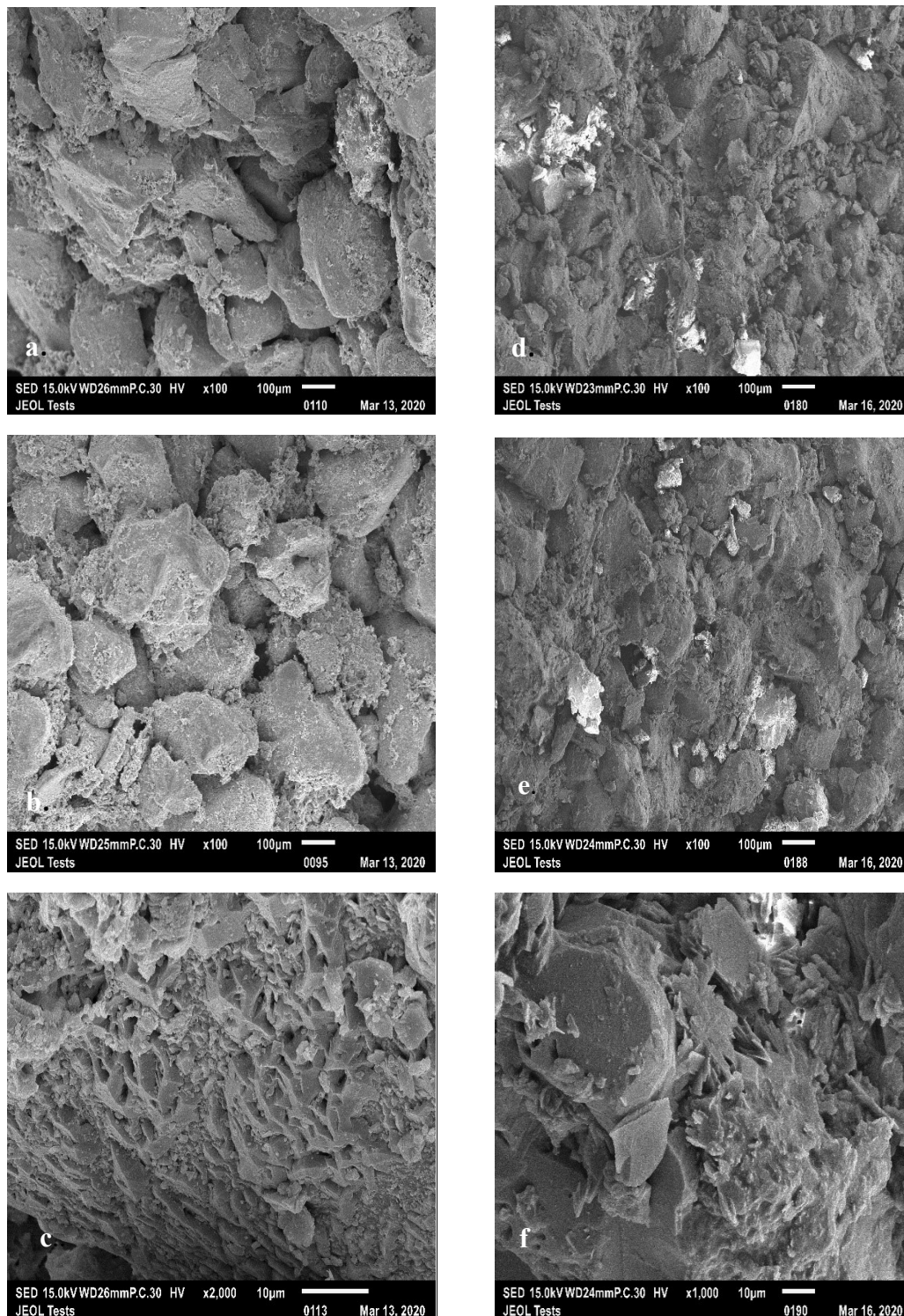
4.5   Geomechanical indices

Table 17 presents the geomechanical indices of the dry sample evaluated after the triaxial compression test. The indices were evaluated from fatigue test and multiple failure test. Figures 23-25 presents the result of the test as curves.

Table 17: Geomechanic indices

Indices	From fatigue test				
σ_{dev} (Mpa)	0	0.5	1	2	4
Primary f_r (μS/sec)	59.7	-	-	-	264.0
Primary f_t (sec)	333	-	-	-	88
Secondary f_r (μS/sec)	14.2	11.8	12.1	12.7	14.6
Secondary f_t (sec)	1377	1786	1786	1760	1646
K (GPa)	1.2164				
β(GPa^{-1})	0.8221				
	From multiple failure test				
σ_3 (Mpa)	16	26	36	46	
E_{t50} (MPa)	4.68	4.90	1.57	3.84	
σ_f (MPa)	59.97	74.84	82.16	88.75	
τ_{max}(MPa)	43.97	48.84	46.16	42.75	
K (GPa)	1.8				
β (GPa^{-1})	0.5556				

E_{t50}=Tangent modulus at 50% peak stress; σ_f=Failure stress; τ_{max}=Maximum shear stress; K=Bulk modulus; β=compressibility; σ_{dev}= Deviatoric stress; σ_3=Confining stress; f_r=Fatigue rate; f_t= Fatigue duration.
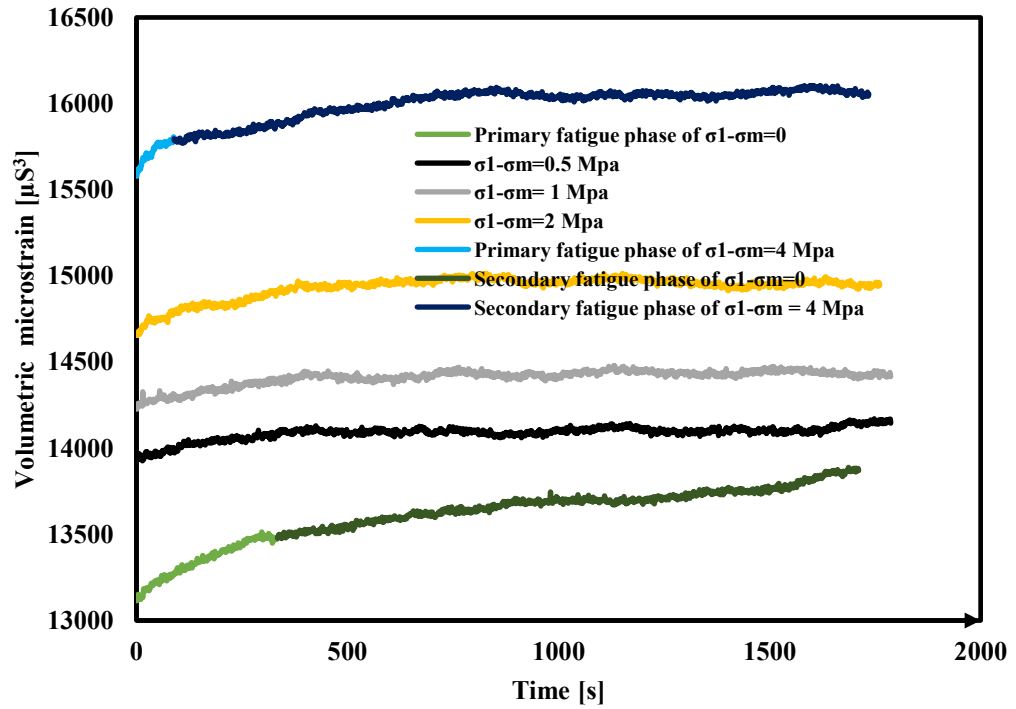
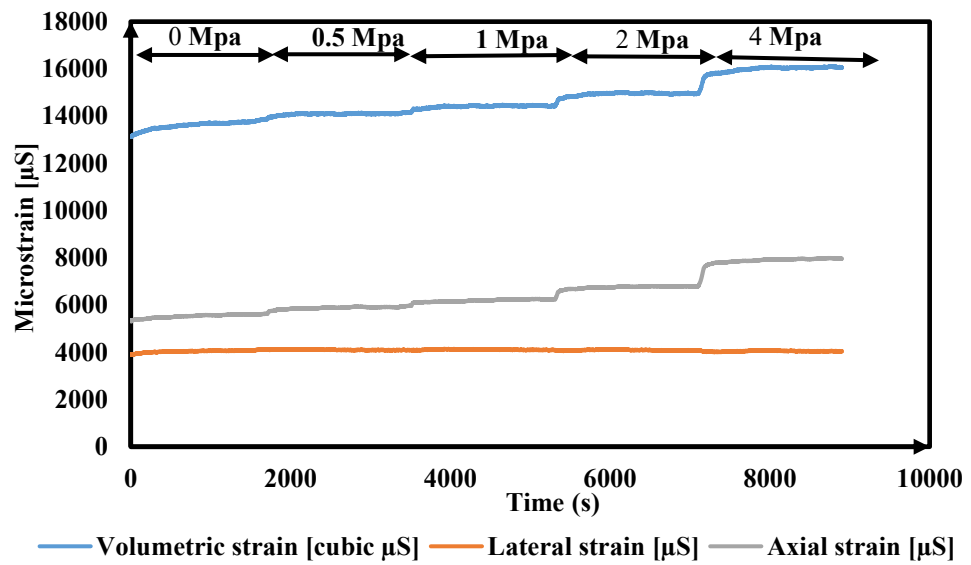Figure 23: Fatigue curve for dry sample under different deviatoric stresses

Figure 24: combined fatigue curves under the different deviatoric stresses from 0 to 4 MPa for dry sample
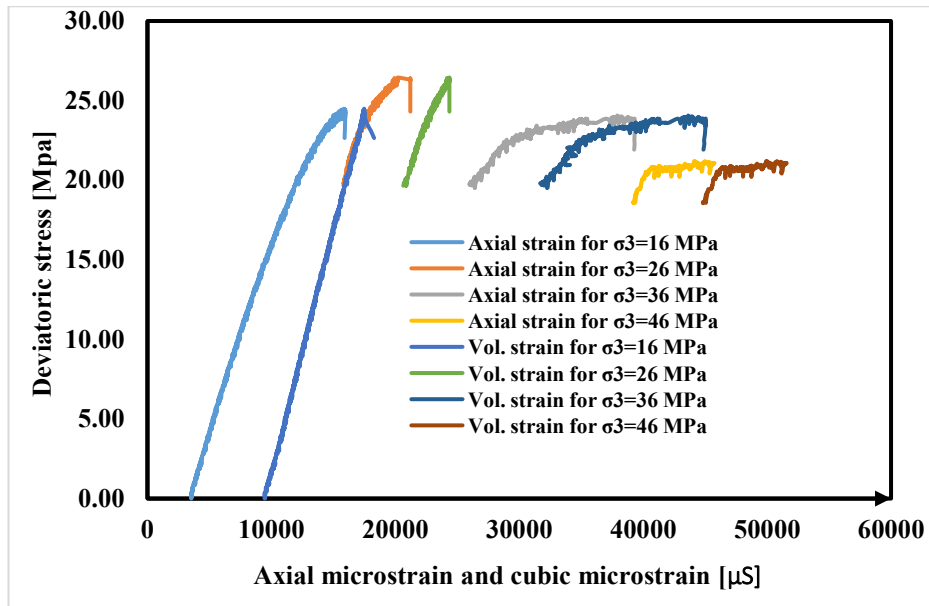
Figure 25: Stress-strain curve of dry sample from multiple failure test

The behaviour of the dry sample during the fatigue test is shown in Figure 23-24, while the behaviour of the sample during the multiple failure test is shown in Figure 25. The fatigue rate of the primary fatigue phase increased by 342% in the 4 MPa stress level when compared to the hydrostatic stress level for the dry sample. The increase in the fatigue rate demonstrates the effect of increased stress on fatigue rate (Fjar et al., 2008). The secondary fatigue rates for the dry sample are 14.2, 11.8, 12.1, 12.7, 14.6 microstrain per second for the hydrostatic, 0.5, 1, 2, and 4 MPa deviatoric stress levels respectively (Table 17), the trend suggests that the secondary fatigue rate and the strain changed with stress level. However, the rate of change was much lower than the primary fatigue at the stress levels where both phases of fatigue apply, with the primary fatigue rate decreasing by 76 and 94.5% at those stress levels. This agrees with the fact that the strain rate is higher at the primary phase of creep compared to the secondary phase. The secondary fatigue rates compared to each other were seen to be higher for stress levels that had the primary fatigue phase i.e the hydrostatic and 4 MPa stress levels respectively. For example, 14.2μS/s and 14.6 μS/s. This may be because the closure of pores and micro-cracks by primary fatiguing creates volume for more grain dilation/contraction for the secondary fatigue phase. The secondary fatigue rate was almost equal for the other stress levels.

The primary fatigue phase in the hydrostatic stress level lasted for 19.5% and 3.8% of the fatigue duration for that stress level and of the entire fatigue duration respectively. For the 4 MPa stress level, the primary fatigue phase lasted for only 5% of the fatigue duration for that stress level, and 1% of the entire fatigue duration for the dry sample. This reduced fatigue duration is the effect of increased stress on the fatigue rate and duration.

To normalise the effect of increased stress on the strain and allow for comparison between the hydrostatic and 4 MPa fatigue behaviour, fatigue duration (f_t) × fatigue rate (f_r) was used to calculate the total strain in the primary phase. The f_t × f_r for the primary fatigue phases show that despite the reduced fatigue duration for the 4 MPa stress level, 16.9% more microstrain was recorded for the dry sample. The total volumetric strain recorded at the hydrostatic stress level was 13115 µS while the total strain recorded during the 4 MPa stress level was 16105 µS. These observations indicate that of the volume of strain recorded under the hydrostatic stress condition, there was more volume of intragranular and intergranular pores and micro-cracks that could not be affected by the hydrostatic stress condition. This suggests that primary fatiguing at lower stress levels do not close up all the genetic pores and micro-cracks as some smaller intragranular and inter-granular pores and micro-cracks are shielded by the rock's effective strength. This makes sense given that the rocks are pre-stressed. The bulk modulus of the dry sample after the fatigue test was 1.2164 GPa and the compressibility was 0.8221GPa^{-1}. After the multiple failure tests, the bulk modulus increased by 50%. This is because the fatigue test led to a reduction of pores and an increase in the shear strength of the rock.

The behaviour of the dry sample as seen in Table 17 and Figures 23-25 follows the theories and empirical studies in rock mechanics. Firstly, In Figure 25, it is seen that increasing the confining stress led to an increase in stiffness, failure stress and shear strength until 36 MPa confining stress when the rock had sheared. This simply represents the role of increasing confining stress on those indices (Fjar et al., 2008; Xia & Zhou, 2010). The reduction in the stiffness and τ_{max} for a dry sample at 36 MPa confining stress is because that point marks the point of critical micro-shearing for the rocks and can be seen as the weakening effect that comes with shearing (Gerbi et al,

2010). It is seen that when the confining stress was increased to 46MPa, the micro-sheared grains increased in stiffness. The dry rock had a shear strength of 48 MPa at the 26 MPa confining stresses and is taken as the critical shearing stress. Beyond this point, the rock starts failing by micro-shearing. Furthermore, at 46 MPa confining stress, even though the stiffness increased, the shear strength reduced. This could be an indication that while shear enhanced compaction may increase the stiffness of rocks, it may not have the same effect on the shear strength. This is plausible when we imagine that the granular material, though deformed and weakened by shear are packed closer together by compaction thereby increasing the stiffness.

The sample deformed by shear enhanced compaction and dilantancy when stress was applied as seen from the curves in Figure 25. The stiffness was seen to increase going from 16 MPa confining stress to 26 MPa confining stress. This shows that the rocks were undergoing compaction hardening. Going from 26 MPa to 36 MPa confining stresses, there was a reduction in the stiffness. But, an increase in stiffness was seen at 46 MPa confining stress due to compaction hardening.

4.6   Mineralogy

Table 18 presents the result of the mineral phases in the dry sample using X-ray Diffraction (XRD). It is seen that the rock is composed mostly of Quartz, Feldspars and Clay minerals, this agrees with the Quartz-arenite lithology name of the rock. Table 19 represents the elemental composition of the dry rocks computed from the Scanning Electron Microscopy-Energy Dispersive Spectroscopy (SEM-EDS) maps shown in Figure 26. The XRD result was used to select the elements to compute in the SEM-EDS.

Table 18: Mineral composition

Sample	Method	Mineralogy
Captain sandstone	XRD	Quartz=79.5%, Plagioclase=0.72% K-feldspar=0.66.1% Illite=1.70% Kaolinite=4.34% Chlorite=1.73% Dickite=6.83%

Table 19: Weight percentage of major elements from SEM-EDS Spectra

Sample	ROI	C	O	Si	Ca	Na	Al	Cl	K	Mg
Dry	1	49.3	31.8	18.0	0.6	0.3	-	-	-	-
	2	46.5	32.1	21.1	-	0.2	-	-	-	-
	3	47.4	34.2	10.9	0.6	-	5.7	0.4	-	-
	4	50.8	32.2	16.4	-	0.2	-	0.4	-	-
	5	51.0	30.1	18.1	-	0.3	-	0.6	-	-
Range		4.5	4.1	10.2	0	0.1	5.7	0.6	-	-
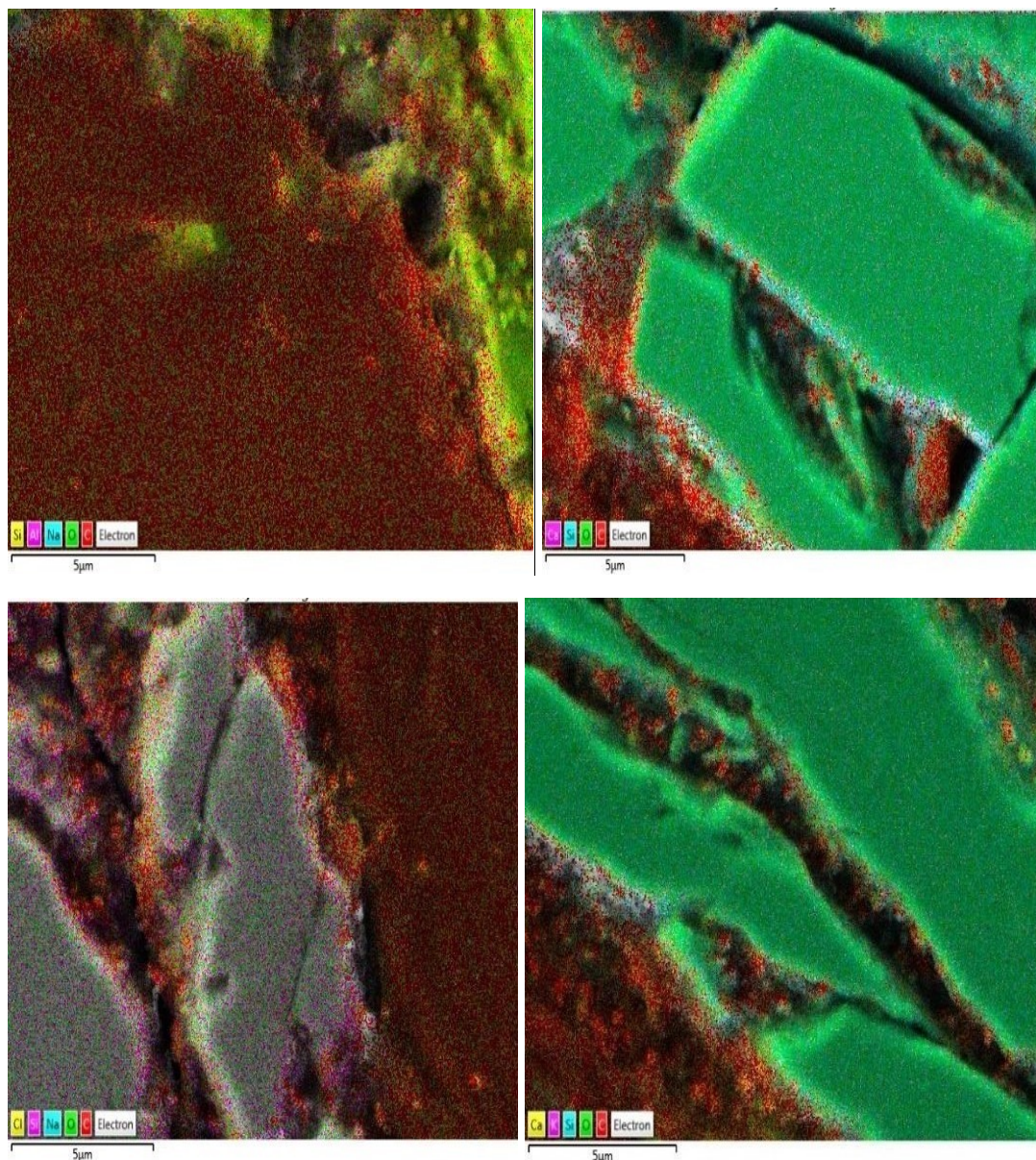
Figure 26: Sample Energy Dispersive map (EDS) map of elements in the dry sample. The weight percentage of each element from 5 different Region of Interest (ROI) was averaged to produce Table 19.
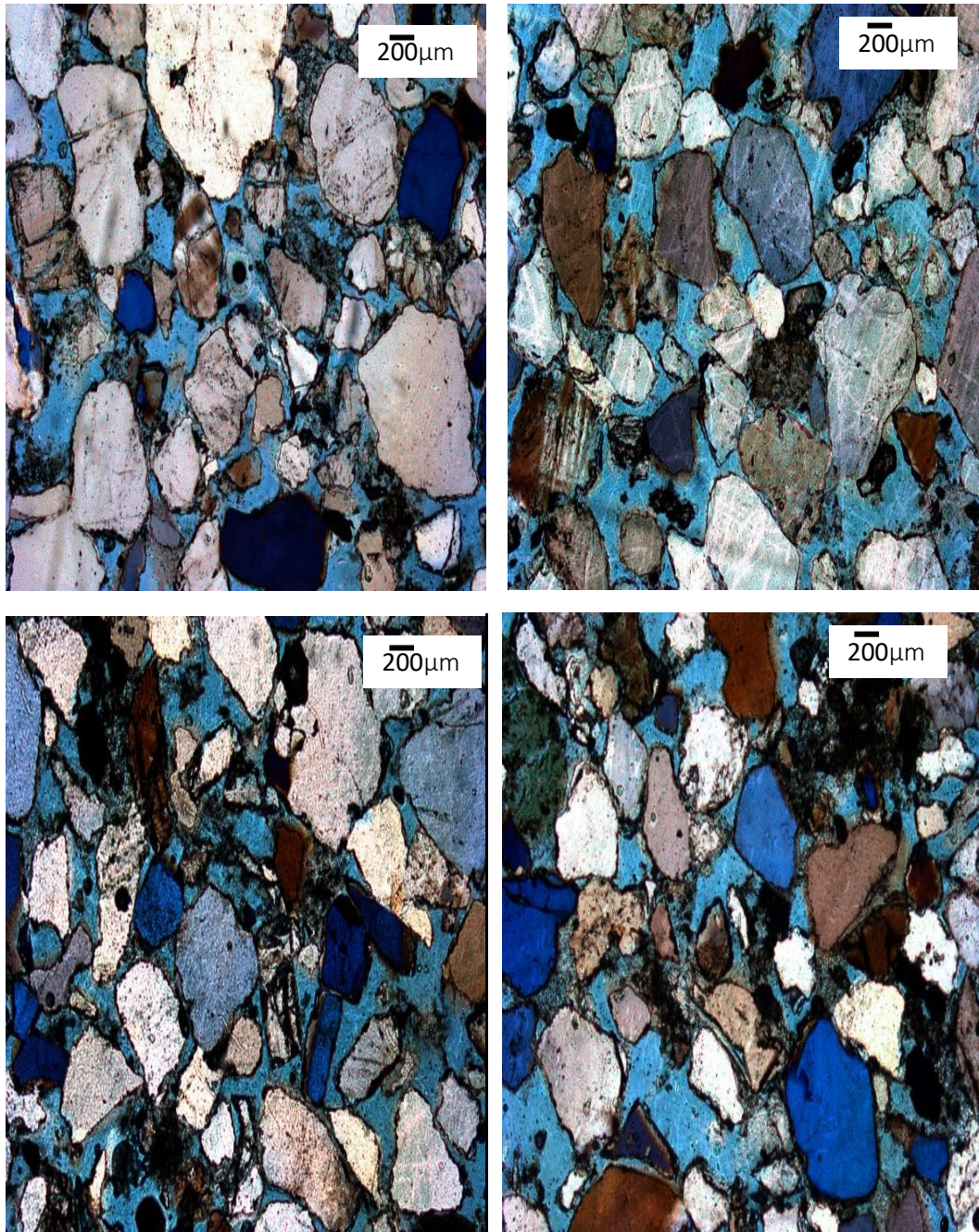
Figure 27: Photomicrograph of the dry sample showing Quartz, feldspar and clay minerals. The blue regions are pores filled with blue resin for contrast. The whitish minerals are the Quartz, the brownish minerals are the feldspars and the dark minerals are the clayey minerals.

The minerals identified in the thin section photomicrograph (Figure 27) are the same as the mineral phases identified from the XRD result. The result of this characterization compares well with the results from previous researches. For instance, measurement of porosity and permeability of Captain Sandstone by Shell (2011) showed 26.3-26.9% and 1.025 to 2.048 Darcy respectively. Others include 1.2 Darcy (Jin et al., 2012) and

26.4 to 29.2% (Hangx et al., 2013). Hangx et al., et al. (2013) reported an average grain size of ~200 μm. The mineralogical characterization of Captain X and Captain D (Goldeneye field) Sandstones using Quantitative Evaluation of Minerals by Scanning Electron Microscopy (QEMSCAN) and X-ray Diffraction (XRD) methods by Rice-Birchall (2018) and Hangx et al., (2013) respectively showed similar minerals seen in the samples used in this research.

4.7   Summary

The petrophysical properties of all the samples used in the experiments are similar. Mineralogical analyses of the samples are also similar. Therefore, the pore and grain geometry properties, geomechanic indices and behavior as well as the mineralogical composition of the dry sample is taken as the original properties of all the other samples.

Chapter 5: Static Fatigue of Saline rocks under Different phaseCO$_2$-Brine States

5.1 Introduction

In this chapter, the results of experimental fatigue tests (deformation under constant but stepped confining stress) performed on Captain sandstone core samples flooded with different phaseCO$_2$-brine under storage reservoir conditions are presented. The deformation rate and static geomechanical properties of the reservoir rocks such as the fatigue behaviour, fatigue rate, fatigue phase duration, static bulk modulus and compressibility due to change in the effective stress from the different CO$_2$-brine states are evaluated and discussed. The results in this chapter provide insights into the response of the bulk modulus and fatigue behaviour of rocks with the different phaseCO$_2$-brine that could exist in Ekofisk CO$_2$ storage reservoir. The understanding of the mechanism of fatigue (deformation under constant stress) in porous rock will also be advanced. CO$_2$ is injected in a supercritical state in most storage reservoir. However, the thermodynamics and the phase behavior of CO$_2$ cause CO$_2$-phase transition. Therefore, the effect of the stored CO$_2$ on the bulk modulus and fatigue behaviour of these storage reservoirs will be better understood and predicted in terms of the evolving CO$_2$ phase.

To provide an understanding of the effect of the different phaseCO$_2$-brine on the fatigue behaviour, fatigue rate, fatigue phase duration, bulk modulus and compressibility, the time-dependent lateral and axial strain of all the rock samples under constant but stepped deviatoric stress were measured and analysed following the ideal rock creep model with three distinct phases; primary, secondary and tertiary phases (Heap, 2009). The end of each creep phase is marked by point of inflection on the curve and are distinct in terms of the mechanism and rate of deformation. The axial strain (ε_a) and lateral strain (ε_L) of the rocks were taken as the averaged $\Delta L/L$ from the top and bottom displacement and averaged $\Delta d/d$ displacements respectively. Where Δd is the change in the diameter of the sample, ΔL is the change in length of the sample, d is the original diameter of the sample and L is the original length of the sample The volumetric strain (ε_{vol}) was taken as ($\varepsilon_{vol=}\varepsilon_a + 2\varepsilon_L$) where $\Delta\varepsilon_{vol}$ is the volumetric strain, εa is the axial strain and ε_L is the lateral strain. Fatigue rate (f_r) was

taken as (ε_{vol}/t) for each fatigue phase observed, where ε_{vol} is the volumetric strain and t is the time. The fatigue duration (f_t) was taken as the time for the fatigue to change from one phase of fatigue to another. The gap in the core holder was filled with steel platen during fatigue testing and a correction was applied on the axial displacement using equation 6 (Ergo Tech).

$$\text{Platen correction } (0 - 50KN) = \frac{-270.66 + \sqrt{270.66^2 + 11364 \times \text{Load}}}{5682} \tag{6}$$

Where Load is the load applied on the sample in Kilo newton (KN).

Since tertiary phase fatigue represents macro-deformation and the aim is to evaluate the microscopic fatigue, the choice of the duration of the static fatigue test and the deviatoric stress applied was therefore informed by the need to avoid the tertiary phase fatigue while also ensuring that the deviatoric stress applied is comparable to the effective stress which can be induced by CO_2 injection and storage. Hence the duration of the static fatigue test was chosen to achieve this purpose.

Deviatoric stress is the stress differential between the axial stresses (σ_1) and confining stress (σ_3) due to increasing axial loading. In this study, it simulates the change in the effective stress that may be due to the phaseCO_2-brine state. Deviatoric stress in the range of 0-4 MPa was chosen to represent scenarios where the pore pressure is equalized with the confining pressure (i.e. effective stress of 0) up till when the pore pressure drops by 4 MPa (effective stress of 4MPa) following CO_2 dissolution and mineralization. The conservative range was chosen because the change in the stress due to injection of CO_2 into the brine saturated reservoir is expected to be low as explained by Rutqvist (2012) and suggested by differential pressure results obtained by Al-Zaidi et al. (2018).

In this study, deviatoric stress (σ_{ev}) is taken as equation 7.

$$\sigma_{dev} = \sigma_1 - \sigma_m \quad (\text{where } \sigma_m = (\sigma_1 + 2\sigma_3)/3)$$

$$\sigma_{dev} = \frac{2}{3}(\sigma_1 - \sigma_3) \tag{7}$$

Where σ_m is the mean effective stress, σ_1 is the axial stress, σ_3 is the confining stress, σ_{dev} is the deviatoric stress.

The bulk modulus (K) and compressibility (β) were measured only from the hydrostatic loading portion (where $\sigma_1 = \sigma_3$). The bulk modulus is given as equation 8 and compressibility is taken as the inverse of the bulk modulus.

$$K = \frac{\Delta\sigma_1}{\Delta\varepsilon_{vol}} \qquad (where\ \Delta\varepsilon_{vol} = \Delta\varepsilon_a + 2\Delta\varepsilon_L) \qquad (8)$$

Where K is the bulk modulus, $\Delta\sigma_1$ is the change in axial stress, $\Delta\varepsilon_{vol}$ is the change in volumetric strain, $\Delta\varepsilon_a$ is the change in axial strain, and $\Delta\varepsilon_L$ is the change in lateral strain.

5.2   Fatigue behavior

Figures 28 and 29 show the fatigue behaviour of the brine saturated sample under constant but stepped deviatoric stress conditions, which represents the fatigue behaviour of the natural reservoir. Any deviation seen in the other samples is therefore due to the phase of CO_2 with which it was saturated. The fatigue behaviour of the other samples is presented in Appendix 3a-d. The primary and secondary creep phases for all the samples were similar. The tertiary fatigue phase was not used for this study because it represents macroscopic deformation. it is seen that only fatigue curves for the hydrostatic and 4 MPa deviatoric stress lvels showed the primary fatigue phase, albeit very short-lived. The brevity of the primary fatigue in the hydrostatic curve may be because the samples were recovered from the depth and have been pre-stressed resulting in reduced diagenetic porosity and micro-cracks which are usually impacted during the primary fatigue. With time, the fatigue progressed from the primary phase to the secondary phase where plastic grain dilation/contraction is normally dominant.
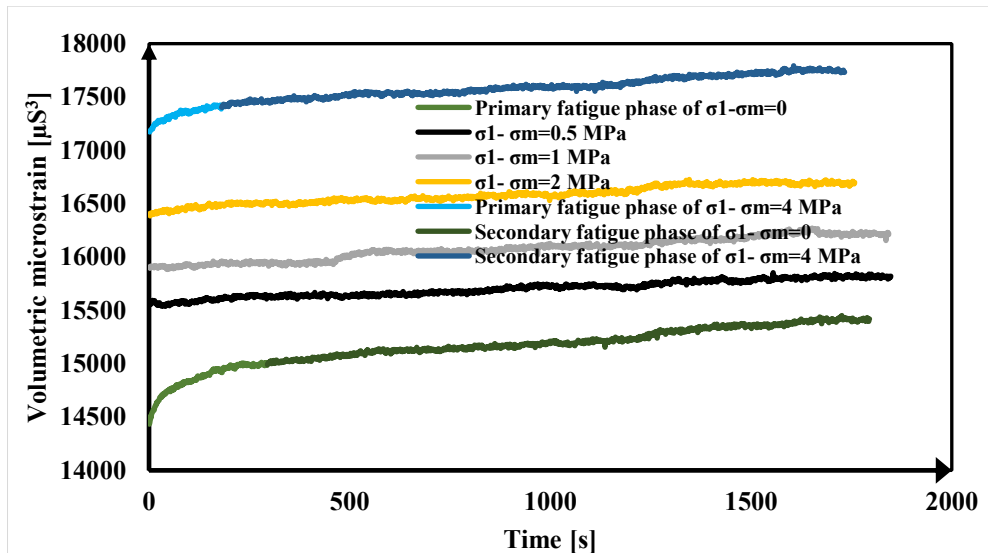
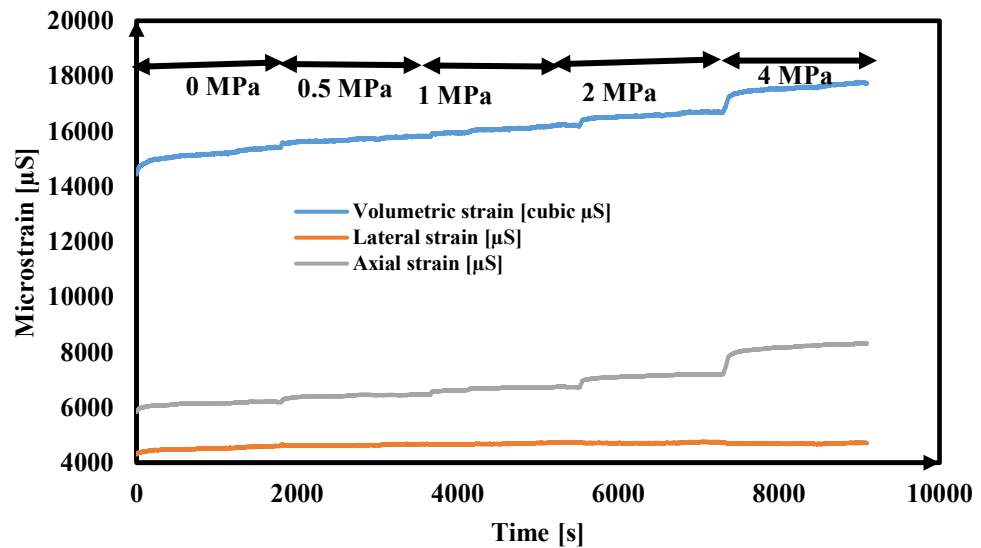Figure 28: Fatigue curve for br sample for different deviatoric stresses

Figure 29: Combined fatigue curves under different deviatoric stresses from 0 to 4MPa for br sample.

Table 20: Measured fatigue rate and Bulk modulus for all the samples

S ID	σ_{dev}	Primary f_r ($\mu S/s$)	Primary f_t (sec)	Sec. f_r ($\mu S/s$)	Sec. f_t (sec)	K (GPa)	β(GPa^{-1})
dry	0	59.7	333	14.2	1377	1.2164	0.8221
	0.5		--	11.8	1786		
	1		--	12.1	1786		
	2		--	12.7	1760		
	4	264.0	88	14.6	1646		
br	0	75.8	294	15.3	1500	1.050	0.9524
	0.5		--	12.8	1847		
	1		--	13.1	1842		
	2		--	14.2	1757		
	4	143.6	180	17.0	1552		
gCO$_2$-br	0	146.4	181	16.7	1629	0.9184	1.0888
	0.5		--	14.6	1894		
	1		--	15.6	1817		
	2		--	17.3	1703		
	4	87.8	356	22.4	1441		
scCO$_2$-br	0	98.9	284	19.5	1474	0.8236	1.2142
	0.5		--	16.3	1798		
	1		--	16.5	1802		
	2		--	17.1	1787		
	4	214.7	148	19.0	1709		
gCO$_2$	0	109.7	203	15.0	1535	0.9195	1.0875
	0.5		--	13.4	1784		
	1		--	13.2	1855		
	2		--	14.6	1753		
	4	194.7	137	16.3	1675		

f_r = Fatigue rate; f_t= Fatigue duration; K=Bulk modulus; β=Compressibility.

5.3   Fatigue rate

The fatigue rate of the primary fatigue phase increased by 342%, 89%, 117% and 77.5% in the 4 MPa stress level when compared to the hydrostatic stress level for the dry, br, scCO$_2$-br, and gCO$_2$ respectively. The primary fatigue rate for the gCO$_2$-br was reduced by 40%. The increase in fatigue rate demonstrates the effect of increased stress on the fatigue rate (Fjar et al., 2008). However, the increase in fatigue rate was varied due to the phase CO$_2$ with which each sample was saturated , while the reduction in the fatigue rate for gCO$_2$-br may be the effect of the accelerated fatigue rate at higher stress due to pore stress corrosion of the gCO$_2$-br. The effect of CO$_2$ onthe rate of deformation of rocks have also been reported by Li et al., (2018).

The secondary fatigue rates for the dry sample are 14.2, 11.8, 12.1, 12.7, 14.6 microstrain per second for hydrostatic, 0.5, 1, 2, and 4 MPa deviatoric stress levels respectively. The secondary fatigue rate for the other samples are shown in Table 20, the trend suggests that the secondary fatigue rate and the recorded strain increased with increasing stress level. But, the rate of increase is much lower than the primary fatigue at stress levels where both phases of fatigue apply with primary fatigue rate decreasing by 76 and 94.5% for dry, 80 and 88% for br, 88.6 and 74.5% for gCO_2-br, 80.3, 91.2% for $scCO_2$-br, and 86, 91.6% for gCO_2 for the hydrostatic stress level going into the secondary fatigue on the hydrostatic and 4 MPa stress levels respectively. The secondary fatigue rates compared to each other were seen to be higher for stress levels that had the primary fatigue phase i.e the hydrostatic and 4MPa stress levels respectively. For example, 14.2µS/s and 14.6 µS/s for dry, 15.3 µS/s and 17 µS/s for br, 16.7 µS/s and 22.4 µS/s for gCO2-br, 19.5 µS/s and 19.0 µS/s for ScCO2-br and 15.0 µS/s and 16.3 µS/s for gCO_2.This may be because the closure of pores and micro-cracks by primary fatiguing creates volume for more grain dilation/contraction for the immediate secondary fatigue. The secondary fatigue rate was almost equal for the other stress levels.

Results of the primary fatigue rate (Table 20) show that fatigue rate depends on the deviatoric stress (Peng et al., 2019), and agrees with results from a conventional creep experiment in which a 10% change in the differential stress resulted in more than two orders of magnitude change in the creep strain rate (Heap, 2009). The secondary fatigue rates were seen to be much lower than the primary fatigue rate for all the stress levels of all the samples. This is expected, because secondary fatigue requires more stress, given that the mechanism at this stage is boundary re-alignment and grain contraction/dilation. The secondary fatigue rate for the gCO_2-br sample was most varied under the different stress conditions. This can be attributed to the continuous and slow nature of the effect of gCO_2-br on the rock grains such that at a slightly different stress level, a slightly different plastic response is produced. The variation in the rate is not noticed in the gCO_2 sample because brine is needed to create this effect. It was observed that the secondary fatigue phase preceded by a primary fatigue showed higher secondary fatigue rates. This is because primary fatigue creates more volume

for the secondary fatigue to propagate. This effect is accentuated in the gCO_2-br sample more than any other samples for the higher stress levels.

5.4   Fatigue phase duration, total strain, and bulk modulus

The primary fatigue phase in the hydrostatic stress level lasted for 19.5% and 3.8% of the fatigue duration for that stress level, and of the entire fatigue duration respectively for the dry sample, 16.4% and 3.3% for br, 10% and 2% for gCO_2-br, 16.2% and 3.2% for $scCO_2$-br and 11.7% and 2.3% for gCO_2. For the 4 MPa stress level, the primary fatigue phase lasted for only 5% of the fatigue duration for that stress level and 1% of the entire fatigue duration for dry, 10% and 2% for br, 19% and 3.9% for gCO_2-br, 8.2% and 1.6% for $scCO_2$-br and 8% and 1.5% for gCO_2. This reduced fatigue duration is the effect of increased stress on the fatigue duration and is seen to be varied due to the effect of the saturating phase of CO_2 and brine. Primary fatigue duration under the hydrostatic stress condition was longest in the dry sample (3.8% of its total fatigue duration), suggesting that the duration of fatigue of the other samples have been affected by the stresses due to the respective CO_2 phases as seen by the higher primary fatigue rates of all the other samples. Comparing the primary fatigue duration at the hydrostatic stress level for brine and the other CO_2 bearing samples showed a reduction with the gCO_2-br sample having the highest reduction. The primary fatigue duration for the higher stress condition was the longest for the gCO_2-br (3.9%) indicating that the weakening effect of the gCO_2-br is mild. So, the impact of the weakening can be seen more at a higher stress level in the form of longer fatigue duration and higher fatigue rate.

To normalise the effect of increased stress on the strain and allow for a comparison between the hydrostatic and 4 MPa fatigue behaviour, $f_r \times f_t$ was used as the total strain in the primary phase. The $f_r \times f_t$ for the primary fatigue phases show that despite the reduced fatigue duration for the 4 MPa stress level, 16.9%, 16%,18%,13%, and 19.8% more microstrain were recorded for dry, br, gCO_2-br, $scCO_2$-br, and gCO_2 samples respectively. This observation indicates that of the volume of strain recorded under the hydrostatic stress condition, there was more volume of intragranular and intergranular pores and micro-cracks that could not be affected by the hydrostatic stress condition (Li et al., 2020). This suggests that primary fatiguing at lower stress levels may not

close up all the genetic pores and micro-cracks as some smaller intragranular and inter-granular pores and micro-cracks are shielded by the rock's effective strength. This makes sense given that the rocks are pre-stressed. That the difference between the volume of strain recorded in the primary fatigue phase at low and high-stress are highest for the gCO_2 (19.8%) and gCO_2-br (18%) show that gaseous CO_2 may be corroding weak margins of the rock matrix at a mildly rate such that higher stress is required to cause significantly more volumetric strain. The difference between the volume of strain recorded at the primary phases of the low and high stress is lower for the brine saturated rock than the dry rock and lowest for the $scCO_2$-br saturated rock, and may indicate that the stress corrosion of these two states happened at a faster and stronger rate such that the grain materials were weakened enough to be deformable at lower stress conditions. The volumetric microstrain which represents the highest change in volume recorded for all samples from the 0 to 4 MPa deviatoric stress cycle is presented in Table 21. The result shows that the dry sample has the lowest volumetric change throughout the test while the $scCO_2$-br sample showed the highest change in volumetric expansion throughout the test.

Table 21: Volumetric microstrain recorded in each sample through the entire test

Sample	ε_{vol} at σ_1-$\sigma_m = 0$ (μS)	ε_{vol} at σ_1-$\sigma m = 4$ MPa (μS)
dry	13115	16105
br	14433	17793
gCO_2-br	17205	21559
$scCO_2$-br	18313	21764
gCO_2	14370	18315

Comparing the bulk modulus of the brine and the CO_2-br samples show the accelerating role of CO_2 in weakening the rocks similar to what has been reported by Bemer & Lombard, (2010); Grombacher et al., (2012); Mikhaltsevitch et al., (2014); Vanorio et al., (2011). The bulk modulus of the dry sample was 1.2164 MPa and the compressibility was 0.8221 MPa^{-1}. The bulk modulus and compressibility of the other samples are shown in Table 20. This shows a general reduction in the bulk modulus of the rocks according to the sample state. In all the samples tested, the primary fatigue phase under the hydrostatic stress conditions was very brief. With an increase in stress,

the fatigue progressed from the primary phase to the secondary phase where plastic grain dilation/contraction is normally dominant.

5.5   Comparison of fatigue behavior, rate, and modulus between br sample and phase CO_2 samples

Figures 30 and 31 show the percentage difference of the measured parameters between the brine saturated and the other CO_2 bearing samples. These bar charts like others in this research do not contain error bars because each bar represents single measurement for a sample. This is to show the effect of the phase of CO_2 on the other samples by showing the percentage difference between each sample. The brine sample represents the natural reservoir state.
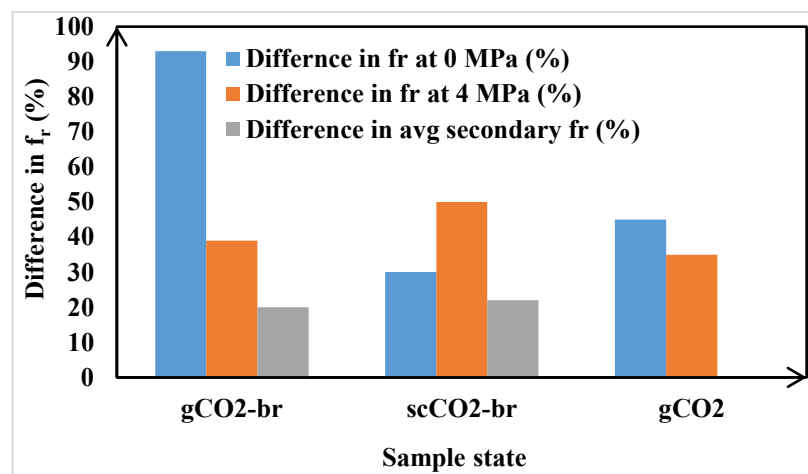

Figure 30: Percentage difference in primary fatigue rates for 0, 4 MPa and average secondary fatigue rate between br and other samples showing the change in strain rate caused by the different phase of CO_2
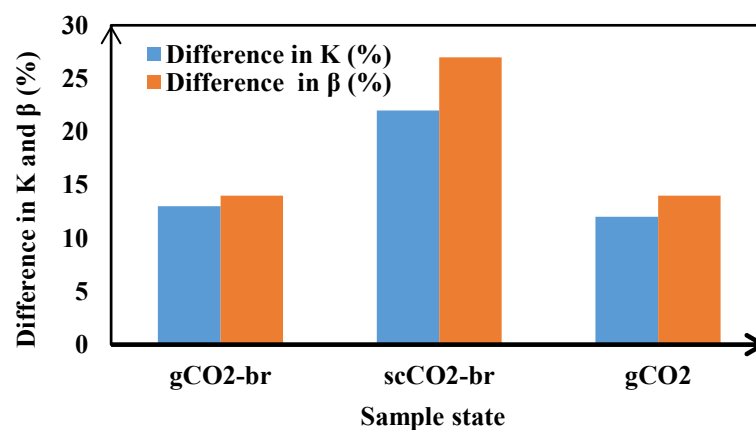

Figure 31: Percentage difference in bulk modulus and compressibility between br and other samples showing the change in bulk modulus and compressibility caused by the different phase of CO_2

It is seen that the primary fatigue rate is higher for all samples containing CO_2 compared to the brine saturated sample at both low stress and high stress as shown in Figure 30. This suggests that stress corrosion due to pore fluid is interfering with the strain rate. The reduction inthe stiffness of the rock is due to stress corrosion inducing more strain at lower stress leaving less possibility of the primary fatigue at higher stress, especially for the $scCO_2$-br sample, while the reduction of stiffness due to the stress corrosion at higher stress was seen in the gCO_2-br and gCO_2 samples. The average secondary fatigue rate of all samples when compared to the dry sample, is seen to increase the most in the $scCO_2$-br sample. This means that this state of CO_2 has the strongest weakening effect on the grain fabric. This also explains why this sample state has the greatest change in the bulk modulus and compressibility. Results of fatigue rate under various CO_2 conditions by Liteanu et al. (2012) reported 50-75 50 and 50 times increase in the fatigue rates respectively. The research shows a 93%, 30%, and 45% increase in primary strain rate at low stress for gCO_2-br, $scCO_2$-br, and gCO_2 samples respectively when compared to the primary strain rate of brine saturated sample.

Results of the static modulus from this research agree with consistent strong reduction effect observed by Bemer and Lombard (2010); Vanorio et al. (2011) and Delle and Sarout (2016) as there was13, 22 and 12% reduction in the bulk modulus for gCO_2-br, $scCO_2$-br and gCO_2 samples respectively when compared to the brine saturated sample. Comparing the results from brine saturated and gCO_2 samples show that CO_2 affects the fatigue rate and bulk modulus of rock significantly without brine. This means that the deformation rate and bulk modulus of the reservoir will be significantly affected by CO_2 storage. Stress corrosion due to pore fluid determines the extent of the effect on fatigue rate and modulus. Stress corrosion under supercritical CO_2 conditions was seen to be stronger at lower stress levels thus affecting bulk modulus the most, while stress corrosion due to gaseous CO_2 was seen to be at a mild rate at low stress. Peng et al. (2020) found that pressurized gases could penetrate micro-cracks and pores and affect the failure rate. For the gCO_2-br sample, the stress corrosion was higher at high-stress levels. All the CO_2-brine states interfered with the fatigue rates and modulus as seen in Table 20.

The result from this study shows that CO_2 affects the strain rate at both low and higher stress conditions as it is seen that the fatigue rate of CO_2 flooded rocks is significantly different from what it was when the rock was brine saturated only. The effect is seen to be sensitive to the phaseCO_2-brine state. For instance, the difference in the recorded strain at high and low stress was higher for the gCO_2 and gCO_2-br samples compared to the scCO_2-br samples. This shows that gCO_2 and gCO_2-br have a higher impact on the rock at higher effective stress compared to the scCO_2-br sample. This implies that if a reservoir is gCO_2-br saturated, there will be a greater reduction in the modulus of the rock at higher effective stress compared to a scCO_2-br saturated reservoir. On the other hand, the scCO_2-br saturated sample when compared to the gCO_2-br sample shows that there was less difference between the volume of strain recorded at low stress and higher stress. It therefore implies that if a reservoir is saturated with scCO_2-br, the volumetric strain will proceed at a lowered difference in rate between the low and high stress (nearly the same strain throughout the storage history) when compared to the gCO_2-br dominated reservoir. It goes to say that the effect of change in effective stress on the geomechanical properties of the reservoir will be most pronounced if the reservoir contains gCO_2-br compared to scCO_2-br. The average secondary fatigue rate was highest in the scCO_2-br saturated sample, this makes sense given that the rock's properties is immediately affected by the scCO_2-br. Therefore, the secondary phase of the fatigue seems to be enhanced by the earlier fatigue.

This research shows that among the CO_2-brine states, the scCO_2-br has the greatest effect on the rock's material compared to the other CO_2-brine states, hence the greatest reduction in the bulk modulus (greatest increase in compressibility) and highest volumetric strain seen in the scCO_2-br sample. It is thought that the higher impact of scCO_2-br over gCO_2-br on the modulus and deformation of rocks maybe because the density of scCO_2 is larger than gas and can itself behave as a liquid resulting in more drag effect, coupled with the ability of scCO_2 to dissolve organic materials.

In all the samples tested, there was a re-appearance of primary fatigue in the 4MPa deviatoric stress levels after secondary fatiguing for the 0.5, 1, and 2 MPa deviatoric stress levels. Earlier researcher had disagreed with a previous assumption that each phase of fatigue occurs only once and explained that there is a possibility of re-

occurrence of a phase of fatigue if the stress condition changes. In this experiment, the re-appearance of primary fatigue in the 4 MPa deviatoric suggests that some smaller diagenetic intragranular and/or inter-granular micro-cracks and pores were shielded from the impact of stress by the effective strength of the rock until the stress is high enough to overcome the shielding work of the effective strength as illustrated in Figure 32. It is assumed that fatigue rate diminishes with time, if this were true, and the limits of static fatigue were approached, the effect of fatigue would cease. However, this is not the case as fatigue is usually seen to progress until complete failure if stress is maintained. It is believed that this assumption may not hold for long term fatigue as it never ceases and continues until complete failure. Our experiment finds that this assumption does not hold for rocks that have pores at multiscale even in the short term. From this research, it is seen that each phase of fatigue contributes an increment to the total strain but this contribution is not constant, and the fatigue rate is affected by CO_2 phases. Also, the strain produced by a given fatigue phase is different if the stresses are different. For instance, the primary fatigue phase in the dry sample produced 16.9% more strain under 4MPa deviatoric stress compared to the hydrostatic stress conditions.
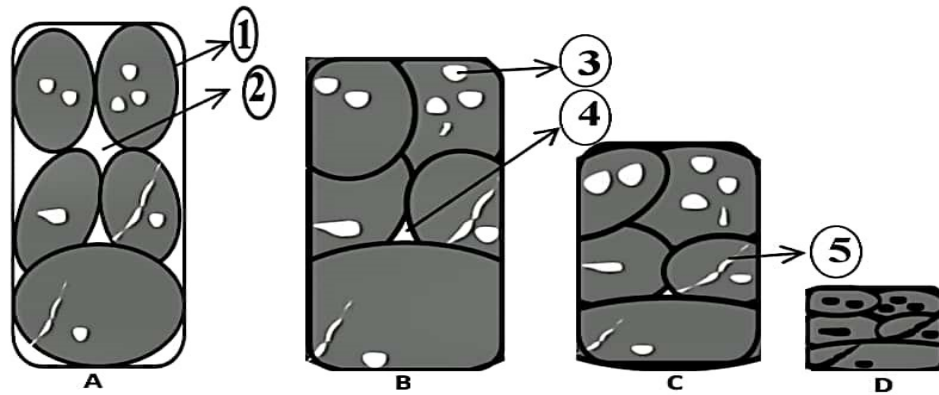

Figure 32: Illustration of rock fatigue under different stresses. (1) Grain boundary, (2) Major Intergranular pore, (3) Intragranular pore (4) Intergranular pore (smaller and shielded), (5) micro-crack. (A) Original grain and pore structure (B) grain and pore structure during primary fatigue; Notice major intergranular pores are closed up due to primary fatigue (at hydrostatic stress in this research). (C) Grain and pore structure during secondary fatigue at 0.5, 1 and 2 MPa stresses in this research; notice there is dilation, contraction, and realignment of grain boundaries with the intragranular pores and micro-cracks unaffected. (D) Grain and pore structure after re-appearance of primary fatigue at 4 MPa. A and D show the primary fatigue scenario while B and C show secondary fatigue but note that the latter part of the A and D fatigue test had secondary fatigue as shown by all the fatigue curves.

Figure 32 illustrates the mechanism for the reduction in pore volume as seen in Figures 33 (b, d, f, h, and j), and is due to the imposition of the 4 MPa deviatoric stress and corresponds to the period of re-appearance of primary fatiguing. Figures 33a-j are micro-CT images of all the samples acquired before and after compression respectively. They are seen to contain relatively smaller intragranular pores and cracks that are noted to be responsible for the re-appearance of primary fatigue. After compression, it is seen that the volume of the intragranular pores was reduced under high stress. It is opined that the volume of the intergranular pores and crack remained unaffected by the 0, 0.5, 1 and 2 MPa deviatoric stress cycles.
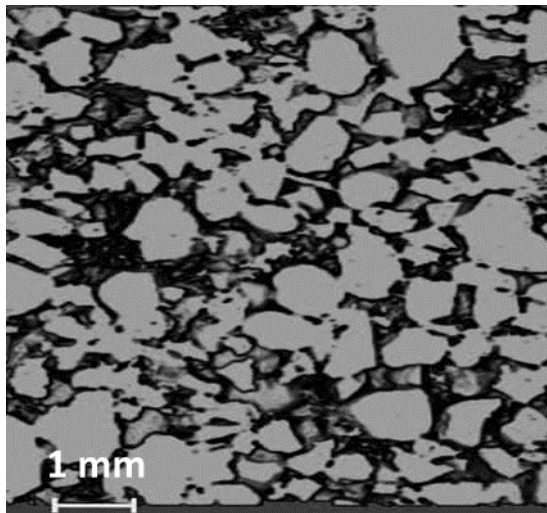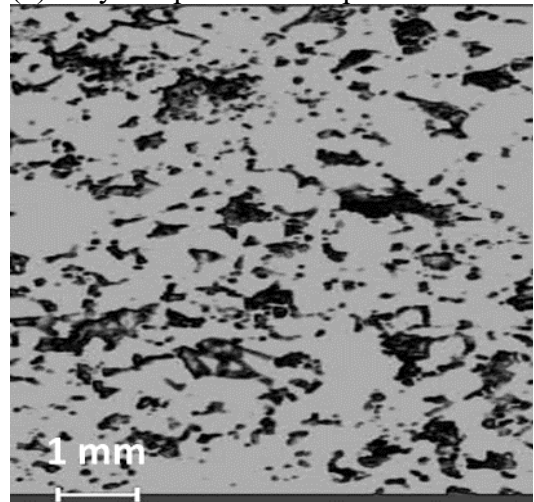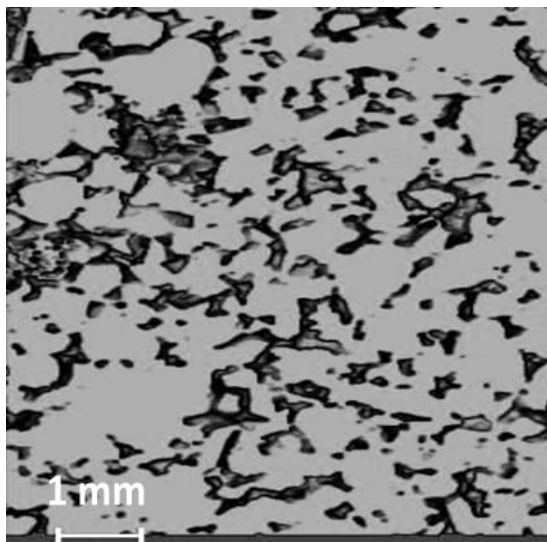
(a): Dry sample before compression
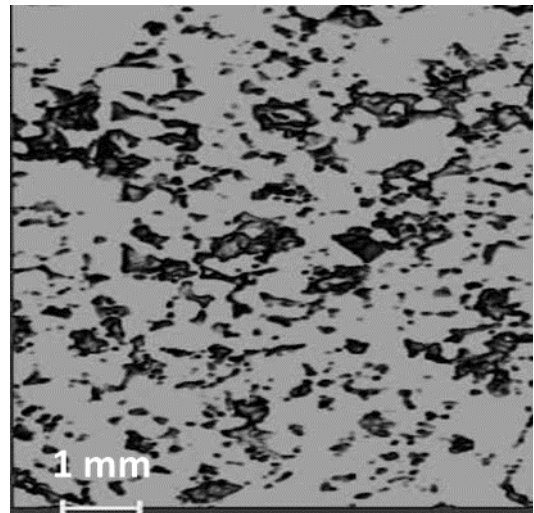
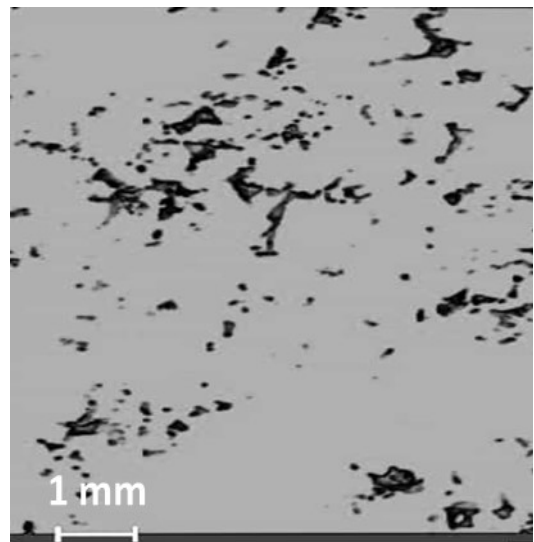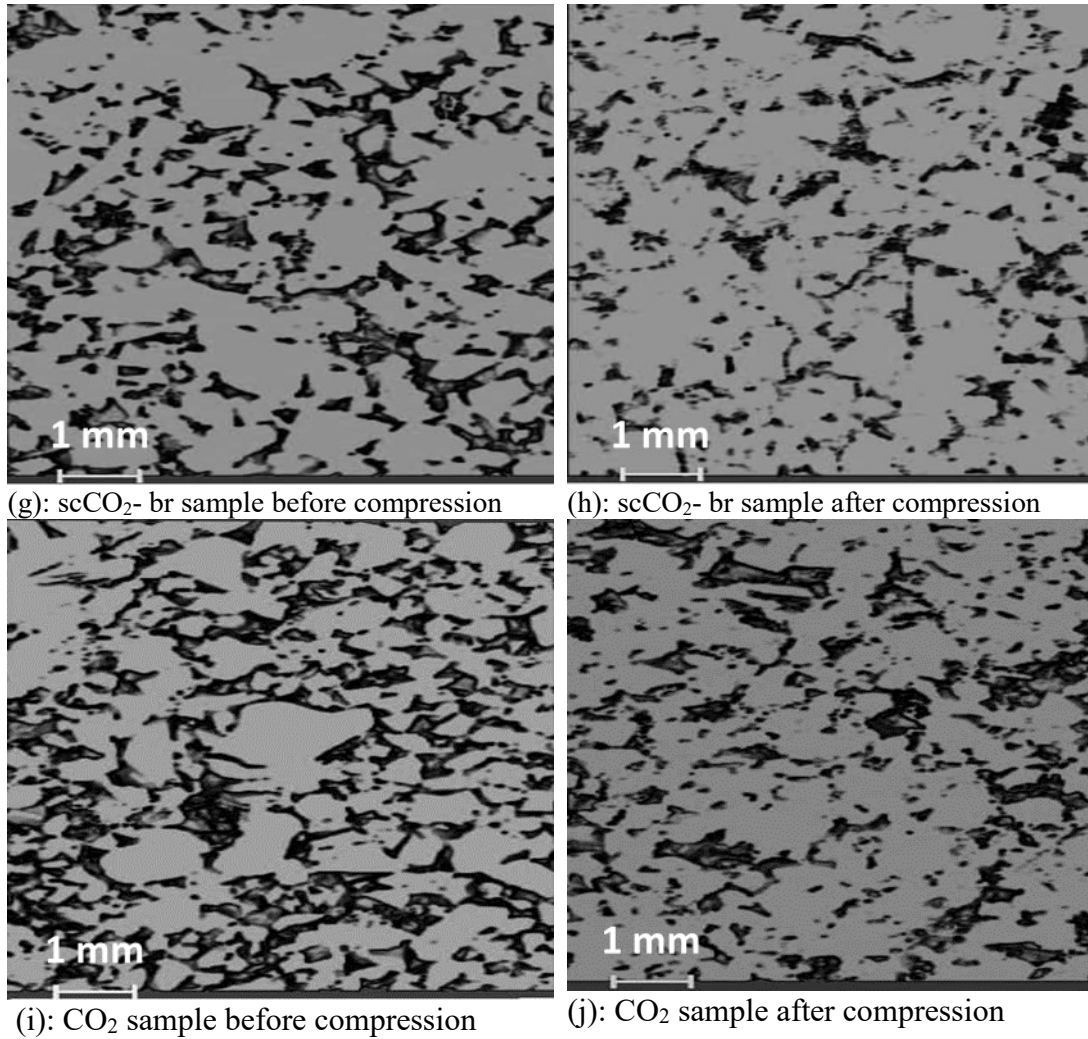(b): Dry sample after compression
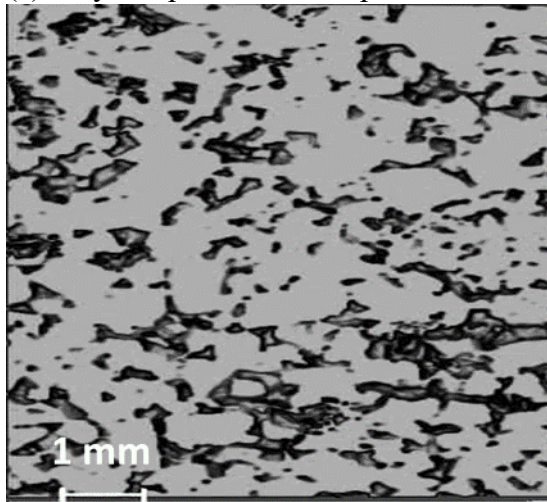
(c): br sample before compression

(d): br sample after compression

(e): gCO$_2$-br sample before compression

(f): gCO$_2$-br sample after compression

(g): scCO$_2$- br sample before compression

(h): scCO$_2$- br sample after compression

(i): CO$_2$ sample before compression

(j): CO$_2$ sample after compression

Figures 33a-j: Micro-CT images of samples used before and after compression. Notice that all the samples show a reduction in porosity and grain smoothening after compression but the magnitude of the reduction varies according to the state of the sample with gCO$_2$- br and scCO$_2$- br showing the highest reduction. The micro-CT images were taken at approximately the same locations in the core sample.

To provide a preliminary quantitative assessment of the change in the porosity, 2D slices of CT images of each sample before and after compression was analysed using ImageJ and the results are presented in Table 22. It is seen that the total pore area, percentage pore area, and average pore size of all the samples reduced after compression. The greatest reduction however was seen in the gCO$_2$-br sample.

Table 22: Porosity measured from a 2D CT image slice of the different sample states before and after compression

Sample ID	Total Pore area (mm^2)		Average pore area (mm^2)		Percentage pore area (%)	
	Before	After	Before	After	Before	After
dry	15.67	9.92	0.073	0.026	42.78	27.93
br	19.97	10.42	0.045	0.043	29.34	26.67
gCO$_2$-br	21.78	6.15	0.089	0.024	27.41	8.17
scCO$_2$-br	21.95	16.34	0.096	0.040	26.34	19.52
gCO$_2$	23.41	21.05	0.077	0.054	31.03	27.87

The reduction in the pores due to primary fatigue,as well as the reduction in the intragranular pores due to the re-appearance of primary fatigue at high deviatoric stress is seen. This clearly shows that the mechanism for primary fatigue is pore and crack closure and that the effective stress of rocks shields smaller intragranular pores from primary fatigue at low stress.

5.6   Summary

This research has evaluated the effect of different phases of CO_2 with brine on the deformation rate and bulk modulus of sample reservoir rocks. The result of this work can be applied to predicting the effect the different possible existing phases of CO_2 in giant CO_2 storage fields such as Sleipner, In Salah, etc. will have on the deformation and bulk modulus of the reservoir rocks. The phase of CO_2 matters. While the effect of CO_2 on the bulk modulus is most pronounced in the supercritical CO_2 phase (decrease of 22 %). The primary fatigue rate is most affected by the gaseous CO_2 phase (an increase of up to 45 %) especially when it is combined with brine (an increase of up to 93 %). Primary fatigue was also seen to be capable of being shielded by the rock's effective stress if the stress condition is low, or not applied for a long enough time, most especially if the material has wide micro-pores and crack size range. This mechanism of fatigue explains why fatigue in the porous material is continuous under constant stress and why a plastically deforming rock may begin to fatigue when the stress is increased. The shielding effect is significantly affected by CO_2 depending on the phase of the CO_2 as well as the presence of other fluids. Stress corrosion due to pore fluid determines the extent of the effect on the fatigue rate and modulus.

Chapter 6: Sensitivity of strength, geomechanical indices and permeability of saline rocks to different phaseCO₂-Brine

6.1 Introduction

In this chapter, the strength, stress-strain behaviour, tangent static modulus, bulk modulus, compressibility, failure stress (σ_f) and maximum shear strength (τ_{max}) of each sample is evaluated from the multiple failure tests performed on Captain Sandstone core samples saturated with brine (br), gaseous CO_2 (gCO_2), gaseous CO_2-brine (gCO_2-br) and supercritical CO_2-brine ($scCO_2$-br) for 7 days. A sample was tested in dry condition. Multiple failure compression test was carried out on each sample as explained in chapter 3. The axial and lateral displacements (Δl and Δd), confining pressure and axial stresses were recorded per second during the entire test. These were processed to yield the axial strain (ε_a), lateral strain (ε_L), and volumetric strain(ε_{vol}). The multiple failure test was done to provide a robust data to evaluate and compare the strength and related geomechanical indices of the rock from the different phaseCO₂-brine samples. This will help to understand how the different phaseCO₂-brine affects these indices and their implication for the CO_2 storage integrity. Results from this study provide useful information for defining the geomechanical effect of the different phaseCO₂-brine in storage modelling. Furthermore, this will help in showing the state of brine that is most critical to the strength and geomechanical properties of rock.

To provide an understanding of the effect of the different phaseCO₂-brine on the stress-strain behaviour, static modulus, bulk modulus, compressibility, failure stress and maximum shear strength (τ_{max}) of each sample, the lateral (ε_L) and axial strain (ε_a) of rocks saturated with different phaseCO₂–brine under increasing confining stress (i.e. changing effective stress) were analysed. Because the axial gap in the core holder was filled with steel platen, a platen correction was applied on the axial displacement according to equations 6 and 9 (Ergo tech). Volumetric strain (ε_{vol}) was taken as $\varepsilon_{vol}=\varepsilon_a +2\varepsilon_L$, where ε_a is the axial strain and ε_L is the lateral strain.

$$\text{Platen correction } (50 - 250\text{KN}) = \frac{\text{Load}}{838} + 0.035 \qquad (9)$$

Where the load is the load applied on the sample in Kilo newton (KN).

In this study, the stress-strain behaviour is shown as the plot of deviatoric stress (σ_{dev}) vs the axial strain (ε_a). **The** eviatoric stress is the stress differential between axial stresses (δ_1) and confining stress (δ_3). The first confining stress was chosen to represent the minimum stress state at the shallowest possible depth for CO_2 storage (i.e at 800m). The other increased confining stress is so as to simulate different effective stresses at greater depths. The deviatoric stress is taken as equation (7).

The peak stress (σ_p) is equal to the failure stress (σ_f) and was taken as the highest σ_1 at which the stress-strain curve shows inflection or a change in the slope. (Fjar et al., 2008). A correction for aspect ratio was applied on the σ_p values according to equation (10).

$$\sigma_p = \frac{\sigma_1}{0.88 + 0.24\left(\frac{dc}{L}\right)} \qquad (10)$$

Where σ_P is the peak stress, σ_1 is the axial stress, dc is the diameter of the core sample and L is the length of the core sample.

The The static modulus (E), was taken as the tangent modulus at 50% of the peak stress and is expressed as the slope of the axial stress-strain curve i. e equation 11.

$$E_{50\%} = \frac{\Delta\sigma_1}{\Delta\varepsilon a} \qquad (11)$$

Where E_{t50} is the tangent modulus at 50% peak stress, $\Delta\sigma_1$ is the change in axial stress and $\Delta\varepsilon_a$ is the change in axial strain

The bulk modulus (K) was taken as the slope of axial stress vs volumetric strain of the hydrostatic loading portion (initial loading phase, where $\sigma_1=\sigma_3$) and is expressed as equation 8. Compressibility (β) is taken as the inverse of the bulk modulus.

The maximum shear stress (τ_{max}) was taken as σ_1- σ_3, where σ_1 is the axial stress, σ_3 is the confining stress. A failure envelope for all the samples was evaluated to map the rock failure. The envelope is presented as a curve of τ_{max} vs mean effective

stress. The mean effective stress (σ_m) is expressed as $\sigma_1 + 2\sigma_3)/3$ where σ_1 is the axial stress, σ_3 is the confining stress.

The permeability of the samples were calculated from Darcy law illustrating the relationship between the fluid flowrate and pressure differential as shown in equations 2 and 3.

6.2   Bulk modulus and compressibility

From Table 23, the greatest change in the bulk modulus and compressibility compared to the brine's was seen in the $scCO_2$-br saturated sample with a 22.2% reduction in bulk modulus and 28.6% increase in compressibility. For gCO_2-br and gCO_2 samples, there was an 11.1% reduction in bulk modulus and a 14.5% increase in compressibility. Bulk modulus is a measure of the resistance to volume compressibility of rock under hydrostatic stress while, static modulus measures the directional elastoplastic resistance of rocks. It implies that in cases where the static modulus changed but not the bulk modulus, the resistance to deformation was entirely plastic. For instance, the gCO_2 saturated sample, observed an 11.1% reduction in bulk modulus but a 2.5% reduction in static modulus while in the brine saturated sample, we observed a 91.1% reduction in static modulus with no change in bulk modulus. This follows that the gCO_2 induced an 11.1% reduction in compressibility while the brine sample did not induce significant elastic compressibility. On the other hand, while the gCO_2 saturated sample induced a 2.5% reduction in elastoplastic resistance, the brine saturated sample induced a 91.1% reduction in elastoplastic resistance.

6.3   Geomechanical indices and strength

Table 23 presents a summary of the geomechanical indices and strength measured from all the samples. The behaviour of the dry sample is such that is expected according to theories and empirical studies in rock mechanics and will be used as the default to evaluating the deviation due to other sample states.

Table 23: Geomechanic indices measured from static multiple failure compression test.

S ID	Approx. σ_3	E_{t50} (MPa)	σ_f (MPa)	τ_{max} (MPa)	K (GPa)	β(GPa^{-1})
dry	16	4.68	59.97	43.97	1.8	0.5556
	26	4.90	74.84	48.84		
	36	1.57	82.16	46.16		
	46	3.84	88.75	42.75		
br	16	6.09	50.86	34.86	1.8	0.5556
	26	2.73	67.84	41.84		
	36	1.40	75.11	39.11		
	46	0.41	81.43	35.43		
gCO$_2$-br	16	3.84	52.68	36.68	1.6	0.6250
	26	3.83	67.31	41.31		
	36	2.62	74.73	38.73		
	46	0.38	101.99	55.99		
scCO$_2$-br	16	4.22	53.59	37.59	1.4	0.7143
	26	3.04	64.50	38.50		
	36	3.06	72.79	36.79		
	46	0.59	77.34	31.34		
gCO$_2$	16	5.23	59.59	43.59	1.6	0.6250
	26	5.19	74.69	48.69		
	36	3.84	84.65	48.65		
	46	3.93	93.24	47.24		

E_{t50}=Tangent modulus at 50% peak stress/stiffness; σ_f=Failure stress; τ_{max}=Maximum shear stress; K=Bulk modulus; β=compressibility.

Firstly, it is seen that increasing confining stress led to an increase in stiffness, failure stress, and shear strength up to a certain level. This simply represents the role of increasing confining stress on those indices (Fjar et al., 2008; Xia & Zhou, 2010). But, there was a reduction in stiffness (E) and maximum shear strength (τ_{max}) at 36 MPa confining stress. This is so because that point marks the point of critical micro-shearing for the rocks and can be seen as the weakening effect that comes with shearing (Gerbi et al., 2010). It is seen that when the confining stress was increased to 46 MPa, the micro-sheared grains increased in stiffness. The failure strength (σ_f) of the rock was seen to increase at all the confining stress levels, this shows that the rock deformation is plastic. The fact that the stiffness reduced while the failure strength increased in all the other samples indicates that the intragranular strength of the grains have been degraded by the pore fluid, and the grains have been deformed/sheared at the micro-level, however, the compaction of the deformed grains made the rock to behave in a

ductile manner thus increasing the failure strength of the rocks. Furthermore, it is seen that with increasing confining stress, the amount of change in the stiffness and failure stress varies depending on the state of the sample (i.e the phaseCO$_2$-brine saturating the sample) as shown in Figure 34.

Secondly, the dry rock had the highest shear strength of 48 MPa at the 26 MPa confining stress, that is taken as the critical shearing stress. Beyond this point, the rock starts failing by micro-shearing. Thirdly, at 46 MPa confining stress, even though the stiffness increased, the shear strengths were seen to reduce. This means that while shear enhanced compaction may increase the stiffness of rocks, it may not have the same effect on the shear strength. This is plausible when we imagine that the granular material, though deformed and weakened by shearing are packed closer together by compaction thereby increasing the stiffness. For the brine saturated sample, no compactive strengthening was seen with the increasing compressive stress as seen in the dry sample, rather the tangent modulus at 50% peak stress (E$_{t50}$) reduced constantly as confining stress increased. For gCO$_2$-br sample there was an increase in E$_{t50}$ until when the grains have been weakened through stress corrosion by gCO$_2$ to the point that the increase in strength brought by compaction could not hold. For scCO$_2$-br saturated sample, the E$_{t50}$ reduced gradually as the confining stress increased. Similar mechanism as in the brine saturated sample is thought to be at play here. The gCO$_2$ behaved similarly to the dry sample. Comparing the critical shearing stress for all the samples to the dry samples shows that the critical shearing stress reduced by 14.33%, 15.41%, 21.17%, and 0.04 % for the br, gCO$_2$-br, scCO$_2$-br and gCO$_2$ samples respectively. The scCO$_2$-br sample showed the highest reduction while the gCO$_2$ changed only marginally. This shows that a combination of brine-CO$_2$ significantly affects the properties of rocks. However, the highest effect on the critical shear strength of the rock is expected in a scCO$_2$-brine reservoir.

From Table 23, it is seen that an increase in confining stress from 36 MPa to 46 MPa led to a decrease in the E$_{t50}$ except for the gCO$_2$ and dry samples as well as an increase in failure strength of all the samples. The increase in failure strength shows the role of an increasing confining stress on plastic deformation (Fjar et al., 2008; Guo et al., 2020; Tang et al., 2019; Wang et al., 2018; Xia & Zhou, 2010). This has been

described by Goodman (1989) as stress hardening (increase in the shear strength due to an increase in the confining stress). The reduction in the Et_{50} of the other samples is counter to the expected behaviour of a rock under increasing confining stress Asef & Najibi, 2013). Therefore, this is seen as the effect of stress corrosion of the different phaseCO_2-brine on the stiffness of the rocks. The fact that the stiffness increased in the gCO_2 sample at 46 MPa confining stress indicates that the corrosion effect of gCO_2 is limited without brine.
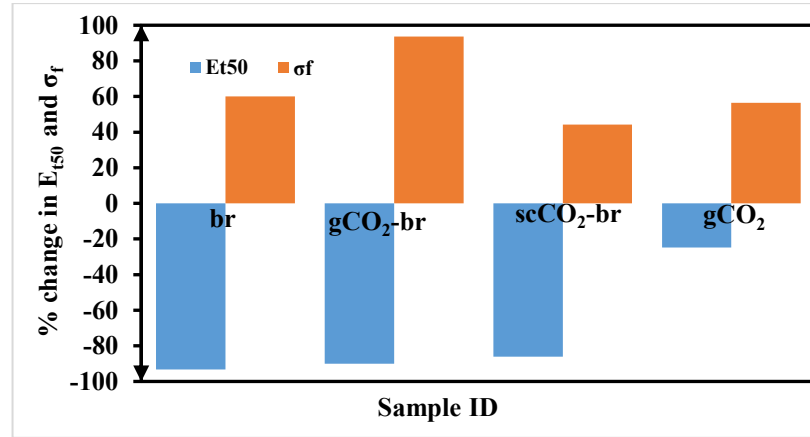
Figure 34: Showing the percentage change in stiffness (Et_{50}) and failure strength (σ_f) from the 16 MPa to the 46 MPa confining stresses. It is seen that the Et_{50} reduced while σ_f increased at 46 MPa for all the samples but the percentage of change varied with the samples.

Figure 34 shows the percentage change in the stiffness (Et_{50}) and failure strength (σ_f) during the entire test (i.e from the initial 16 MPa confining stress cycle to the final 46 MPa confining stress cycle). It is seen that the gCO_2-br sample showed the highest increase in the failure strength, while the gCO_2 sample showed the lowest decrease in the stiffness. Again, the ductile behavior that leads to an increase in the failure strength was seen to be highest in the gCO_2-br sample, followed by the gCO_2 sample. This suggests that the presence of CO_2 increases ductile behavior in rocks especially in the presence of brine (Zheng et al., 2015).
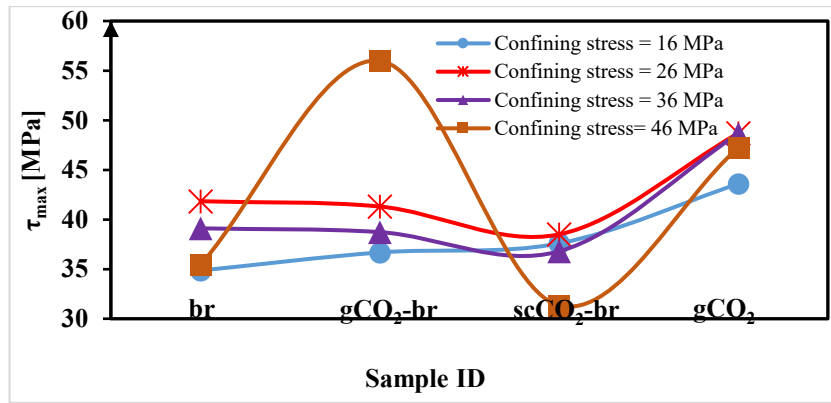
Figure 35: Comparing the τ_{max} for all the samples at all the confining stress levels.

The shear strength of all the samples is seen to increase for the first two confining stress cycles (16 and 26 MPa) but reduced in the 36 and 46 MPa confining stress cycles (Figure 35). The fact that the shear strength decreased after the 26 MPa confining stress cycle indicates that the rock had gone past the critical shear stress, beyond which the rock began shear deformation microscopically. Both the stiffness and the shear strength shows that beyond the critical shear stress (i.e after the 26 MPa confining stress cycle), the grains of the rock had lost significant intragranular strength and started deforming microscopically but the failure stress is seen to increase (Table 23) because of the ductile behaviour of the rock due to the increasing confining stress (Fjar et al., 2008; Ramezanian & Emadi, 2020; Zheng et al., 2015). As seen in Figure 35, the shear strength at the different confining stresses varies with the sample states. The gCO_2 sample showed the least variation in the shear strength for the different stress cycles. The brine saturated sample showed variation that is more than that of the gCO_2 sample but less than the CO_2-br bearing samples. The gCO_2-br sample showed the highest variation at different confining stress levels. This observation highlights the role of CO_2 in the change in shear strength of rocks during CO_2 storage, and implies that the shear strength of reservoir rocks saturated with gCO_2-br is expected to be most sensitive to change in stress condition when compared to the other sample states. The most reduction in shear strength is seen in the $scCO_2$-br sample such that the shear strength at the 46 MPa confining stress was even lower than the shear strength at the initial 16 MPa confining stress. This shows the effect of the different phaseCO_2-brine on the shear strength of rocks during CO_2 storage and implies that at high stress (great depth), a reservoir with $scCO_2$-br will experience the greatest change in shear strength compared to the others.

All the samples deformed by shear enhanced compaction and dilantancy when stress was imposed as seen from the curves in Figure36 (a-e). The stiffness of the dry sample was seen to increase going from16 MPa confining stress to 26 MPa confining stress. This shows that the rock was undergoing compaction hardening. Going from 26 MPa to 36 MPa confining stresses, there was a reduction in stiffness and this suggests that the increase in stiffness with increasing confining stress has a critical point. Assuming the default behaviour of porous rocks is that compaction of sheared grains lead to an increase in stiffness, It was seen that all the samples saturated with different phases of CO_2 and brine did not follow the default behaviour. The state of the sample is responsible for this misnomer. It is noted that all the samples that contain CO_2 and brine showed a very high percentage of this misnomer. The sample without brine (gCO_2) had only a marginal effect. This shows the role of brine in accelerating the effect of CO_2 on rocks.
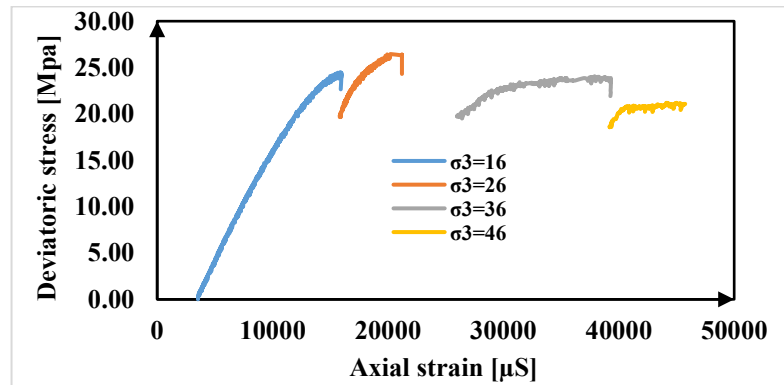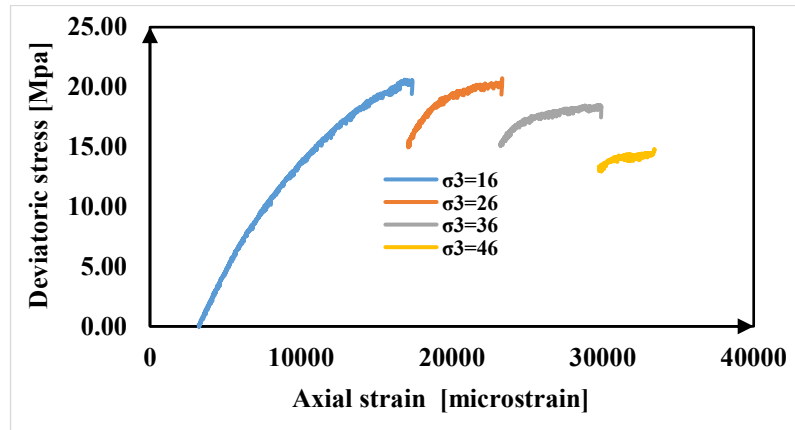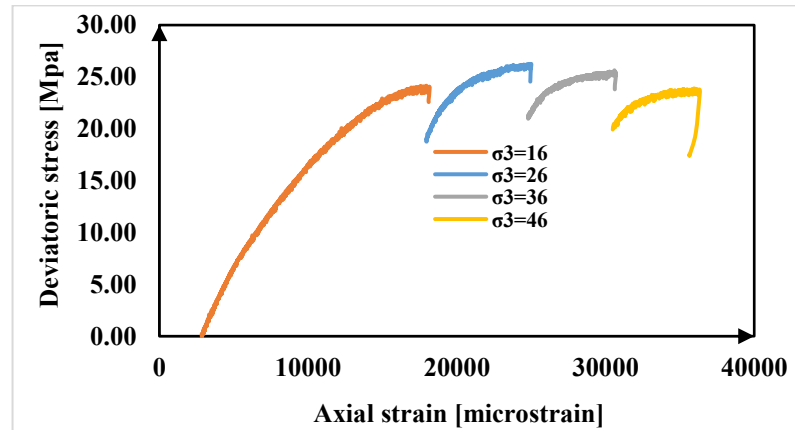

(a)
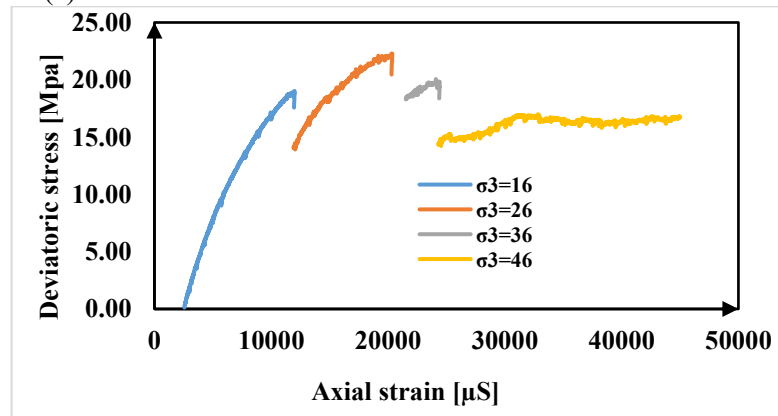
(b)
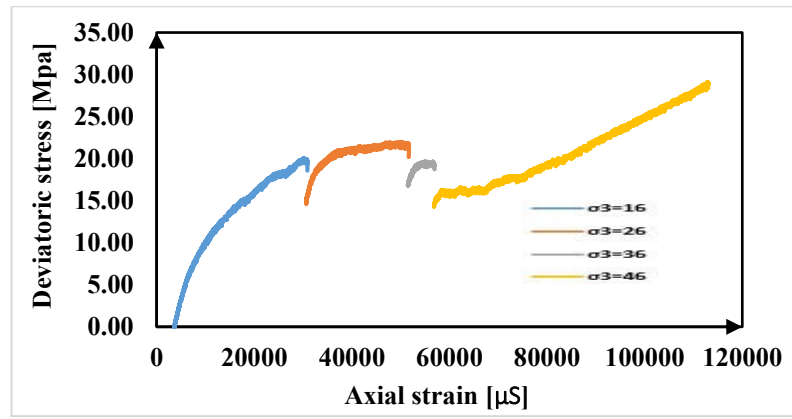
(c)

(d)

(e)

Figure 36: Stress- strain curve of: (a) dry sample (b) br sample (c) gCO_2-br sample (d) $scCO_2$-br sample (e) gCO_2 sample.

6.4   Stress-strain

Figure 36(a-e) present the stress-strain of each sample during the multiple failure compression test. It is seen that at 16 and 26 MPa confining stresses, the stiffness of

the samples increased. The increase in stiffness upon the increase in confining stress was greatly reduced after the 26 MPa confining stress cycle. This observation indicates that the critical shear stress is around this region i.e. maximum τ_{max} for each curve in Figure 35. Beyond the critical shear stress, the deformation becomes plastic. The duration of the plastic deformation varied in different samples (Figure36a-e). This is due to the fact that the effect of pore stress corrosion by the different phaseCO_2-brine varies.

During the multiple triaxial compression test, axial stress was increased until shear-enhanced compaction ends (Figures 36a-e). It is difficult to exactly pinpoint the end of shear enhanced compaction or the onset of dilation following the compaction (commonly termed C*') without acoustic emission (AE) data. In this experiment, the end of shear enhanced compaction is taken as the point where the stress-strain curve just begins to deflect. It marks the point where the hardening due to compaction stops and the sample begins to dilate. The test was stopped at the onset of dilation following compaction to avoid macro-failure/shearing as the aim of the experiment was such that all the samples should be brought to the same stage of deformation.

Shear enhanced compaction is the hardening of rocks due to a reduction in porosity in response to an increase in stress. It is a micromechanical process that occurs alongside grain-scale micro-cracking which eventually coalesce to cause marked shearing and failure (Baud et al., 2006). Shear enhanced compaction was originally thought to be a phenomenon observed at the transition from brittle faulting in porous rocks (Wong & Baud, 2012). However, research has shown that change in stress state causes a change in the porosity and this relationship affects the mode of failure. It is thought that shear-enhanced compaction caused pore collapse and grain compaction across the entire sample leading to rock hardening with an increase in the modulus. This mode of deformation of rock has been ascribed to the mineralogy, and grain size (Klein et al. 2001), but the mode of deformation seen in this experiment is more likely due to the mineralogy, grain size and the influence of the phaseCO_2-brine that saturates the rock sample.

Shear enhanced compaction is the precursor to the onset of macro-failure/shearing in the rocks as has been explained in Baud et al. (2006). The multiple triaxial compression

test is a great method for estimating the strength and failure mode of rocks. However, it may introduce difficulty in continuing the test beyond a certain stress state after the sample has approached failure or post-peak strain softening. To mitigate this issue, the deformation of the rocks in this research was not allowed to advance into macro-shearing that would adversely affect the subsequent data. That is also a reason why the test was stopped at end of shear enhanced compaction or the onset of dilation (C*') for each loading step.

The result as seen from Figure 36 (b-e) shows that the samples exhibit significant ductility for all the confining pressures. A similar ductile behaviour of a highly porous sandstone has been reported by Klein et al. (2001) in Bentheim sandstone as "quasi-ductile failure". Similar ductile behaviour was reported by Sun et al., (2017), and they explained that it is a result of a reduction in the cement size due to CO_2-brine-rock interaction. Rohmer et al., (2017) assessed the ductile failure in cap rock due to CO_2 and found thatthe ductile failure is likely under fixed vertical stress conditions and that the ductile failure would reduce the zone of influence of the CO_2 induced changes. All these indicate that CO_2-brine makes porous rock become ductile.

In Figures 36 (b-e), the total strain recorded by each sample varied. The strain was allowed to continue for each confining stress level at a constant strain rate of 10^{-5} s^{-1} until shear enhanced compaction ends in each sample. This is because the aim of the experiment requires that all the samples reach the end of shear enhanced compaction for each stress level. This means that the difference in the total strain recorded in each sample is the effect of the phaseCO_2 brine that saturates the sample. For example, at 16 MPa, the brine saturated sample had about 12000 microstrains before shear enhanced compaction ended, while the gCO_2-br sample underwent about 30000 microstrains before shear enhanced compaction ended. This shows that gCO_2-br increased the ductility of samples compared to brine at that stress level. The volumetric strain recorded in each sample (Table 24) was influenced by the state of the sample. It is seen that the gCO_2-br sample had the highest total volumetric strain. It is understandable that the difference in the total strain recorded between the samples will also reflect on the pore geometry properties and Figure 44 shows that the gCO_2-br sample showed the highest reduction in porosity after compression.

Table 24: Axial and volumetric strain in each samples

Sample	Dry	Brine	gCO$_2$-br	scCO$_2$-br	gCO$_2$
Axial strain at 16 MPa confining stress (μS)	14728	11255	33433	16942	17818
Axial strain at 46 MPa confining stress (μS)	6008	20351	56156	3354	5724
Total volumetric strain (μS)	51154	56053	110707	46686	41612

The axial strain recorded in each sample is seen to vary according to the confining stress and the sample state (Table 24). For instance, the gCO$_2$-br sample is the most strained at both 16 and 46 MPa confining stress levels. The scCO$_2$-br sample is the least strained at the 46 MPa stress level. This implies that a reservoir saturated with gCO$_2$-br will undergo significant strain at both high and low stress (i.e. high and low depth), while a reservoir saturated with scCO$_2$-br will undergo much less strain at high stress level (high depth). All the samples containing CO$_2$ had higher strain at 16 MPa confining stress compared to the samples without CO$_2$. This means that the presence of CO$_2$ increased the strain recorded at that stress level. The strain recorded in the 46 MPa confining stress compared to the strain in the 16 MPa stress reduced in the dry, scCO$_2$-br and gCO$_2$ samples, while the strain recorded in the brine and gCO$_2$-br samples increased. This means that at higher stress or greater depth, reservoirs saturated with gCO$_2$-br and brine behave normally by undergoing higher strain, while there will be a lowered strain in reservoirs containing scCO$_2$-br and gCO$_2$. The lowered strain may be due to the fact the scCO$_2$-br and gCO$_2$ affect the effective strength of the rock at a very fast rate even at low stress and less straining occurs at the higher stress level due to the resultant stress hardening and shear-enhanced compaction hardening.

In all the samples, stress hardening or shear enhanced-compaction hardening is responsible for the increase in the stiffness. However, there was a decrease in stiffness as against stress hardening at some stress levels for some samples. This is due to the effect of stress corrosion depending on phaseCO$_2$-brine that saturated the sample. Stress corrosion is a progressive chemo-mechanical action of pore fluid that weakens exposed surface bonds and facilitates progressive sub-critical crack growth, reduces

the rock's strength, and influences other properties of the rock (Brantut et al., 2013; Heap et al., 2015). The mechanism for this has been explained by Heap, (2009). The exposed bond in contact with the fluid breaks and accepts a new atom into the bridging bond. This is followed by bond lengthening and weakening, then newer surfaces are exposed and the crack grows deeper.
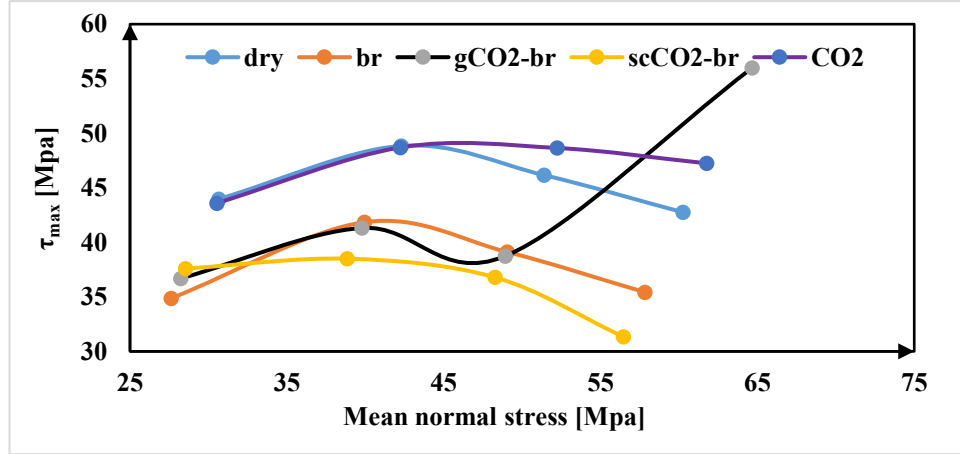

Figure 37: P-Q curves of the different samples from multiple failure tests.

6.5 Maximum shear stress vs mean normal stress

Figure 37 shows a plot of the shear stress against the mean stress (p-q curve). This is a good way to show the stress path in a multiple failure triaxial compression. Originally used in critical state soil mechanics, it is used here because it better represents the micro-deformation. q is the deviatoric shear stress calculated as equation (14) while p is the mean effective stress calculated as equation 15 (Wood, 1990).

$$q = \frac{\sqrt{(\sigma 2 - \sigma 3)^2 + (\sigma 3 - \sigma 1)^2 + (\sigma 1 - \sigma 2)^2}}{2} \tag{12}$$

$$p = \frac{\sigma 1 + \sigma 2 + \sigma 3}{3} \tag{13}$$

However, for triaxial conditions, σ2=σ3, therefore;

$$q = \sigma 1 - \sigma 3 \tag{14}$$

$$p = \frac{\sigma 1 + 2\sigma 3}{3} \tag{15}$$

Where q is the deviatoric shear stress, p is the mean effective stress, σ_1 is the axial stress, σ_2 is the intermediate stress and σ_3 is the confining stress.

Figure 37 shows the stress path for all the samples by connecting the maximum shear strength of the samples at all the stress cycles. Comparison of the curves shows that the dry and gCO_2 saturated samples had the highest shear strength for all the failure cycles. This implies that the presence of saturating fluid reduces the shear strength. More specifically, the presence of brine reduces the shear strength/stress path. The combination of different phaseCO_2 with brine affects the shear strength differently as seen from the gCO_2-br and $scCO_2$-br curves. For the dry and gCO_2 saturated sample, critical micro-failure started at approximately 49 MPa. For br, gCO_2-br and $scCO_2$-br samples, critical micro-failure started at a lower shear strength of approximately 42, 41 and 38 MPa respectively. This observation means that the critical shear stress was reduced by a 14.3%, 16.3% and 22.4% for the br, gCO_2-br and $scCO_2$-br samples respectively when compared to the dry sample. However, this does not mean that the sample failed completely after critical shearing stresses, the sample still retained some stiffness. It can be said that the presence of CO_2 saturated brine reduced the critical shearing stress of the sample. It is opined that this is the effect of pore stress corrosion due to CO_2-saturated brine.

6.6   Permeability

The permeability of the samples was measured before and after compression. The permeability of the dry sample represents the initial permeability of the samples. The permeability of the samples measured after saturation with the different phaseCO_2-brine (before compression) shows the change in the permeability due to saturation with the different phaseCO_2-brine. The permeability measured after compression of the samples shows the change in permeability brought about by compression of the different samples under reservoir stress conditions. This way, the changes in the permeability due to saturation with different phaseCO_2-br and the change in the permeability due to compression of the saturated sample are evaluated.

Table 25: Permeability of samples measure before and after compression testing

Sample ID	dry	br	gCO$_2$-br	scCO$_2$-br	gCO$_2$
Permeability before compression(Darcy)	1.14	1.76	1.27	1.24	1.80
Permeability after compression (Darcy)	0.34	0.10	0.10	0.90	1.25
% change in permeability after compression	71	94	92	27	31

From Table 25, it is seen that the permeability changed the most in the gCO$_2$-br sample after compression. This means that if stress condition changes, the permeability of a reservoir will be most affected if the phaseCO$_2$-brine is gCO$_2$-br. Also, Peter et al.,(2020) showed that the pore volume after compression also changed the most in the gCO$_2$-br sample compared to the other samples. Thus, the change in permeability can be explained to be due to constriction of pores and the closure of flow paths. The reduction of shear strength due to stress corrosion accelerated closure of pores in the samples that contain CO$_2$ and brine. This is supported by the fact that the gCO$_2$-br sample had the highest change (reduction) in pore volume, as well as the highest change (reduction) in the permeability.
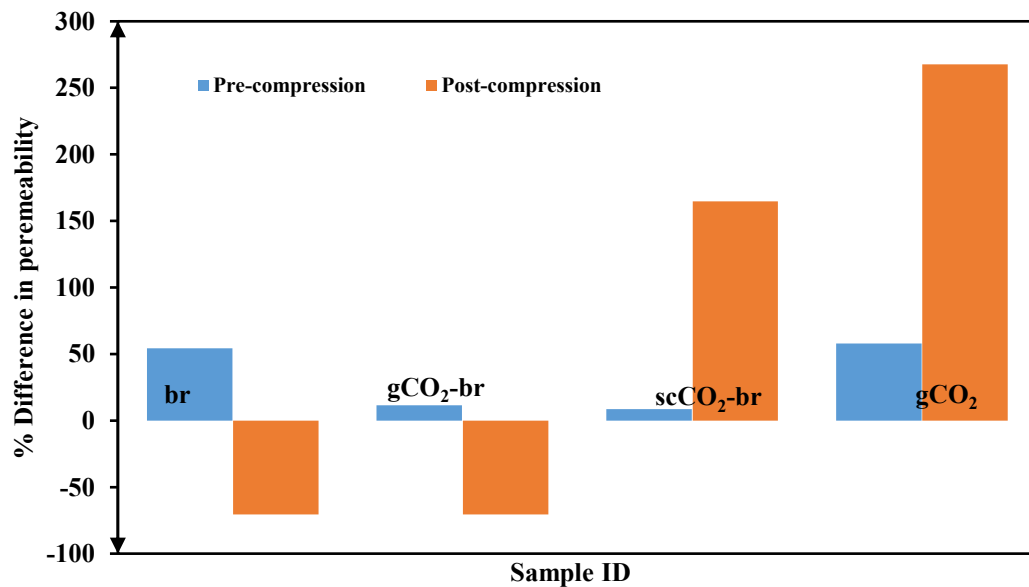
Figure 38: Comparison of the percentage difference in permeability between the dry and other samples.

Figure 38 shows the difference between the permeability of the dry sample and the other samples before and after compression in percentages. It is seen that the permeability of the brine saturated sample was higher by 54% when compared to the

dry sample. Also, the effect of stress on the permeability of the brine sample after compression was 70% lower than the dry sample. This implies that stress corrosion due to brine caused dissolution and an increase in the pore volume after saturation, but when stress was applied, there was an increased closure of pores (flow paths) compared to that of the dry sample due to the reduced effective strength. The effect on the permeability of the other samples compared to the dry sample is seen in Figure 38. The permeability of the gCO_2-br sample is reduced the most by 81% and increased the most in the gCO_2 sample after compression. The change in the permeability in each of the samples correlates with the magnitude of change in the pore volume shown by each sample in Peter et al. (2020). The increase in permeability in the gCO_2 and $scCO_2$-br samples despite compression and reduction in pore volume may be due to the fact that the compression changed the geometry of the pores in a way that increased the connectedness. Permeability depends on the geometry, volume and connectedness of the pores.
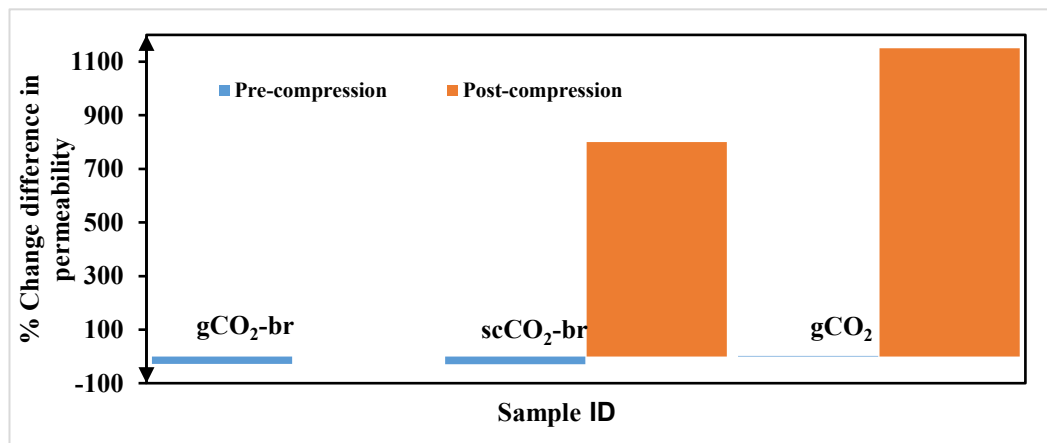
Figure 39: Comparison of the percentage difference in permeability between the brine saturated sample and other samples.

Because saline reservoirs in their natural state contain brine, the difference between the permeability of the brine saturated sample and the other CO_2-bearing samples before and after compression are shown in Figure 39. This shows the change in the permeability in a brine saturated reservoir due to the presence of the different phases of CO_2. When compared to brine saturated reservoir, the permeability of the gCO_2 saturated sample was three orders of magnitude higher than that of brine sample after compression, but was similar to that of the brine sample after saturation. This means

that the permeability of the gCO_2 saturated sample was three orders of magnitude affected by stress compared to the brine saturated sample. The permeability of the brine saturated sample was two orders of magnitude lower than the $scCO_2$ sample. These show how the different phaseCO_2-brine causes a change in reservoir's permeability under stress.

6.7   Summary

This result shows that the change in the geomechanical indices, strength and permeability of rocks due to the storage of CO_2 is sensitive to the phase of the CO_2. Different phaseCO_2-brine affects the shear strength differently. The critical shear stress for the gCO_2 saturated sample was approximately 49 Mpa while the critical shear stress for the br, gCO_2-br and $scCO_2$-br samples are 42, 41 and 38 Mpa respectively. The failure stress is seen to increase initially by stress hardening, and later by shear enhanced-compaction hardening. Shear enhanced-compaction is responsible for the ductility in the rocks at higher confining stresses. Pore stress corrosion by the br, $scCO_2$-br and gCO_2-br caused the samples to not increase in the stiffness even with an increase in the confining stress.

Chapter 7: Effect of CO_2 phase on pore geometry of saline reservoir rock

7.1   Introduction

This chapter focuses on the changes in the pore geometry properties (pore volume, shape, flatness, equivalent radius, and sphericity) in the reservoir rocks when saturated with different phaseCO_2-brine. In this research, the phaseCO_2-brine states of the reservoir considered include the brine saturated sample (reservoir saturated with brine), gCO_2-br saturated sample (reservoir saturated with brine and gaseous CO_2), scCO_2-br saturated sample (reservoir saturated with brine and supercritical CO_2) and gCO_2 saturated sample (reservoir saturated with gaseous CO_2). A sample was also tested in dry conditions to represent the property of the dry natural reservoir rock. The gCO_2-br and the scCO_2-br reservoir conditions represent a scenario where gaseous and supercritical CO_2 exist with the brine, respectively. The gCO_2 saturated reservoir represents when gaseousCO_2 migrates into a dry reservoir while the br saturated reservoir represents the normal saline reservoir before saturation with CO_2. Liquid CO_2 is not considered because the pressure-temperature (P-T) condition of the reservoir at the suitable storage depth does not favour the existence of liquid CO_2. The result of this research will provide a better understanding of reservoir's response to CO_2 storage and also provide information with which to better constrain CO_2 storage modeling studies as well as open up new ways of simulating CO_2-brine-rock interaction.

To the best of my knowledge, no research has been carried out regarding the effect of different phaseCO_2-brine on the pore geometry properties of reservoir rocks. There is a need to investigate how the different phaseCO_2-brine that can exist in CO_2 storage reservoir affects the pore geometry of the reservoir rocks. Therefore, this research sets out to evaluate the changes in the pore geometry of a saline rock due to the different phaseCO_2-brine in a saline CO_2 reservoir using digital rock physics.

Digital rock physics was used to obtain the pore geometrical properties such as pore volume, shape, flatness, equivalent radius, and sphericity, which are then analysed using Avizo software, to obtain the changes in the pore geometry properties in the different samples.

Flatness of a pore is commonly used to express the amount of waviness or variation in the pore just as in any plane surface (GD&T, 2014), and it is measured as the width of the tolerance zone. The tolerance zone is defined by two parallel planes that bound the surface of the pore. Numerical methods for evaluating the flatness of surfaces include the best fit and the minimum zone method. The best fit method is prone to the error of false negatives (Faro., 2019). The minimum zone method, is the preferred method and is used in this research, it requires that two envelop planes enclosing the data points and their associated uncertainty are measured. The data points are sampled from the whole surface, therefore the path of measurement and the number of points are important (Calvo et al., 2014).

The shape of the pore was taken as the ratio of the maximum Feret diameter to the minimum Feret diameter (Sympatec, 2017; Thermofisher, 2018). Typical shapes corresponding to various aspect ratios can be seen in Vision (2012) and Chen et al. (2018). In this research, pores with an aspect ratio greater than 1.9 are rod-like (Delle Piane & Sarout, 2016) while those with aspect ratio 1<S<1.9 are sub-rounded. Pores with 0.8 < S < 1 are rounded.

The porosity refers to the volume occupied by each pore according to the shape. The bulk porosity is the sum of the volume occupied by all the pores. The change in porosity (contraction/dilation) is evaluated based on the evolution of pore structure during CO_2 underground storage. The sphericity of a pore (ψ) is the ratio of the surface area of a sphere that has the same volume (V) as the pore to the surface area (a) of the pore. According to Ji et al. (2012), the sphericity is expressed as:

$$\Psi = \pi^{\frac{1}{3}} \frac{(6V)^{\frac{2}{3}}}{\text{à}} \tag{16}$$

Where ψ is the tortuosity of the pores, V is the volume of the pore, π is 3.142, and a is the surface area of the pore.

$\psi = 1$ is a sphere and a ψ value increasingly less than one is highly non-spherical. The equivalent radius is the radius of a sphere whose volume is identical to a pore. According to Ji et al. (2012) the equivalent radius (R) and the equivalent diameter (D) of a pore is expressed as:

$$D= \frac{(6V)^{\frac{1}{3}}}{\pi} \qquad\qquad (17)$$

$$R= \frac{D}{2} \qquad\qquad (18)$$

Where D is the equivalent diameter of the pore, V is the volume of the pore, π is 3.142 and R is the equivalent radius of the pore.

Natural core samples suitable for core flooding triaxial experiments are scarce, hence, one sample was used to represent each phaseCO_2-brine state of the reservoir. Initial characterisation of the samples was done and the samples are seen to be homogenous (Table 15). The samples are of the same lithology i.e., weak, sub-rounded, medium grained quartz-arenite. Therefore, the permeability, pore geometry properties and mineralogy of the dry sample is taken to represent the initial values of the other samples

As this research seeks to evaluate the effect of different phaseCO_2-brine on the pore geometry properties, it is necessary to determine the resident time needed for the different phaseCO_2-brine to have a marked impact on the rock materials. Dissolution of CO_2 in brine produces an acidic solution. Results from Peter et al. (2020); Pimienta et al. (2017); Zou et al. (2018) and Olabode and Radonjic (2013) showed that the impact of CO_2 on the properties of rock starts vigorously almost immediately. It was hence decided that for this experiment, more than 5 days of would be good enough for the phaseCO_2 saturated-brine to have an effect on the properties of the rocks. The samples were saturated in the different phaseCO_2-brine for 7 days.

7.2   Determination of representative element volume (REV)

Different methods have been used in literature to achieve numerical efficiency in the computation of multi-scale and heterogeneous properties in digital rock physics (Lesueur et al., 2017). One of such is the Representative Element Volume (REV) of the digital rock. Sometimes, multi-scale imaging is used, especially for highly heterogeneous rocks as the smallest pores determine the resolution to be used for optimal imaging (Goral et al., 2020). Upscaling has also been used in different researches to circumvent this challenge (Long et al. (2013); Piller et al. (2014);

Mehmani et al. (2020). Studying the properties of rock encompassing the inherent heterogeneity has remained a challenge due to the limitation of the size of rocks that can be studied and how well they represent the core or field scale.

REV is the domain size where the material properties are representative of a heterogeneous material and was first proposed by Jacob bear and have been applied in numerous fields. Hurley et al. (2012) described REV as the volume size that can be modeled to yield consistent results, within an acceptable limit of the modeled property. Fernandes et al. (2012) described REV as the size of the digital rock that is big enough to represent the property of the sample and small enough to allow for successful computation. This implies that REV is a trade-off between computationally efficient rock volume and an accurate measurement. REV can be found for an entire rock type or for a phase of the rock. A phase is a mineral or textural component of the rock. REV for a porous material has been found to be different for different properties or phases (Mehmani et al., 2020). In this research, REV was used to ensure that all the rock properties evaluated from the digital rock are representative of the inherent heterogeneity in the scanned core samples.

As explained in section 2.9, physical quantities such as mass, density, grain and pore geometry, and pore volume etc. contained in a large volume or mass of a material can be represented by a representative element volume (REV) for a 3D image like CT-image. This assumption, therefore, allows for the macroscopic variable of the entire volume to be taken as averaged variable over the REV. The use of REV is necessary in this research because of the heterogeneity in the distribution of pores as seen in Figure 40. Also, reconstruction, visualization, analysis of the 3D images, and modeling over the entire image requires huge computational resources. Consequently, it is not possible to analyze and model the entire image of the core sample. Therefore, a workable volume of the digital rock is desired. Here, REV is taken as the minimum domain size where material properties are continuous and representative of a heterogeneous material.
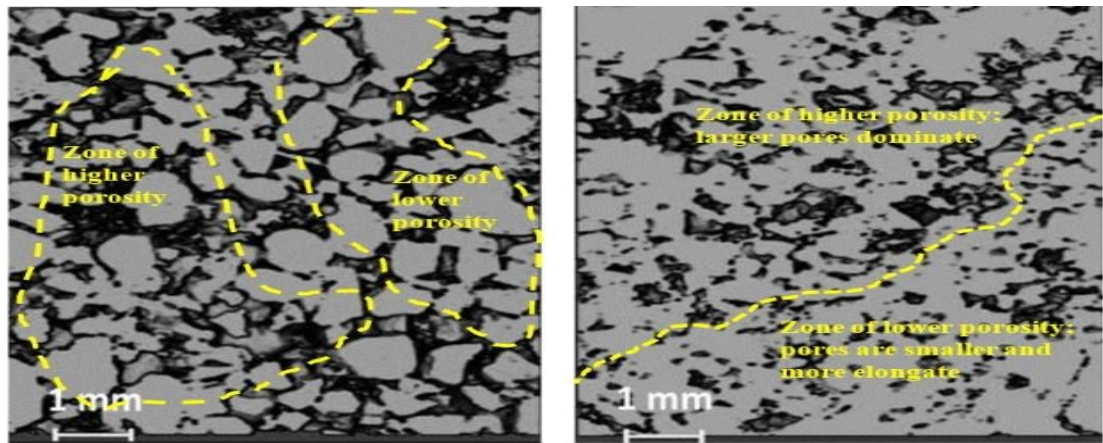
Figure 40: 2D slices of micro-CT image showing variation in the size, shape, and distribution of pores in different zones

Therefore, the REV is the sub-volume of the micro-CT images, which when taken from different locations of the whole image, shows the least or no variation in the measured porosity. A workflow to establish the REV is shown in Figure 41. The REV was evaluated from the scanned images of the samples. The total volume of the digital rock refers to the whole volume of the image obtained from the scanned image and is equal to the volume bounded by 3.36×3.43×3.37 mm. The sub-volume of the digital rock is a portion of the total volume of the digital rock. The total volume of each digital rock was cropped to remove the edges and then divided into sub-volumes from which REV was determined. This was achieved by taking incremental sub-volume sizes from different parts of the image and measuring the porosity similar to Fernandes et al. (2012). The sub-volume size was successively increased until the largest possible sub-volume size, which allows more than one sub-volume within the total volume. The measured porosity is presented in Figure 42. The sub-volume size (E) bounded by 1.04×2.15×3.37 mm was chosen as the REV because the measured porosity showed the least variation. This volume meets the criteria for REV, and is the representative volume of the sample in this research. The sub-volume sizes used are shown in Table 26.
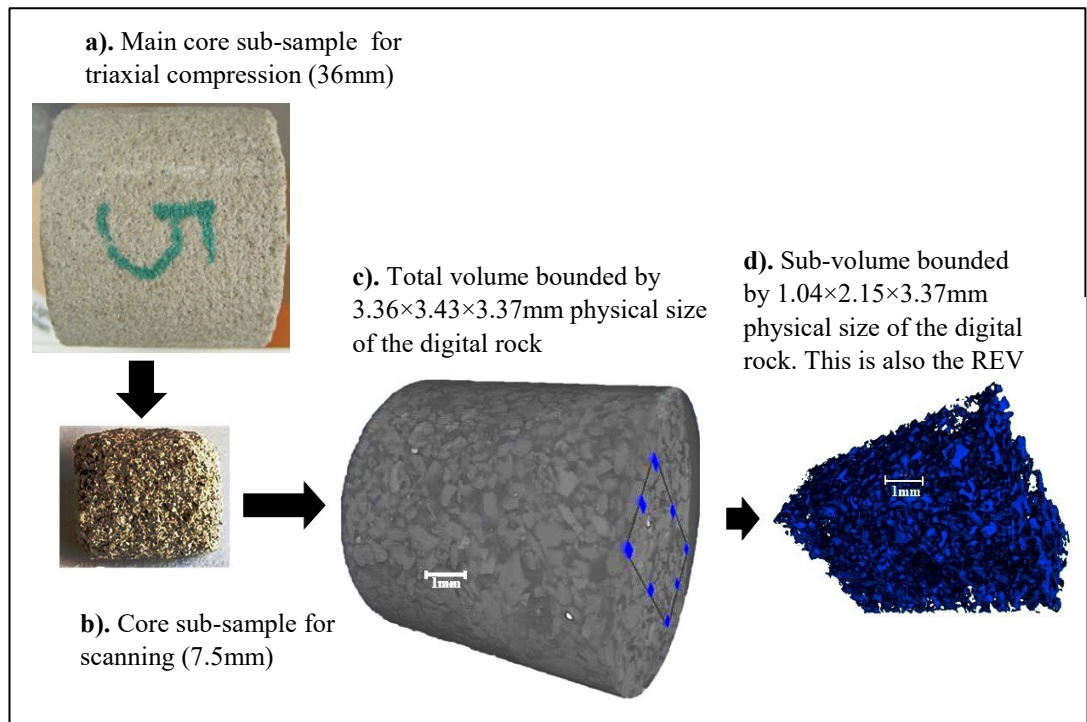
Figure 41: Schematic workflow for transforming core samples into digital rock REV
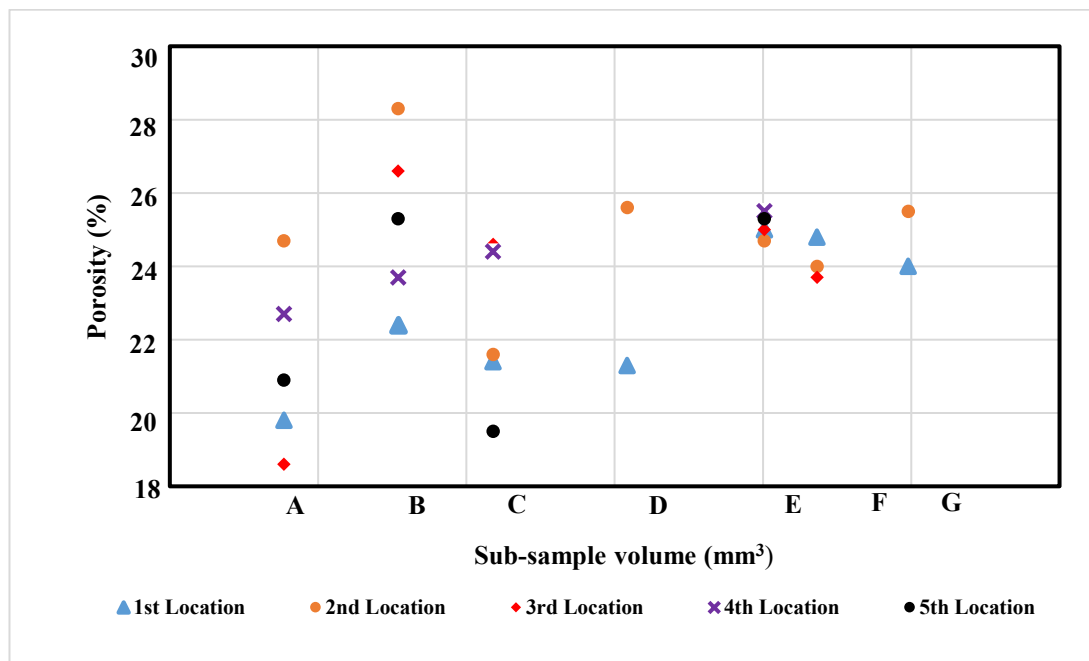
Figure 42: Porosity measured from different sub-volumes sizes (A-G) of the original sub-sampled digital rocks.

Table 26: Bounding physical size dimensions of the sub-volumes

Sub-volume	Bounding physical size of digital rock (mm)	Volume of sub-volume (mm³)
A	0.74×0.58×3.37	1.45
B	0.74×1.16×3.37	2.89
C	0.81×1.65×3.37	4.50
D	1.48×1.16×3.37	5.79
E	1.04×2.15×3.37	7.54
F	1.48×1.65×3.37	8.23
G	1.48×1.88×3.37	9.38

The permeability of the dry sample is 1.14 Darcy. This compares well with the permeability of Captain Sandstone measured by Shell (2011), Jin et al. (2012) and Hangx et al. (2013). Theinitial mineralogical characterization of the dry sample by XRD method showed that the sample contain Quartz (79.5%), K-feldspar (Orthoclase (0.66%), Microcline (4.57%), Plagioclase feldspar (Anorthite (0.72%) and clayey minerals (illite (1.7%), Kaolinite (4.34%), Chlorite (1.73%) and Dickite 6.83%). In summary, the sample is composed of Quartz, Feldspars and different types of clay minerals. The minerals identified in the photomicrograph (Figure 43) are the same as the mineral phases identified from the XRD result.

The effect of the phaseCO_2 on the pore geometry properties is shown by comparing it with that of the brine sample. The processed X-ray micro-CT scans in Figure 44 show the pores in the digital rocks of the different samples before and after compression. There was a reduction in the porosity of all the samples after compression. SEM images of the micro-structure of all the samples also show a reduction of the pores in all the samples after compression (Figure 45).

During the multiple triaxial compression test, the axial stress was increased until shear-enhanced compaction ends for all the samples, therefore all the samples were brought to the same stage of deformation. Hence, all the changes in pore the geometry are a result of the identical deformational process. A dry sample from the same formation was also tested to obtain the stress-strain characteristics before the experiment and the stress-strain curve.
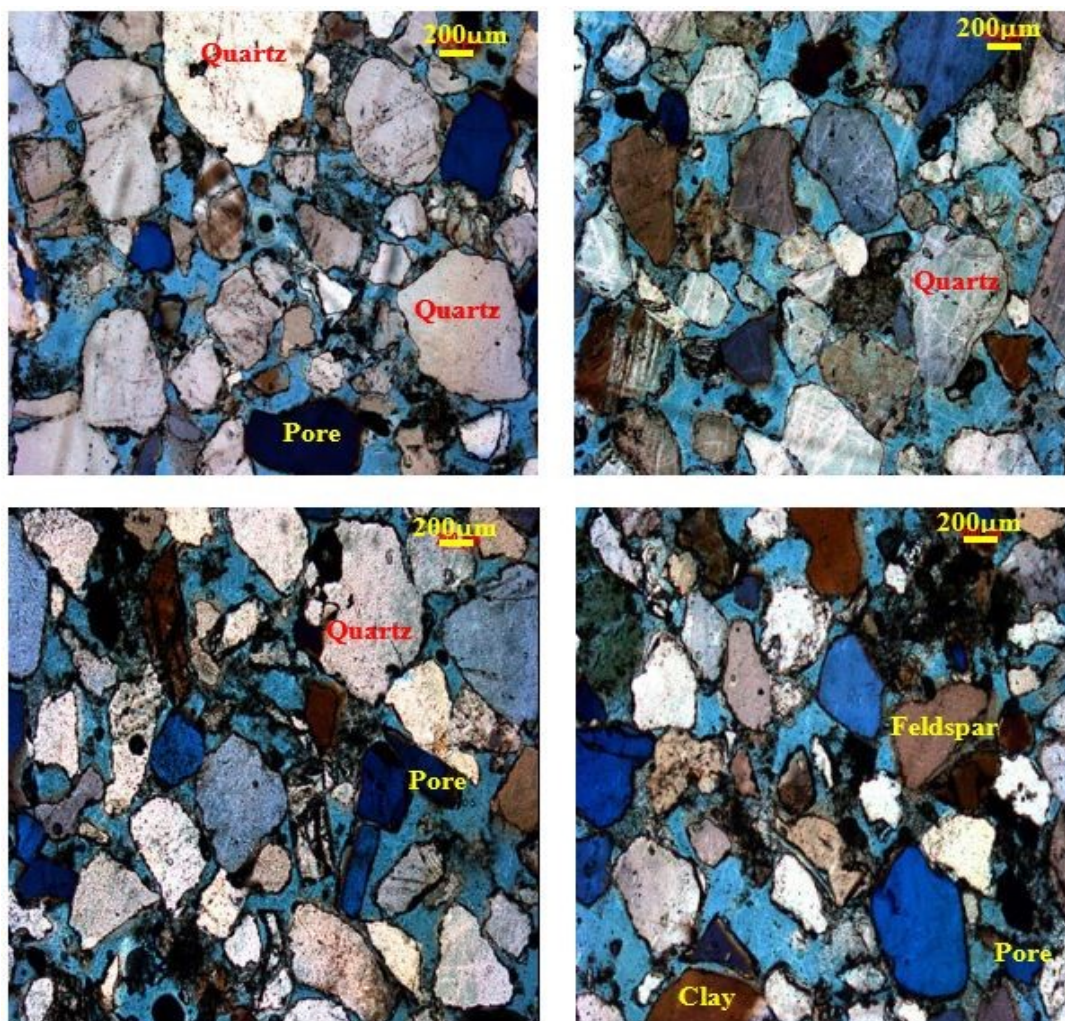
Figure 43: Photomicrograph of the dry sample showing Quartz, feldspar and clayey minerals. Blue resin was used to for contrast

Table 27: Weight % of minerals in dry natural sample before the experiment vs all samples after the experiment

Mineral (wt. %)	Samples				
	dry	br	gCO_2-br	$scCO_2$-br	gCO_2
Quartz	79.5	82.5	82.2	78.4	80.4
Anorthite	0.72	1.31	0.97	1.49	4.28
Illite	1.7	2.27	1.24	1.53	1.56
Kaolinite	4.34	3.62	3.96	3.88	1.74
Chlorite	1.73	1.2	2.11	1.96	1.12
Microcline	4.57	3.61	4.42	6.33	5.56
Orthoclase	0.66	0.39	0.22	1.02	2.88
Dickite	6.83	5.12	4.88	5.35	2.51

Table 27 provides evidence of the change in mineral composition in the samples saturated with different phaseCO_2-brine. It shows that injecting CO_2 into the brine-

rock system induces geochemical reaction that alters the composition of the minerals and the alteration in the composition of the minerals is affected by the phase of CO_2.
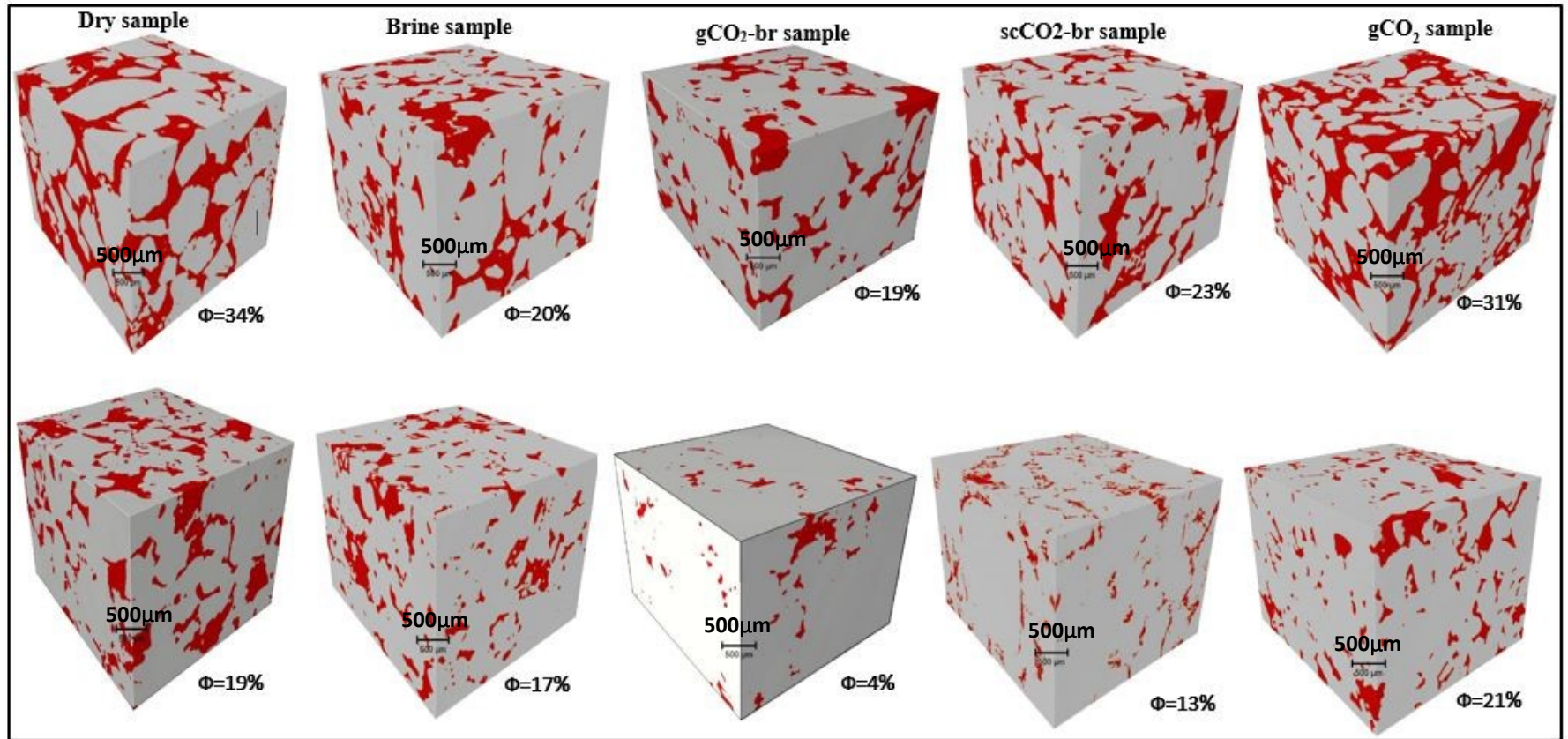
Figure 44: 3D digital rock models of all the samples at pre-compression (top images) and post- compression (bottom images) to show the changes in pore geometry properties with porosity (Φ) measured from the digital rock
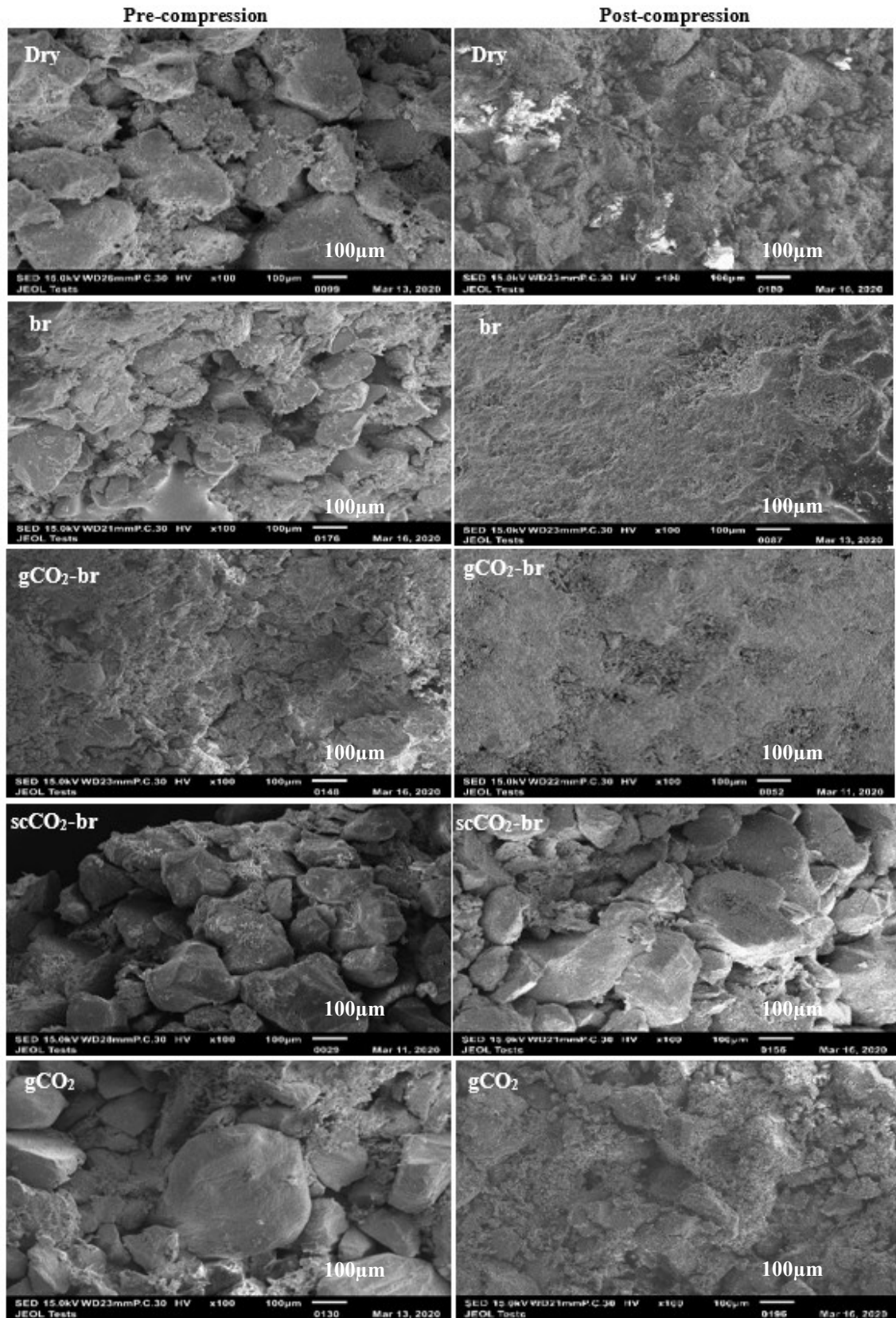
Figure 45: SEM images showing the microstructures at pre-compression and post-compression for each of the samples. Note that the pre-compression images were taken after saturation of the sample with the different phaseCO2-brine.

7.3   Bulk porosity

The bulk porosity of the samples which is the total pore volume of all the pores in each sample was measured using the digital rock physics method. The result is presented in Figure 46 at the pre-compression and post-compression stages. The pre-compression porosity is seen to vary with the samples, this shows the effect of the different phaseCO_2-br on the porosity of the rock during saturation. All samples containing brine showed a significant reduction in porosity compared to the dry sample. This indicates that the brine solutions caused the closure of pores by precipitation of fines. This is contrary to Foroutan et al. (2020) who observed a 3.6-2.87% increase in porosity. This difference may be due to the mineralogy of the rocks. There was calcite and anorthoclase feldspar in the samples used by Foroutan et al. (2020), while those were absent in the sample used in this research. Aside from the fact that calcite readily dissolves in an acidic medium, anorthoclase is known to be stable only at very high temperatures, hence they are likely to have dissolved at the temperature under which the test was performed. Furthermore, the brine solution used by Foroutan et al. (2020) is a mixture of $NaCl$, KCl, $CaCl_2$, Na_2SO_4, $MgCl_2$, and $MgSO_4$ and this will understandably trigger a different effect compared to the $NaCl$ brine used in this research. It is also seen that there is a reduction in the porosity after compression for all the samples. However, the amount of reduction varied according to the state of the sample. For instance, the gCO_2-br saturated rock showed the greatest reduction in the bulk porosity (~13%), followed by both $scCO_2$-br and gCO_2 saturated rocks, at 10% each (Figures 44 and 46).
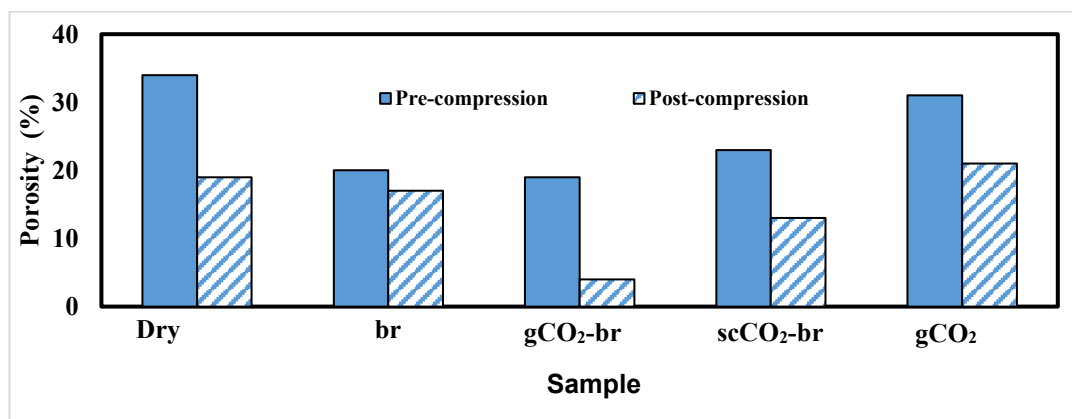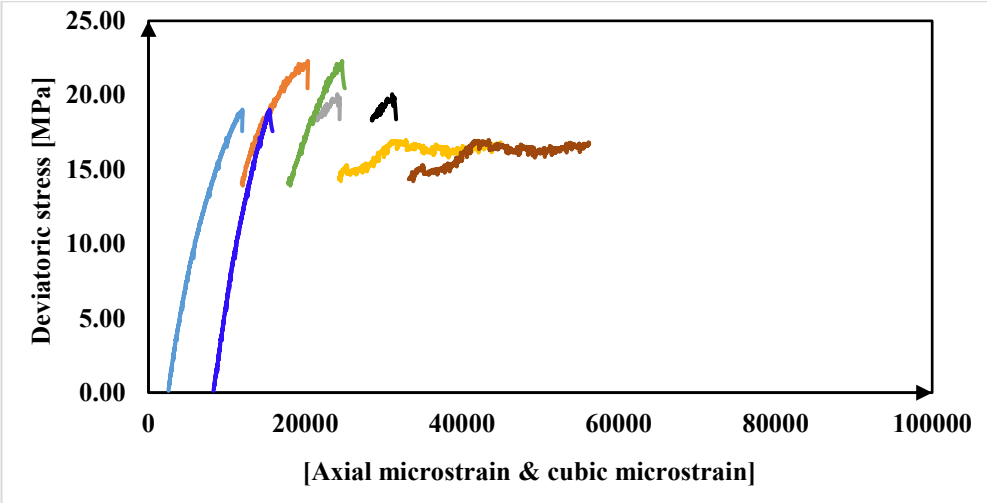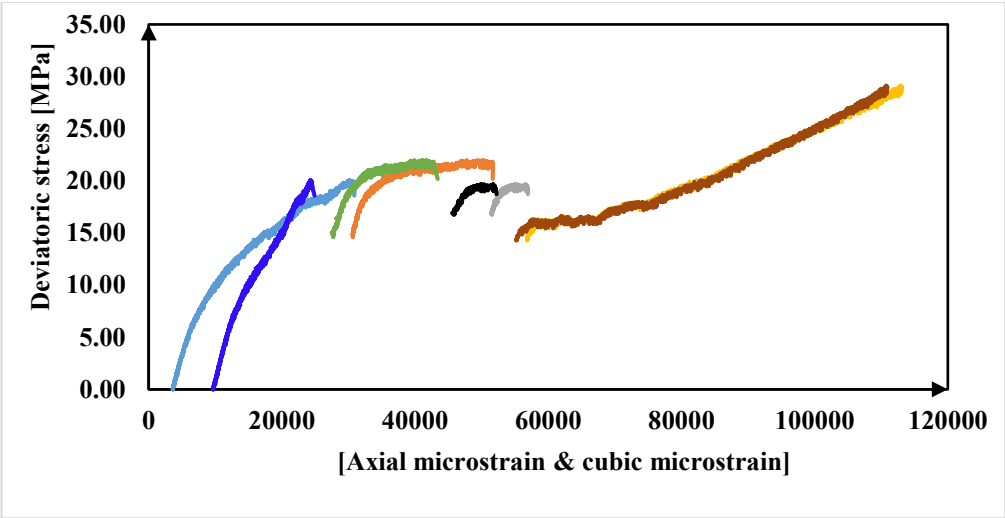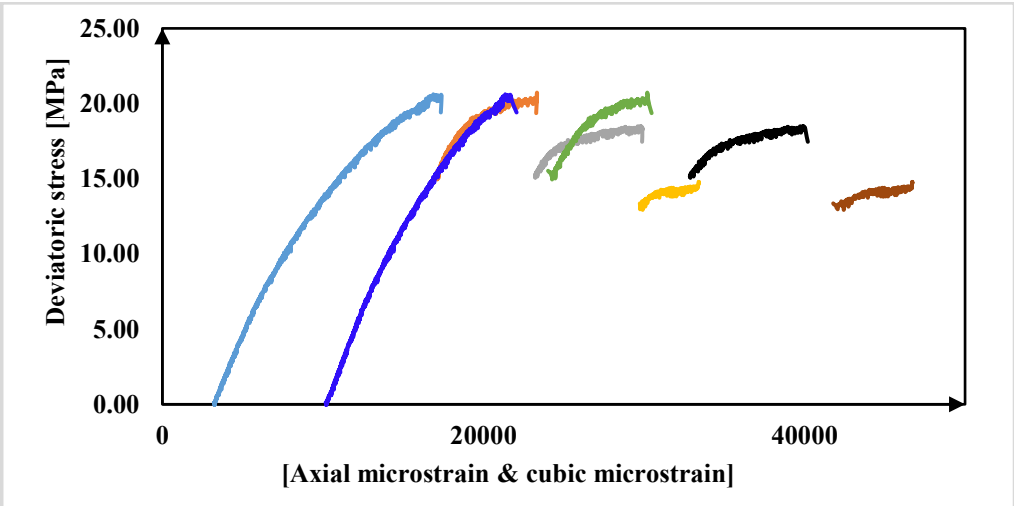

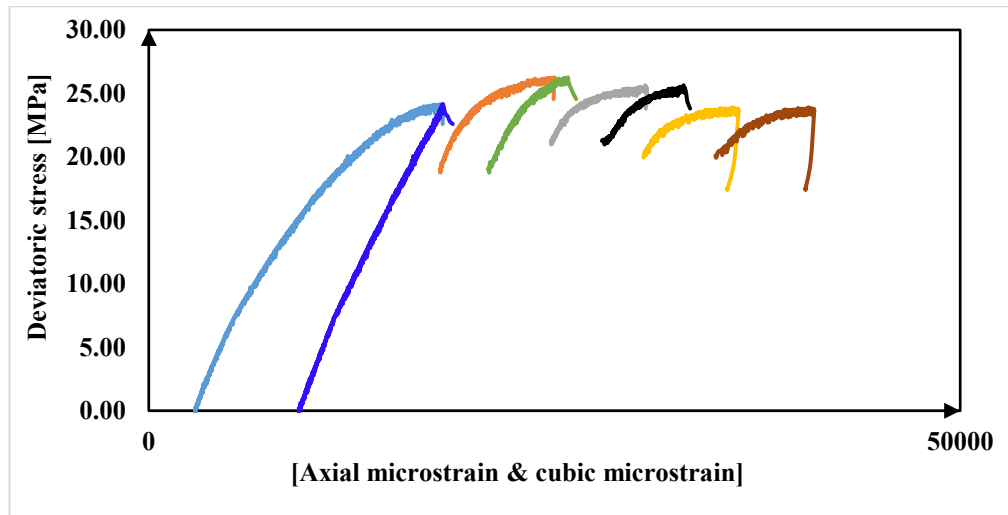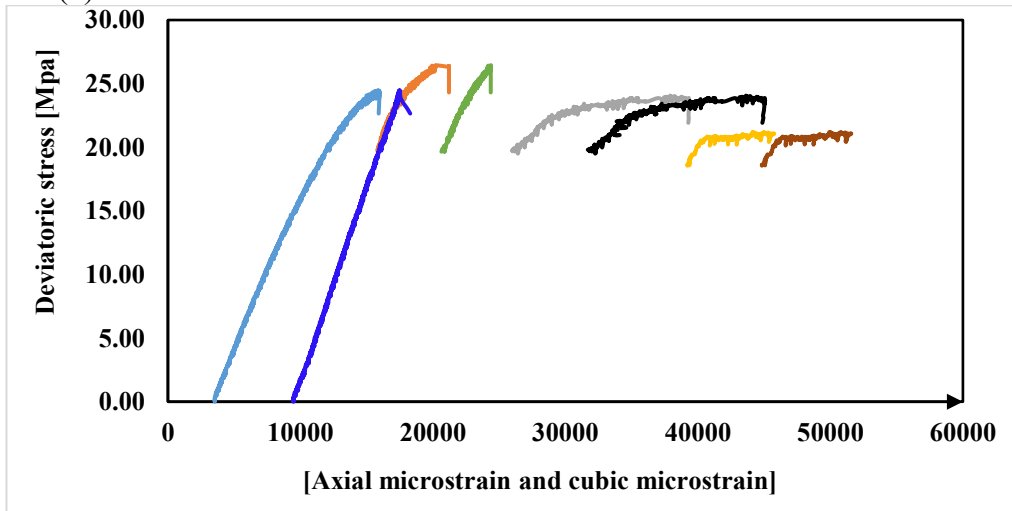Figure 46: Porosity of the different samples before and after compression evaluated from digital rocks.

(a)

(b)

(c)

135

(d)

(e)

Figure 47: Stress-strain curve of: (a) br saturated sample (b) gCO_2-br saturated sample (c) $scCO_2$-br saturated sample (d) gCO_2 saturated sample (e). Dry sample. The stress-strain curves show the evolution of both the axial and volumetric strain for each sample.

Figures 46 and 47 reveal that there is a relationship between the volumetric strain and the change in porosity. The volumetric strain recorded in each sample (Table 24) was influenced by the state of the sample. It is seen that the gCO_2-br sample had the highest total volumetric strain. It is understandable that the difference in the total strain recorded between the samples will also reflect on the pore geometry properties, and

Figure 44 shows that the gCO_2-br sample showed the highest reduction in the porosity after compression. Amongst the samples that contain CO_2 and/or brine, it is seen that the total volumetric strain is in the order: gCO_2-br sample >brine sample >$scCO_2$-br sample>gCO_2 sample. It is also seen that the gCO_2-br sample had the least porosity after compression. Furthermore, it was observed in this study that the reduction in the porosity as a function of volumetric strain is higher in all the CO_2-bearing samples compared to the brine sample.

CO_2-brine has been shown to trigger chemical precipitation or dissolution (Olabode & Radonjic, 2013, 2017) or swelling (Fuchs et al., 2019). This either decreases or increases the porosity of the rock. The porosity after saturation (pre-compression) was seen to be reduced but the reduction varied according to the phaseCO_2-br. For instance, compared to the dry sample, the porosity of br, gCO_2-br, $scCO_2$-br, and gCO_2 samples in Figure 46 was lower by 14%, 15%, 11% and 3% respectively after saturation. After compression, the porosity of the br, gCO_2-br, $scCO_2$-br, and gCO_2 samples was lower by 2%, 15%, and 6% and higher by 2% respectively. These results imply that the presence of brine cause a reduction in the porosity of reservoir rocks under stress but this reduction is further accelerated by the presence of CO_2 (gCO_2-br>$scCO_2$-br), that the gCO_2-br saturated sample showed the highest reduction in porosity after saturation and after compression indicates that the process responsible for the change in bulk porosity in this research (precipitation) is most active if the CO_2 in the brine saline reservoir is gaseous, compared to the other phases. This result shows that the saline reservoir in its natural brine-containing state is undergoing a change in porosity which is further triggered by CO_2, most especially the gaseous CO_2.

In this research, there is the need for all parameters especially the porosity of all the samples to be well characterized. The initially connected porosities of all the samples used are similar as seen in Table 15. The initial total porosity ($\emptyset_T$) was then calculated from the measured densities and the mineral composition of the samples from equation 19.

$$\emptyset_{T=}\left(1 - \frac{\rho}{\rho_p}\right) * 100 \qquad (19)$$

Where ρ is the bulk density of the samples shown in Table 28 and ρ_p is the particle density taken as the average density of the minerals that make up the rock i.e. 2.58g/cm^3.

The initial total porosity of all the samples before the commencement of the experiments showed that the samples have similar porosities (Table 28). The initially connected porosities measured from all the core samples using saturation and buoyancy technique (see Table 15) are also similar.

Table 28: Initial total porosity estimated from density

Sample	dry	br	gCO_2-br	$scCO_2$-br	$_gCO_2$
Bulk density (g/cm^3)	1.77	1.76	1.78	1.78	1.78
Initial total porosity	31	32	31	31	31

The original porosity of the dry samples measured from the digital rock physics (Figure 46) is higher than that measured by the saturation and buoyancy method (Table 15) because some of the pores are unconnected and so are not measured by the saturation and buoyancy method. However, such closed pores are measured by a well resolved digital rock physics method. Since the initial connected porosity measured from the saturation technique (Table 15) and the initial total porosity calculated from the density of all the samples (Table 28) follows a similar trend, it implies that the porosity of the dry sample measured using the digital rock physics represents the initial porosity of the other samples when measured digitally before the commencement of the experiments. Therefore a comparison of the changes in the porosity measured digitally before compression and after compression is shown in Figure 46.

The pre-compression porosities shown in Figure 46 are seen to be different from each other, with the dry sample having the highest porosity of 34%. The difference in porosity is due to the precipitation of fines from the different phaseCO_2-brine-rock reaction, which clogs the pores as seen in Figure 48. The reduction in the porosity after compression as shown in Figure 46 is a resultant effect of both the precipitation of fines that clogs the pores (Figure 48) and the closure of pores due to compression through volumetric strain. The precipitates are a product of the dissolution of feldspars by the CO_2-brine. Akono et al. (2019) had reported the dissolution of K-feldspars in a CO_2-brine saturated rock. Pimienta et al (2017) reported dissolution after two hours

exposure of rocks to supercritical CO_2 and precipitation after four hours of exposure. This implies that the exposure time of CO_2, and reactivity of the rock minerals affect the nature or stage of rock-CO_2-brine reaction (dissolution or precipitation). Differences in exposure time of CO_2 and the reactivity of the minerals explains why some research report dissolution (Foroutan et al 2020) while others report precipitation (Pimienta et al 2017).
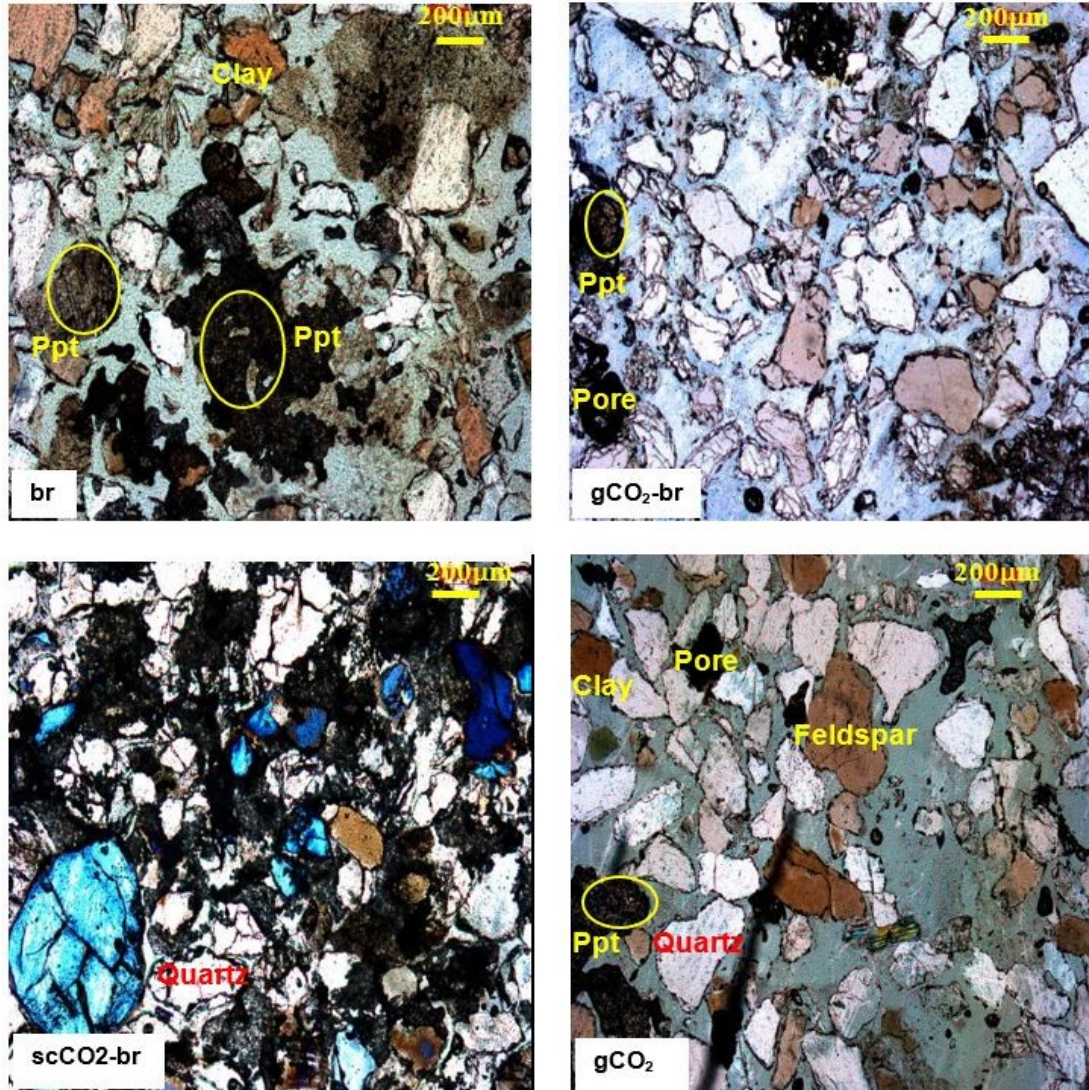

Figure 48: Photomicrograph of the different samples. Precipitation of fines is seen compared to the photomicrograph of the dry sample.

7.4   Cumulative percentage of pore volume

Figure 49 shows the Pore Volume Distribution (PVD) of the different classes of pore volume. A change in the PVD of the pores after compression is an indication of closure, contraction, or expansion of some of the pores.

For the gCO_2-br saturated rock as seen in Figure 49, there was a significant downward movement of the PVD curve after compression for all the classes of pore volume. The pre-compression and post-compression PVD for the gCO_2-br showed the highest deviation from each other compared to the other curves. This implies that there was a significant change (reduction) in the population of the pores in all the classes of pore volumes after compression due to pore filling or pore closure. Before compression, there was no significant difference between the PVD of the gCO_2-br and brine sample. However, after compression, there was a significant difference in the PVD between the two samples for all the classes of pore volume.

For the $scCO_2$-br saturated rock as seen in Figure 49, there was an upward movement of the PVD curve after compression for smaller classes of pore volume. This suggests that there was an increase in the population of the smaller pores while the population of the larger pores remained the same. An increase in the population of the smaller pores is suggestive of the contraction of some larger pores to smaller ones. There was a significant difference in the PVD of $scCO_2$-br and br samples for the smaller classes of pore volume before and after compression. Similarly, Huang et al. (2020) have reported an increase in micro-pores after $scCO_2$ injection into a brine saturated sandstone sample.

For the gCO_2 saturated rock, as seen in Figure 49, there was a downward movement of the PVD curve after compression for the smaller classes of the pore volume. This suggests that there was a decrease in the population of the smaller pores, while the population of the larger pores did not change significantly. A decrease in the population of a smaller pore is suggestive of expansion or coalesce of some smaller pores to form larger ones. There was a significant difference in the PVD of gCO_2 and br samples for the smaller classes of pore volume before and after compression. There was a higher population of smaller pores in the gCO_2 sample compared to the brine.
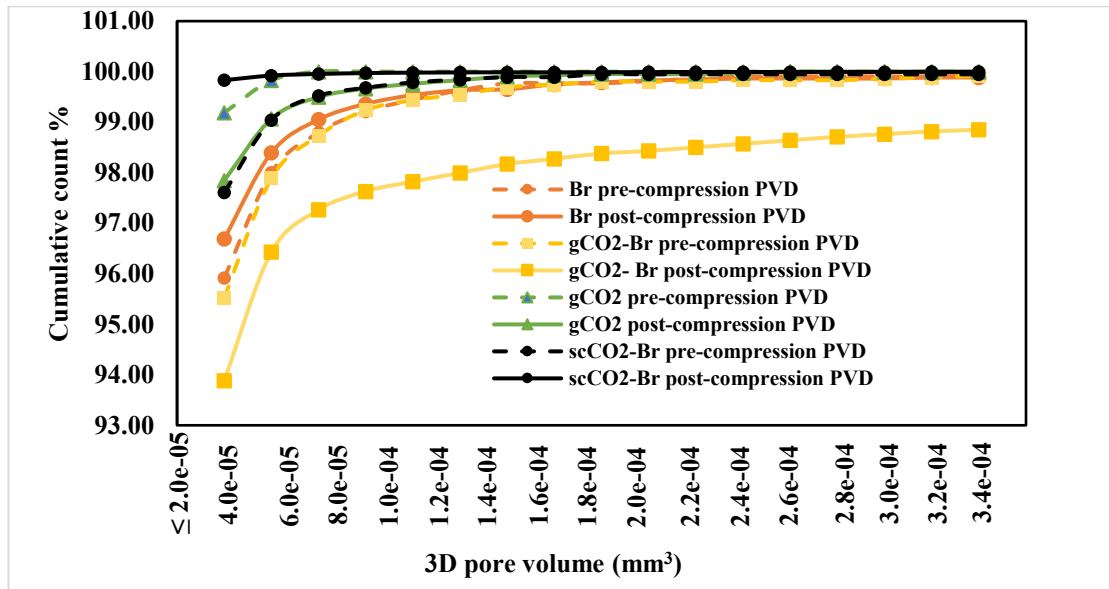
Figure 49: Comparison of the PVD for br, gCO$_2$-Br, scCO$_2$-Br, and gCO$_2$ samples

7.5 Pore surface flatness

The saturation of the rocks with brine-CO$_2$ and compression affected the pore surface flatness. Flatness index approaching zero indicates a flat pore surface, while flatness index approaching one indicates a wavy pore surface. Figure 50 shows the cumulative percentage count of pores for all classes of flatness index after saturation and after compression for all the samples. After saturation, the percentage count of pores in all classes of the flatness index was similar for all the samples irrespective of the nature of saturation. After compression, the percentage count of pores in each class of the flatness index is similar for all samples of rock except the scCO$_2$-br, where the percentage count of pores with flatness index greater than 0.37 differed considerably (Figure 50). This indicates that there are more pores with an index above 0.37 in the scCO$_2$-br rock compared to the others after compression. This implies that reservoir with scCO$_2$-brine have the tendency to make pore surface become wavy under stress, which could be because scCO$_2$ has a higher density and can dissolve edges of organic materials more easily compared to the gCO$_2$, and scCO$_2$ samples.
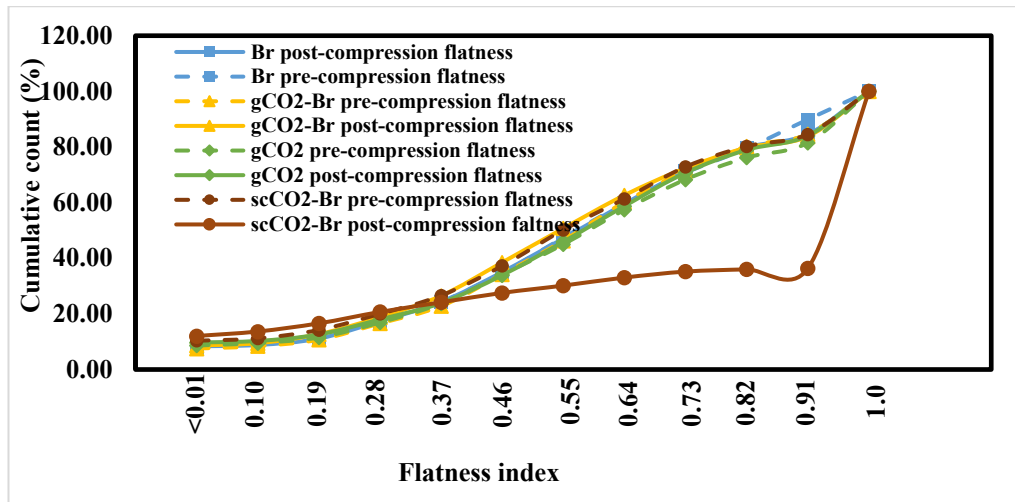
Figure 50: Cumulative percentage count of pores belonging to each pore flatness index before and after compression

7.6   Pore shape

The percentage count of pores belonging to each shape (aspect ratio) after saturation and after compression is shown as curves. After saturation, the percentage count of pores belonging to each shape in the CO_2-bearing samples compared to the brine sample is largely similar (Figure 52). This implies that the shape of pores may be insignificantly affected by the different phaseCO_2-brine during saturation. However, after compression (Figure 52), there was a significant difference in the percentage count of pores in both sub-rounded and rod-like shaped pores when the brine sample is compared to the other CO_2-bearing samples. This difference was also seen to vary according to the phaseCO_2-brine. For instance, the difference is highest in the gCO_2 sample followed by the $scCO_2$-br sample (Figure 52). Generally, there was an increase in the percentage of the sub-rounded and rod-like shaped pores in the gCO_2 and $scCO_2$-br samples after compression as seen in Figure 51, while the shape of the pores in the gCO_2-br sample remained similar to the brine sample.
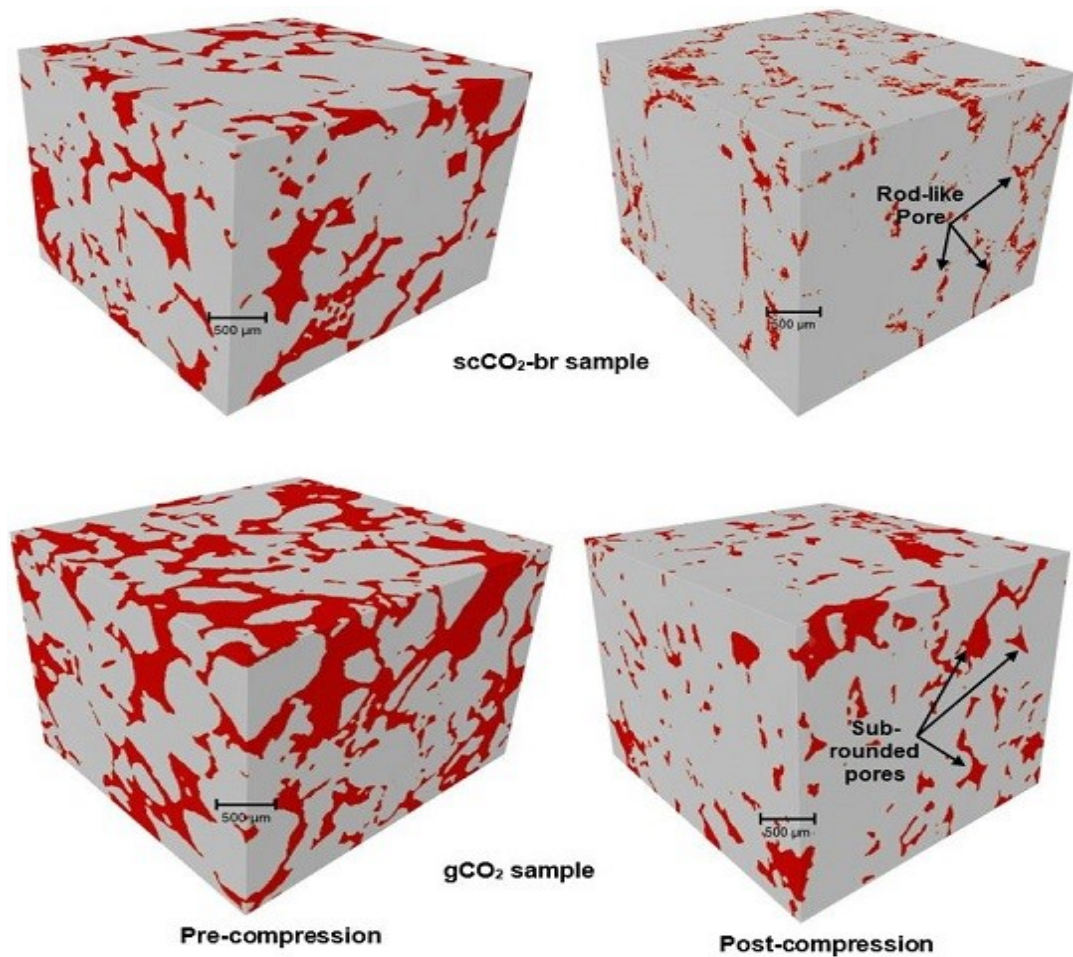
Figure 51: Showing Sub-rounded and rock-like pores after compression

There was no rounded pore in the sample and this may be a reflection of the diagenetic processes. Delle Piane and Sarout (2016) had reported no major difference in terms of the statistical distribution of shape descriptors in the identified pores and grains of minerals except kaolinite. However, our findings indicate that some pores in the $scCO_2$-br and gCO_2 saturated samples showed a significant alteration in shape after compression.
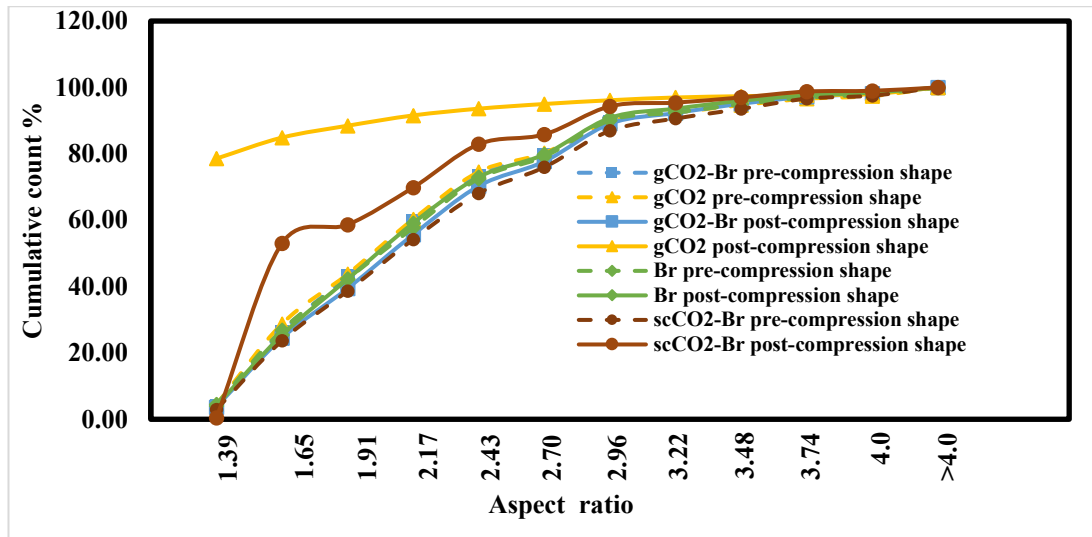
Figure 52: Cumulative percentage count of pores belonging to different pore shapes before and after compression.

7.7 Equivalent pore radius and sphericity

The distribution of the equivalent radius of the pores as well as the distribution of the sphericity within each class of pore radius for all the sample is shown in Figure 53 and Appendix 5. Spherical pores dominate and the sphericity of smaller sized pores remained largely unchanged even after compression. However, the sphericity of the larger-sized pores changed significantly. In the CO_2-bearing samples, compression led to a reduction of pore radius and a reduction of the sphericity of more pores compared to the brine sample. The change in the pore size and sphericity is seen to depend on the phaseCO_2-brine state of the sample and this has implications for the porosity, pore connectivity, transport properties, and storage capacity of the reservoir.
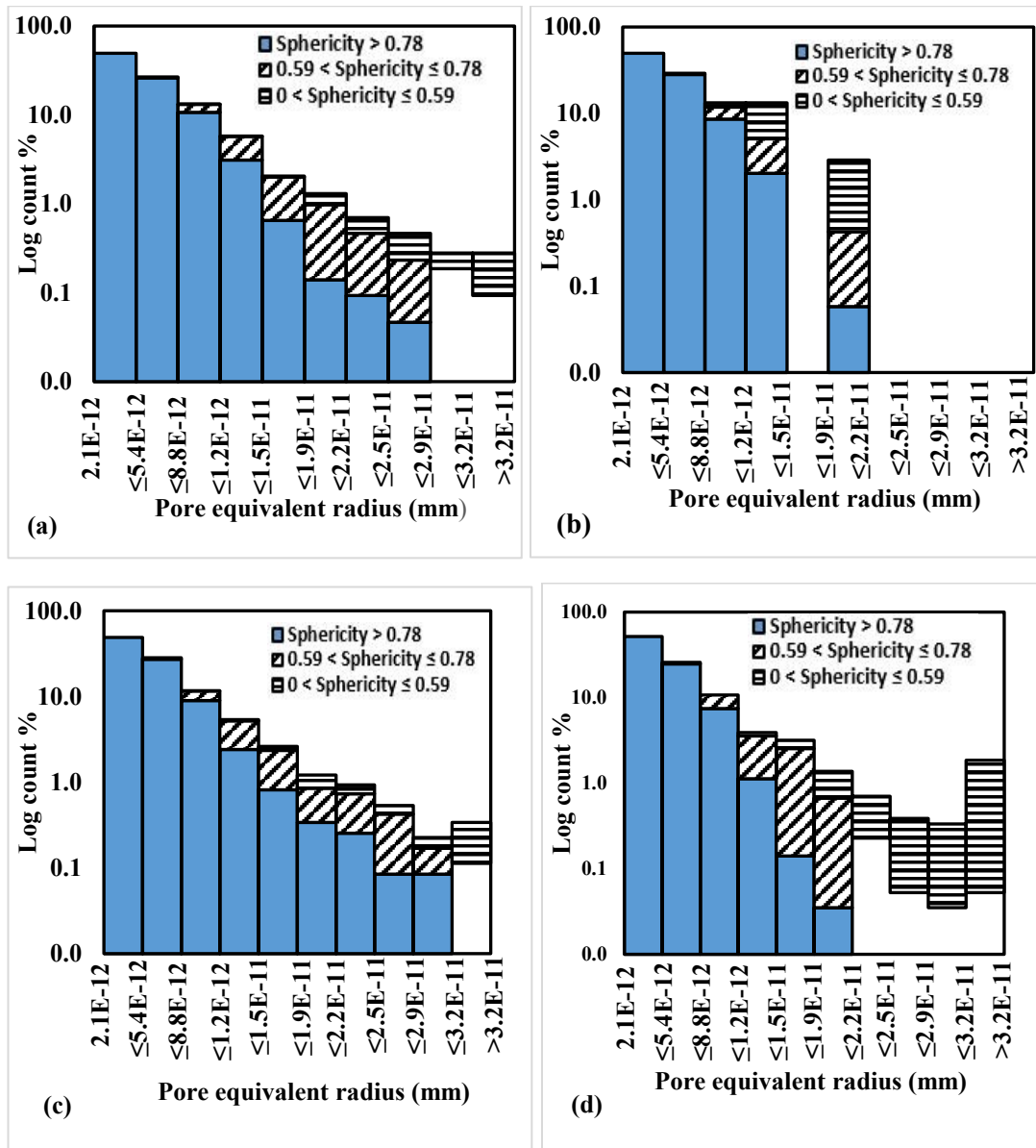
Figure 53: Distribution of equivalent pore radius and sphericity for (a) brine sample at pre-compression (b) brine sample at post-compression (c) gCO₂-br sample at pre-compression (d) gCO₂-br sample at post-compression. (Notice that the pre-compression samples in both cases had more spherical pores compared to the post-compression samples).

7.8 Hydro-Chemo-Mechanical Framework for the Change in the Rock Properties

Earlier, it was discussed that the pressure of pore fluid triggers a geochemical reaction between the minerals and the CO_2-brine. In this research, the change in pore geometry is due to the pore pressure of the different phaseCO_2-brine that saturates the rocks. The different phaseCO_2-brine and pressure of the different phaseCO_2-brine triggered

different geochemical reaction that caused different change in the mineral composition of the rocks as seen in Table 28. This change in the mineral composition is then reflected as different changes in the mechanical properties such as the different stress-strain (Figure 47), bulk modulus (Table 28) as well as porosity and pore geometry. For instance, Quartz is the most stable mineral in the rock. It is the cementing agent and accounts for most of the strength of the rock. The fact that the wt. % of Quartz is lowest in the $scCO_2$-br sample means that the Quartz is most degraded by the $scCO_2$-br compared to the others. Consequently, it also had the lowest bulk modulus. This agrees with Vanorio et al. (2011) who opined that compositional changes control the change in the fabric as well as other changes in the rock's properties, and that injecting CO_2 into brine-rock system induces chemo-mechanical processes that permanently alter the rock's framework.

7.9   Summary

The changes in pore geometry of sandstone in CO_2 storage conditions were evaluated with different phaseCO_2-brine. The results showed that change in pore geometry properties is dependent on the phase of CO_2. $scCO_2$-br saturation caused the highest change in the flatness and shape of the pores while gCO_2-br saturation caused the greatest reduction in the porosity. The presence of CO_2 cause pores to become rod-like especially $scCO_2$. There was a lowered porosity in the phaseCO_2-brine samples after saturation, this is indicative of precipitation. Hence, precipitation as a result of CO_2-brine-rock interaction can lead to a reduction in porosity. All samples showed a reduction in porosity after compression. The results showed that $scCO_2$-br saturation caused the highest change in the flatness of pore surface and shape of pores. This is because $scCO_2$ has a higher density compared to gCO_2, and it dissolves edges of organic materials more easily. gCO_2-br saturation caused the greatest reduction in porosity with the highest volumetric strain. This is because at both low and high-stress levels, the gCO_2-br affect the intergranular/effective strength of the rocks more than the other phaseCO_2-br. The presence of CO_2 increased the strain recorded in the samples. This implies that CO_2 affect the geomechanical behavior of rocks. More specifically, a reservoir containing gCO_2-br will undergo a significant strain at both shallow and greater depth with about 70% more strain at the greater depth, while a

reservoir containing scCO$_2$-br will show a comparatively lower strain at both shallow and greater depth with about 80% less strain at the greater depth. The result of this work can be useful for predicting the change in the geometry of pores and the strain of saline reservoir rocks in planned and already existing giant CO$_2$ storage sites such as Sleipner, In Salah, etc. Understanding the change in the geometry properties of a pore is critical to understanding the change in the transport, petrophysical and geomechanical properties of the reservoir rocks. Further research is recommended to model pore geometry control of the geomechanical and transport properties of reservoir rocks in a geosequestration site using the different possible phaseCO$_2$-brine.

Chapter 8: Microscopy and image analysis of the micro-fabric and composition of saline rocks under different phaseCO₂-brine states

8.1 Introduction

Here in this chapter, an evaluation of the micro-fabric, topology of minerals, and elemental composition of minerals in the rocks under the different phaseCO$_2$-brine conditions are presented from the analysis of the rock image. This is important because the micro-fabric, topology of grains, and mineral composition of the rock affect the transport, petrophysical properties and geomechanical properties of the rocks. From this research, the effect of the different phaseCO$_2$-brine on the topology of minerals, micro-fabric, as well as the elemental composition of rock minerals under reservoir conditions will be understood. The relationship between the micro-fabric, mineral topology and transport properties of the rocks is also explained. The output of this research will be useful in CO$_2$ reservoir evaluation, monitoring and modeling. Micro-fabric refers to the description of size, roundness, and solidity of the pores and grains in the rock. Topology has been described as the property of space that remains unchanged during deformation such as overlap, adjacent, disjoint, inside or equals etc. (Thiele et al., 2016). In this study, the topology of minerals refer to the spatial relationship (such as overlap, adjacent, disjoint, inside, covered, equal, meets or contains) between the grains that make up the rock.

Rock image analysis is an analytical process that involves the use of high-resolution images of rocks and advanced algorithms to create a digital model of the pore and grains of the rock for the purpose of evaluating the properties of rocks. This process involves processing the rock's SEM or micro-CT image and segmenting it into relevant phases. Aside from the use of these digital models as input for simulation of transport properties, models from a rock image analysis can be used to provide information such as grain and pore size distribution and mineralogy (Berg et al.,2017). The application of rock image analysis in rock characterisation is wide and becoming popular as seen in (Cheng & Song, 2018; Faisal et al., 2019; Lesueur et al., 2017; Shan & Lai, 2019; Vanorio et al., 2011; Zhang et al., 2020).

Furthermore, a tenth of the REV of the digital rock was used to conduct FE analysis of the strain distribution for each of the samples. Conducting pore scale numerical simulation directly on a real model of porous rocks requires huge computational resource. A finite element software with multiphysic capability is needed. These requirements posed a challenge in this study. Secondly, the complexity in tortuosity and heterogeneity of pore and grain sizes in a real rock model created issues around optimizing mesh size. This resulted in an inverted mesh error. A solution to this challenge is to smoothen/filter the finest part of the rock geometry. However, this may affect the results of the simulation. Different mesh sizes can be used, larger mesh is computationally efficient but affects the accuracy of results significantly. Finer mesh will produce a more accurate result but requires a huge compute time and resource, and has a higher probability for inverted mesh error.

8.2   Thermodynamics, phase behavior of CO_2 and solubility of CO_2 in brine

The phase diagram for CO_2 shows the phase behavior of CO_2 with temperature and pressure. The phase diagram of carbon dioxide can be found in Ricketts (2016). Prominent in the CO_2 phase diagram is the triple point and the critical point. Above the critical point, CO_2 is in the supercritical phase and there is no change in phase when pressure or heat is increased. At pressures below the critical point, CO_2 can exist in either gaseous or liquid phases depending on the temperature. At temperatures below the triple point down to -73.15°C, changes in pressure transform CO_2 to a solid phase. Given that CO_2 is thermodynamically unstable, various equations of states and theories have been proposed to solve the pressure-temperature phase equilibrium problem (Shin & Wu, 2010). The thermodynamics and phase behavior of CO_2 under pressure affects CO_2 underground storage as temperature and pressure conditions of reservoirs are variable.

CO_2 dissolves in water and brine to form weak carbonic acid. Temperature and pressure affect the solubility of CO_2 in brine, and the solubility of CO_2 in brine affects the CO_2-brine-rock interaction and rate. Jeon and Lee (2021) reported that the solubility of CO_2 in CO_2-saturated brine is different from the solubility of CO_2 in pure brine. This implies that as CO_2 dissolves in the brine, the solubility of CO_2 in a saline reservoir is constantly evolving. Shiflett et al., (2008) observed that the solubility of

CO$_2$ in ionic rich liquid does not produce vapor pressure at low CO$_2$ concentration, but at high CO$_2$ concentration there is an immiscible layer (vapor-liquid equilibria). Mosavat and Torabi (2014) presented that the increase in pressure leads to an increase in the solubility of CO$_2$ while the increase in temperature leads to a decrease in the solubility of CO$_2$ in a CO$_2$-brine system.

In a CO$_2$ storage system, once CO$_2$ mixes with and dissolves into the brine, there is a change in the solubility, density, and chemical composition of the brine and the CO$_2$. Chemically, the brine becomes weakly acidified and the pH increases. The change in the pH of brine is an indication of the solubility of CO$_2$ in the brine. It is necessary to understand the change in the density, solubility and composition, because such changes affect the CO$_2$-brine-rock interaction. It is known that such changes are affected by the temperature, pressure and salinity of the reservoir.

Mohammadian et al. (2015) provided solubility data of CO$_2$ in brine for low salinity, at a temperature range of 60-100 ^{o}C and pressure up to 25 MPa. It is seen that the solubility of CO$_2$ in brine increases with pressure and decreases with the temperature. Ratnakar et al.,(2020) presented that the solubility of CO$_2$ decreases with increased salt content in single ion brines, while the solubility of CO$_2$ in multi-ion brine depends on the salts present. Similarly, Li et al., (2021) presented that an increase in salinity reduces the solubility of CO$_2$ in saline rocks. This shows that the ionic composition of brine affects the solubility of CO$_2$. Lamy-Chappuis (2015) provided an estimate of the changes in the density of CO$_2$ at depths >800m. The density of CO$_2$ was seen to reduce with distance from the well. This implies that the mobility and tendency of CO$_2$ to change phase and density increases as the CO$_2$ moves further away from the injection well. Li et al. (2021) investigated the impact of pH on the solubility of CO$_2$ in brine, and found that ions from brines have higher affinity for silica pore surfaces as the pH increases. Therefore, the solubility of CO$_2$ in brine reduces as the pH increases.

Higher density CO$_2$ promotes density-settling, convection current and fingering; these processes are more favorable for CO$_2$ storage by dissolution. Higher solubility of CO$_2$ in brine promotes storage of CO$_2$ by dissolution trapping and then, mineralization trapping. An increase in the solubility of CO$_2$ in brine implies an increase in the pH,

which can reduce CO_2 dissolution in brine, consequently retarding mineralization trapping and CO_2 storage.

CO_2 storage in reservoir is achieved by trapping mechanisms. Trapping mechanisms include solubility trapping, residual trapping, mineralization trapping, structural trapping and hydrodynamic trapping. In a saline reservoir, solubility trapping is the most popular form of trap, and it leads to mineralization. However, it takes a long time for all the CO_2 to dissolve into the brine, hence other forms of traps such as structural, hydrodynamic and residual traps can serve to trap the CO_2 until dissolution can commence. In solubility trapping, the CO_2 exist as CO_2-brine. In the later forms of trapping, CO_2 can be trapped as single phase CO_2 (like gCO_2) or two phase (like gCO_2-br or $scCO_2$-br). Therefore, this study evaluates changes from both single phase and two phase CO_2-br scenarios.

8.3   Determination of Representative Element Area (REA)

Due to the variations in the distribution of the grains and pore areas across the images, Representative Element AREA (REA) needs to be established. As explained in section 2.9, physical quantities such as mass, density, grain and pore geometry etc. contained in a large mass of a material can be represented by a representative element area (REA) for a 2D image like Scanning Electron Microscopy (SEM). REA is different from REV used in Chapter 7 in that REV applies to 3D images like CT-images while REA applies to 2D images like SEM. In this research, the REA is taken as the sub-area size of the digital model of pore and grain in which the variability of a given property (pore and grain) from the different Region of Interest (ROI) in a sample is minimum.

In rock image analysis, representative element area (REA) is the minimum domain size where material properties have little or no variance and is representative of a heterogeneous scale (Hurley et al., 2012). It has been used in several fields of research for property evaluation (Oliveira et al., 2014). Like representative element volume (REV), REA can be found for an entire rock type or for a phase of the rock where a phase is a mineral or fabric component of the rock (Mehmani et al., 2020).

The SEM images taken from five different ROI of each thin section were processed with Image J software (Figure 54). The edge of the image was cropped and a median filter was applied. The total area of the SEM image is equal to 4224.42 µm × 3168.32 µm. A sub-area of the SEM image is a portion of the total area of the image. The cropped and filtered SEM images of each of the ROI was divided into sub-areas and then segmented into pore and the grain domain to create the digital model of pore and grains.

To determine the REA size, the areas occupied by pores and grains in the sub-area sizes of the SEM images (sub-area sizes are shown in Table 29) were measured from the five different SEM images taken from the different ROI. The plot of the measured pore and grain areas from the different sub-areas are presented in Figures 55-56. The sub-area sizes were selected to allow for a successive increment in sub-areas until the largest possible sub-area size was obtained as shown in Table 29 and Figure 54b. This method is similar to the method for the determination of REA and REV in a porous mediaproposed by Hurley et al. (2012). The median filter was applied and segmentation was performed on the REA size by setting a greyscale threshold that segments the rock into the pore and grain materials in each SEM image before the micro-fabric descriptors were evaluated. The REA size for grain and pore area was found to be 2000.73 µm^2 × 2000.73 µm^2, i.e. sub-area C in Figures 55-56. Note that Region of interest (ROI) refers to the SEM image of a given field of view. Five ROIs were taken from each sample and one REA size was taken from each ROI for analysis of the micro-fabric. Therefore, the evaluation of the micro-fabric descriptors for each sample in section 8.7 is from a combination of micro-fabric descriptors obtained from five different REA sizes taken from the five different ROIs of the sample.

Table 29: Sub-area sizes

Sub-area	Area size (µm^2)
A	1000.78 ×1000.78
B	1500.75 ×1500.75
C	2000.73 ×2000.73
D	2500.70 ×2500.70

Micro-fabric descriptors such as the area, roundness, and solidity of pores and grains were evaluated using ImageJ software. To achieve this, five different 2D SEM images

collected from five different ROI of each of the thin section slices were processed into the REA size of the SEM image. One ROI was taken from each of the four corners and one from the centre of the thin section slice to make the five ROI's.
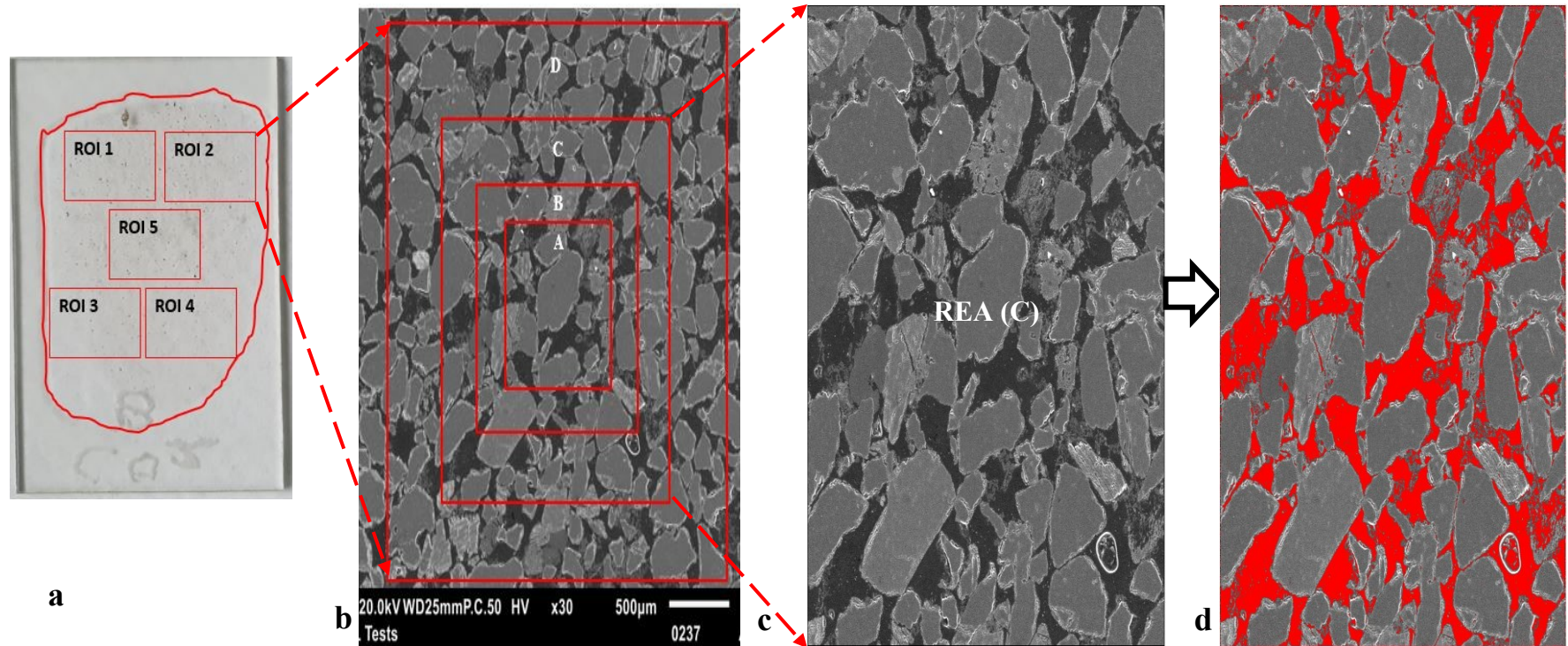
Figure 54: Schematic for making REA for digital model of pores and grains from SEM image (a). Thin section slice with the red circle showing a very thin slice of the rock pasted on glass. The red rectangles representations of the imaged region of interest on the slice. (b). SEM image of one of the ROI showing the different sub-area sizes (A, B,C,D) used for the measurement of pore and grain areas. (c). REA size (C) of SEM image made from ROI 2 (d). Segmented pore and grain areas of the SEM image REA (grain area in grey, the pore is red).

154
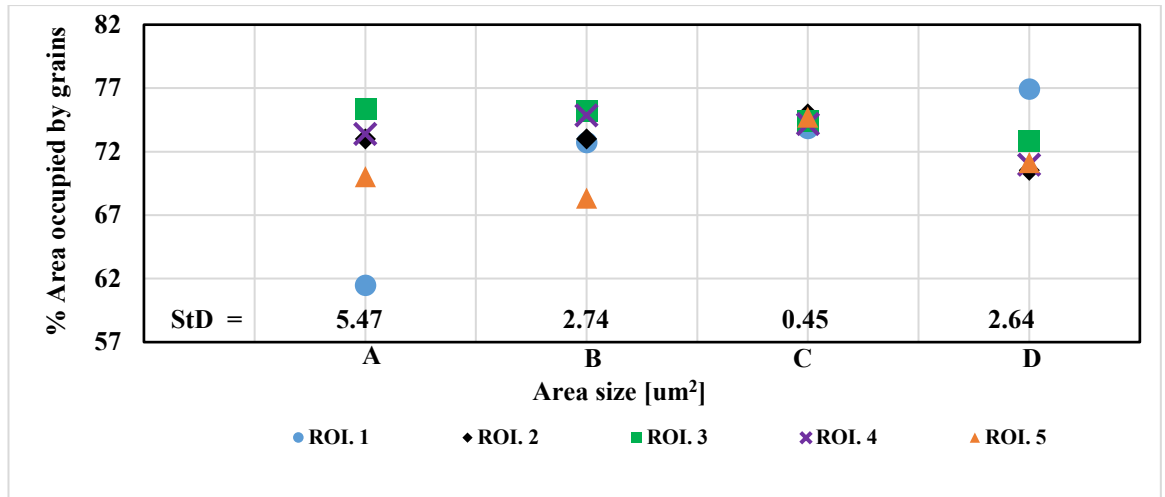
Figure 55: REA for grain domain
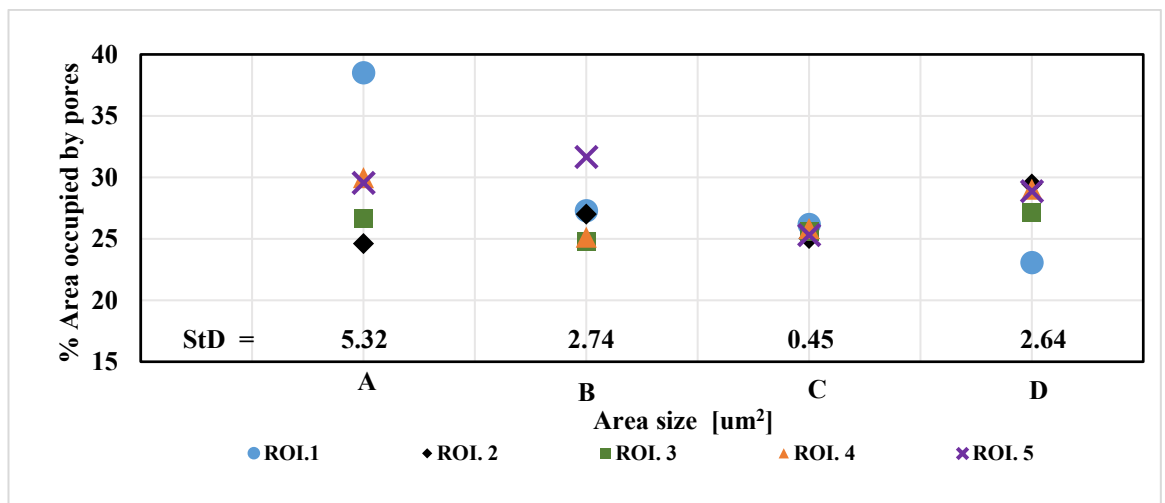
Figure 56: REA for pore domain

From Figures 55 and 56, sizes corresponding to A and B show high variability due to the dominance of the micro-scale effect. Sizes corresponding to C show little or no variability due to the integration of both macro and micro-scale effects. It is seen that C will be representative of macro and micro effects in the rock and thus would be the ideal REA size. Sub-area D shows a return of variability in the measured pore and grain area due to the dominance of the macro-scale effect. Sub-area C is therefore taken as the REA. Quantitative evaluation of the probability density function of the micro-fabric descriptors was done from the REA size of the digital model of the SEM images.

155

Description of the micro-fabric of rocks was achieved by describing fabric descriptors such as the shape and size of the grains and pores. Shape descriptors include the roundness and solidity (Cox & Budhu, 2008). Solidity is the measure of the density of the feature (pore or grain) and is used to describe the smoothness of the surface of the pore and grain. It is a useful index for tracking the impact of shear stress on the surface of the grains and pores of rocks. With an increase in the shear stress, irregular surfaces will smoothen out and more pores and grains will have their solidity approaching 1. A solidity value approaching 1 signifies high smoothness, and a value approaching 0 signifies poor smoothness. Mathematically, it is expressed as Equation 20 (Ferreira & Rasband, 2012). i.e., the ratio of the area of the feature (pore or grain) to the area of an imaginary convex hull around and it is illustrated as Figure 57.

$$Solidity = \frac{Area\ of\ the\ feature}{Area\ of\ the\ convex\ hull} \tag{20}$$
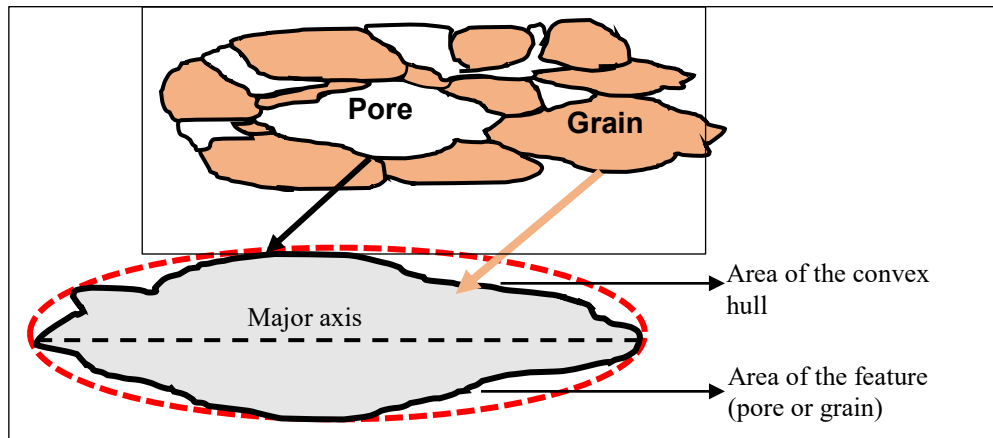
Figure 57: Illustrating solidity of shape of pore or grain in a mass of porous material.

Furthermore, roundness is illustrated in Figure 58 and is calculated using equation 21 (Ferreira & Rasband, 2012), where the area refers to the area occupied by the pore or grain. A value of roundness approaching 1 implies high rounding while values approaching 0 implies poor rounding. A description of roundness can be found in Takashimizu and Iiyoshi (2016). On the other hand, the description of the size of grains and pores in rocks is commonly by the area occupied by a feature in square pixels or a given square unit.

156

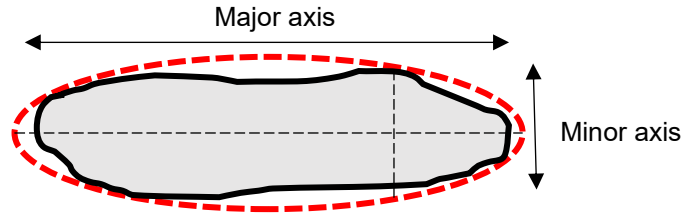$$Roundness = 4 \times \frac{[Area]}{\pi \times [Major\ axis]^2} \tag{21}$$

Figure 58: Illustrating roundness of pore or grain of a porous material.

8.4 Effect of different phaseCO$_2$-brine on topology and microfabric descriptors

In this research, the evaluation of the topology of minerals from the SEM image of bulk samples at microscale was done at two different stages. The first stage is the evaluation of the topology of the samples after saturation with the different phaseCO$_2$-brine and is hereafter referred to as "pre-compression topology of mineral" (Note that "after saturation" and "pre-compression" refer to the same stage). The second stage is the evaluation of the mineral topology after the saturated samples have been subjected to triaxial compression. This shows the response of the topology of the different saturated samples to stresses after being compressed and is hereafter referred to as "post-compression topology of minerals". Finally, the effect of the different phaseCO$_2$-brine on the probability density function of micro-fabric descriptors is presented.

8.5 Effect of the different phaseCO$_2$-brine on the topology of minerals

In this section, the topology of minerals in the rocks is evaluated in terms of the influence of the different phaseCO$_2$-brine at pre-compression and post-compression. Firstly, the effect of the different phaseCO$_2$-brine on the topology of mineral is described qualitatively by comparing the pre-compression topology of the brine saturated sample to the pre-compression topology of the other CO$_2$-bearing samples (Figure 59a-d). Secondly, the effect of stress on the topology of the different samples is described qualitatively by comparing the post-compression topology of the minerals of the different saturated samples (Figure 59e-h) to the pre-compression topology of

minerals of the same sample. Images of the topology of mineral scale features were shown in two scales (i.e., 10 μm and 100 μm), allowing good visualisation of the changes at different scales.

Figure 59(a-d) shows an example of the pre-compression topology of mineral-scale features in all the samples with the different phase CO_2-brine. The topology of minerals in the brine saturated sample (Figure 59a) represents the topology of minerals in a natural brine saturated reservoir. Here, the grains are seen to be covered by a clay layer. The clay layer may be a product of the dissolution of feldspars. The alteration of feldspars to form clay and the coating of other minerals by the clay has been reported by Daneshvar and Worden (2018); Yuan et al. (2015); Yuan et al. (2015b); Yuan et al. (2019). The pores contain fines that clog it and the edges of the grain appear rough and disjointed. From the higher resolution image of the brine sample (Figure 59a), the surface of the brine saturated sample shows dissolution channels similar to a splash erosion surface. In the gCO_2 saturated sample (Figure 59b), the higher resolution image of the gCO_2 sample shows the grains to be ridged and overlapping, but with considerably lower relief compared to the brine saturated sample. Edges of grains are more disjointed compared to the brine.

The gCO_2-br saturated sample (Figure 59c) shows the grains having a flat surface. The relief of the grains is levelled into a plain. Pores were seen to contain fines. The $scCO_2$-br saturated sample (Figure 59d) shows a thin covering on the grains. Edges are more disjointed compared to the brine saturated samples. A close-up view of the $scCO_2$-br saturated sample (Figure 59d) reveals the intragranular pores that may be the product of stress corrosion on the grain surface. Li et al. (2019) reported stress corrosion in the form of spatially dispersed fractures in sandstones due to sc-CO_2. Also, He et al. (2019) showed that $scCO_2$ creates dense and complex fractures and micro-cracks. Furthermore, Hu et al., (2017) and Li et al. (2019) showed that these microcracks lead to an increase in the permeability. The images of all the CO_2 bearing samples (Figure 59b-d) show differences in the topology compared to the brine saturated sample. The difference is seen to be at surfaces and this supports the fact that stress corrosion weakens exposed bonds at the surface and consequently facilitates progressive rupture, exposing newer surfaces while the rupture deepens. Carroll et al. (2016) explained

stress corrosion as a consequence of bond breakage and ion exchange. Qualitatively, the topology of minerals in scCO$_2$-br saturated sample appears to be the most altered before compression compared to the others.
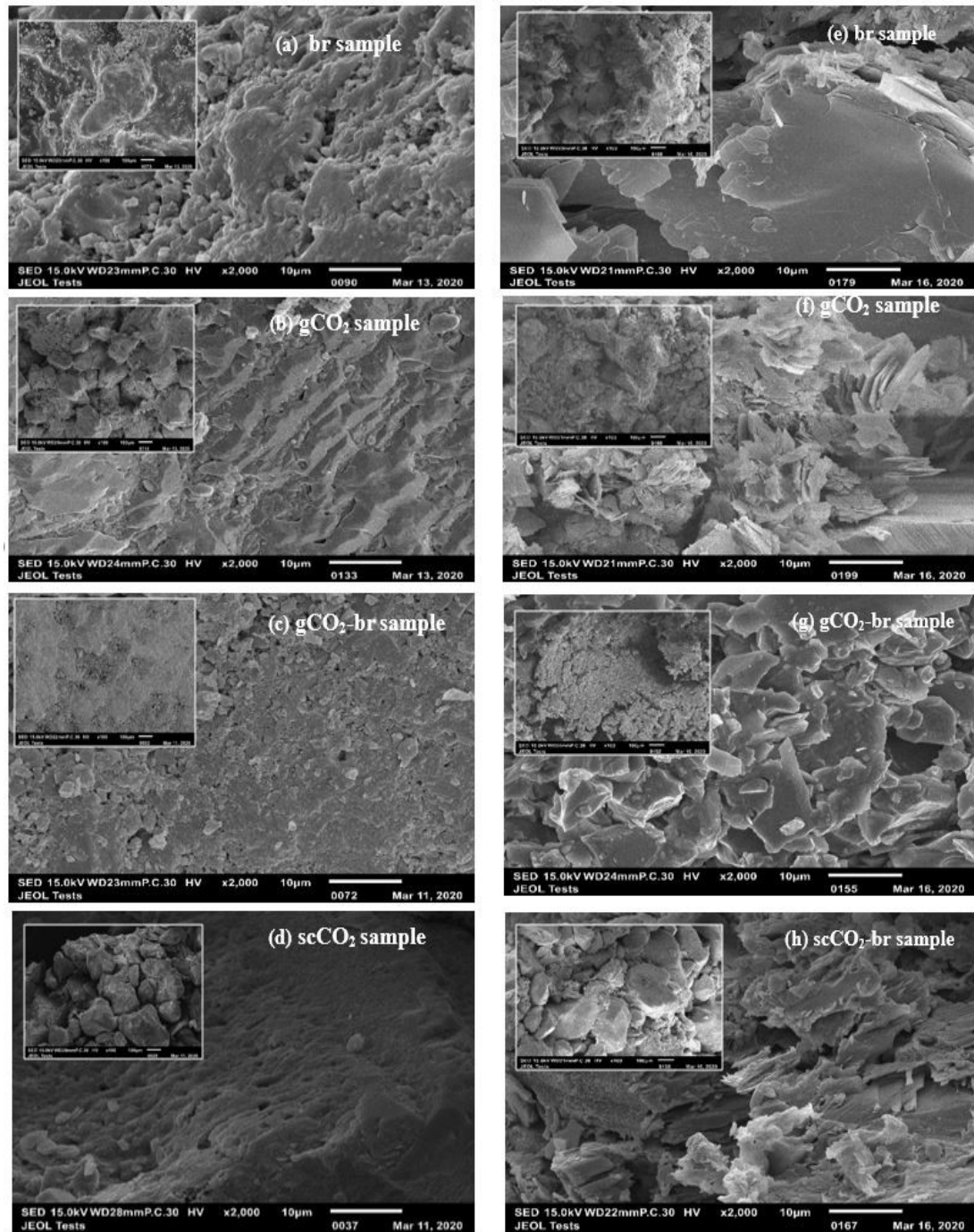

Figure 59: SEM images of the pre-compression topology of minerals (a-d) and post-compression topology of minerals (e-h) at 10 µm scales. Insets are at 100 µm.

Figure 59(e-h) shows the post-compression topology of minerals in all the samples saturated with the different phaseCO$_2$-brine. The topological features as seen in the images are widespread in each sample and is representative as can be seen from Figure 60. The brine saturated sample shows fissile overlapping sheets with a tendency to exfoliate. The gCO$_2$ saturated sample appears more fissile with overlapping sheets. The gCO$_2$-br saturated sample appears flaky and disjointed with a thin covering layer while the scCO$_2$-br saturated sample appears fibrous and disjointed. All the samples (Figures 59e-h) show differences in the topology of minerals compared to their respective pre-compression topology. This shows that stress induces changes in the topology during stress corrosion. Hu et al. (2017) indicated that such stress-induced changes could cause an increase or a decrease in the permeability by the creation of micro-cracks or compaction of pores respectively. Furthermore, the change between pre and post-compression topology of all the CO$_2$ bearing samples is different from the change seen between the pre and post-compression topology of brine saturated samples. Samples that contain CO$_2$ and brine (Figures 59g-h) had a more intense change in pre-compression topology after compression. This suggests that CO$_2$ increases the stress corrosion that a brine saturated reservoir would experience. Qualitatively, the most altered topology of minerals after compression is seen in the gCO$_2$-br saturated sample.

Figure 60 presents the minerals in a thin section. It is seen that the samples are composed mainly of Quartz, Feldspar and Clay minerals. Alteration of the minerals is seen in all the samples. However, the alteration was more intense in samples that contain both brine and CO$_2$. In the brine sample (Figure 60a) there is a dissolution of feldspar to leave the pore. In the gCO$_2$-br sample, feldspars are dissolved and micro-cracks are also seen on the feldspar grains. The scCO$_2$-br sample appears to be the most altered as feldspars are dissolved and micro-cracks are seen in quartz and feldspar grains.
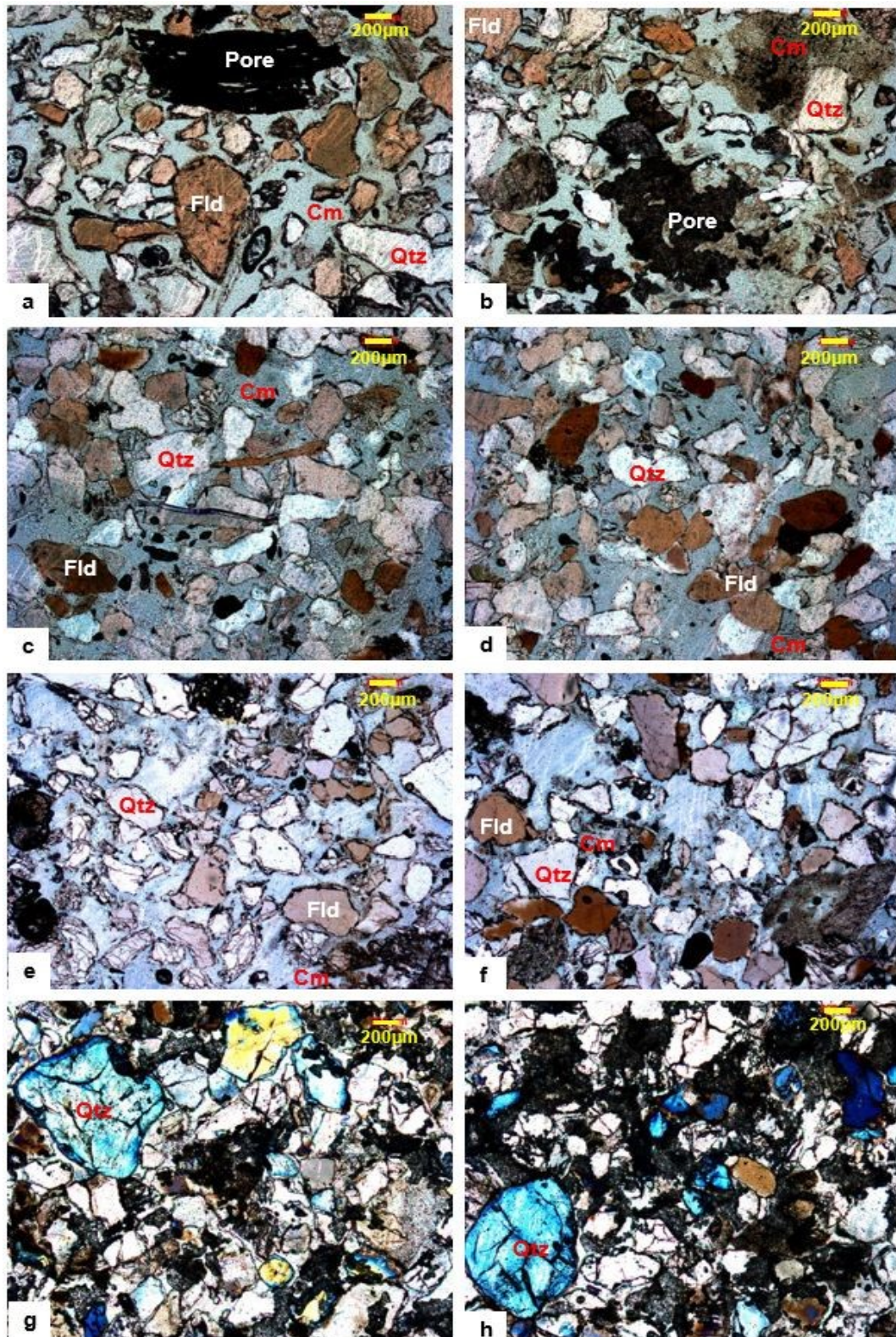
Figure 60: Sample photomicrograph of all the samples showing the minerals in thin section. Two images are shown per sample to populate the result. (a & b) brine sample (c & d) gCO₂ sample (e & f) gCO₂-br sample (g & h) scCO₂-br sample (Qtz=Quartz, Fld=Feldspar, Cm=Clay material).

161

8.6 Effect of different phaseCO$_2$-brine on the elemental composition of minerals

In this section, the change in the weight percent of elements in the minerals of the rocks due to the reaction of the minerals with different phaseCO$_2$-brine is evaluated. Usually, sandstone is composed principally of quartz, feldspars and some small amount of accessory minerals with a cementing agent that can either be silica or calcite. XRD analysis of the mineralogy of the original rock sample before saturation have been presented in section 4.6. Results from the mineral analysis served as a guide for the elements captured in the SEM-EDS elemental map shown in Figure 61 and listed in Table 30. Figure 61 gives an idea of the distribution of elements in the different phaseCO$_2$-brine samples.

Table 30: Percentage weight of constituent element mapped from EDS-spectra off the entire image of five different ROI from each sample.

| Sample	ROI	C	O	Si	Ca	Na	Al	Cl	K	Mg
Brine	1	26.5	49.7	23.8	-	-	-	-	-	-
	2	28.0	45.0	15.8	-	-	6.5	4.7	-	-
	3	37.9	44.2	12.0	-	0.4	-	-	2.5	-
	4	30.7	46.9	21.3	-	-	7.5	-	4.8	-
	5	37.9	42.0	12.7	-	0.4	3.9	-	1.6	-
Range		11.4	7.7	11.1		0	3.6	4.7	3.2	
gCO$_2$	1	57.8	32.0	9.8	-	-	0.4	-	-	-
	2	57.8	30.1	11.1	-		0.7	0.5	-	-
	3	55.2	27.4	14.7	-	0.4	1.6	0.6	-	-
	4	57.2	32.1	10.0	-	-	0.7	-	-	-
	5	10.5	46.9	26.9	3.6	8.7	2.4	-	-	4.4
Range		47.3	19.5	17.1	3.6	8.3	2.0	0.1		4.4
gCO$_2$-br	1	57.5	32.2	6.1	-	0.6	3.2	-	-	0.4
	2	50.2	35.6	7.3	-	0.5	4.8	-	1.0	0.5
	3	19.8	53.7	16.4	-	7.6	0.7	-	-	1.8
	4	27.4	47.3	15.6	-	6.3	-	-	-	1.6
	5	60.9	27.1	8.3	-	0.7	2.3	-	0.7	-
Range		41.1	26.6	10.3		7.1	4.1		0.3	1.4
scCO$_2$-br	1	53.6	36.3	9.1	-	-	1.0	-	-	-
	2	55.5	36.3	7.5		0.7	-	-	-	-
	3	51.0	42.9	4.4	-	-	-	-	-	-
	4	37.8	45.8	13.0	0.9	-	1.4	-	-	1.1
	5	41.5	43.6	13.8		0.5	0.7	-	-	-
Range		17.7	9.5	9.4	0.9	0.2	0.7			1.1
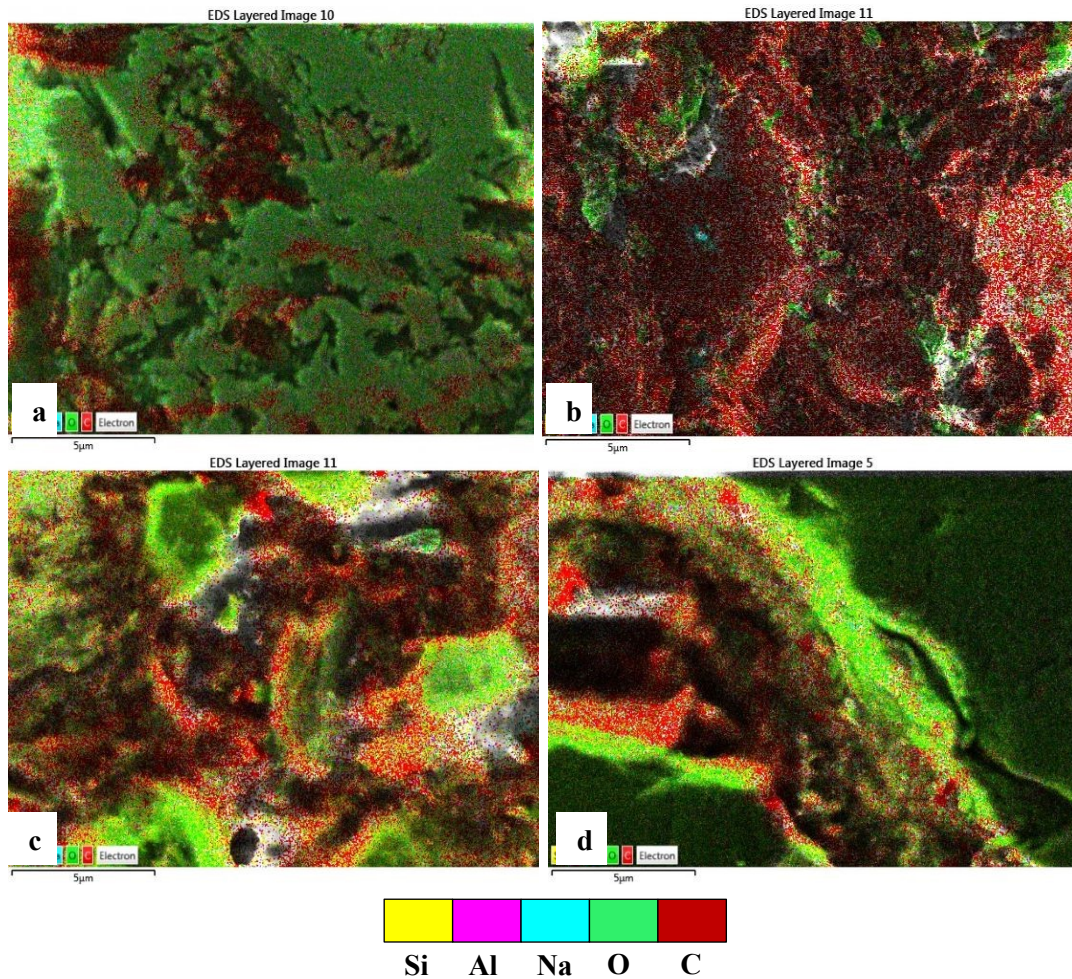
Figure 61: Sample EDS map for elements in all the samples after saturation. (a) Brine sample (b) gCO_2 sample (c) gCO_2-br sample (d) $scCO_2$-br sample. There is a difference in the concentration and distribution of the major elements across the different samples. Using the brine sample as the control, the difference in the distribution and concentration of the different elements in the other samples is an indication of the effect of the different phaseCO_2-brine on the elemental composition of saline rocks.

From Table 30, carbon, oxygen, and silicon are classified as major elements because they are present in all the ROI of all the samples in high weight percentages. This shows that the dominant mineral in the rock is Quartz. Therefore, Quartz is taken as the index mineral for evaluating the elemental changes due to the different phases of CO_2. It is seen that there is a difference in the distribution of the various major elements in the different samples.

The range in Table 30 indicate the difference in the weight percent of elements in different ROI's of a sample, this gives the sample-representative range of the elements in each sample. From the range of weight percentages, the weight percentage of carbon, oxygen and silicon varies in the different CO_2-bearing samples compared to the brine's. The range of the weight percentage of carbon in the CO_2 bearing samples are higher compared to the brine saturated sample. The high weight percent of carbon in the gCO_2 sample compared to the gCO_2-br samples may be due to the absence of brine that accelerates the CO_2-rock reaction. This means the weight percent of carbon increased in most ROI's of the CO_2-bearing samples but increased the most in the gCO_2 saturated sample. The high weight percent of carbon in the gCO_2 sample compared to the gCO_2-br and $scCO_2$-br samples may be due to the absence of brine that accelerates the CO_2-rock reaction. Similarly, the range of weight percent of oxygen in the CO_2 bearing samples are higher compared to the brine's. This implies that the weight percent of oxygen increased in most ROI's of the CO_2-bearing samples. This may be due to the fact that reaction (oxidation) was higher in the CO_2 bearing samples compared to the brine sample.

The range of the weight percent of Si in the CO_2-bearing samples relative to the brine sample increased in gCO_2 but reduced in the gCO_2-br and $scCO_2$-br saturated samples. This suggests that a combination of CO_2-brine reduces the weight percent of silicon. This is consistent with the EDS result from Lyu et al., (2016) which showed that a CO_2-water-rock interaction decreased the percentages of metals on the surface of the saturated samples when compared to samples without saturation. On the other hand, the presence of gaseous CO_2 caused an increase in the weight percent of silicon by reducing the weight percent of other metals relative to silicon due to the low reactivity of silicon. This means that silicon is more reactive to CO_2-brine than gaseous CO_2. The changes in weight percentage of elements can be seen as an effect of stress corrosion because stress corrosion involves the exchange of ions resulting in the change of elemental composition of minerals (Heap, 2009; Vanorio et al., 2011). Heap (2009) reported that stress corrosion occurs as a result of the chemical action of the fluid which facilitates the exchange of ions and weakens exposed bonds at the surface and consequently, and facilitates a progressive crack propagation depending on the nature of the pore fluid. Vanorio et al. (2011) had suggested that the compositional

changes control the change in fabric and strength as well as other changes in rock's properties.

8.7 Probability density functions of micro-fabric descriptors from SEM images

In this research, the cumulative percent distribution of the area size, roundness and solidity of the pores and grains are used to characterize the fabric of the rocks at the pore scale. Roundness characterise the shape of the grains and pores, the solidity characterise the irregularity or smoothness in the surface of the grains and pores while the area is used to characterise the size of the pores and grains. Changes in these sets of micro-fabric descriptors in the different phaseCO_2-br rock samples, when subjected to stress, are evaluated to track the changes under stress.

8.8 Pore and grain area size distribution

The percentage distribution of the different classes of pore and grains sizes are presented as percentage cumulative curves for all the samples (Figures 62-65).
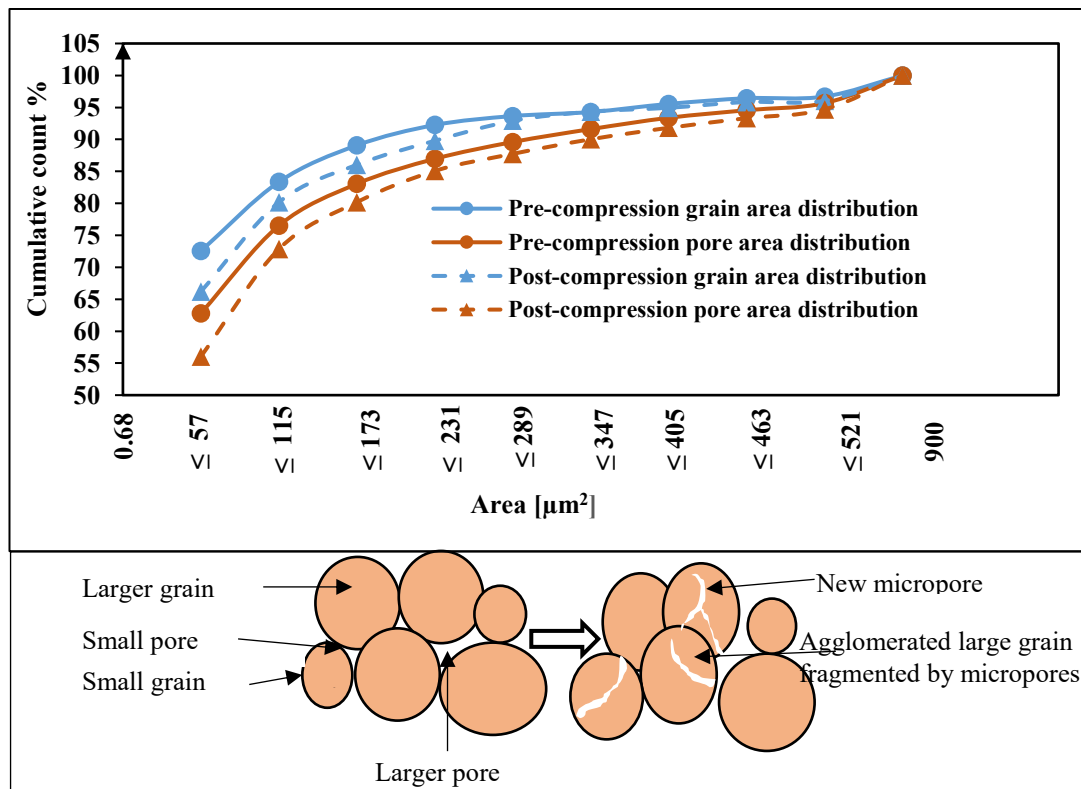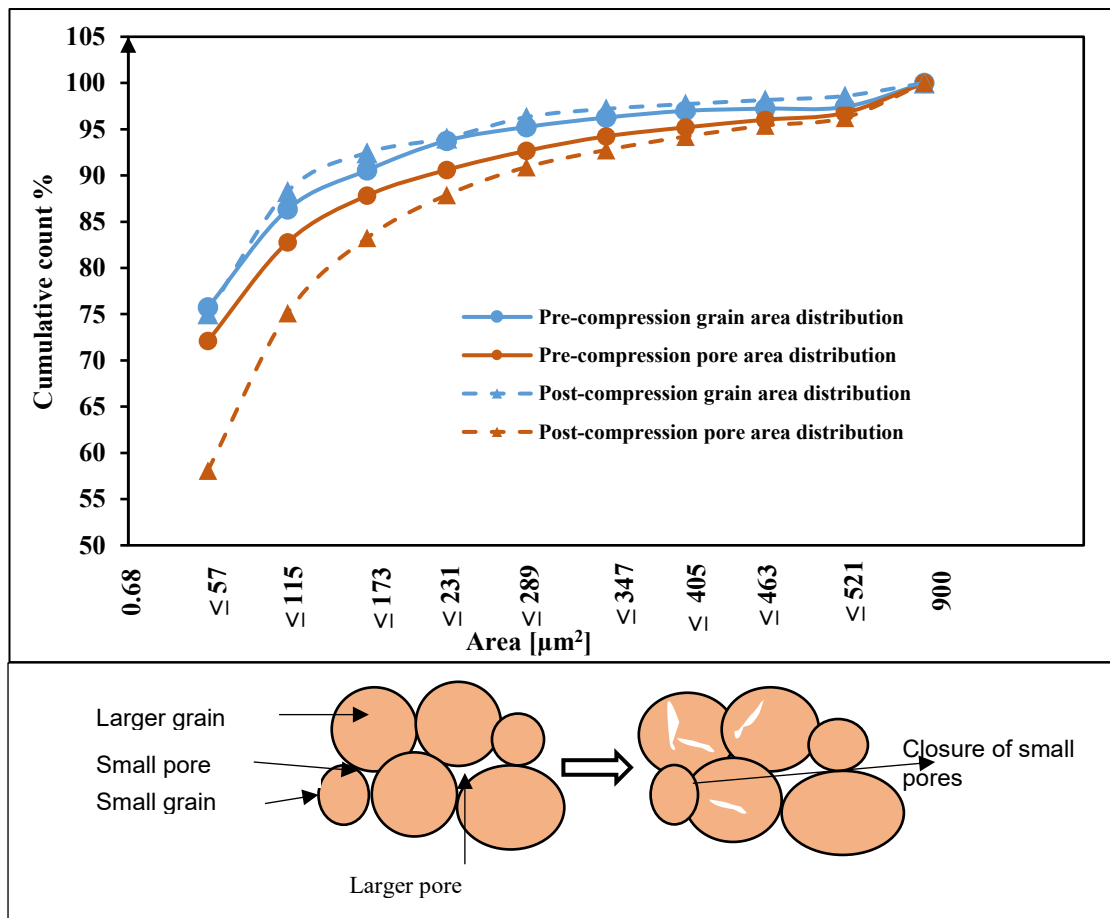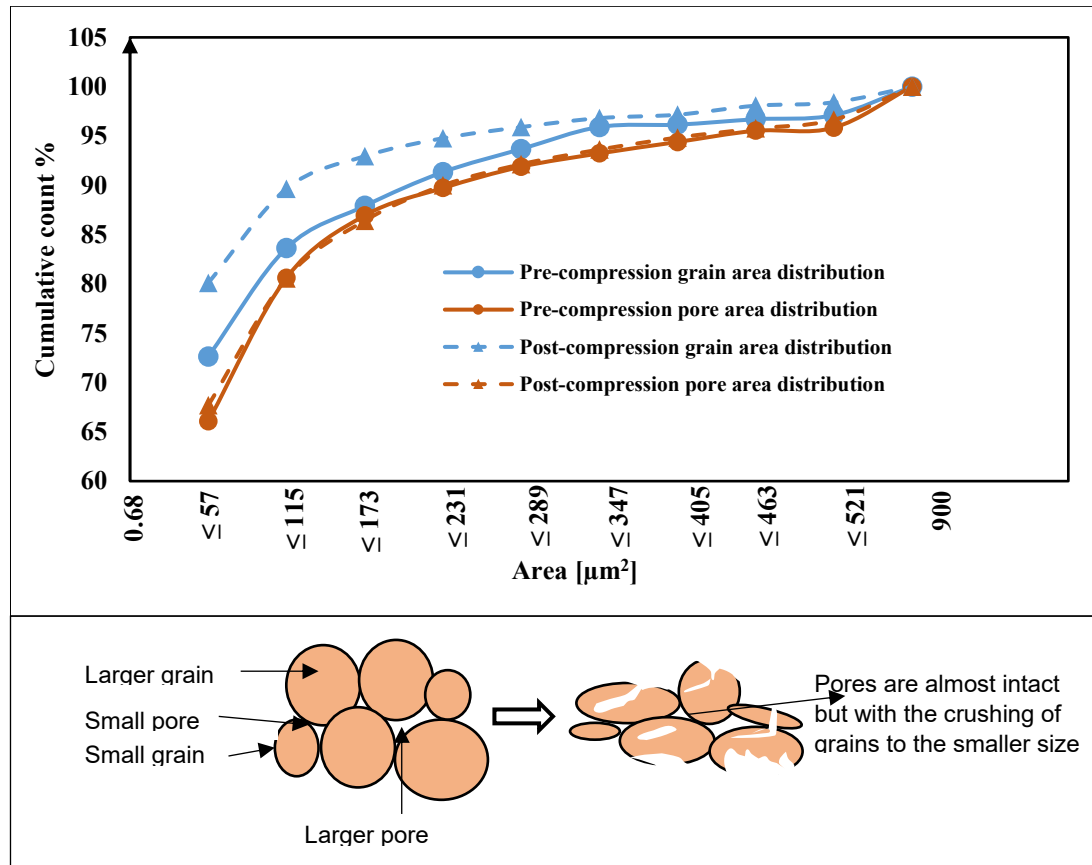
Figure 62: Cumulative percentage contribution of the different sizes to the total pore and grain for the br saturated sample before and after compression with an illustration of the changes in pore and grains after compression.

From Figure 62, there was a movement of both the grain and pore distribution curves downward after compression. This indicates that there is a decrease in the percentage of grains in each size class, and is attributable to the shear enhanced compaction through the agglomeration of small grains to create larger grains. There is the closure of some of the pores (compaction) after compression with creation of new micro-pores. Such increase in the size of grains have been called static grain growth, and it is a simple transformation in which the grain sizes increase depending on pore fluid among other factors. A similar agglomeration of smaller nano-sized grains to form bigger sizes due to charge clustering has been reported by Rawat et al. (2008), and that the agglomeration increased with temperature.
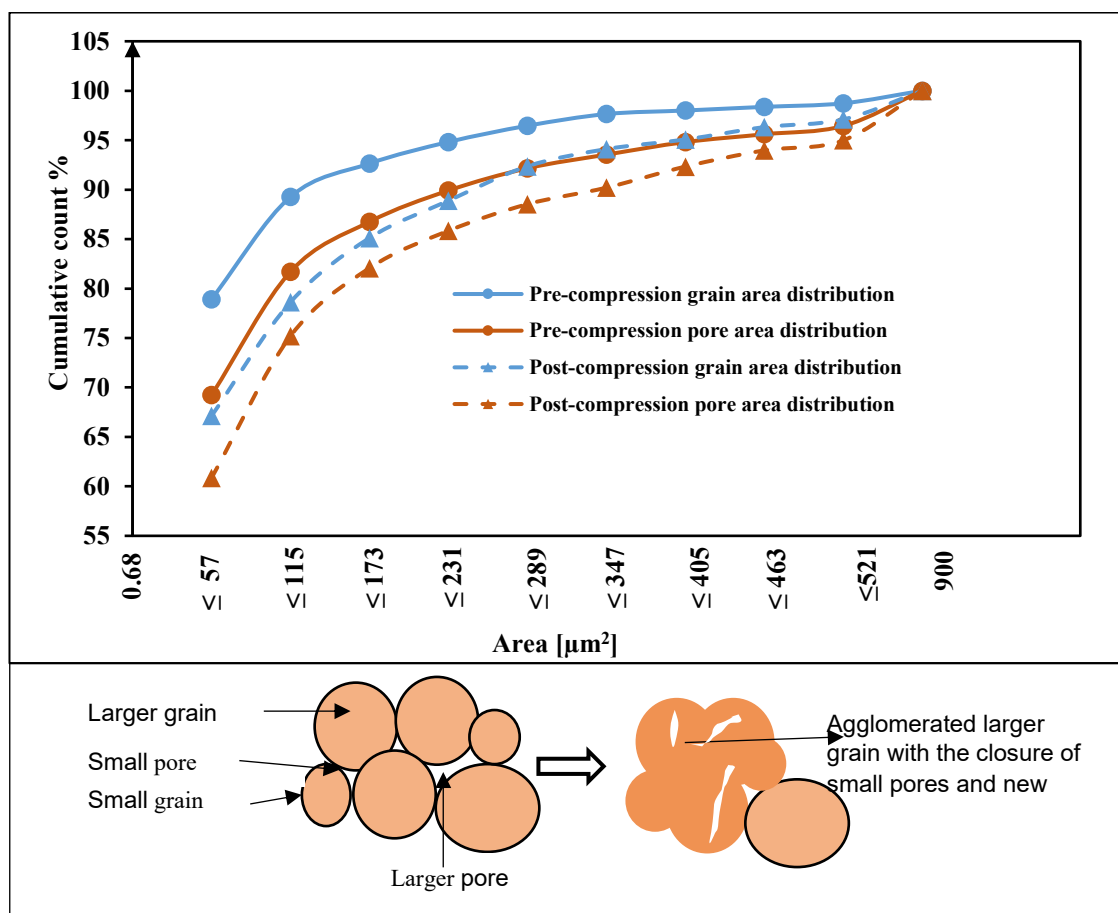
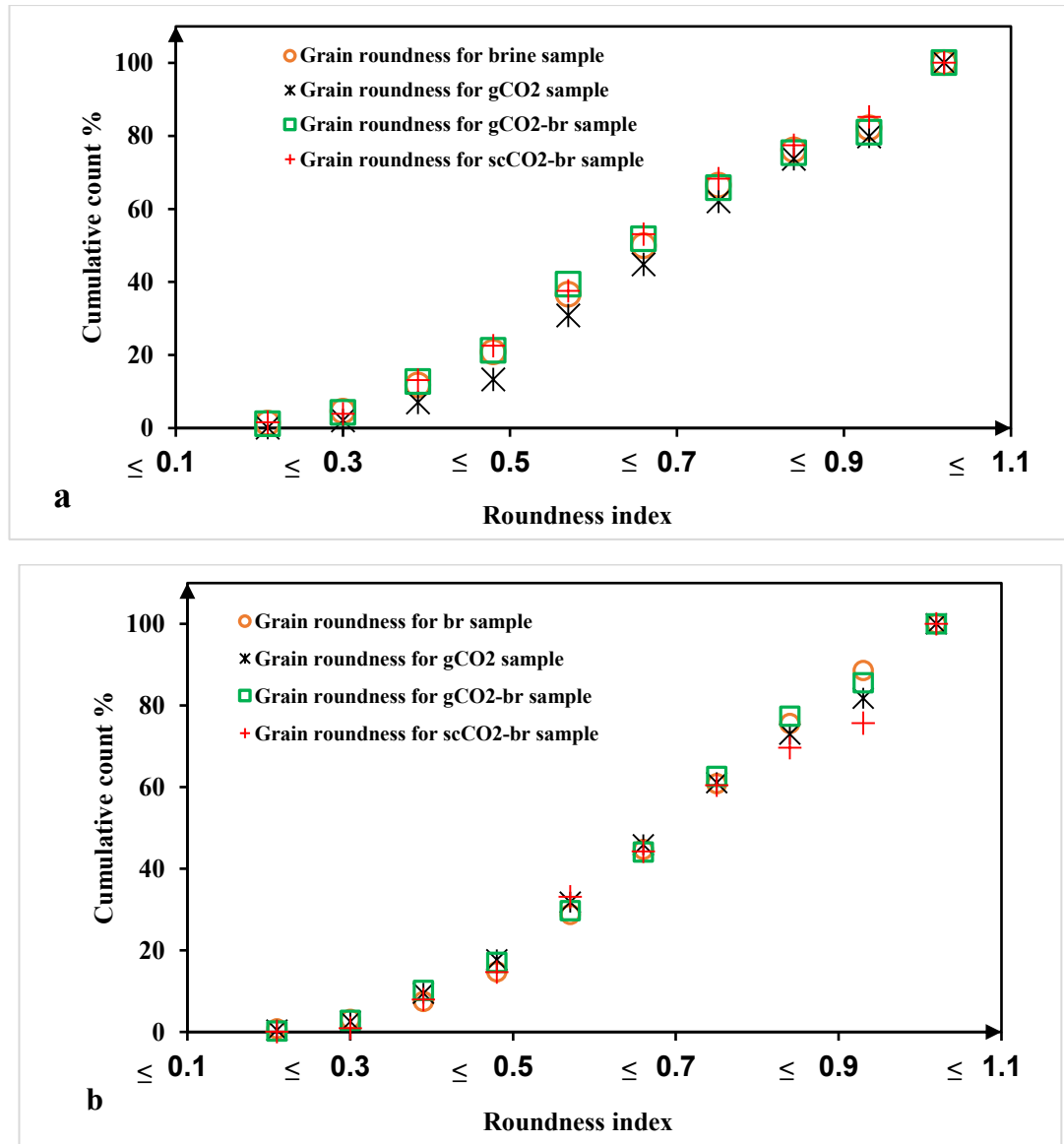Figure 63: Cumulative percentage contribution of the different sizes to the total pore and grain for the gCO_2 saturated sample before and after compression with an illustration of changes in the pore and grains after compression.

From Figure 63, there was a downward movement of the grain and pore curves after compression. This means that there is a decrease in the percentage of grains in each size class as well as an obliteration of some pores. This is similar to the behaviour exhibited by the brine saturated sample except that in the gCO_2 sample, the percentage of the pore and grains affected is almost doubled.

Figure 64: Cumulative percentage contribution of the different sizes to the total pore and grain for the gCO_2-br saturated sample before and after compression with an illustration of changes in the pore and grains after compression.

From Figure 64, there was no significant change in the movement of the grain curve after compression, but there was a downward movement of the pore distribution curve. The movement of the pore curves indicates an obliteration of some pores. The mechanism for closure of pore has been shown in Peter et al. (2020), where their CT

images of the gCO$_2$-br sample showed the greatest quantitative change in pore area compared to other phaseCO$_2$-brine samples.

Figure 65: Cumulative percentage contribution of the different sizes to the total pore and grain for the scCO$_2$-br saturated sample before and after compression with an illustration of the changes in pore and grains after compression.

From Figure 65, there was a movement of the grain curve upwards after compression. This upward movement indicates an increase in the percentage of the grains in each size class. This is attributed to grain crushing/fragmentation resulting in smaller grains with new micro-cracks. This suggests that scCO$_2$-br reduces the intragranular strength as have been previously reported by (He et al., 2016; Liteanu et al, 2013). The bulk modulus of the scCO$_2$ saturated sample (Table 31) was also seen to be the lowest compared to the others. On the other hand, the pore distribution curve of the scCO$_2$-br sample changed only slightly after compression. This indicates that the change in the pore distribution is a cumulative effect of precipitation of fines and compression. Depending on the surrounding minerals and the pore size, some pores were affected

by the precipitation of fines while others were closed up due to the impact of compression.

8.9   Roundness and solidity of grains and pores

The cumulative percentage for each of the class of roundness and solidity for grains, before and after compression is shown in Figures 66a–d for all the samples.

a

b
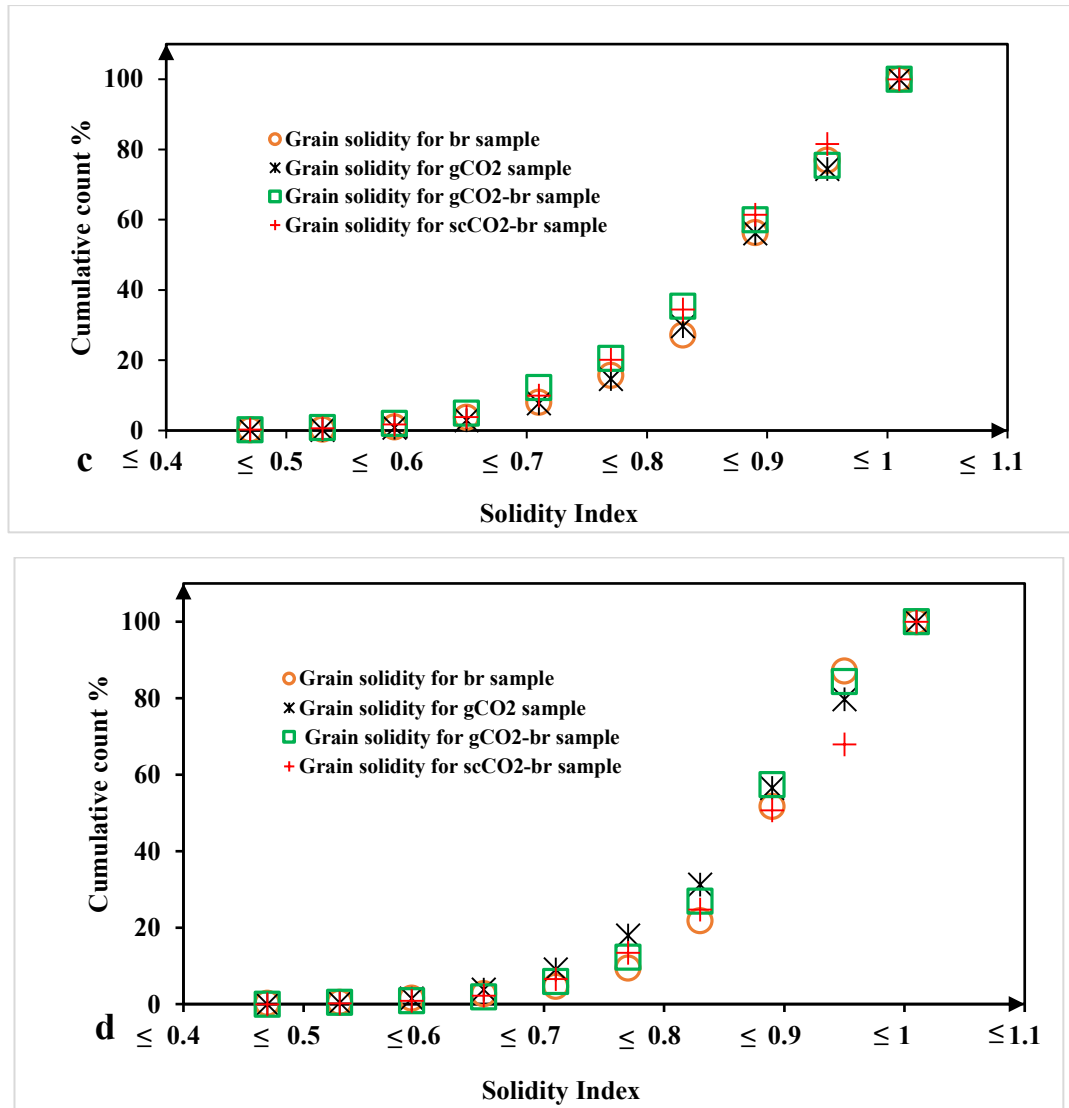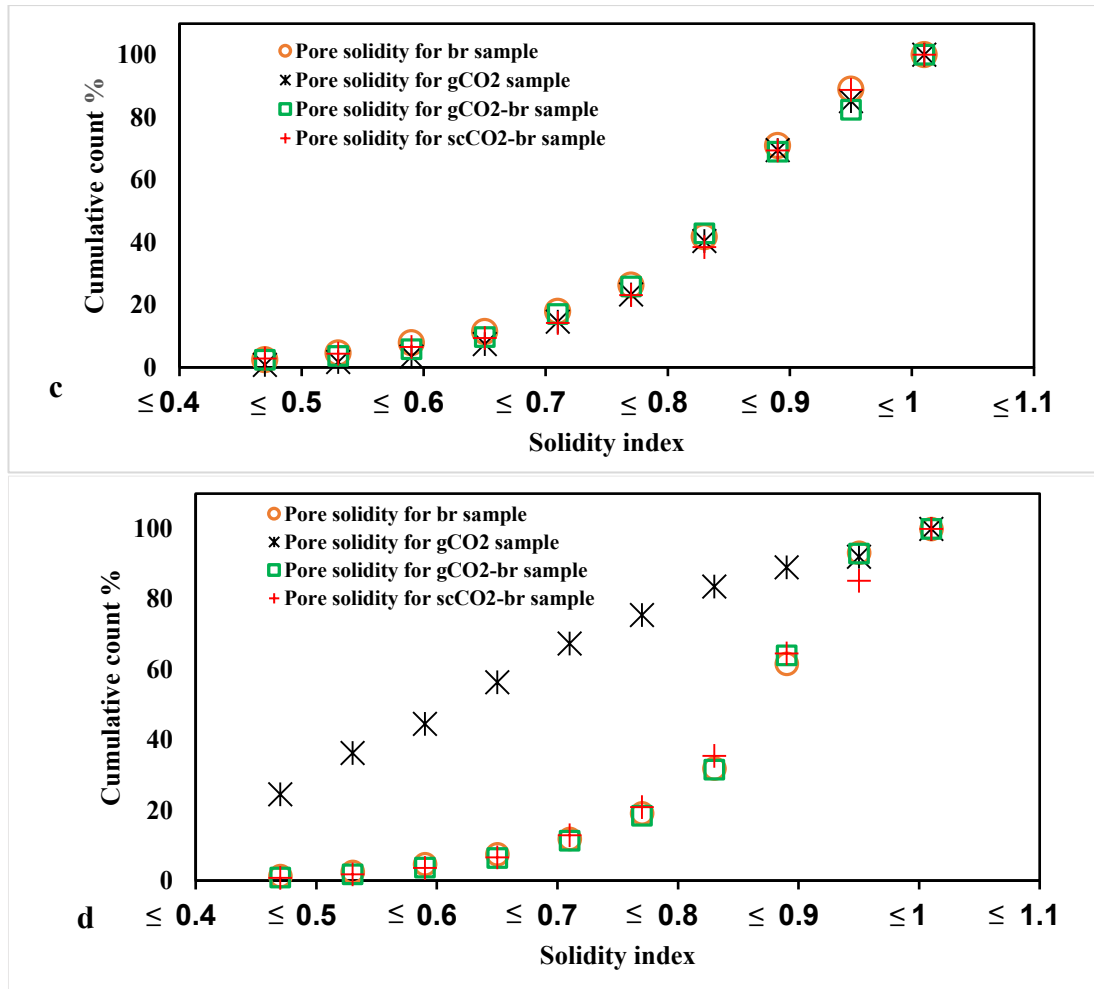
Figure 66: Cumulative percentage distribution for (a). Roundness distribution of grains for all the samples before compression; (b). Roundness distribution of grains for all the samples after compression; (c). Solidity distribution of grains for all the samples before compression. (d). Solidity distribution of grains for all the samples after compression.

The distribution of grain roundness before compression (Figure 66a) shows a slight variation in the different samples. The difference in roundness in the different samples is due to the action of the respective phaseCO_2-brine on the grain's micro-fabric. The distribution of grain roundness after compression (Figure 66b) for all the samples show the overriding role of stress in the rounding of the grains. Upon compression, the distribution of the roundness for all the samples became similar irrespective of the state of the sample. Generally, as seen from Appendix 6a, there is an increase in the

percentage of the rounded grains after compression in the samples. For instance, in the brine sample (Appendix 6a), 10%, 6% and 18% of the grains have a roundness index corresponding to the last three roundness classes before compression compared to the 15%, 13% and 11% after compression.

Figure 66c shows the solidity of the grain surfaces before compression. The distributions of solidity in the different samples are slightly different. The difference in the distribution of solidity shows the role of the different phaseCO_2-brine-induced stress corrosion in smoothening the micro-fabric of grains. Figure 66d shows the solidity of the grain after compression, while the distribution of poorly smooth grains was similar in all the samples, there was a slight variation in the percentage of highly smooth grains in the different samples. As seen from Appendix 6b, there is a general increase in the percentage of smooth grains. For example in the brine sample, about 27% of the total grain had solidity less than or equal to 0.83 before compression, and only about 22% of the total grain had solidity less than or equal to 0.83 after compression. This indicates that stress smoothens out irregularities in the surface of the grains and increases smoothness in grains. The impact of stress on the roundness and solidity of grains are seen by comparing the pre and post-compression solidity and roundness distribution curves for grains in Figures 66a-d.

a

b
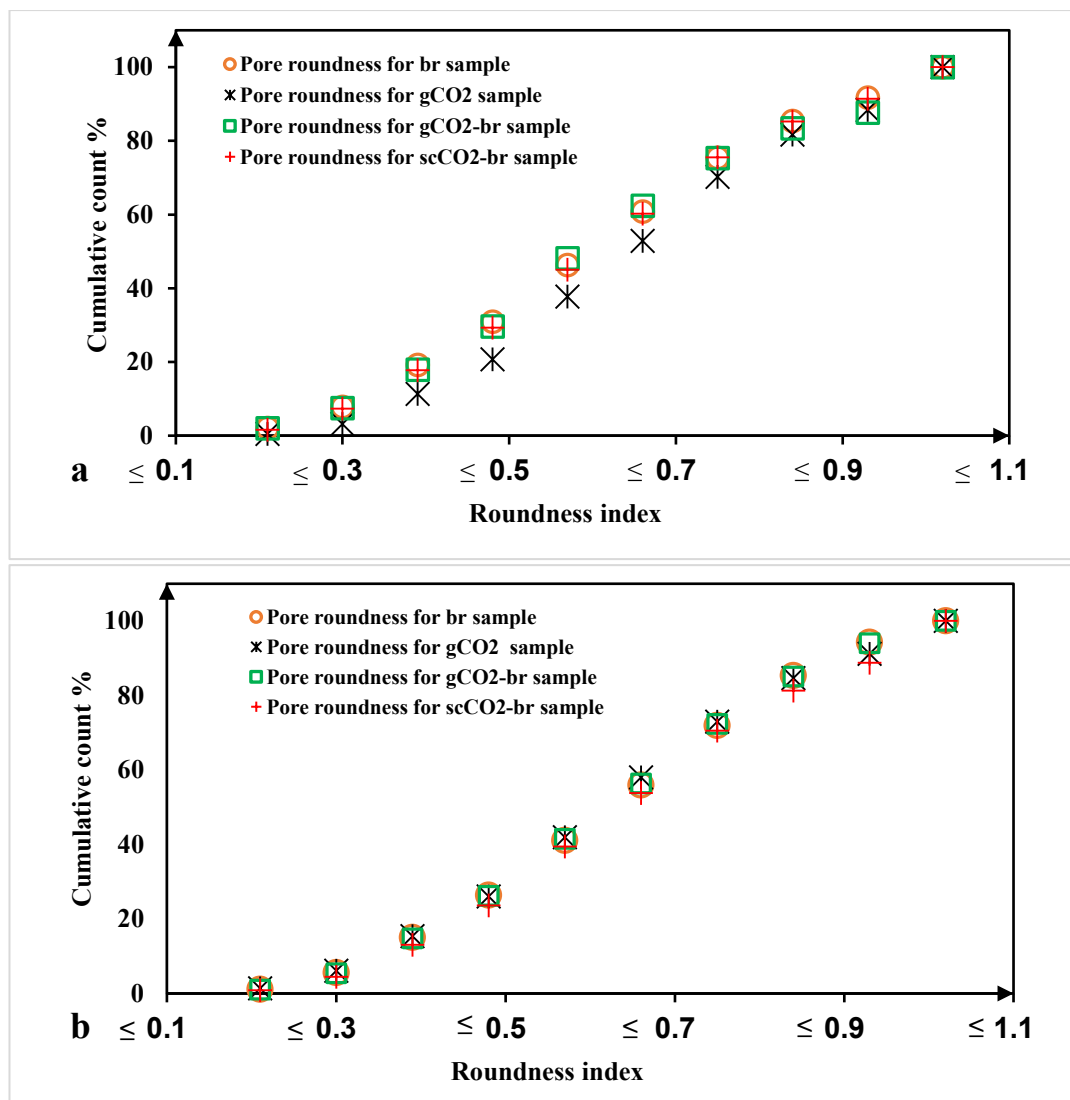
Figure 67: Cumulative count percentage distribution for (a). Roundness distribution of pores for all the samples before compression; (b). Roundness distribution of pores for all the samples after compression; (c). Solidity distribution of pores for all the samples before compression; (d). Solidity distribution of pores for all the samples after compression.

Figures 67a–d show the cumulative percentage for each of the class of roundness and solidity of pores before and after compression for all the samples. Before compression (Figure 67a), the distribution of the pore roundness for all the samples are similar, except in the gCO_2 sample where the percentage count of pores with roundness index between 0.39 and 0.66 was slightly different. After compression (Figure 67b), there was similarity in the distribution of pore roundness irrespective of the nature of the saturating fluid. The distribution of the solidity of pores (Figures 67c) was similar for all the samples before compression. After compression, there was also similarity in the distribution of the solidity of pores except in the gCO_2 sample where there was a

173

significantly lower percent count of highly smooth pores. This is due to the absence of brine, and this suggests that brine facilitates the smoothening of pores. The presence of the different phaseCO_2-brine is thought to alter the rock's micro-fabric subtly. The impact of stresses on the solidity and roundness of pores is seen by comparing the pre and post-compression solidity distribution curves (Figure 67a-d) and Appendix 6c-d. In a related research, Berrezueta et al., (2015) quantified pore network in sandstones under CO_2 injection conditions using image analysis, and reported changes in the roughness, roundness of pore edges and pore aspect ratio. Changes in the fabric of porous rocks have implications for the bulk and transport properties of the rocks. Such implications as seen in this research are summarised in Table 31 and discussed in section 8.10.

8.10   Implication of change in micro-fabric and topology on rock properties and storage integrity.

Here, porosity measured from the 2D CT images of the different samples and the bulk modulus from Peter et al. (2020) as shown in Table 31 was integrated with the changes evaluated in this study, to assess the implication of the changes for bulk and transport properties. The bulk modulus of all the samples from Peter et al. (2020) was calculated using equation 8.

The absolute permeability of the samples was measured using the method proposed by Lenormand et al. (2010) and calculated from Darcy's law illustrating the relationship between the flowrate and differential pressure (Equations 2 and 3).

The tortuosity (τ) of a porous rock is a measure of the connectedness of pores and is defined as the ratio of the distance between two points along a streamline to the distance along a straight-line between those points. Tortuosity as shown in Table 31 was calculated from the Kozeny-Carman equation (equation 22) relating permeability to tortuosity, grain diameter and porosity (Lala, 2018).

$$k = \frac{\emptyset^3 \times d^2}{72(1-\emptyset)^2 \tau^2} \tag{22}$$

Where Ø is the average porosities calculated from the weight difference between the dry and wet core samples for each sample (Table 15), k is the permeability measured

for each sample (Table 31) and d is the diameter of the grain taken as 0.0223 cm (measured from image analysis).

Table 31: Porosity, Permeability, tortuosity and bulk modulus of all the samples measured before and after compression.

Sample ID	br	gCO_2-br	$scCO_2$-br	gCO_2
Porosity before compression (%)	29.3	27.4	26.3	31.0
Porosity after compression (%)	26.7	8.2	19.5	27.9
% change in porosity after compression	8.9	70.1	25.9	10
Permeability before compression (Darcy)	1.76	1.27	1.24	1.80
Permeability after compression (Darcy)	0.10	0.10	0.90	1.25
% Change in permeability after compression	94	92	27	31
Tortuosity before compression	12.72	9.82	10.66	12.86
Tortuosity after compression	3.03	2.75	9.09	10.72
% change in tortuosity after compression	76.2	72.0	16.6	14.7
K (MPa) from static fatigue test	1.1	0.9	0.8	0.9

The variation in the percent weight of silicon, carbon and oxygen in the CO_2-containing samples compared to the brine sample indicates the chemical action of stress corrosion on the rock minerals. The transport and geomechanic properties in Table 31 also varies according to samples. This indicates that stress corrosion leads to change in the transport and geomechanic properties of rocks.

From Table 31, the porosity of the brine sample before compression was 29.3%, the porosity of the gCO_2-br and $scCO_2$-br samples are lower. After compression, the porosity of the brine sample was 26.7%, the porosity of the gCO_2-br and $scCO_2$-br samples are lower. The fact that the porosity of all the samples that contains CO_2 and brine are lower than the porosity of the sample that contains brine demonstrates the effect of the different phaseCO_2-brine and stress on the porosity of the rocks. Hu et al., (2017) explained that the dissolution and precipitation of fines are the processes that could lead to a change in the porosity of fluid-saturated rock materials. Therefore, the reduction of porosity in the gCO_2-br and $scCO_2$-br samples is seen as a sum effect of clogging by the clay precipitates and compression. The $scCO_2$-br sample have the most of this clogging from the precipitates because it had the lowest porosity before

compression. This implies that a shallow saline reservoir that contains $scCO_2$ will have a higher change in porosity and permeability compared to gaseous phase CO_2.

Table 31 shows a reduction in the porosity of all the samples after compression. However, the reduction in porosity after compression is seen to vary with samples. For example, the gCO_2-br sample had the greatest reduction in porosity (70.1%) while the lowest reduction is seen in the brine saturated sample (8.9%). This shows that the effect of the pore fluid on the porosity of the rock varies according to the phaseCO_2-brine. This effect is seen to be higher when CO_2 and brine are combined but highest in gCO_2-br sample. This implies that a deep saline reservoir that contains gCO_2 will have a higher change in porosity and permeability compared to supercritical phase CO_2.

The changes in topology and micro-fabric affected the permeability of the rocks. Permeability of all the samples was seen to increase after saturation compared to the permeability of the original dry sample. Agreeably, Li et al., (2019) had observed that micro-cracks created by fluid-rock interaction alters the permeability of rocks. Also, Hu et al., (2017) had reported that stress reduces the permeability by pore compaction, here, the permeability of the samples are seen to reduce due to stress. However, the different phaseCO_2-brine reaction with the rock also affected the reduction in permeability by the precipitation of fines that clogs the pores.

It is known that permeability is dependent on the porosity, grain size, and pore tortuosity. From Table 31, the brine sample showed the highest reduction in the permeability (94%) despite having the lowest reduction in the porosity (8.9%). This, therefore, suggests that the tortuosity of the pores (controlled by shape, solidity, and roundness of the pore) had a greater effect on the permeability than the porosity. For instance, in the case of the brine saturated sample, the change in shape, solidity and roundness of the pores are thought to be such that compression caused the most reduction in the tortuosity of the pores and explains the high reduction in the permeability compared to other samples. Furthermore, a comparison of alterations in the porosity and permeability of the different rock samples shows how the shape, solidity and roundness of pores control permeability, and how the changes in these parameters are sensitive to the phaseCO_2-brine. This exemplifies the implication of

different phaseCO$_2$-brine on the storage integrity and transport properties of the reservoir rocks.

Foroutan et al. (2020) explained that factors that affect changes in properties of rock are the mineralogy, nature of the fluid and grain size. The scale of the change in permeability is affected by the grain size amongst others, while the direction of change in permeability (whether reduction or increment) is affected by the mineralogy and nature of the fluid. In this research, change in properties is a function of phaseCO$_2$-brine and mineralogy. So, if a rock with a different permeability is used, there will be a change in scale but the direction of change of properties remains the same.

8.11   Finite element analysis of the distribution of strain using the digital rock

Due to the challenges explained earlier, only FE analysis of the distribution of strain on the digital rock was done using ABAQUS. Images of the scanned sample and the processed REV is shown in Figures 68-71. To allow for a successful simulation, only a tenth of the REV volume of the original rock model was used. An example of the model and the mesh elements used for the FEA is shown in Figure 72. Tetrahedral element was used. Meshing was precise and optimized, and adaptive mesh refinement was used to build the mesh in areas with tiny features, while other elements have the cell size of 135.415, facet distance of 6.771 and facet size of 135.415 in Avizo software. The number of elements in the model range from 94848-131780. On a machine with 8 cores CPU and 32G RAM, it takes approximately 30 minutes to mesh the model. The model computes in approximately 16 minutes. The simulation is aimed at qualitatively visualizing the distribution of strain under in-situ confining pressure conditions. The Z- boundary was fixed. The density used in the simulation was the measured density of the different samples, the bulk modulus was that evaluated from the different triaxial test data, and pressure load was used to represent the in-situ confining pressure as used in the triaxial compression test. The properties used are summarized in Table 32.
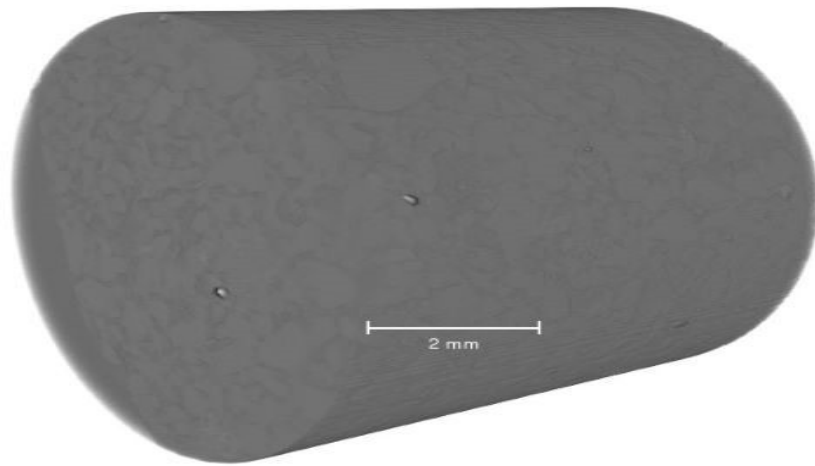
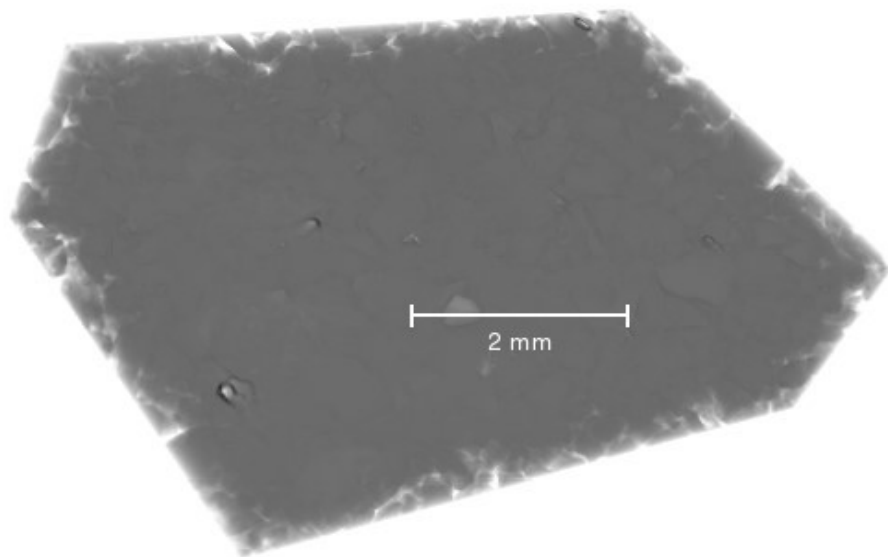Figure 68: Sample of raw CT image of therock

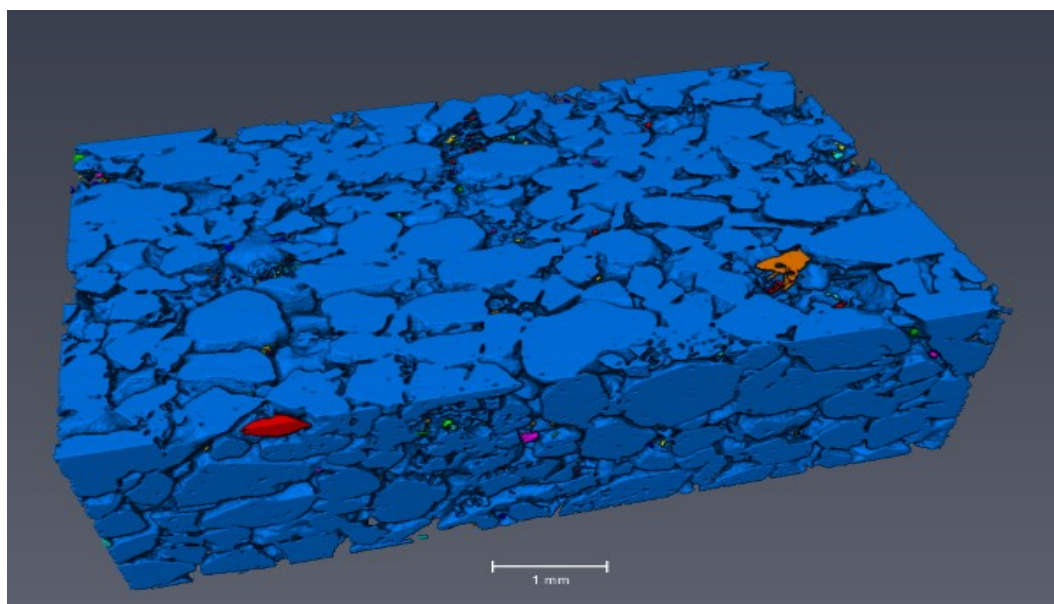Figure 69: Sample of REV size of raw CT image of the rock.

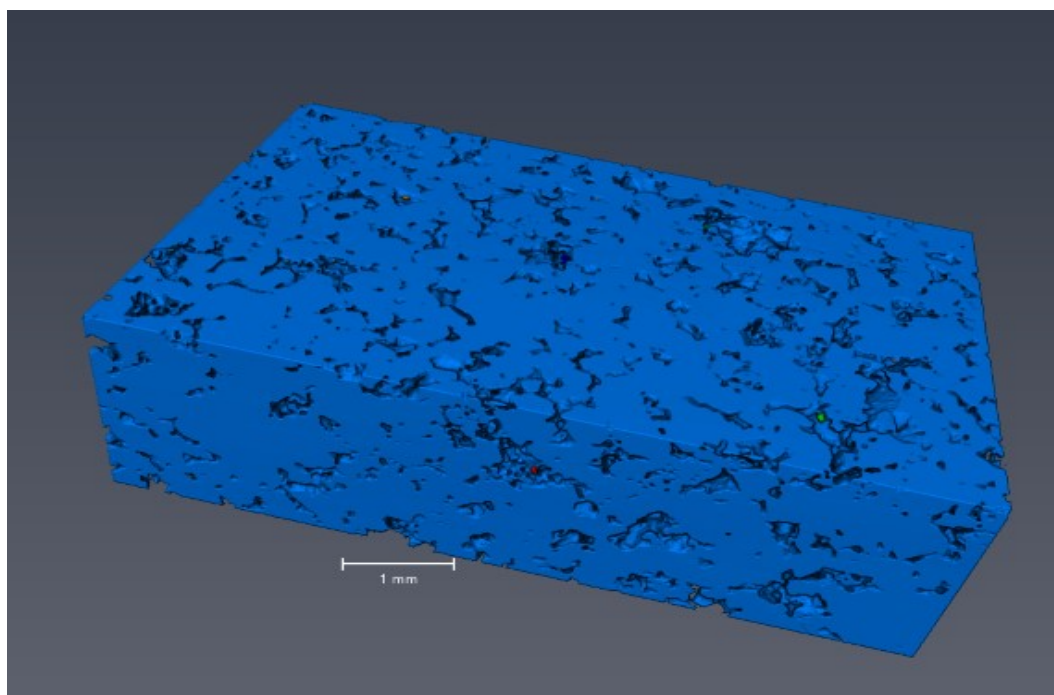Figure 70: Pre-compression digital rock model for the dry sample

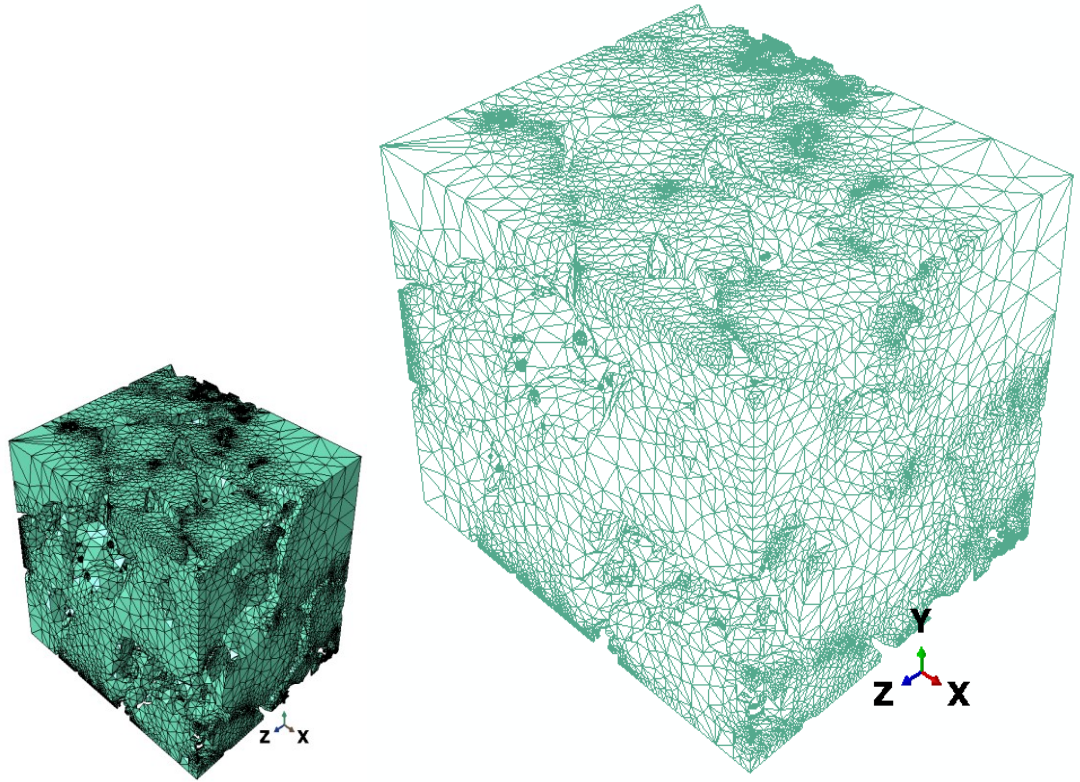Figure 71: Post-compression digital rock model for the dry sample

Figure 72: 3D model showing the mesh elements

Table 32: Material properties used for the 3D numerical simulation

Property	Dry	Brine	gCO$_2$-br	ScCO$_2$-br	gCO$_2$
Density (Kg/m^3)	1790	1780	1800	1780	1790
Confining pressure (MPa)	16	16	16	16	16
Modulus (GPa)	1.2164	1.0500	0.9184	0.8236	0.9195
Poisson ratio	0.23	0.23	0.23	0.23	0.23

a. Dry sample

The distribution of strain in the dry rock when subjected to in-situ stress conditions is shown in Figure 73. It is seen that the sample was straining differently at different parts. The whole sample is seen to be undergoing straining. However, grains at the surface in some portions are the most stressed. This is expected, given that the intergranular strength of the grains at the surface needs to be broken before stress is transferred to inner grains. This is the mechanism for creep/fatigue failure in rocks. The strain observed compliments the bulk modulus evaluated from the triaxial test result.
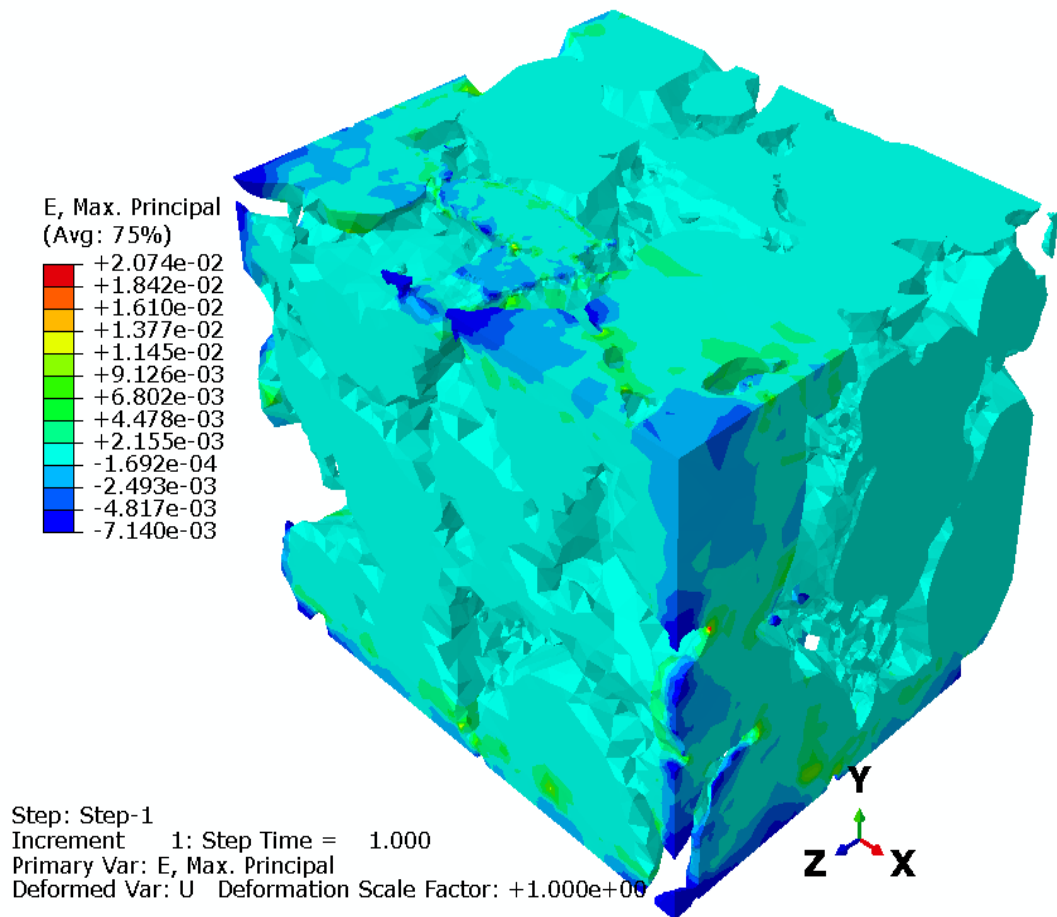
Figure 73: Distribution of strain across the dry sample

b. Brine saturated sample

Figures 74 shows the distribution of strain across the brine saturated sample. The distribution of strain in the rock is seen to be different from the distribution in the dry sample. This is the effect of the brine. As seen in Figure 74, there was a differential distribution of strain and higher strain is concentrated in a region.
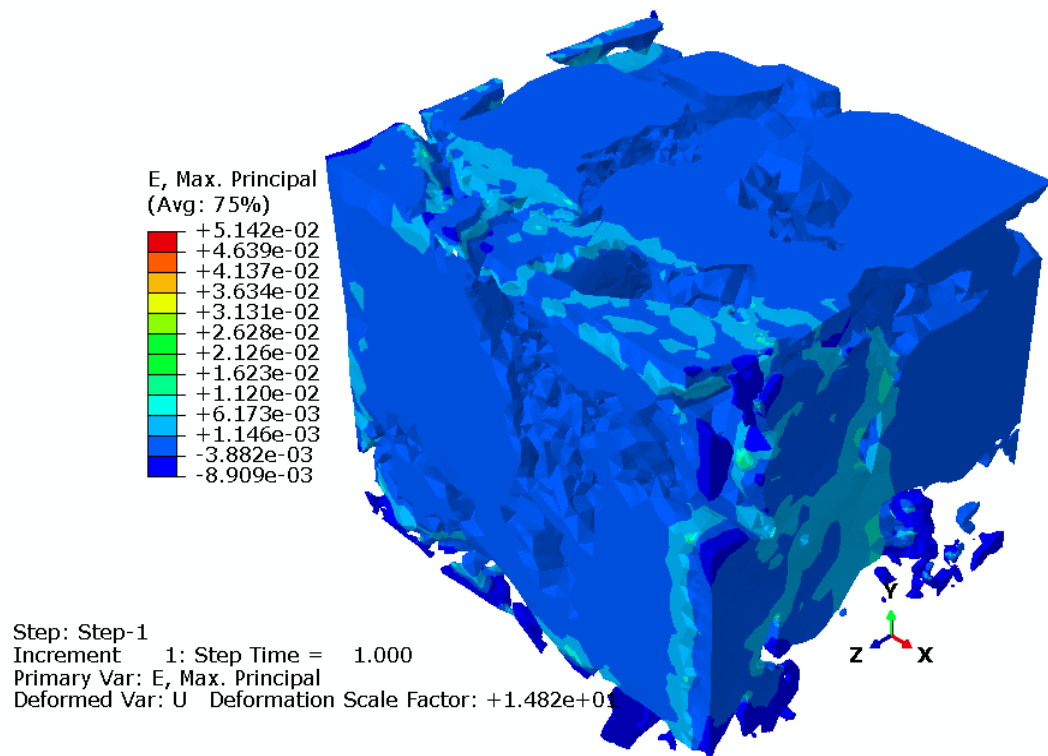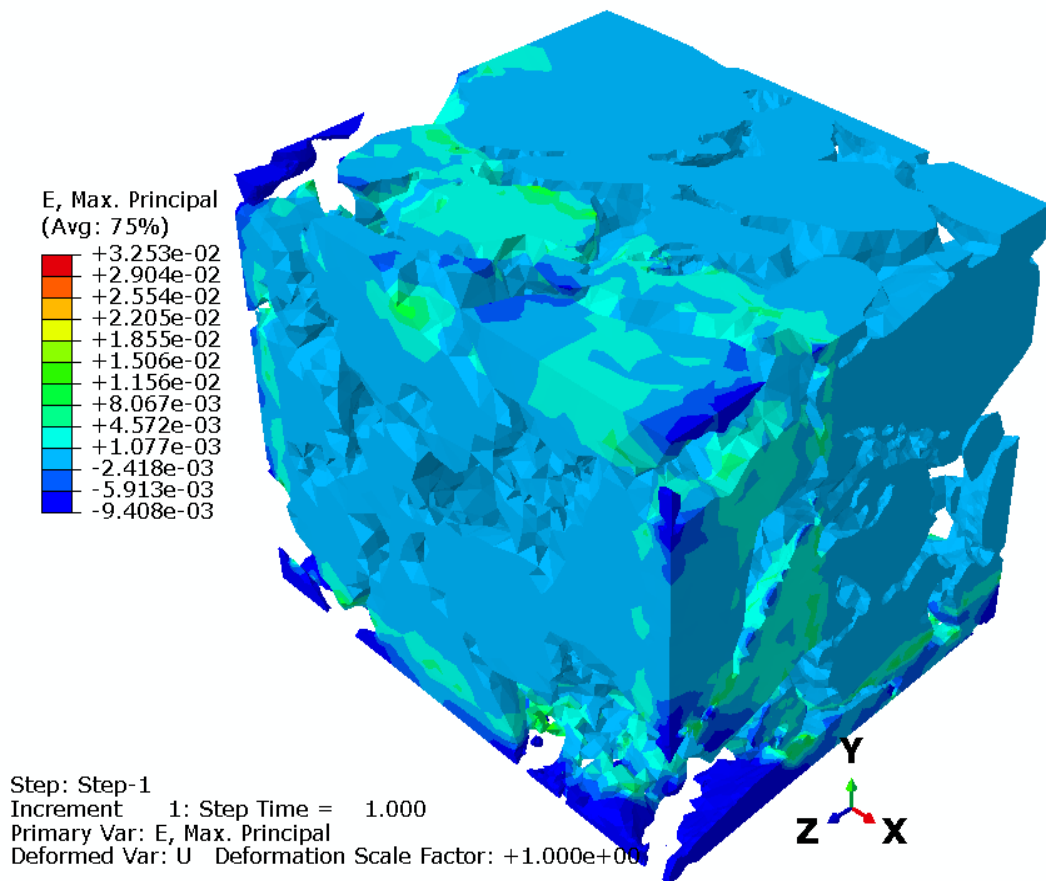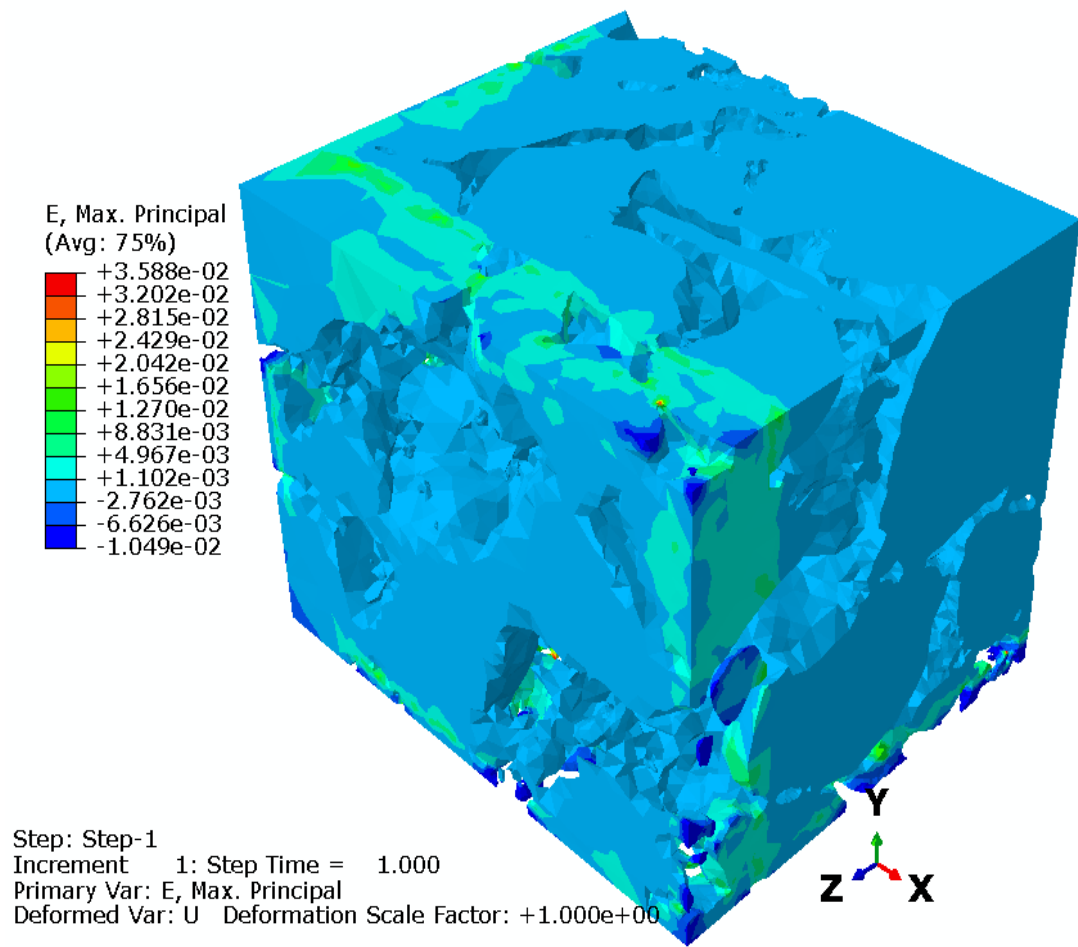
Figure 74: Distribution of strain across the brine sample

c. gCO$_2$-brine saturated sample

Figures 75 shows the distribution of strain across the gCO$_2$-br saturated sample. The strain was higher on some grains especially those grains adjoining large pores. It is seen that the strain distribution is similar to that of the brine sample, but different in scale of magnitude. This is due to the effect of the gCO$_2$-br on the intergranular strength of the grains.

Figure 75: Distribution of strain across the gCO$_2$-br sample.

d. scCO$_2$-brine saturated sample

Figures 76 shows the distribution of strain across the scCO$_2$-br saturated sample. Similarly, the strain was higher on the surface and in a region. These are regions where the minerals reacted more to the scCO$_2$-br. There was a differential distribution of strain across the entire sample though the entire sample was strained. This sample appears to be the most strained sample and it agrees with the fact that the scCO$_2$-br sample had the highest change in the bulk modulus from the triaxial compression test result.

183

Figure 76: Distribution of strain across the scCO$_2$-br sample

e. gCO$_2$ saturated sample

Figures 77 shows the distribution strain across the gCO$_2$ saturated sample. It is similar to the distribution of strain in the dry sample except for the scale/magnitude.
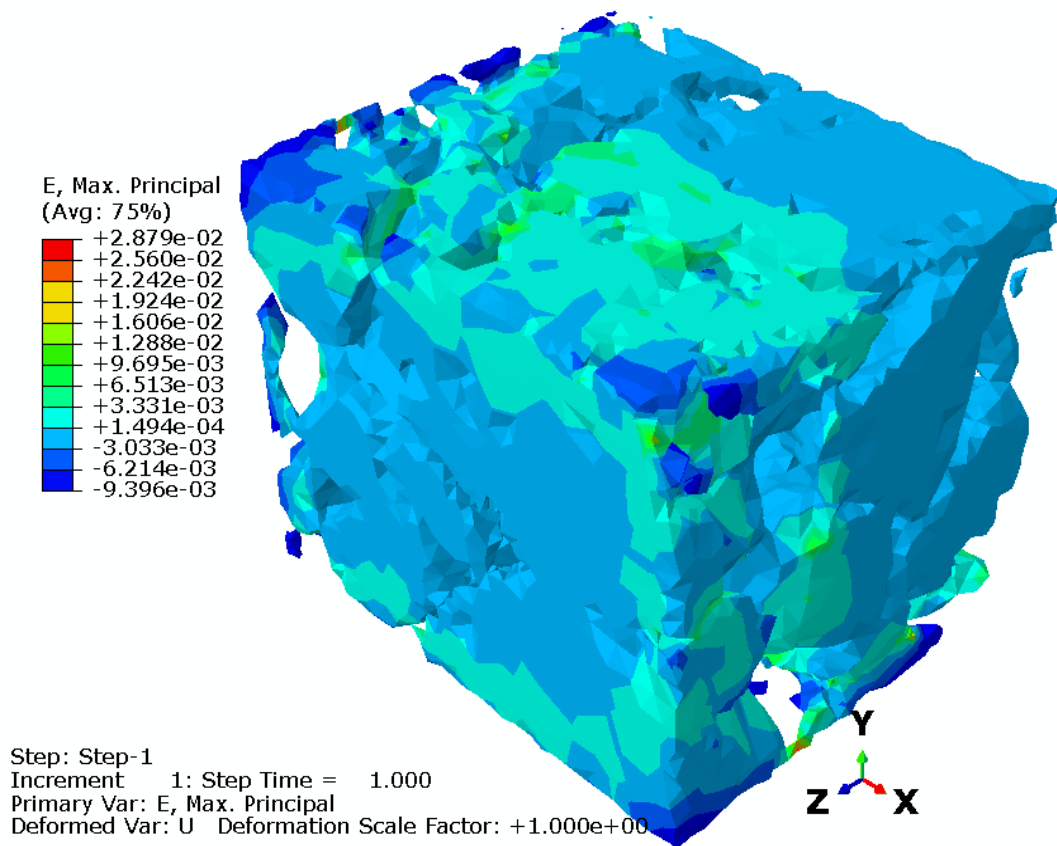
Figure 77: Distribution of strain across the gCO_2 sample

8.12 Summary

Microscopic image analysis has been applied to provide evidence of changes in themicro-fabric, the topology of minerals and the elemental composition in saline rocks resulting from the different phaseCO_2-br that can exist in a saline CO_2 storage reservoir. This research shows that the change in the micro-fabrics and the topology of saline rocks is linked to the composition of the rock and change in the micro-fabric and topology through grain crushing, grain agglomeration, and pore compaction is caused by stress, but such change is affected by the nature of the pore fluid. After saturation, the topology of mineral scale features is seen to be most altered in the scCO_2-br sample while the topology of mineral scale features in the gCO_2-br saturated samples is the most altered after compression. Change in elemental composition in the rock minerals in a CO_2-brine-rock system depends on the reactivity of the minerals with CO_2 and/or brine. The presence of brine accelerates such changes.

It is seen that the distribution of strain obtained from the image-based FE analysis varies in the different samples. This clearly shows that the different phaseCO_2-brine affect rock's geomechanical deformation behavior differently. This compliments the variations in the bulk modulus and compressibility of the different samples obtained from the triaxial compression experiments. Generally, strain was higher at the surfaces of the rocks. This agrees with the shielding concept illustrated in Figure 32. However, saturation with brine and CO_2 caused higher strains which are concentrated in preferred regions. The preferred regions are thought to be regions where the saturating phaseCO_2-brine was more reactive to the minerals. More work is needed to fully exploit the benefit of image-based pore scale modelling in CO_2 geosequestration, in which case, fully coupled FSI modelling is a great option.

It is recommended that good computing resources, and software with good multiphysic capability be available for a FSI simulation. Also, the level of details to be preserved in the model geometry should be determined before the digital rock is created and the simulation. Minute grains and pores cause mesh inversion errors, therefore, a threshold of pore size and grains should be filtered out. However, the impact of the filtered pore and grains on the result should be understood.

Chapter 9: Conclusion and recommendations for future work

9.1   Conclusion

This thesis presents the effects of the different phaseCO$_2$-brine on the properties of reservoir rocks using an experimental and image-based approach. Samples were saturated with the different phaseCO$_2$-brine, then subjected to reservoir conditions in a triaxial compression test. The REV/REA for the rock samples have been determined from processed digital images, and the rock properties were evaluated using the digital rock physics and rock image analysis techniques.

With the thermodynamics, phase behavior, solubility of CO$_2$ in brine and the variable P-T conditions of the reservoir, there will be undissolved CO$_2$ in a CO$_2$ storage reservoir alongside the brine for a long time, there is a potential for a phase evolution of the undissolved CO$_2$. Therefore, four different samples representing different reservoir's phaseCO$_2$-brine states were investigated in this research namely, brine (br) saturated sample, gaseous CO$_2$ (gCO$_2$) saturated sample, gaseous CO$_2$-brine (gCO$_2$-br) saturated sample and supercritical CO$_2$-brine (scCO$_2$-br) saturated sample. A sample was also tested in dry conditions to represent the property of the dry natural reservoir rock.

This research has evaluated the effect of different phaseCO$_2$-brine on the deformation rate and deformation behavior, bulk modulus, compressibility and strength, as well as the pore geometry, mineral topology, porosity and permeability. Changes in the pore geometry and porosity of the rocks in CO$_2$ storage conditions was evaluated using the digital rock physics and rock image analysis techniques. Microscopic rock image analysis has been applied to provide evidence of changes in the micro-fabric, the topology of minerals and elemental composition in saline rocks, highlighting their implication for storage and properties of the rock. The result of this work can be applied to predicting the effect the different possible phases of CO$_2$ in giant saline CO$_2$ storage fields such as Sleipner, In Salah, etc. will have on the deformation and geomechanic indices, and other properties of the reservoir rocks.

Some original contributions to knowledge from this research include:

1. **Fatigue rate for the different samples**

   At low and high stresses, the strain rate for the CO_2 bearing samples was higher compared to the brine saturated sample. The magnitude of the change in primary strain rate, when compared to the brine saturated sample, depends on the state of the sample, with the gCO_2-br having the highest change (93% and 39 %) for low and higher stress respectively. The primary fatigue rate is affected by the gaseous CO_2 phase (an increase of up to 45 %). The strain rate of all the CO_2 flooded rocks was affected more at lower stress conditions or initial fatigue stages compared to higher stress conditions. The averaged secondary strain rate of all the CO_2 bearing samples increased compared to the brine saturated sample and the highest increase was in the $scCO_2$-br (22 %) followed by gCO_2-br (20 %). The change in the gCO_2 saturated sample is negligible. These observations mean that while the primary strain rate of a CO_2 reservoir will be most affected if the reservoir contains gCO_2-br, the secondary strain rate will be the most impacted if the reservoir contains $scCO_2$-br. This implies that while a gCO_2-br reservoir will experience higher, immediate strain, a $scCO_2$-br reservoir would experience higher, long term strain.

2. **Fatigue behavior**

   Primary fatigue was also seen to be capable of being shielded by the rock's effective strength if the stress condition is low or not applied for a long enough time, especially if the material has a wide range of micro-pores and crack sizes. This mechanism of fatigue explains why fatigue in the porous rock is continuous under constant stress and why a ductile deforming rock begins to fatigue when the stress is increased. The shielding effect was seen to be significantly affected by CO_2 depending on the phase of the CO_2 with the brine.

3. **Bulk modulus and compressibility of the samples**

   All the CO_2 containing samples showed reduced bulk modulus and an increased compressibility compared to the brine saturated sample. From the static fatigue test, the highest change (reduction) in the bulk modulus and

compressibility was seen in scCO$_2$-br (22 and 27 %) followed by gCO$_2$-br (13 and 14 %) and gCO$_2$ (12% and 14%) respectively. Also, from the multiple failure test, the highest change in the bulk modulus and compressibility was seen in the scCO$_2$-br with a 22.2% reduction in the bulk modulus and 28.6% increase in the compressibility. For gCO$_2$-br and gCO$_2$ samples, there was 11.1% reduction in the bulk modulus and 14.5% increase in the compressibility. This means that CO$_2$ affects these geomechanical properties of rocks, but the effect is more significant if CO$_2$ and brine are combined especially scCO$_2$. Hence, the phase of CO$_2$ in a saline reservoir matters.

4. **Strength and geomechanical indices**

Different phaseCO$_2$-brine affects the shear strength differently. The critical shear stress for the gCO$_2$ saturated sample was approximately 49 MPa while the critical shear stress for the br, gCO$_2$-br and scCO$_2$-br samples are 42, 41 and 38 MPa respectively. This shows the effect of the different phaseCO$_2$-brine on the shear strength during CO$_2$ storage, and it implies that at high stress (great depth), a reservoir with scCO$_2$-br will experience the greatest reduction in shear strength compared to the brine saturated sample. Samples containing both CO$_2$ and brine showed a lowered stiffness compared to brine's. Pore stress corrosion due to the br, scCO$_2$-br and gCO$_2$-br caused the samples to not increase stiffness even with increase in the confining stress. The failure stress is seen to increase initially by stress hardening, and later by shear enhanced-compaction hardening. Shear enhanced-compaction causes ductility in rocks at higher confining stresses.

5. **Permeability**

The saturation of rocks with the different phaseCO$_2$-brine increases the permeability of the rocks. The increase was highest in the gCO$_2$ sample because of the absence of brine that was found to combine with the CO$_2$ to facilitate the precipitation of fines that clog the pores. The permeability of all the samples reduced after compression. The gCO$_2$-br sample changed the most with 92%. Furthermore, the change in the permeability of the gCO$_2$, gCO$_2$-br

and scCO$_2$-br samples was influenced by the alteration of the geometry of the pores and consequently, the tortuosity/connectedness, depending on the phaseCO$_2$-br state of the sample.

6. Porosity and pore geometry properties

There was a lowered porosity in all the phaseCO$_2$-brine saturated samples after saturation and after compression, but the reduction in the porosity is also influenced by the CO$_2$ phases. The highest reduction in porosity after compression occurred in the gCO$_2$-br saturated rock (~15 %). The porosity of the samples after saturation are seen to vary from 26.3%-31%, gCO$_2$-br and scCO$_2$-br showed the lowest porosity. This suggests that there was precipitation of fines that clogged the pores and reduced the porosity in the scCO$_2$-br and gCO$_2$-br samples. The precipitation of fines as a result of CO$_2$-brine-rock interaction leads to a reduction in porosity. There was no significant change in the flatness of the pore surfaces before and after compression except for scCO$_2$-br saturated sample where the pore surface became significantly less flat (wavy) after compression. The presence of CO$_2$ causes more pores to become rod-like shaped especially in the scCO$_2$-br.

7. Micro-fabric, topology and composition of minerals

Compression causes change in the micro-fabric and topology through grain crushing, grain agglomeration, and pore compaction, but such change is affected by the nature of the pore fluid and by the composition of the rock. For all samples, the roundness and smoothness of grains as well as the smoothness of the pores increased after compression while the roundness of the pores decreased.

8. Elemental composition of rock minerals

Change in the elemental composition in rock minerals in the CO$_2$-brine-rock system depends on the reactivity of the minerals with CO$_2$ and/or brine. The presence of brine accelerates such changes. Carbon, Oxygen and Silicon can be used as index elements for the chemical changes in a CO$_2$-brine system.

9.2   Recommendation for future work

Firstly, it has been seen that the changes in the reservoir properties of rocks due to CO_2-brine-rock interaction in a geosequestration site is affected by the phase of the mobile undissolved CO_2 in the reservoir, there is a great need to conduct future CO_2-brine-rock interaction studies with a consideration for the phase of the CO_2. This will help improve the understanding of the changes due to theCO_2-brine-rock interaction and also improve the accuracy of models/prediction of reservoir properties in geosequestration sites. Additionally, more experimental studies is recommended to understand the effect of different phase of CO_2 on the tertiary phase of fatigue in a saline reservoir, as well as investigate the role of pore shape and size on the changes in rock properties in a saline CO_2 storage site.

Secondly, future experimental or numerical modelling researches on CO_2-brine-rock interaction should be done with reference to a particular phase of CO_2 or the changing phases. This will improve the accuracy of predictions from the experiments or models. Previous researches on the effects of CO_2 on saline reservoir have assumed that the stored CO_2 remains permanently in a single phase throughout storage. Given the rate of CO_2 dissolution in brine, it is possible that the phase of CO_2 will change with the pressure and temperature conditions of the reservoir, de-pressurization of the reservoir can also lead to a change in the phase of the CO_2.

Thirdly, the application of this research extended the understanding of CO_2-brine-rock interaction, including new knowledge of the effect of phase of CO_2 on CO_2-brine-rock interaction in geosequestration sites. Overall, the understanding and knowledge generated by this research is of value to the industry in improving the prediction of the effects of CO_2-brine- rock interaction on the physical, geomechanical, chemical and petrophysical properties of reservoir rocks, and contributes to ensuring CO_2 storage integrity in geosequestration towards meeting the target of net zero.

Finally, a major challenge with the study of CO_2-brine–rock is the scarcity of natural core samples from the depth that are suitable for storage. Therefore, there is the need to develop and conduct FSI numeral modelling studies using a digital rock for evaluating the reservoir properties factoring the different phases of CO_2 that could

exist in a saline storage reservoir. A major challenge that will be encountered in numerical modeling using the digital rock model is the resolution of the image used vs the nature of the rock as well as the computational resources needed to process the REV size of the digital rock. It is very necessary to spare a thought for this challenge in future studies. Furthermore, upscaling the output of such numerical modeling study into core-scale and field scale could be carried out in future.

9.3 List of Publications from this thesis

1. Peter, A., Jin, X., Sheng, Y., Fan, X., & Yang, D. (2020). Static fatigue of saline rocks under different CO2 phase conditions. *Journal of Petroleum Science and Engineering*. https://doi.org/10.1016/j.petrol.2020.107940

   This published article forms Chapter 5 of this dissertation.

2. Peter, A., Jin, X., Fan, X., Kenneth, I., Sheng, Y., & Yang, D. Effect of CO_2 phase on 3D pore geometry of saline reservoir rock. Rock Mechanics and Rock Engineering (in press).

   This forms Chapter 7 of this dissertation.

3. Peter, A., Jin, X., Fan, X., Kenneth, I., Sheng, Y., & Yang, D. .Microscopy and image analysis of the micro-fabric and composition of saline rocks under different phaseCO_2-Brine states. Petroleum Science and Engineering. https://doi.org/10.1016/j.petrol.2021.109411

   This forms part of Chapter 8 of this dissertation.

Reference

Abdoulghafour, H., Sarmadivaleh, M., Hauge, L. P., Fernø, M., & Iglauer, S. (2020). Capillary pressure characteristics of CO2-brine-sandstone systems. *International Journal of Greenhouse Gas Control, 94*, 102876.

Acevedo, l., & Chopra, A. (2017). Influence of Phase Behaviour in the Well Design of CO2 Injectors. *Energy procedia, 114*, 5083-5099.

Agada, S., Kolster, C., Williams, G., Vosper, H., MacDowell, N., & Krevor, S. (2017). Sensitivity analysis of the dynamic CO2 storage capacity estimate for the Bunter Sandstone of the UK Southern North Sea. *Energy procedia, 114*, 4564-4570.

Aghaei, A., & Piri, M. (2015). Direct pore-to-core up-scaling of displacement processes: Dynamic pore network modeling and experimentation. *Journal of Hydrology, 522*, 488-509.

Ahmad, N., Wörman, A., Sanchez-Vila, X., Jarsjö, J., Bottacin-Busolin, A., & Hellevang, H. (2016). Injection of CO2-saturated brine in geological reservoir: A way to enhanced storage safety. *International Journal of Greenhouse Gas Control, 54*, 129-144.

Ajibola, J., Adam, A., & Muggeridge, A. (2016). *Gravity Driven Fingering and Mixing During CO2 Sequestration.* Paper presented at the SPE Asia Pacific Oil & Gas Conference and Exhibition.

Akbar, M. N. A., Salam, A., Awab, M., & Prakoso, S. (2019). *Interrelationships of Rock Elastics Properties to Petrophysical Pore Structure and Geometric Details of Sandstone.* Paper presented at the SPE/IATMI Asia Pacific Oil & Gas Conference and Exhibition.

Akbarabadi, M., & Piri, M. (2013). Relative permeability hysteresis and capillary trapping characteristics of supercritical CO2/brine systems: An experimental study at reservoir conditions. *Advances in Water Resources, 52*, 190-206.

Akono, A.-T., Kabir, P., Shi, Z., Fuchs, S., Tsotsis, T. T., Jessen, K., & Werth, C. J. (2019). Modeling $\hbox{CO}_2$ CO 2-Induced Alterations in Mt. Simon Sandstone via Nanomechanics. *Rock mechanics and rock engineering, 52*(5), 1353-1375.

Ali Ahmadi, M., & Ahmadi, A. (2016). Applying a sophisticated approach to predict CO2 solubility in brines: application to CO2 sequestration. *International Journal of Low-Carbon Technologies, 11*(3), 325-332.

Al-Khdheeawi, E. A., Vialle, S., Barifcani, A., Sarmadivaleh, M., & Iglauer, S. (2017). Influence of rock wettability on CO2 migration and storage capacity in deep saline aquifers. *Energy procedia, 114*, 4357-4365.

Al-Khdheeawi, E. A., Vialle, S., Barifcani, A., Sarmadivaleh, M., & Iglauer, S. (2018). Impact of injected water salinity on CO2 storage efficiency in homogenous reservoirs. *The APPEA Journal, 58*(1), 44-50.

Al-Khdheeawi, E. A., Vialle, S., Barifcani, A., Sarmadivaleh, M., & Iglauer, S. (2019). Effect of the number of water alternating CO2 injection cycles on CO2 trapping capacity. *The APPEA Journal, 59*(1), 357-363.

Al-Traboulsi, M., Sjögersten, S., Colls, J., Steven, M., & Black, C. (2013). Potential impact of CO 2 leakage from Carbon Capture and Storage (CCS) systems on growth and yield in maize. *Plant and Soil, 365*(1-2), 267-281.

Al-Zaidi, E., Fan, X., & Edlmann, K. (2018). The Effect of CO2 Phase on Oil Displacement in a Sandstone Core Sample. *Fluids, 3*(1), 23.

Al-Khdheeawi, E. A., Vialle, S., Barifcani, A., Sarmadivaleh, M., Zhang, Y., & Iglauer, S. (2018). Impact of salinity on CO2 containment security in highly heterogeneous reservoirs. *Greenhouse Gases: Science and Technology, 8*(1), 93-105.

Al-Menhali, A., Niu, B., & Krevor, S. (2015). Capillarity and wetting of carbon dioxide and brine during drainage in b erea sandstone at reservoir conditions. *Water resources research, 51*(10), 7895-7914.

Al Hattamleh, O., Razavi, M., & Muhunthan, B. (2009). Experimental determination of representative elementary volume of sands using X-ray computed tomography. *Materials characterisation IV, WIT Trans. Engng Sci, 64*, 145-153.

Alemu, B. L., Aagaard, P., Munz, I. A., & Skurtveit, E. (2011). Caprock interaction with CO2: A laboratory study of reactivity of shale with supercritical CO2 and brine. *Applied geochemistry, 26*(12), 1975-1989. doi:10.1016/j.apgeochem.2011.06.028

Allen, M. R., Dube, O. P., Solecki, W., Aragón-Durand, F., Cramer, W., Humphreys, S., . . . Mulugetta, Y. (2018). Framing and context. *Global warming of, 1*(5).

Amar, M. N., Ghriga, M. A., Ouaer, H., Seghier, M. E. A. B., Pham, B. T., & Andersen, P. Ø. (2020). Modeling viscosity of CO2 at high temperature and pressure conditions. *Journal of Natural Gas Science and Engineering, 77*, 103271.

Anderson, S. T., & Jahediesfanjani, H. (2017). Case study-Dynamic pressure-limited capacity and costs of CO2 storage in the Mount Simon sandstone.

Andrä, H., Combaret, N., Dvorkin, J., Glatt, E., Han, J., Kabel, M., . . . Madonna, C. (2013). Digital rock physics benchmarks—Part I: Imaging and segmentation. *Computers & Geosciences, 50*, 25-32.

Apps, J. A., Zhang, Y., Zheng, L., Xu, T., & Birkholzer, J. T. (2009). Identification of thermodynamic controls defining the concentrations of hazardous elements in potable ground waters and the potential impact of increasing carbon dioxide partial pressure. *Energy Procedia, 1*(1), 1917-1924.

Armitage, P., Worden, R., Faulkner, D., Aplin, A., Butcher, A., & Iliffe, J. (2010). Diagenetic and sedimentary controls on porosity in Lower Carboniferous fine-grained lithologies, Krechba field, Algeria: A petrological study of a caprock to a carbon capture site. *Marine and Petroleum Geology, 27*(7), 1395-1410.

Arson, C. (2020). Micro-macro mechanics of damage and healing in rocks. *Open Geomechanics, 2*, 1-41.

Asef, M. R., & Najibi, A. R. (2013). The effect of confining pressure on elastic wave velocities and dynamic to static Young's modulus ratio. *Geophysics, 78*(3), D135-D142.

Azadi Tabar, M., & Ghazanfari, M. (2019). Experimental study of surfapore nanofluid effect on surface free energy of calcite rock. *Modares Mechanical Engineering, 19*(3), 709-718.

Bachu, S., & Celia, M. A. (2009). Assessing the potential for CO2 leakage, particularly through wells, from geological storage sites. *Carbon Sequestration and Its Role in the Global Carbon Cycle, 183*, 203-216.

Basirat, F., Yang, Z., & Niemi, A. (2017). Pore-scale modeling of wettability effects

on CO2–brine displacement during geological storage. *Advances in Water Resources, 109*, 181-195. Baud, Vajdova, Wong. (2006). Shear-enhanced compaction and strain localization: Inelastic deformation and constitutive modeling of four porous sandstones. *Journal of Geophysical Research: Solid Earth, 111*(B12).

Bemer, E., & Lombard, J. (2010). From injectivity to integrity studies of CO2 geological storage-chemical alteration effects on carbonates petrophysical and geomechanical properties. *Oil & Gas Science and Technology–Revue de l'Institut Français du Pétrole, 65*(3), 445-459.

Bemer, E., Nguyen, M. T., Dautriat, J., Adelinet, M., Fleury, M., & Youssef, S. (2016). Impact of chemical alteration on the poromechanical properties of carbonate rocks. *Geophysical Prospecting, 64*(4), 810-827.

Bentham, M., Mallows, T., Lowndes, J., & Green, A. (2014). CO2 STORage Evaluation Database (CO2 Stored). The UK's online storage atlas. *Energy Procedia, 63*, 5103-5113. doi:https://doi.org/10.1016/j.egypro.2014.11.540

Berg, C. F., Lopez, O., & Berland, H. (2017). Industrial applications of digital rock technology. *Journal of Petroleum Science and Engineering, 157*, 131-147.

Berrezueta, E., González-Menéndez, L., Breitner, D., & Luquot, L. (2013). Pore system changes during experimental CO2 injection into detritic rocks: Studies of potential storage rocks from some sedimentary basins of Spain. *International Journal of Greenhouse Gas Control, 17*, 411-422.

Berrezueta, E., González-Menéndez, L., Ordóñez-Casado, B., & Olaya, P. (2015). Pore network quantification of sandstones under experimental CO2 injection using image analysis. *Computers & Geosciences, 77*, 97-110.

Bickle, M. J. (2009). Geological carbon storage. *Nature Geoscience, 2*(12), 815. Blunt, M. J., Bijeljic, B., Dong, H., Gharbi, O., Iglauer, S., Mostaghimi, P., . . . Pentland, C. (2013). Pore-scale imaging and modelling. *Advances in Water Resources, 51*, 197-216.

Bogdanov, I. I., Guerton, F., Kpahou, J., & Kamp, A. M. (2011). *DIRECT PORE-SCALE MODELING OF TWO-PHASE FLOW THROUGH NATURAL MEDIA*.

Bolster, D. (2014). The fluid mechanics of dissolution trapping in geologic storage of CO 2. *Journal of Fluid Mechanics, 740*, 1-4.

Borges, J. A. R., Pires, L. F., & Belmont Pereira, A. (2012). Computed tomography to estimate the representative elementary area for soil porosity measurements. *The Scientific World Journal, 2012*.

Borrero-Santiago, A., Ribicic, D., Bonnail, E., Netzer, R., Koseto, D., & Ardelan, M. (2020). Response of bacterial communities in Barents Sea sediments in case of a potential CO2 leakage from carbon reservoirs. *Marine Environmental Research, 160*, 105050.

BP. (2010). *Statistical review of world energy*.

Brantut, N., Heap, M., Meredith, P., & Baud, P. (2013). Time-dependent cracking and brittle creep in crustal rocks: A review. *Journal of Structural Geology, 52*, 17-43.

Bultreys, T., Boone, M. A., Boone, M. N., De Schryver, T., Masschaele, B., Van Hoorebeke, L., & Cnudde, V. (2016). Fast laboratory-based micro-computed tomography for pore-scale research: illustrative experiments and perspectives on the future. *Advances in Water Resources, 95*, 341-351.

195

Bultreys, T., De Boever, W., & Cnudde, V. (2016). Imaging and image-based fluid transport modeling at the pore scale in geological materials: A practical introduction to the current state-of-the-art. *Earth-science reviews, 155*, 93-128.

Burnside, N., & Naylor, M. (2014). Review and implications of relative permeability of CO2/brine systems and residual trapping of CO2. *International Journal of Greenhouse Gas Control, 23*, 1-11.

Busch, A., Amann-Hildenbrand, A., Bertier, P., Waschbuesch, M., & Krooss, B. M. (2010). *The significance of caprock sealing integrity for CO2 storage.* Paper presented at the SPE International Conference on CO2 Capture, Storage, and Utilization.

Buscheck, T. A., Mansoor, K., Yang, X., Wainwright, H. M., & Carroll, S. A. (2019). Downhole pressure and chemical monitoring for CO2 and brine leak detection in aquifers above a CO2 storage reservoir. *International Journal of Greenhouse Gas Control, 91*, 102812.

Calvo, R., Gómez, E., Domingo, R.(2014). Vectorial method of minimum zone tolerance for flatness, straightness, and their uncertainty estimation. *International journal of precision engineering and manufacturing, 15*(1), 31-44.

Cao, S. C., Dai, S., & Jung, J. (2016). Supercritical CO2 and brine displacement in geological carbon sequestration: Micromodel and pore network simulation studies. *International Journal of Greenhouse Gas Control, 44*, 104-114.

Carroll, S., Carey, J. W., Dzombak, D., Huerta, N. J., Li, L., Richard, T., . . . Zhang, L. (2016). Role of chemistry, mechanics, and transport on well integrity in CO2 storage environments. *International Journal of Greenhouse Gas Control, 49*, 149-160.

CCICED. (2009). *China's pathway towards low carbon economy.*

Chadwick, A., Arts, R., Bernstone, C., May, F., Thibeau, S., & Zweigel, P. (2008a). *Best practice for the storage of CO2 in saline aquifers-observations and guidelines from the SACS and CO2STORE projects* (Vol. 14): British Geological Survey.

Chadwick, A., Arts, R., Bernstone, C., May, F., Thibeau, S., & Zweigel, P. (2008b). *BEST PRACTICE FOR THE STORAGE OF CO2 IN SALINE AQUIFERSObservations and guidelines from the SACS and CO2STORE projects*. Kingsley Dunham Centre, Keyworth, Nottingham NG12 5GG

Chen, F., Sevostianov, I., Giraud, A., Grgic, D. (2018). Combined effect of pores concavity and aspect ratio on the elastic properties of a porous material. *International Journal of Solids and Structures, 134*, 161-172.

Chen, G., Gao, H., Fu, K., Zhang, H., Liang, Z., & Tontiwachwuthikul, P. (2020). An improved correlation to determine minimum miscibility pressure of CO2–oil system. *Green Energy & Environment, 5*(1), 97-104.

CHENG, G., & SONG, B. (2018). Application of FCM clustering algorithm in rock image analysis. *Intelligent Computer and Applications*(4), 15.

Connell, L., Sander, R., Pan, Z., Camilleri, M., & Heryanto, D. (2011). History matching of enhanced coal bed methane laboratory core flood tests. *International Journal of Coal Geology, 87*(2), 128-138.

Cook, P. (2014). *Geologically storing carbon: Learning from the Otway Project experience*: CSIRO PUBLISHING.

Costanza-Robinson, M. S., Estabrook, B. D., Fouhey, D. F. (2011). Representative elementary volume estimation for porosity, moisture saturation, and air-water interfacial areas in unsaturated porous media: Data quality implications. *Water resources research, 47*(7).

Cox, M. R., & Budhu, M. (2008). A practical approach to grain shape quantification. *Engineering Geology, 96*(1-2), 1-16.

CO2CRC, *CO2 dispersion.* Coop Res Cent Greenh Gas Technol, 2015.

Cui, G., Wang, Y., Rui, Z., Chen, B., Ren, S., & Zhang, L. (2018). Assessing the combined influence of fluid-rock interactions on reservoir properties and injectivity during CO2 storage in saline aquifers. *Energy, 155*, 281-296.

Daneshvar, E., & Worden, R. H. (2018). Feldspar alteration and Fe minerals: origin, distribution and implications for sandstone reservoir quality in estuarine sediments. *Geological Society, London, Special Publications, 435*(1), 123-139.

Delle, C., & Sarout, J. (2016). Effects of water and supercritical CO2 on the mechanical and elastic properties of Berea sandstone. *International Journal of Greenhouse Gas Control, 55*, 209-220.

Denney, D. (2009). Numerical Modeling of Pressure and Temperature Profiles Including Phase Transitions in Carbon Dioxide Wells. *Journal of Petroleum Technology, 61*(07), 69-70.

DOE. (2017). *CO2-EOR: Untapped Domestic Energy Supply and Long Term Carbon Storage Solutions.* Retrieved from

Doherty, B., Vasylkivska, V., Huerta, N. J., & Dilmore, R. (2017). Estimating the Leakage along Wells during Geologic CO2 Storage: Application of the Well Leakage Assessment Tool to a Hypothetical Storage Scenario in Natrona County, Wyoming. *Energy Procedia, 114*, 5151-5172.

Eshiet, K., & Sheng, Y. (2017). An overview of principles and designs of hydraulic fracturingexperiments and an enquiry into the influence of rock permeability and strength on failure mode. In: Sustainable energy environment and educational development (SEEED), School of Engineering, University of Leeds.

Espinoza, D. N., Jung, H., Major, J. R., Sun, Z., Ramos, M. J., Eichhubl, P., . . . Dewers, T. A. (2018). CO2 charged brines changed rock strength and stiffness at Crystal Geyser, Utah: Implications for leaking subsurface CO2 storage reservoirs. *International Journal of Greenhouse Gas Control, 73*, 16-28.

Espinoza, D. N., Kim, S. H., & Santamarina, J. C. (2011). CO2 geological storage — Geotechnical implications. *KSCE Journal of Civil Engineering, 15*(4), 707-719. doi:10.1007/s12205-011-0011-9

Faisal, T. F., Islam, A., Jouini, M. S., Devarapalli, R. S., Jouiad, M., & Sassi, M. (2019). Numerical prediction of carbonate elastic properties based on multi-scale imaging. *Geomechanics for Energy and the Environment, 20*, 100125.

Fang, Z., & Li, X. (2013). A preliminary evaluation of carbon dioxide storage capacity in unmineable coalbeds in China. *Acta Geotechnica, 9*(1), 109-114. doi:10.1007/s11440-013-0228-5

FARO. (2019). How to evaluate flatness in GD and T. Retrieved from https://insights.faro.com/buildit-software/how-to-evaluate-flatness-in-gd-t

Fernandes, J. S., Appoloni, C. R., & Fernandes, C. P. (2012). Determination of the representative elementary volume for the study of sandstones and siltstones by X-Ray microtomography. *Materials Research, 15*(4), 662-670.

Ferreira, T., & Rasband, W. (2012). ImageJ user guide. *ImageJ/Fiji, 1*, 155-161.

Fischer, S., Knopf, S., May, F., & Rebscher, D. (2016). CO2 Storage related Groundwater Impacts and Protection. *Grundwasser, 21*(1), 5-21. doi:10.1007/s00767-015-0315-7

Fjar, E., Holt, R. M., Raaen, A., Risnes, R., & Horsrud, P. (2008). *Petroleum related rock mechanics* (Vol. 53): Elsevier.

Foroutan, Ghazanfari, Amirlatifi, Perdrial. (2020). Variation of pore-network, mechanical and hydrological characteristics of sandstone specimens through CO2-enriched brine injection. *Geomechanics for Energy and the Environment*, 100217.

Fu, P., Settgast, R. R., Hao, Y., Morris, J. P., & Ryerson, F. J. (2017). The influence of hydraulic fracturing on carbon storage performance. *Journal of Geophysical Research: Solid Earth, 122*(12), 9931-9949.

Fuchs, S. J., Espinoza, D. N., Lopano, C. L., Akono, A.-T., Werth, C. J. (2019). Geochemical and geomechanical alteration of siliciclastic reservoir rock by supercritical CO2-saturated brine formed during geological carbon sequestration. *International Journal of Greenhouse Gas Control, 88*, 251-260.

Garg, A., & Shukla, P. (2009). Coal and energy security for India: Role of carbon dioxide (CO2) capture and storage (CCS). *Energy, 34*(8), 1032-1041.

GCCSI. (2018). *GEOLOGICAL STORAGE OF CO2: SAFE, PERMANENT, AND ABUNDANT*.

GD&T. (2014). GD & T Basics- Flatness. Retrieved from https://www.gdandtbasics.com/flatness/

Gerbi, C., Culshaw, N., & Marsh, J. (2010). Magnitude of weakening during crustal-scale shear zone development. *Journal of Structural Geology, 32*(1), 107-117.

Gheibi, S., Vilarrasa, V., & Holt, R. M. (2018). Numerical analysis of mixed-mode rupture propagation of faults in reservoir-caprock system in CO 2 storage. *International Journal of Greenhouse Gas Control, 71*, 46-61.

Giwelli, A., Kashim, M., Clennell, M., Esteban, L., Noble, R., White, C., . . . Saeedi, A. (2019). *CO2-brine injectivity tests in high co2 content carbonate field, sarawak basin, offshore east Malaysia.* Paper presented at the E3S Web of Conferences.

Godec, M., Kuuskraa, V., Van Leeuwen, T., Stephen Melzer, L., & Wildgust, N. (2011). CO2 storage in depleted oil fields: The worldwide potential for carbon dioxide enhanced oil recovery. *Energy Procedia, 4*, 2162-2169. doi:10.1016/j.egypro.2011.02.102

Goral, J., Andrew, M., Olson, T., & Deo, M. (2020). Correlative core-to pore-scale imaging of shales. *Marine and Petroleum Geology, 111*, 886-904.

Grgic, D. (2011). Influence of CO2 on the long-term chemomechanical behavior of an oolitic limestone. *Journal of Geophysical Research: Solid Earth, 116*(B7).

Griffiths, L., Heap, M. J., Xu, T., Chen, C.-f., & Baud, P. (2017). The influence of pore geometry and orientation on the strength and stiffness of porous rock. *Journal of Structural Geology, 96*, 149-160.

Grombacher, D., Vanorio, T., & Ebert, Y. (2012). Time-lapse acoustic, transport, and NMR measurements to characterize microstructural changes of carbonate rocks during injection of CO 2-rich water. *Geophysics, 77*(3), WA169-WA179.

Guo, S., Qi, S., Zhan, Z., Ma, L., Gure, E. G., & Zhang, S. (2020). Numerical study on the progressive failure of heterogeneous geomaterials under varied confining stresses. *Engineering Geology*, 105556.

Gupta, P. K., & Yadav, B. (2020). Leakage of CO 2 from geological storage and its impacts on fresh soil–water systems: a review. *Environmental Science and Pollution Research, 27*(12), 12995-13018.

Han, J., Han, S., Kang, D. H., Kim, Y., Lee, J., & Lee, Y. (2020). Application of digital rock physics using X-ray CT for study on alteration of macropore properties by CO2 EOR in a carbonate oil reservoir. *Journal of Petroleum Science and Engineering, 189*, 107009.

Hangx, S., Bakker, E., Bertier, P., Nover, G., & Busch, A. (2015). Chemical–mechanical coupling observed for depleted oil reservoirs subjected to long-term CO2-exposure–A case study of the Werkendam natural CO2 analogue field. *Earth and Planetary Science Letters, 428*, 230-242.

Hangx, S., van der Linden, A., Marcelis, F., & Bauer, A. (2013). The effect of CO2 on the mechanical properties of the Captain Sandstone: Geological storage of CO2 at the Goldeneye field (UK). *International Journal of Greenhouse Gas Control, 19*, 609-619.

He, J., Zhang, Y., Li, X., & Wan, X. (2019). Experimental Investigation on the Fractures Induced by Hydraulic Fracturing Using Freshwater and Supercritical CO 2 in Shale Under Uniaxial Stress. *Rock mechanics and rock engineering, 52*(10), 3585-3596.

He, Z., Li, G., Tian, S., Wang, H., Shen, Z., & Li, J. (2016). SEM analysis on rock failure mechanism by supercritical CO2 jet impingement. *Journal of Petroleum Science and Engineering, 146*, 111-120.

Heap. (2009). *Creep: time-dependent brittle deformation in rocks.* UCL (University College London),

Heap, Brantut, Baud, Meredith. (2015). Time-dependent compaction band formation in sandstone. *Journal of Geophysical Research: Solid Earth, 120*(7), 4808-4830.

Hitchon, B., & Bachu, S. (2017). ARSENIC AND SELENIUM IN FORMATION WATERS: ENVIRONMENTAL IMPLICATIONS FOR CARBON DIOXIDE STORAGE IN GEOLOGICAL MEDIA. *WIT Transactions on Ecology and the Environment, 224*, 477-488.

Holloway, S., Vincent, C. J., & Kirk, K. (2006). Industrial carbon dioxide emissions and carbon dioxide storage potential in the UK.

Holloway, S., Vincent, C. J., Bentham, M. S., & Kirk, K. L. (2006a). Top-down and bottom-up estimates of CO2 storage capacity in the United Kingdom sector of the southern North Sea basin. *Environmental Geosciences, 13*(2), 71-84.

https://www.bigskyco2.org/node/127. *CO2 trapping mechanisms.* [cited 2021 30/12/2021].

Hu, D., Zhou, H., Shao, J., & Zhang, F. (2017). Stress-induced permeability evolutions and erosion damage of porous rocks. In *Porous Rock Fracture Mechanics* (pp. 63-92): Elsevier.

Hu, R., Wan, J., Kim, Y., & Tokunaga, T. K. (2017). Wettability effects on supercritical CO2–brine immiscible displacement during drainage: Pore-scale observation and 3D simulation. *International Journal of Greenhouse Gas Control, 60*, 129-139.

Hu, Y., Liu, Y., Cai, C., Kang, Y., Wang, X., Huang, M., & Chen, F. (2017). Fracture Initiation of an Inhomogeneous Shale Rock under a Pressurized Supercritical CO_2 Jet. *Applied Sciences, 7*(10), 1093.

Huang, Y.-H., Yang, S.-Q., Li, W.-P., & Hall, M. R. (2020). Influence of super-critical CO_2 on the strength and fracture behavior of brine-saturated sandstone specimens. *Rock mechanics and rock engineering, 53*(2), 653-670.

Huerta, N. J., Cantrell, K. J., White, S. K., & Brown, C. F. (2020). Hydraulic fracturing to enhance injectivity and storage capacity of CO_2 storage reservoirs: Benefits and risks. *International Journal of Greenhouse Gas Control, 100*, 103105.

Hunter, K., Bielicki, J. M., Middleton, R., Stauffer, P., Pawar, R., Harp, D., & Martinez, D. (2017). Integrated CO_2 Storage and Brine Extraction. *Energy Procedia, 114*, 6331-6336.

Hurley, N. F., Zhao, W., Zhang, T., Buiting, J. J., Leseur, N. X., & Al Ibrahim, M. (2012). Method to determine representative element areas and volumes in porous media. In: Google Patents.

Iassonov, P., Gebrenegus, T., & Tuller, M. (2009). Segmentation of X-ray computed tomography images of porous materials: A crucial step for characterization and quantitative analysis of pore structures. *Water resources research, 45*(9).

IEO, *International Energy outlook 2021 (IEO2021): Independent Statistics and Analysis by Stephen Nalley and Angelina LaRose*. 2021. p. 21.

Ilgen, A. G., Newell, P., Hueckel, T., Espinoza, D. N., & Hu, M. (2019). Coupled Chemical-Mechanical Processes Associated With the Injection of CO_2 into Subsurface. In *Science of Carbon Storage in Deep Saline Formations* (pp. 337-359): Elsevier.

Isaka, B. A., Ranjith, P., Wanniarachchi, W., & Rathnaweera, T. (2020). Investigation of the aperture-dependent flow characteristics of a supercritical carbon dioxide-induced fracture under high-temperature and high-pressure conditions: A numerical study. *Engineering Geology, 277*, 105789.

Islam, A., Faisal, T. F., Chevalier, S., Jouini, M. S., Sassi, M. (2019). Multi-scale experimental and numerical simulation workflow of absolute permeability in heterogeneous carbonates. *Journal of Petroleum Science and Engineering, 173*, 326-338.

Islam, A. W., Meckel, T. A., Sun, A. Y., & Krishnamurthy, P. G. (2016). Numerical experiments of density driven CO_2 saturated brine migration in heterogeneous two-dimensional geologic fabric materials. *International Communications in Heat and Mass Transfer, 71*, 148-156.

Jacob, R., & Saylor, B. Z. (2016). CO_2 solubility in multi-component brines containing NaCl, KCl, $CaCl_2$ and $MgCl_2$ at 297 K and 1–14 MPa. *Chemical geology, 424*, 86-95.

Jamshidi, T., Zeng, F., Tontiwachwuthikul, P., & Torabi, F. (2019). Laboratory measurements of solubility and swelling factor for CO_2/Brine and CO_2/heavy oil binary systems under low-medium pressure and temperature. *The Canadian Journal of Chemical Engineering, 97*(7), 2137-2145.

Jeanne, P., Rutqvist, J., Foxall, W., Rinaldi, A. P., Wainwright, H. M., Zhou, Q., . . . Layland-Bachmann, C. (2017). Effects of the distribution and evolution of the coefficient of friction along a fault on the assessment of the seismic activity associated with a hypothetical industrial-scale geologic CO_2 sequestration operation. *International Journal of Greenhouse Gas Control, 66*, 254-263.

Jeon, P. R., & Lee, C.-H. (2021). Reaction of drilled-cores from the Janggi basin with CO2-saturated brine from subcritical to supercritical condition of CO2: Implications on sequestration of dissolved CO2. *Journal of Natural Gas Science and Engineering, 88*, 103804.

Jeong, G. S., Ki, S., Lee, D. S., & Jang, I. (2021). Effect of the Flow Rate on the Relative Permeability Curve in the CO2 and Brine System for CO2 Sequestration. *Sustainability, 13*(3), 1543.

Jeong, G. S., Lee, J., Ki, S., Huh, D.-G., & Park, C.-H. (2017). Effects of viscosity ratio, interfacial tension and flow rate on hysteric relative permeability of CO2/brine systems. *Energy, 133*, 62-69.

Jeong, H.-s., Kang, S.-s., & Obara, Y. (2007). Influence of surrounding environments and strain rates on the strength of rocks subjected to uniaxial compression. *International Journal of Rock Mechanics and Mining Sciences, 44*(3), 321-331.

Jessen, K., Lin, W., & Kovscek, A. R. (2007). *Multicomponent sorption modeling in ECBM displacement calculations.* Paper presented at the SPE Annual Technical Conference and Exhibition.

Ji, Baud, Vajdova, Wong. (2012). Characterization of pore geometry of Indiana limestone in relation to mechanical compaction. *Oil & Gas Science and Technology–Revue d'IFP Energies nouvelles, 67*(5), 753-775.

Ji, X., Ma, X., Han, Y., Yu, M., & Meng, C. (2018). Effect of different leakage speeds on plants in carbon capture and storage by simulation in chamber. *Transactions of the Chinese Society of Agricultural Engineering, 34*(2), 242-247.

Jia, W., Pan, F., Dai, Z., Xiao, T., & McPherson, B. (2017). Probabilistic risk assessment of CO2 trapping mechanisms in a sandstone CO2-EOR field in northern texas, USA. *Energy procedia, 114*, 4321-4329.

Jiang, F., & Tsuji, T. (2014). Changes in pore geometry and relative permeability caused by carbonate precipitation in porous media. *Physical Review E, 90*(5), 053306.

Jin, M., Mackay, E. J., Quinn, M., Hitchen, K., Akhurst, M. (2012). *Evaluation of the CO2 storage capacity of the Captain Sandstone Formation.* Paper presented at the SPE Europec/EAGE Annual Conference.

Jin, X., Chao, C., Wu, K., Xia, C., & Fan, X. (2020). The effect of CO2 phase on drainage process by analysis of transient differential pressure. *Chemical Engineering Science, 218*, 115581.

Joekar-Niasar, V., & Hassanizadeh, S. (2012). Analysis of fundamentals of two-phase flow in porous media using dynamic pore-network models: A review. *Critical Reviews in Environmental Science and Technology, 42*(18), 1895-1976.

Jung, J., & Hu, J. W. (2016). Impact of pressure and brine salinity on capillary pressure-water saturation relations in geological CO2 sequestration. *Advances in Condensed Matter Physics, 2016*.

Jung, Y., Zhou, Q., & Birkholzer, J. T. (2013). Early detection of brine and CO2 leakage through abandoned wells using pressure and surface-deformation monitoring data: concept and demonstration. *Advances in Water Resources, 62*, 555-569.

Keshavarz, V., Taheri-Shakib, J., Khosravanian, R., Hosseini, S. A., Salimidelshad, Y., & Saadati, P. (2019). Experimental investigation of rock-solvent

interaction on the properties of carbonate reservoir rock. *Journal of Petroleum Science and Engineering, 181*, 106246.

KGS. (2003). Online tolols to evaluate saline aquifers for CO2 sequestration. Retrieved from http://www.kgs.ku.edu/PRS/publication/2003/ofr2003-33/P1-07.html

Khan, S., Khulief, Y., & Al-Shuhail, A. (2020). Effects of reservoir size and boundary conditions on pore-pressure buildup and fault reactivation during CO 2 injection in deep geological reservoirs. *Environmental earth sciences, 79*, 1-23.

Kharaka, Y. K., Thordsen, J. J., Kakouros, E., Ambats, G., Herkelrath, W. N., Beers, S. R., . . . Zheng, L. (2010). Changes in the chemistry of shallow groundwater related to the 2008 injection of CO 2 at the ZERT field site, Bozeman, Montana. *Environmental Earth Sciences, 60*(2), 273-284.

Kim, A.-R., Cho, G.-C., & Kwon, T.-H. (2013). Site characterization and geotechnical aspects on geological storage of CO2 in Korea. *Geosciences Journal, 18*(2), 167-179. doi:10.1007/s12303-013-0065-4

Klass, A. B., & Wilson, E. J. (2008). Climate change and carbon sequestration: Assessing a liability regime for long-term storage of carbon dioxide. *Emory LJ, 58*, 103.

Ko, K., Lee, J.-y., & Chung, H. (2020). Highly efficient colorimetric CO2 sensors for monitoring CO2 leakage from carbon capture and storage sites. *Science of the Total Environment, 729*, 138786.

Krevor, S., Reynolds, C., Al-Menhali, A., & Niu, B. (2016). The impact of reservoir conditions and rock heterogeneity on CO 2-brine multiphase flow in permeable sandstone. *Petrophysics, 57*(01), 12-18.

Krevor, S. C., Pini, R., Zuo, L., & Benson, S. M. (2012). Relative permeability and trapping of CO2 and water in sandstone rocks at reservoir conditions. *Water resources research, 48*(2).

Kuo, C.-W., Perrin, J.-C., & Benson, S. M. (2011). Simulation studies of effect of flow rate and small scale heterogeneity on multiphase flow of CO2 and brine. *Energy procedia, 4*, 4516-4523.

Kvashnin, A. G., Kvashnin, D. G., & Oganov, A. R. (2019). Novel Unexpected Reconstructions of (100) and (111) Surfaces of NaCl: Theoretical Prediction. *Scientific reports, 9*(1), 1-9.

Lala, A. M. S. (2018). Modifications to the Kozeny–Carman model to enhance petrophysical relationships. *Exploration Geophysics, 49*(4), 553-558.

Lamy-Chappuis, B. (2015). *Mineral-Fluid interactions and their implications for the sequestration of CO2 in saline aquifers.* University of Leeds.

Lamy-Chappuis, B., Angus, D., Fisher, Q. J., & Yardley, B. W. (2016). The effect of CO2-enriched brine injection on the mechanical properties of calcite-bearing sandstone. *International Journal of Greenhouse Gas Control, 52*, 84-95.

Lee, H., Shinn, Y. J., Ong, S. H., Woo, S. W., Park, K. G., Lee, T. J., & Moon, S. W. (2017). Fault reactivation potential of an offshore CO2 storage site, Pohang Basin, South Korea. *Journal of Petroleum Science and Engineering, 152*, 427-442.

Lei, X., & Xue, Z. (2009). Ultrasonic velocity and attenuation during CO2 injection into water-saturated porous sandstone: Measurements using difference seismic tomography. *Physics of the Earth and Planetary Interiors, 176*(3-4), 224-234.

Lenormand, Bauget, Ringot, Cydarex. (2010). *Permeability measurement on small rock samples.* Paper presented at the Intern. Symp. of the Society of Core Analysts (SCA2010), Canada, presentation SCA2010-73.

Leslie, S. A., & Mitchell, J. C. (2007). Removing gold coating from SEM samples. *palaeontology, 50*(6), 1459-1461.

Lesueur, Casadiego, Veveakis, Poulet. (2017). Modelling fluid-microstructure interaction on elasto-visco-plastic digital rocks. *Geomechanics for Energy and the Environment, 12*, 1-13.

Li, Yang, D., Zhong, Z., Sheng, Y., Liu, X. (2018). Experimental investigation on the micro damage evolution of chemical corroded limestone subjected to cyclic loads. *International Journal of Fatigue, 113*, 23-32.

Li, C., & Laloui, L. (2016). Coupled multiphase thermo-hydro-mechanical analysis of supercritical CO2 injection: Benchmark for the In Salah surface uplift problem. *International Journal of Greenhouse Gas Control, 51*, 394-408. doi:https://doi.org/10.1016/j.ijggc.2016.05.025

Li, D., Ren, S., & Rui, H. (2019). CO2 Leakage Behaviors in Typical Caprock–Aquifer System during Geological Storage Process. *ACS omega, 4*(18), 17874-17879.

Li, D., Zhang, L., Ren, S., & Rui, H. (2019). Leakage mitigation during CO2 geological storage process using CO2 triggered gelation. *Industrial & Engineering Chemistry Research, 58*(8), 3395-3406.

Li, L., & Iskander, M. (2021). Comparison of 2D and 3D dynamic image analysis for characterization of natural sands. *Engineering Geology*, 106052.

Li, L., Tan, Y., Huang, B., Deng, X. (2020). Pore property as an indicator of macro-deterioration in slightly weathered tuffs. *Engineering Geology, 267*, 105492.

Li, Q. (2010). Coupled reactive transport model for heat and density driven flow in CO 2 storage in saline aquifers. *Journal of Hazardous, Toxic, and Radioactive Waste, 15*(4), 251-258.

Li, S., Zhang, S., Ma, X., Zou, Y., Li, N., Wu, S., & Zhang, Z. (2019). Coupled Physical–Chemical Effects of CO 2 on Rock Properties and Breakdown During Intermittent CO 2-Hybrid Fracturing. *Rock mechanics and rock engineering*, 1-19.

Li, W., Nan, Y., You, Q., & Jin, Z. (2021). CO2 solubility in brine in silica nanopores in relation to geological CO2 sequestration in tight formations: Effect of salinity and pH. *Chemical Engineering Journal, 411*, 127626.

Li, X., Peng, C., Crawshaw, J. P., Maitland, G. C., & Trusler, J. M. (2018). The pH of CO2-saturated aqueous NaCl and NaHCO3 solutions at temperatures between 308 K and 373 K at pressures up to 15 MPa. *Fluid Phase Equilibria, 458*, 253-263.

Li, X., Qi, C., & Zhang, P. (2020). A micro-macro confined compressive fatigue creep failure model in brittle solids. *International Journal of Fatigue, 130*, 105278.

Lindeberg, E., & Bergmo, P. J. G. g. c. t. (2003). The long-term fate of CO2 injected into an aquifer. *1*, 489-494.

Liteanu, E., Niemeijer, A., Spiers, C., Peach, C., & De Bresser, J. (2012). The effect of CO2 on creep of wet calcite aggregates. *Journal of Geophysical Research: Solid Earth, 117*(B3).

Liteanu, E., Spiers, C., & De Bresser, J. (2013). The influence of water and supercritical CO2 on the failure behavior of chalk. *Tectonophysics, 599*, 157-169.

Liu, B., Suzuki, A., & Ito, T. (2020). Estimating the seepage effect of SC-CO2 and water fracturing with a steady-state flow model considering capillary and viscous forces at the pore scale. *Journal of Petroleum Science and Engineering, 184*, 106483.

Liu, L.-C., Li, Q., Zhang, J.-T., & Cao, D. (2014). Toward a framework of environmental risk management for CO2 geological storage in china: gaps and suggestions for future regulations. *Mitigation and Adaptation Strategies for Global Change, 21*(2), 191-207. doi:10.1007/s11027-014-9589-9

Liu, L.-C., Li, Q., Zhang, J.-T., & Cao, D. (2016). Toward a framework of environmental risk management for CO 2 geological storage in China: gaps and suggestions for future regulations. *Mitigation and Adaptation Strategies for Global Change, 21*(2), 191-207.

Liu, Y., Hou, M., Yang, G., & Han, B. (2011). Solubility of CO2 in aqueous solutions of NaCl, KCl, CaCl2 and their mixed salts at different temperatures and pressures. *The Journal of supercritical fluids, 56*(2), 125-129.

Long, H., Nardi, C., Idowu, N., Carnerup, A., Øren, P., Knackstedt, M., . . . Lithicon, A. (2013). *Multi-scale imaging and modeling workflow to capture and characterize microporosity in sandstone.* Paper presented at the International Symposium of the Society of Core Analysts, Napa Valley, California, USA.

Lopez, O., Mock, A., Øren, E., Long, H., Kalam, Z., Vahrenkamp, V., . . . Al Hammadi, M. (2012). *Validation of fundamental carbonate reservoir core properties using digital rock physics.* Paper presented at the International Symposium of the Society of Core Analysts held in Aberdeen, Scotland, UK, SCA2012-19.

Lopez, O., Mock, A., Skretting, J., Petersen Jr, E. B., Øren, P.-E., & Rustad, A. B. (2010). *Investigation into the reliability of predictive pore-scale modeling for siliciclastic reservoir rocks.* Paper presented at the SCA2010-41 presented at the 2010 SCA International Symposium, Halifax, Canada.

Lu, J., Partin, J. W., Hovorka, S. D., & Wong, C. (2010). Potential risks to freshwater resources as a result of leakage from CO 2 geological storage: a batch-reaction experiment. *Environmental Earth Sciences, 60*(2), 335-348.

Lu, M., & Connell, L. D. (2014). Transient, thermal wellbore flow of multispecies carbon dioxide mixtures with phase transition during geological storage. *International journal of multiphase flow, 63*, 82-92.

Luo, Y. (2020). Influence of water on mechanical behavior of surrounding rock in hard-rock tunnels: an experimental simulation. *Engineering Geology, 277*, 105816.

Luquot, L., & Gouze, P. (2009). Experimental determination of porosity and permeability changes induced by injection of CO2 into carbonate rocks. *Chemical Geology, 265*(1-2), 148-159.

Luquot, L., Gouze, P., Niemi, A., Bensabat, J., & Carrera, J. (2016). CO2-rich brine percolation experiments through Heletz reservoir rock samples (Israel): Role of the flow rate and brine composition. *International Journal of Greenhouse Gas Control, 48*, 44-58.

Lyu, Q., Ranjith, P. G., Long, X., & Ji, B. (2016). Experimental investigation of mechanical properties of black shales after CO2-water-rock interaction. *Materials, 9*(8), 663.

Madonna, Almqvist, Saenger,(2012). Digital rock physics: numerical prediction of pressure-dependent ultrasonic velocities using micro-CT imaging. *Geophysical Journal International, 189*(3), 1475-1482.

Mahmoodpour, S., Rostami, B., Soltanian, M. R., & Amooie, M. A. (2019). Effect of brine composition on the onset of convection during CO2 dissolution in brine. *Computers & Geosciences, 124*, 1-13.

Makhnenko, R. Y., Vilarrasa, V., Mylnikov, D., & Laloui, L. (2017). Hydromechanical aspects of CO2 breakthrough into clay-rich caprock. *Energy procedia, 114*, 3219-3228.

Mann&Kump, *Dire Predictions Understanding Climate Change: An illustrated guide to the findings of the IPCC, 2nd Ed*. 2015, DK Publishing: New York, US. p. 225.

Mao, S., & Duan, Z. (2008). The P, V, T, x properties of binary aqueous chloride solutions up to T= 573 K and 100 MPa. *The Journal of Chemical Thermodynamics, 40*(7), 1046-1063.

Mao, S., Duan, Z., Hu, J., & Zhang, D. (2010). A model for single-phase PVTx properties of CO2–CH4–C2H6–N2–H2O–NaCl fluid mixtures from 273 to 1273 K and from 1 to 5000 bar. *Chemical geology, 275*(3-4), 148-160.

Marbler, H., Erickson, K. P., Schmidt, M., Lempp, C., & Pöllmann, H. (2013). Geomechanical and geochemical effects on sandstones caused by the reaction with supercritical CO 2: an experimental approach to in situ conditions in deep geological reservoirs. *Environmental earth sciences, 69*(6), 1981-1998.

Mazzoldi, A., Rinaldi, A. P., Borgia, A., & Rutqvist, J. (2012). Induced seismicity within geological carbon sequestration projects: maximum earthquake magnitude and leakage potential from undetected faults. *International Journal of Greenhouse Gas Control, 10*, 434-442.

Mehic, M., Ranjith, P. G., Choi, S., & Haque, A. (2006). The geomechanical behavior of Australian black coal under the effects of CO2 injection: uniaxial testing. In *Advances in Unsaturated Soil, Seepage, and Environmental Geotechnics* (pp. 290-297).

Mehmani, A., Kelly, S., & Torres-Verdín, C. (2020). Leveraging digital rock PHYSICS workflows in unconventional petrophysics: A review of opportunities, challenges, and benchmarking. *Journal of Petroleum Science and Engineering*, 107083.

Mehmani, A., Verma, R., & Prodanović, M. (2020). Pore-scale modeling of carbonates. *Marine and Petroleum Geology, 114*, 104141.

Menad, N. A., Hemmati-Sarapardeh, A., Varamesh, A., & Shamshirband, S. (2019). Predicting solubility of CO2 in brine by advanced machine learning systems: Application to carbon capture and sequestration. *Journal of CO2 Utilization, 33*, 83-95.

Meredith, P., Brantut, N., Heap, M., & Baud, P. (2017). *Time-Dependent Weakening and Failure in the Crust: Subcritical Crack Growth and Brittle Creep.* Paper presented at the ISRM Progressive Rock Failure Conference.

Mikhaltsevitch, V., Lebedev, M., & Gurevich, B. (2014). Measurements of the elastic and anelastic properties of sandstone flooded with supercritical CO2. *Geophysical Prospecting, 62*(6), 1266-1277.

Mohammadian, E., Hamidi, H., Asadullah, M., Azdarpour, A., Motamedi, S., & Junin, R. (2015). Measurement of CO2 solubility in NaCl brine solutions at different temperatures and pressures using the potentiometric titration method. *Journal of Chemical & Engineering Data, 60*(7), 2042-2049.

Morris, J. P., Hao, Y., Foxall, W., & McNab, W. (2011). A study of injection-induced mechanical deformation at the In Salah CO2 storage project. *International Journal of Greenhouse Gas Control, 5*(2), 270-280.

Mosavat, N., & Torabi, F. (2014). Application of CO2-saturated water flooding as a prospective safe CO2 storage strategy. *Energy procedia, 63*, 5408-5419.

Naveed, M., Moldrup, P., Arthur, E., Wildenschild, D., Eden, M., Lamandé, M., . . . De Jonge, L. W. (2016). Prediction of biopore- and matrix-dominated flow from X-ray CT-derived macropore network characteristics. *Soil Science Society of America Journal, 77*(2), 403-411.

Nguyen, V. A. (2020). *Investigation of Reactions between Glauconite and Carbon Dioxide, with Implications for Carbon Sequestration.* Mississippi State University, .

Niu, Y., Mostaghimi, P., Shabaninejad, M., Swietojanski, P., & Armstrong, R. T. (2020). Digital rock segmentation for petrophysical analysis with reduced user bias using convolutional neural networks. *Water resources research, 56*(2), e2019WR026597.

Njiekak, G., & Schmitt, D. R. (2019). Effective Stress Coefficient for Seismic Velocities in Carbonate Rocks: Effects of Pore Characteristics and Fluid Types. *Pure and Applied Geophysics, 176*(4), 1467-1485.

Noiriel, C., Bernard, D., Gouze, P., & Thibault, X. (2005). Hydraulic properties and microgeometry evolution accompanying limestone dissolution by acidic water. *Oil & gas science and technology, 60*(1), 177-192. Retrieved from https://ogst.ifpenergiesnouvelles.fr/articles/ogst/pdf/2005/01/noiriel_vol60n1.pdf

Noiriel, C., Luquot, L., Madé, B., Raimbault, L., Gouze, P., & Van Der Lee, J. (2009). Changes in reactive surface area during limestone dissolution: An experimental and modelling study. *Chemical Geology, 265*(1-2), 160-170. Retrieved from https://ac.els-cdn.com/S0009254109000643/1-s2.0-S0009254109000643-main.pdf?_tid=c08b580d-c4a7-434d-8d23-fae97acd01dd&acdnat=1540382644_e66bc67531231d7d328e0af68b279029

Olabode, A., & Radonjic, M. (2013). Experimental investigations of caprock integrity in CO2 sequestration. *Energy procedia, 37*, 5014-5025.

Olabode, A., & Radonjic, M. (2017). Geochemical Markers in Shale-CO2 Experiment at Core Scale. *Energy procedia, 114*, 3840-3854.

Oldenburg, C. M. (2006). Migration mechanisms and potential impacts of CO2 leakage and seepage.

Oliveira, R., Pepin, A., & Carvalho, M. (2014). *Estimation for Representative Element Area of a Coquinas Analogue Using Statistical and Numerical Methods.* Paper presented at the SPE Latin America and Caribbean Petroleum Engineering Conference.

Onuma, T., & Ohkawa, S. (2009). Detection of surface deformation related with CO2 injection by DInSAR at In Salah, Algeria. *Energy procedia, 1*(1), 2177-2184.

Orlic, B. (2016). Geomechanical effects of CO 2 storage in depleted gas reservoirs in the Netherlands: Inferences from feasibility studies and comparison with

aquifer storage. *Journal of Rock Mechanics and Geotechnical Engineering, 8*(6), 846-859. doi:10.1016/j.jrmge.2016.07.003

Osisanya, S. O., & Harris, O. O. (2005). *Evaluation of equivalent circulating density of drilling fluids under high pressure/high temperature conditions.* Paper presented at the SPE Annual technical conference and Exhibition.

Pang, Z., Li, Y., Yang, F., & Duan, Z. (2012). Geochemistry of a continental saline aquifer for CO2 sequestration: The Guantao formation in the Bohai Bay Basin, North China. *Applied Geochemistry, 27*(9), 1821-1828.

Paterson, L., Lu, M., Connell, L., Ennis-King, J. P. (2008). *Numerical modeling of pressure and temperature profiles including phase transitions in carbon dioxide wells.* Paper presented at the SPE annual technical conference and exhibition.

Pearce, J., Dawson, G., Golab, A., Knuefing, L., Sommacal, S., Rudolph, V., & Golding, S. (2019). A combined geochemical and μCT study on the CO2 reactivity of Surat Basin reservoir and cap-rock cores: porosity changes, mineral dissolution and fines migration. *International Journal of Greenhouse Gas Control, 80*, 10-24.

Peng, Fan, J., Zhang, X., Chen, J., Li, Z., Jiang, D., & Liu, C. (2020). Computed tomography analysis on cyclic fatigue and damage properties of rock salt under gas pressure. *International Journal of Fatigue, 134*, 105523.

Peng, K., Zhou, J., Zou, Q., & Yan, F. (2019). Deformation characteristics of sandstones during cyclic loading and unloading with varying lower limits of stress under different confining pressures. *International Journal of Fatigue, 127*, 82-100.

Peter, A., Jin, X., Sheng, Y., Fan, X., & Yang, D. (2020). Static fatigue of saline rocks under different CO2 phase conditions. *Journal of Petroleum Science and Engineering*, 107940.

Peters, C. A. (2009). Accessibilities of reactive minerals in consolidated sedimentary rock: An imaging study of three sandstones. *Chemical Geology, 265*(1-2), 198-208.

Pierce, S., & Sjögersten, S. (2009). Effects of below ground CO2 emissions on plant and microbial communities. *Plant and Soil, 325*(1-2), 197-205. doi:10.1007/s11104-009-9969-1

Piller, M., Casagrande, D., Schena, G., & Santini, M. (2014). *Pore-scale simulation of laminar flow through porous media.* Paper presented at the Journal of Physics: Conference Series.

Pimienta, L., Esteban, L., Sarout, J., Liu, K., Dautriat, J., Delle Piane, C., & Clennell, M. B. (2017). Supercritical CO2 injection and residence time in fluid-saturated rocks: Evidence for calcite dissolution and effects on rock integrity. *International Journal of Greenhouse Gas Control, 67*, 31-48. doi:10.1016/j.ijggc.2017.09.014

Postma, T. J., Bandilla, K. W., & Celia, M. A. (2019). Estimates of CO2 leakage along abandoned wells constrained by new data. *International Journal of Greenhouse Gas Control, 84*, 164-179.

Prieditis, J., Wolle, C., & Notz, P. (1991). *A laboratory and field injectivity study: CO2 WAG in the San Andres formation of West Texas.* Paper presented at the SPE annual technical conference and exhibition.

Pruess, K., & Nordbotten, J. (2011). Numerical simulation studies of the long-term evolution of a CO 2 plume in a saline aquifer with a sloping caprock. *Transport in Porous Media, 90*(1), 135-151.

Quale, S., & Rohling, V. (2016). The European carbon dioxide capture and storage laboratory infrastructure (ECCSEL). *Green Energy & Environment, 1*(3), 180-194.

Rabbani, H. S., Or, D., Liu, Y., Lai, C.-Y., Lu, N. B., Datta, S. S., . . . Shokri, N. (2018). Suppressing viscous fingering in structured porous media. *Proceedings of the National Academy of Sciences, 115*(19), 4833-4838.

Ramezanian, M., & Emadi, H. (2020). Investigating effects of temperature and confining pressure on dynamic elastic properties and permeability—An experimental study. *Geomechanics for Energy and the Environment, 22*, 100179.

Ramírez, A., Hagedoorn, S., Kramers, L., Wildenborg, T., & Hendriks, C. (2010). Screening CO2 storage options in The Netherlands. *International Journal of Greenhouse Gas Control, 4*(2), 367-380. doi:10.1016/j.ijggc.2009.10.015

Rathnaweera, T., Ranjith, P., & Perera, M. (2016). Experimental investigation of geochemical and mineralogical effects of CO 2 sequestration on flow characteristics of reservoir rock in deep saline aquifers. *Scientific reports, 6*, 19362.

Ratnakar, R. R., Venkatraman, A., Kalra, A., & Dindoruk, B. (2020). On the prediction of gas solubility in brine solutions with single or mixed salts: Applications to gas injection and CO2 capture/sequestration. *Journal of Natural Gas Science and Engineering, 81*, 103450.

Rawat, R., Aggarwal, V., Hassan, M., Lee, P., Springham, S., Tan, T., & Lee, S. (2008). Nano-phase titanium dioxide thin film deposited by repetitive plasma focus: Ion irradiation and annealing based phase transformation and agglomeration. *Applied Surface Science, 255*(5), 2932-2941.

Razavi, M. R., Muhunthan, B., & Al Hattamleh, O. (2006). Representative elementary volume analysis of sands using X-ray computed tomography. *Geotechnical Testing Journal, 30*(3), 212-219.

Rempel, K. U., Liebscher, A., Heinrich, W., & Schettler, G. (2011). An experimental investigation of trace element dissolution in carbon dioxide: Applications to the geological storage of CO2. *Chemical Geology, 289*(3-4), 224-234.

Reynolds, C., & Krevor, S. (2015). Characterizing flow behavior for gas injection: Relative permeability of CO2-brine and N2-water in heterogeneous rocks. *Water resources research, 51*(12), 9464-9489.

Rice-Birchall, E. (2018). Geomechanical and geochemical analysis of the Captain X Sandstone Member in relation to CO2 sequestration.

Ricketts, B. (2016). Geological Trappings; Carbon Capture and Storage. Retrieved from http://www.geological-digressions.com/carbon-capture-and-storage-geological-traps/

Rigby, S. P., Jahan, H., Stevens, L., Uguna, C., Snape, C., Macnaughton, B., . . . Fletcher, R. S. (2020). Pore structural evolution of shale following thermochemical treatment. *Marine and Petroleum Geology, 112*, 104058.

Rinaldi, A. P., Vilarrasa, V., Rutqvist, J., & Cappa, F. (2015). Fault reactivation during CO2 sequestration: Effects of well orientation on seismicity and leakage. *Greenhouse Gases: Science and Technology, 5*(5), 645-656.

Rinehart, A. J., Dewers, T. A., Broome, S. T., & Eichhubl, P. (2016). Effects of CO2 on mechanical variability and constitutive behavior of the Lower Tuscaloosa Formation, Cranfield Injection Site, USA. *International Journal of Greenhouse Gas Control, 53*, 305-318.

Roberts, J. J., & Stalker, L. (2020). What have we learnt about CO2 leakage from CO2 release field experiments, and what are the gaps for the future? *Earth-science reviews*, 102939.

Rohmer, J., Tremosa, J., Marty, N., & Audigane, P. (2017). Modelling of the CO 2-Induced Degradation of a Fractured Caprock During Leakage: Potential for a Mechanical Self-Limiting Process. *Rock mechanics and rock engineering, 50*(10), 2763-2783.

Roy, P., Morris, J. P., Walsh, S. D., Iyer, J., & Carroll, S. (2018). Effect of thermal stress on wellbore integrity during CO2 injection. *International Journal of Greenhouse Gas Control, 77*, 14-26.

Rozhko, A. Y. (2020). Effects of pore fluids on quasi-static shear modulus caused by pore-scale interfacial phenomena. *Geophysical Prospecting, 68*(2), 631-656.

Rubin, E., & De Coninck, H. J. U. C. U. P. T. C. C. f. C. S., Part. (2005). IPCC special report on carbon dioxide capture and storage. *2*, 14.

Rutqvist, J. (2012). The geomechanics of CO 2 storage in deep sedimentary formations. *Geotechnical and Geological Engineering, 30*(3), 525-551.

Rutqvist, J., Vasco, D. W., & Myer, L. (2010). Coupled reservoir-geomechanical analysis of CO2 injection and ground deformations at In Salah, Algeria. *International Journal of Greenhouse Gas Control, 4*(2), 225-230.

Sadeghi, M. A., Agnaou, M., Barralet, J., & Gostick, J. (2020). Dispersion modeling in pore networks: A comparison of common pore-scale models and alternative approaches. *Journal of Contaminant Hydrology, 228*, 103578.

Saeedi, A., Rezaee, R., Evans, B., & Clennell, B. (2011). Multiphase flow behaviour during CO2 geo-sequestration: Emphasis on the effect of cyclic CO2–brine flooding. *Journal of Petroleum Science and Engineering, 79*(3-4), 65-85.

Samsonov, S., Czarnogorska, M., & White, D. (2015). Satellite interferometry for high-precision detection of ground deformation at a carbon dioxide storage site. *International Journal of Greenhouse Gas Control, 42*, 188-199.

Santibanez-Borda, E., Govindan, R., Elahi, N., Korre, A., & Durucan, S. (2019). Maximising the dynamic CO2 storage capacity through the optimisation of CO2 injection and brine production rates. *International Journal of Greenhouse Gas Control, 80*, 76-95.

Scheibe, T. D., Perkins, W. A., Richmond, M. C., McKinley, M. I., Romero-Gomez, P. D., Oostrom, M., . . . Zachara, J. M. (2015). Pore-scale and multiscale numerical simulation of flow and transport in a laboratory-scale column. *Water resources research, 51*(2), 1023-1035.

Schwartz, B., Huffman, K., Thornton, D., & Elsworth, D. (2019). The effects of mineral distribution, pore geometry, and pore density on permeability evolution in gas shales. *Fuel, 257*, 116005.

Seyyedi, M., Giwelli, A., White, C., Esteban, L., Verrall, M., & Clennell, B. (2020). Effects of geochemical reactions on multi-phase flow in porous media during CO2 injection. *Fuel, 269*, 117421.

Shan, P., & Lai, X. (2019). Mesoscopic structure PFC~ 2D model of soil rock mixture based on digital image. *Journal of Visual Communication and Image Representation, 58*, 407-415.

Shell. (2011). *Carbon capture and storgae demonstration competition. UKCCS-KT-S7.19-Shell-002*. Retrieved from 2011:

Shi, J., Yang, H., Peng, J., Wu, L., Xu, B., Liu, Y., & Zhao, B. (2019). InSAR Monitoring and Analysis of Ground Deformation Due to Fluid or Gas Injection in Fengcheng Oil Field, Xinjiang, China. *Journal of the Indian Society of Remote Sensing, 47*(3), 455-466.

Shiflett, M. B., Kasprzak, D. J., Junk, C. P., & Yokozeki, A. (2008). Phase behavior of {carbon dioxide+[bmim][Ac]} mixtures. *The Journal of Chemical Thermodynamics, 40*(1), 25-31.

Shin, H. Y., & Wu, J. (2010). Modelling of state for the phase behavior of carbon dioxide− polymer systems. *Industrial & Engineering Chemistry Research, 49*(16), 7678-7684.

Shukla, P., & De Wit, A. (2016). Fingering dynamics driven by a precipitation reaction: Nonlinear simulations. *Physical Review E, 93*(2), 023103.

Shukla, R., Ranjith, P., Haque, A., & Choi, X. (2010). A review of studies on CO2 sequestration and caprock integrity. *Fuel, 89*(10), 2651-2664.

Sidiq, H., Amin, R., & Kennaird, T. (2017). The study of relative permeability and residual gas saturation at high pressures and high temperatures. *Advances in Geo-Energy Research, 1*(1), 64-68.

Siriwardane, H. J., Gondle, R. K., Varre, S. B., Bromhal, G. S., & Wilson, T. H. (2016). Geomechanical response of overburden caused by CO2 injection into a depleted oil reservoir. *Journal of Rock Mechanics and Geotechnical Engineering, 8*(6), 860-872. doi:https://doi.org/10.1016/j.jrmge.2016.06.009

Sokama-Neuyam, Y. A., & Ursin, J. R. (2018). The coupled effect of salt precipitation and fines mobilization on CO2 injectivity in sandstone. *Greenhouse Gases: Science and Technology, 8*(6), 1066-1078.

Song, Z., Shi, H., Zhang, X., & Zhou, T. (2020). Prediction of CO2 solubility in ionic liquids using machine learning methods. *Chemical Engineering Science, 223*, 115752.

Srodon, A., Radlinski, A., Szymczak, P. (2018). *Changes in pore geometry of limestone rocks as a result of a natural dissolution process.* Paper presented at the EGU General Assembly Conference Abstracts.

Stenhouse, M. J., Gale, J., & Zhou, W. (2009). Current status of risk assessment and regulatory frameworks for geological CO2 storage. *Energy Procedia, 1*(1), 2455-2462. doi:10.1016/j.egypro.2009.02.007

Sun, H., Belhaj, H., Tao, G., Vega, S., Liu, L. (2019). Rock properties evaluation for carbonate reservoir characterization with multi-scale digital rock images. *Journal of Petroleum Science and Engineering, 175*, 654-664.

Sun, X., Wang, Z., Li, H., He, H., & Sun, B. (2021). A simple model for the prediction of mutual solubility in CO2-brine system at geological conditions. *Desalination, 504*, 114972.

Sun, Y., Aman, M., & Espinoza, D. N. (2016). Assessment of mechanical rock alteration caused by CO2 water mixtures using indentation and scratch experiments. *International Journal of Greenhouse Gas Control, 45*, 9-17.

Sun, Y. K., Li, Q., Yang, D. X., & Liu, X. H. (2016). Laboratory core flooding experimental systems for CO2 geosequestration: An updated review over the past decade. *Journal of Rock Mechanics and Geotechnical Engineering, 8*(1), 113-126. doi:10.1016/j.jrmge.2015.12.001

Sun, Z., Espinoza, D. N., Balhoff, M. T., & Dewers, T. A. (2017). Discrete Element Modeling of Micro-scratch Tests: Investigation of Mechanisms of CO 2 Alteration in Reservoir Rocks. *Rock mechanics and rock engineering, 50*(12), 3337-3348.

Suppe, J. (2014). Fluid overpressures and strength of the sedimentary upper crust. *Journal of Structural Geology, 69*, 481-492.

Sympatec, G. (2017). Particle shape analysis. Retrieved from https://www.sympatec.com/en/particle-measurement/glossary/particle-shape/

Takashimizu, Y., & Iiyoshi, M. (2016). New parameter of roundness R: circularity corrected by aspect ratio. *Progress in Earth and Planetary Science, 3*(1), 2.

Tan, Q., You, L., Kang, Y., Zhang, X., Meng, S. (2020). Changes in pore structures and porosity-permeability evolution of saline-lacustrine carbonate reservoir triggered by fresh water-rock reaction. *Journal of Hydrology, 580*, 124375.

Tan, W., Mikhaltsevitch, V., Lebedev, M., Glubokovskikh, S., & Gurevich, B. (2019). The sample boundary effect in the low-frequency measurements of the elastic moduli of rocks. *ASEG Extended Abstracts, 2019*(1), 1-3.

Tang, J.-Z., Yang, S.-Q., Tian, W.-L., & Tao, Y. (2019). Effect of confining pressure on mechanics and deformation behavior of sandstone containing a single inclined joint. *European Journal of Environmental and Civil Engineering*, 1-24.

Tatar, A., Shokrollahi, A., Lee, M., Kashiwao, T., & Bahadori, A. (2015). Prediction of supercritical CO2/brine relative permeability in sedimentary basins during carbon dioxide sequestration. *Greenhouse Gases: Science and Technology, 5*(6), 756-771.

Tatar, A., Naseri, S., Sirach, N., Lee, M., & Bahadori, A. (2015a). Prediction of reservoir brine properties using radial basis function (RBF) neural network. *Petroleum, 1*(4), 349-357.

Teng, Y., Wang, P., Jiang, L., Liu, Y., Song, Y., & Wei, Y. (2020). An experimental study of density-driven convection of fluid pairs with viscosity contrast in porous media. *International Journal of Heat and Mass Transfer, 152*, 119514.

Thermofisher. (2018). *Thermo scientific Avizo software user guide*: Thermofisher.

Thiele, S. T., Jessell, M. W., Lindsay, M., Ogarko, V., Wellmann, J. F., & Pakyuz-Charrier, E. (2016). The topology of geology 1: Topological analysis. *Journal of Structural Geology, 91*, 27-38.

Tooseh, E. K., Jafari, A., & Teymouri, A. (2018). Gas-water-rock interactions and factors affecting gas storage capacity during natural gas storage in a low permeability aquifer. *Petroleum Exploration and Development, 45*(6), 1123-1128.

Tsai, C.-H., Yang, C.-H., Yu, C.-W., Wang, Y.-R., Chiao, C.-H., & Yang, M.-W. (2013). Mineral migration and regeneration reactions in the two phase flow experiment. *Energy Procedia, 37*, 5580-5587.

Valle, L., Grima, C., Rodríguez, R., & Llopis, C. (2020). Effect of scCO2-brine mixture on injectivity and storage capacity in rock samples of naturally

fractured carbonate formations. *Journal of Natural Gas Science and Engineering, 81*, 103452.

Vanorio, T., Nur, A., & Ebert, Y. (2011). Rock physics analysis and time-lapse rock imaging of geochemical effects due to the injection of CO 2 into reservoir rocks. *Geophysics, 76*(5), O23-O33.

Vialle, S., & Vanorio, T. (2011a). Laboratory measurements of elastic properties of carbonate rocks during injection of reactive CO2-saturated water. *Geophysical Research Letters, 38*(1), n/a-n/a. doi:10.1029/2010gl045606

Vialle, S., & Vanorio, T. (2011b). Laboratory measurements of elastic properties of carbonate rocks during injection of reactive CO2-saturated water. *Geophysical Research Letters, 38*(1).

Viete, D. R., & Ranjith, P. G. (2006). The effect of CO2 on the geomechanical and permeability behaviour of brown coal: implications for coal seam CO2 sequestration. *International journal of coal geology, 66*(3), 204-216.

Vilarrasa, V., & Carrera, J. (2015). Geologic carbon storage is unlikely to trigger large earthquakes and reactivate faults through which CO2 could leak. *Proceedings of the National Academy of Sciences*, 201413284.

Vilarrasa, V., Carrera, J., Olivella, S., Rutqvist, J., & Laloui, L. (2019). Induced seismicity in geologic carbon storage. *Solid Earth, 10*(3), 871-892.

Vilarrasa, V., Makhnenko, R. Y., & Laloui, L. (2017). Potential for fault reactivation due to CO2 injection in a semi-closed saline aquifer. *Energy procedia, 114*, 3282-3290.

Vilarrasa, V., Rinaldi, A. P., & Rutqvist, J. (2017). Long-term thermal effects on injectivity evolution during CO2 storage. *International Journal of Greenhouse Gas Control, 64*, 314-322.

Vilarrasa, V., Silva, O., Carrera, J., & Olivella, S. (2013). Liquid CO2 injection for geological storage in deep saline aquifers. *International Journal of Greenhouse Gas Control, 14*, 84-96.

Vision, A. (2012). Uniformity of Particle Shape for Chromatography Packing Materials Used in HPLC. Retrieved from https://particleshape.com/particle-shape-application-example-chromatography-packing-materials/

Vivek, R., & Suresh Kumar, G. (2021). Evolution of hysteresis relative permeability of wetting brine phase using contact angle hysteresis in a partially saturated CO2-brine system. *Energy Sources, Part A: Recovery, Utilization, and Environmental Effects, 43*(11), 1290-1306.

Voorn, Exner, Barnhoorn, Baud, Reuschlé. (2015). Porosity, permeability and 3D fracture network characterisation of dolomite reservoir rock samples. *Journal of Petroleum Science and Engineering, 127*, 270-285.

Walls, J. D., & Sinclair, S. W. (2011). Eagle Ford shale reservoir properties from digital rock physics. *First Break, 29*(6).

Wang, D., Dong, B., Breen, S., Zhao, M., Qiao, J., Liu, Y., . . . Song, Y. (2015). Approaches to research on CO 2/brine two-phase migration in saline aquifers. *Hydrogeology Journal, 23*(1), 1-18.

Wang, J., Hu, L., Pan, L., & Zhang, K. (2018). Numerical studies of CO 2 and brine leakage into a shallow aquifer through an open wellbore. *Hydrogeology Journal, 26*(2), 495-509.

Wang, R.-h., Huo, H.-j., Huang, Z.-y., Song, H.-f., Ni, H.-j.(2014). Experimental and numerical simulations of bottom hole temperature and pressure distributions of supercritical CO 2 jet for well-drilling. *Journal of Hydrodynamics, 26*(2), 226-233.

Wang, S., Li, X., Du, K., Wang, S., & Tao, M. (2018). Experimental study of the triaxial strength properties of hollow cylindrical granite specimens under coupled external and internal confining stresses. *Rock mechanics and rock engineering, 51*(7), 2015-2031.

Wang, Y., Zhang, L., Ren, S., Ren, B., Chen, B., & Lu, J. (2020). Identification of potential CO2 leakage pathways and mechanisms in oil reservoirs using fault tree analysis. *Greenhouse Gases: Science and Technology, 10*(2), 331-346.

Wang, Z., Wang, R., Li, T., & Zhao, M. (2017). The combined effects of pore structure and pore fluid on the acoustic properties of cracked and vuggy synthetic rocks. *Journal of Petroleum Science and Engineering, 156*, 202-211.

White, S., Carroll, S., Chu, S., Bacon, D., Pawar, R., Cumming, L., . . . Middleton, R. (2020). A risk-based approach to evaluating the Area of Review and leakage risks at CO2 storage sites. *International Journal of Greenhouse Gas Control, 93*, 102884.

Whittaker, S., Rostron, B., Hawkes, C., Gardner, C., White, D., Johnson, J., . . . Seeburger, D. (2011). A decade of CO2 injection into depleting oil fields: monitoring and research activities of the IEA GHG Weyburn-Midale CO2 Monitoring and Storage Project. *Energy procedia, 4*, 6069-6076.

Wiegers, C. E., & Schäfer, D. (2015). Numerische Szenariosimulationen zur Ausbreitung von hochmineralisiertem Wasser in oberflächennahen SüßwasseraquiferenNumerical simulations of spreading scenarios of highly mineralized water in shallow freshwater aquifers. *Grundwasser, 20*(2), 85-95.

Wong, & Baud, P. (2012). The brittle-ductile transition in porous rock: A review. *Journal of Structural Geology, 44*, 25-53.

Wong, Szeto, Zhang. (1992). Effect of loading path and porosity on the failure mode of porous rocks.

Wood, D. M. (1990). *Soil behaviour and critical state soil mechanics*: Cambridge university press.

Wu, L., Thorsen, R., Ottesen, S., Meneguolo, R., Hartvedt, K., Ringrose, P., & Nazarian, B. (2021). Significance of fault seal in assessing CO2 storage capacity and containment risks–an example from the Horda Platform, northern North Sea. *Petroleum Geoscience*.

Wu, Y., Tahmasebi, P., Yu, H., Lin, C., Wu, H., & Dong, C. (2020). Pore-Scale 3D Dynamic Modeling and Characterization of Shale Samples: Considering the Effects of Thermal Maturation. *Journal of Geophysical Research: Solid Earth, 125*(1), e2019JB018309.

Wu, Z., Luhmann, A., Rinehart, A., Mozley, P., Dewers, T., Heath, J., & Majumdar, B. (2018). *Controls of Cement Texture and Composition on Sandstone Mechanical Property Changes From Reaction With CO2-Rich Brine.* Paper presented at the AAPG ACE 2018.

Xia, M., & Zhou, K.-p. (2010). Particle simulation of the failure process of brittle rock under triaxial compression. *International Journal of Minerals, Metallurgy, and Materials, 17*(5), 507-513.

Xiao, T., Xu, H., Moodie, N., Esser, R., Jia, W., Zheng, L., . . . McPherson, B. (2020). Chemical-Mechanical Impacts of CO2 Intrusion Into Heterogeneous Caprock. *Water resources research, 56*(11), e2020WR027193.

Xie, H., Li, X., Fang, Z., Wang, Y., Li, Q., Shi, L., . . . Hou, Z. (2014). Carbon geological utilization and storage in China: current status and perspectives. *Acta Geotechnica, 9*(1), 7-27.

Xie, Y., Dong, H., Zhang, S., Lu, X., & Ji, X. (2016). Solubilities of CO2, CH4, H2, CO and N2 in choline chloride/urea. *Green Energy & Environment, 1*(3), 195-200.

Xu, Q., Wang, X., & Chen, J. (2020). Quantitative evaluation of pore-scale heterogeneity based on statistical analysis of a pore network model of unconsolidated porous media. *HYDROGEOLOGY JOURNAL*.

Xu, T., Kharaka, Y. K., Doughty, C., Freifeld, B. M., & Daley, T. M. (2010). Reactive transport modeling to study changes in water chemistry induced by CO2 injection at the Frio-I Brine Pilot. *Chemical geology, 271*(3-4), 153-164.

Yamasaki, A. (2003). An overview of CO2 mitigation options for global warming—emphasizing CO2 sequestration options. *Journal of chemical engineering of Japan, 36*(4), 361-375.

Yan, W., Huang, S., & Stenby, E. H. (2011). Measurement and modeling of CO2 solubility in NaCl brine and CO2–saturated NaCl brine density. *International Journal of Greenhouse Gas Control, 5*(6), 1460-1477.

Yang, C., Zhang, D., Zhao, C., Han, B., Sun, R., Du, J., & Chen, L. (2019). Ground deformation revealed by Sentinel-1 MSBAS-InSAR time-series over karamay oilfield, China. *Remote Sensing, 11*(17), 2027.

Yang, Q., Zhao, W., Dixon, T. H., Amelung, F., Han, W. S., & Li, P. (2015). InSAR monitoring of ground deformation due to CO2 injection at an enhanced oil recovery site, West Texas. *International Journal of Greenhouse Gas Control, 41*, 20-28.

Yang, R., Zhang, J., Chen, H., Jiang, R., Sun, Z., & Rui, Z. (2019). The injectivity variation prediction model for water flooding oilfields sustainable development. *Energy, 189*, 116317.

Yang, X., Buscheck, T. A., Mansoor, K., Wang, Z., Gao, K., Huang, L., . . . Carroll, S. A. (2019). Assessment of geophysical monitoring methods for detection of brine and CO2 leakage in drinking water aquifers. *International Journal of Greenhouse Gas Control, 90*, 102803.

Yasmaniar, G., Prakoso, S., & Sitaresmi, R. (2019). *The Effect of Pore Geometry on the Flow Unit and Its Impact to Permeability of the Reservoir Rock.* Paper presented at the IOP Conference Series: Materials Science and Engineering.

Yuan, G., Cao, Y., Gluyas, J., Li, X., Xi, K., Wang, Y., . . . Oxtoby, N. H. (2015). Feldspar dissolution, authigenic clays, and quartz cements in open and closed sandstone geochemical systems during diagenesis: Typical examples from two sags in Bohai Bay Basin, East ChinaDiagenesis in Open and Closed Sandstone Geochemical Systems. *AAPG Bulletin, 99*(11), 2121-2154.

Yuan, G., Cao, Y., Jia, Z., Gluyas, J., Yang, T., Wang, Y., & Xi, K. (2015). Selective dissolution of feldspars in the presence of carbonates: The way to generate secondary pores in buried sandstones by organic CO2. *Marine and Petroleum Geology, 60*, 105-119.

Yuan, G., Cao, Y., Schulz, H.-M., Hao, F., Gluyas, J., Liu, K., . . . Li, F. (2019). A review of feldspar alteration and its geological significance in sedimentary basins: From shallow aquifers to deep hydrocarbon reservoirs. *Earth-science reviews, 191*, 114-140.

Yusof, M. A., Ibrahim, M. A., Idress, M., Idris, A. K., M Saaid, I., Mohd Rodzi, N., . . . Azhari Awangku Matali, A. A. (2020). *Effects of CO/Rock/Formation Brine Parameters on CO Injectivity for Sequestration.* Paper presented at the Offshore Technology Conference Asia.

Zhang. (2017). Examination of effective stress in clay rock. *Journal of Rock Mechanics and Geotechnical Engineering, 9*(3), 479-489.

Zhang, Jia, N., Liu, L. (2019). CO2 storage in fractured nanopores underground: Phase behaviour study. *Applied energy, 238*, 911-928.

Zhang, G., Zhou, D., Wang, P., Zhang, K., & Tang, M. (2020). Influence of supercritical CO2-water on the micromechanical properties of sandstone. *International Journal of Greenhouse Gas Control, 97*, 103040.

Zhang, Q., Hu, S., Li, X., & Shi, L. (2019). Preliminary Experimental Study of Effect of CO2-H2O Biphasic Fluid on Mechanical Behavior of Sandstone under True Triaxial Compression. *International Journal of Geomechanics, 19*(2), 06018036.

Zhang, Y., Zhong, H.-R., Zhang, X., Gao, S.-C., & Zhang, D. (2020). Orthogonal microscopy image acquisition analysis technique for rock sections in polarizer angle domain. *Journal of Structural Geology, 140*, 104174.

Zhao, J., Qin, F., Derome, D., & Carmeliet, J. (2020). Simulation of Quasi-static Drainage Displacement in Porous Media on Pore-scale: Coupling Lattice Boltzmann Method and Pore Network Model. *Journal of Hydrology*, 125080.

Zheng, H., Feng, X.-T., & Pan, P.-Z. (2015). Experimental investigation of sandstone properties under CO2–NaCl solution-rock interactions. *International Journal of Greenhouse Gas Control, 37*, 451-470.

Zoback, M. D., & Gorelick, S. M. (2012). Earthquake triggering and large-scale geologic storage of carbon dioxide. *Proceedings of the National Academy of Sciences, 109*(26), 10164-10168. Retrieved from https://www.ncbi.nlm.nih.gov/pmc/articles/PMC3387039/pdf/pnas.201202473.pdf

Zou, Y., Li, S., Ma, X., Zhang, S., Li, N., & Chen, M. (2018). Effects of CO2–brine–rock interaction on porosity/permeability and mechanical properties during supercritical-CO2 fracturing in shale reservoirs. *Journal of Natural Gas Science and Engineering, 49*, 157-168.

Zulqarnain, M., Zeidouni, M., & Hughes, R. G. (2017). *Static and dynamic CO2 storage capacity estimates of a potential CO2 geological sequestration site in Louisiana chemical corridor.* Paper presented at the Carbon Management Technology Conference.

Appendices

Appendix 1a: SEM Images of the dry sample before compression
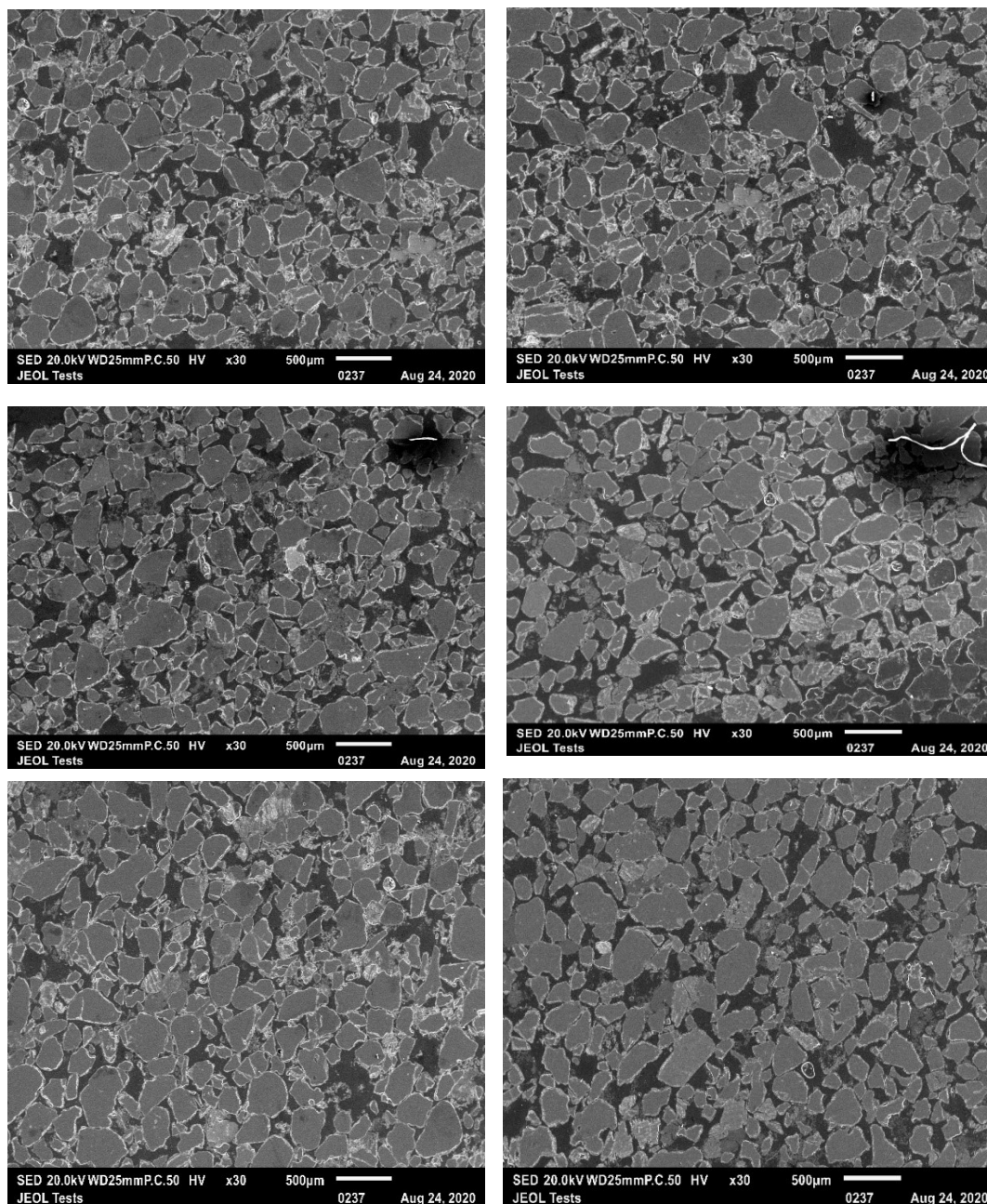
Appendix 1b: SEM images of the dry sample after compression
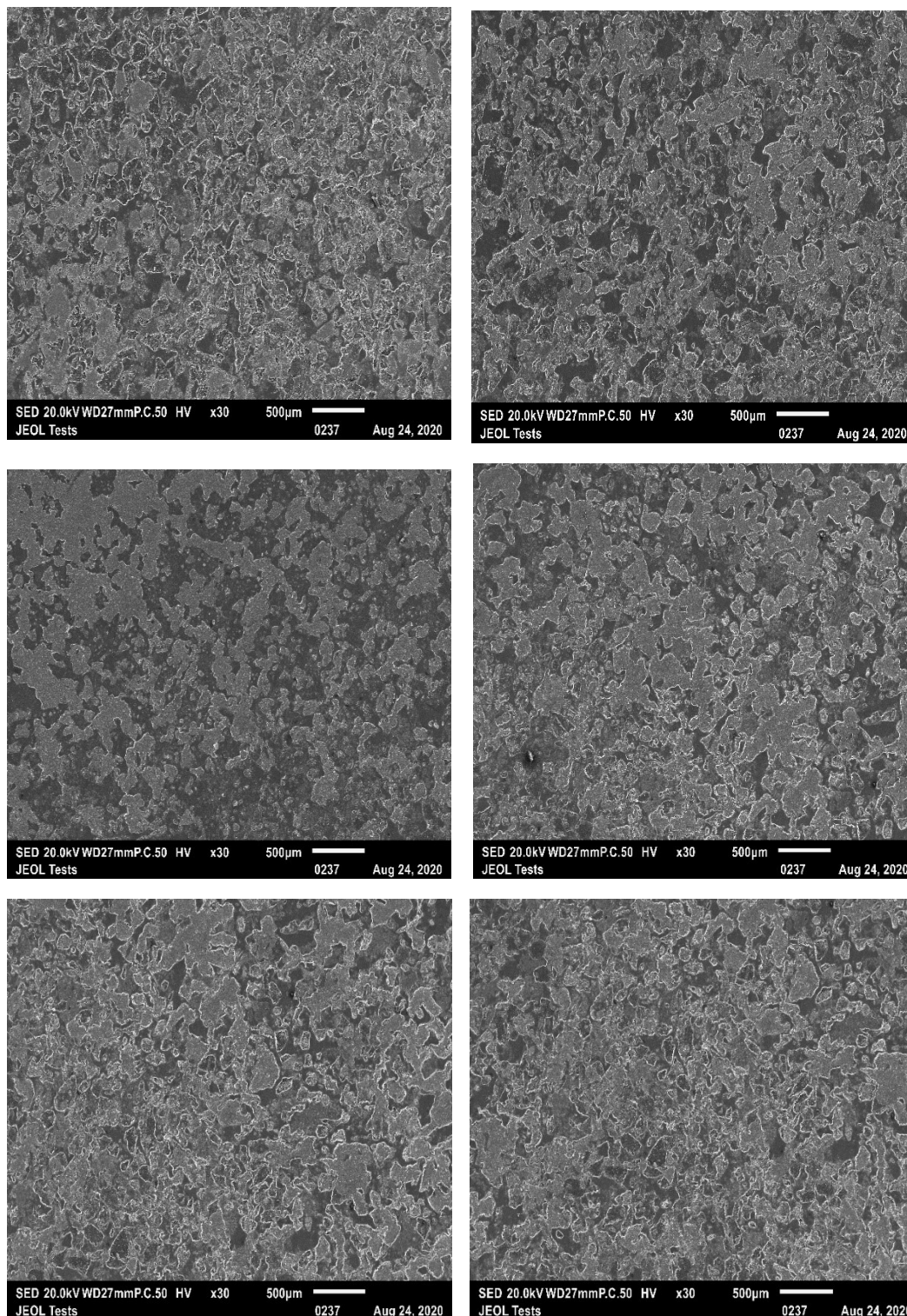
Appendix 1c: The topology of minerals in dry rock at higher resolution before compression
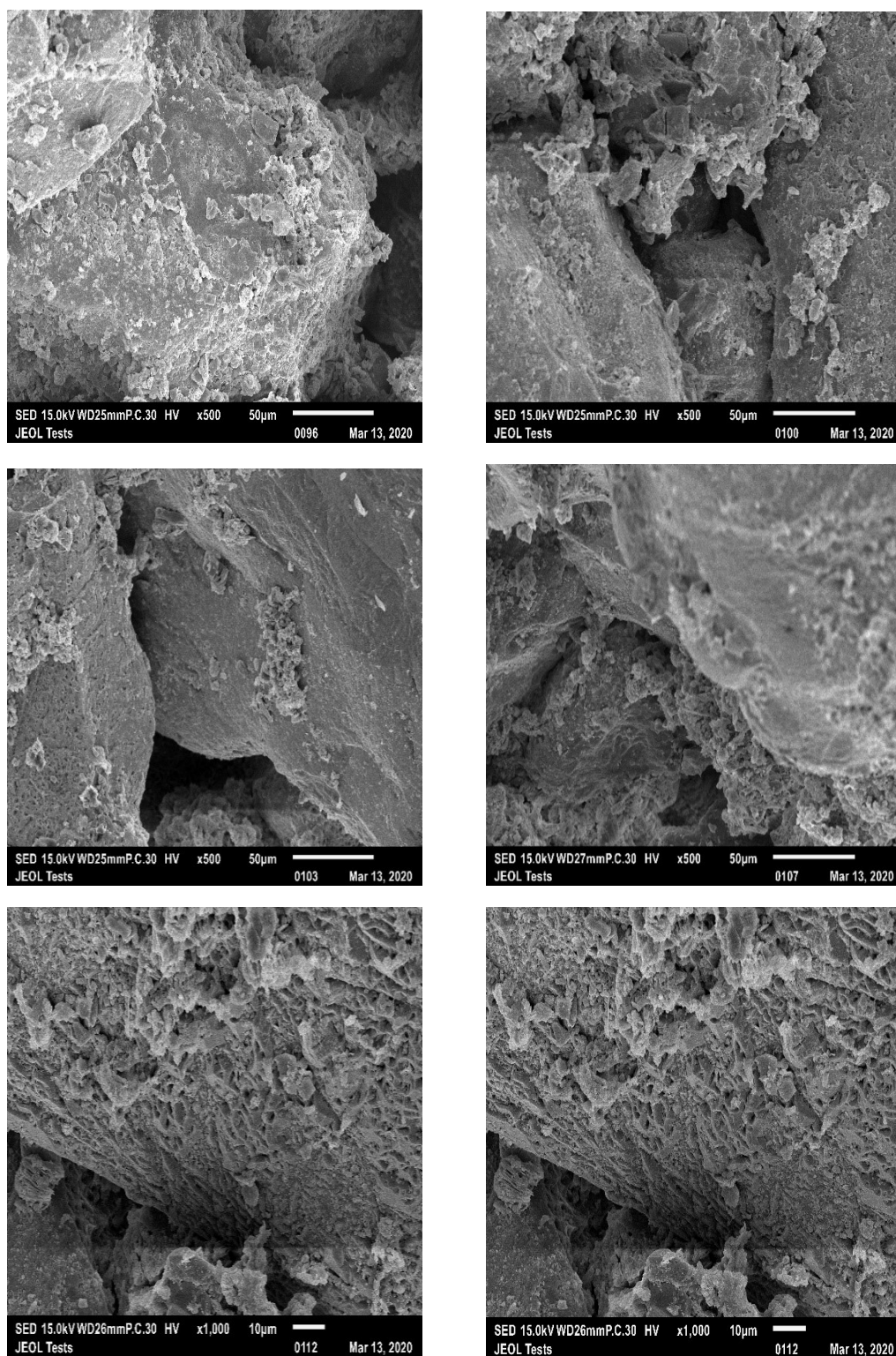
Appendix 1d: The topology of minerals in dry rock at higher resolution after compression
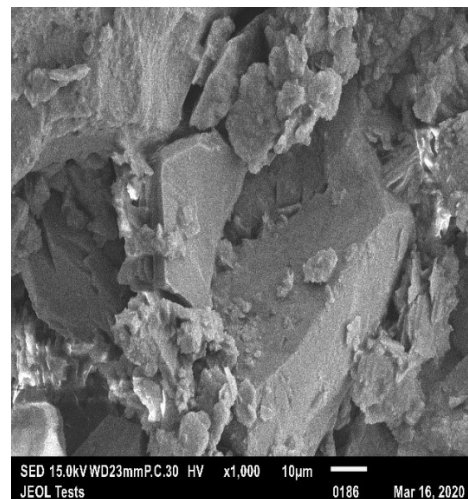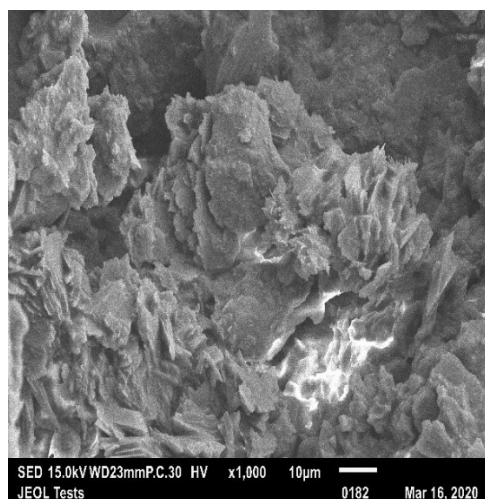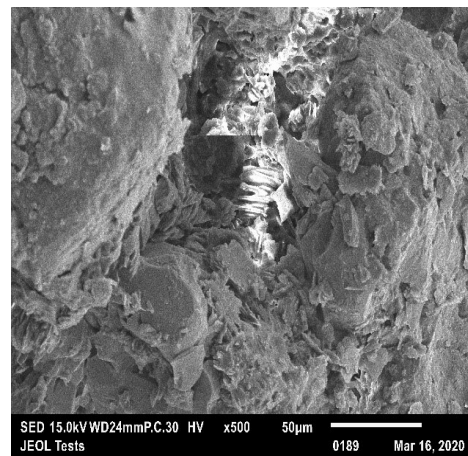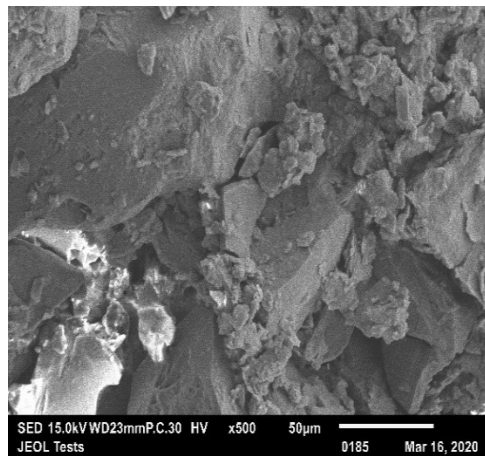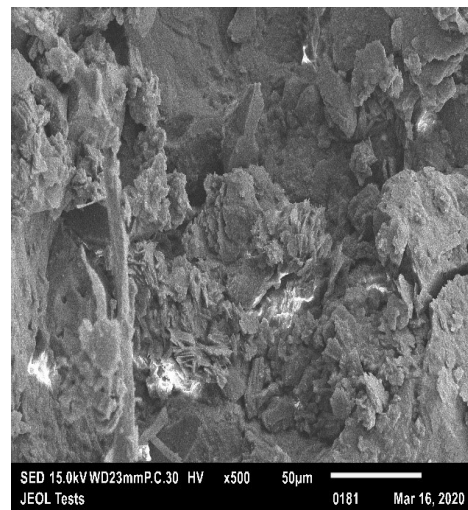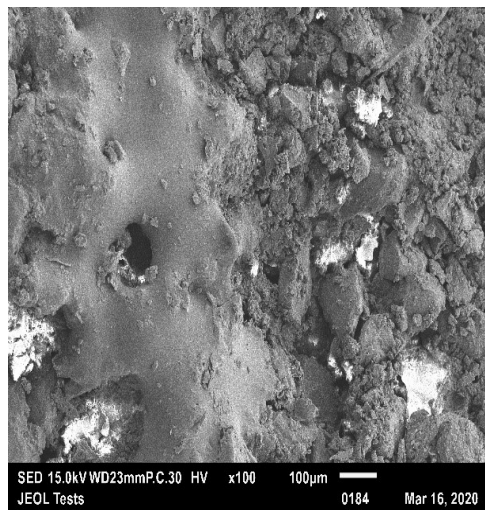
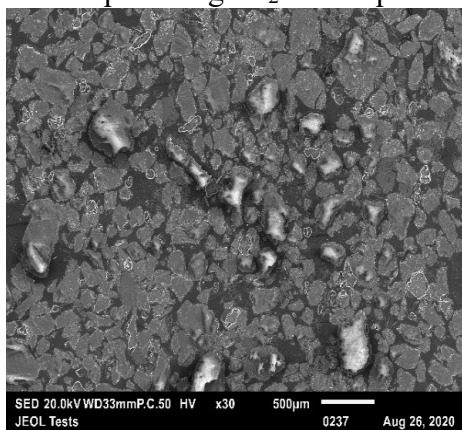**Appendix 2:** Pore scale and mineral topology SEM Images of the other samples
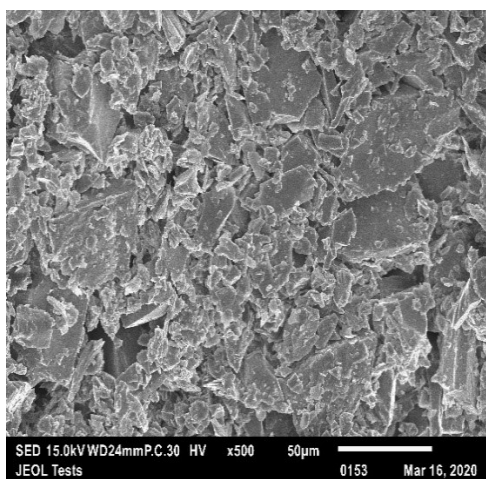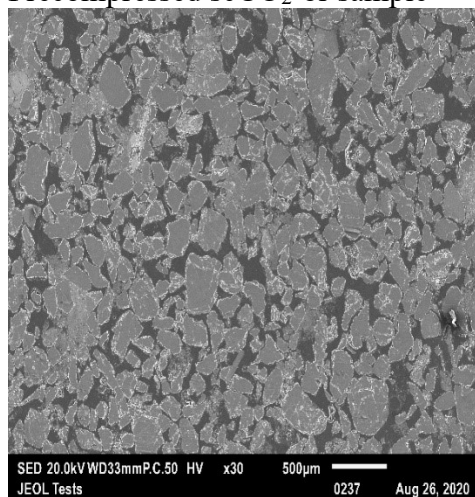
Precompressed brine sample   Postcompressed brine sample
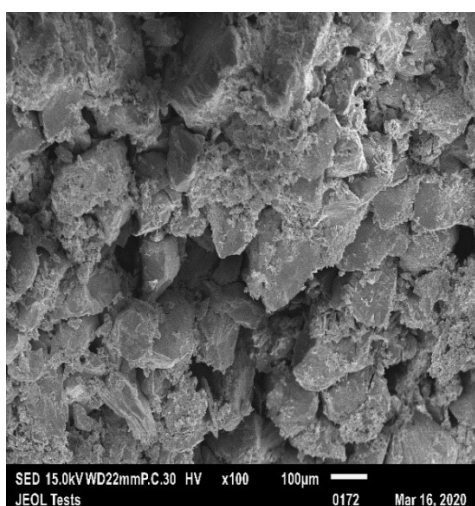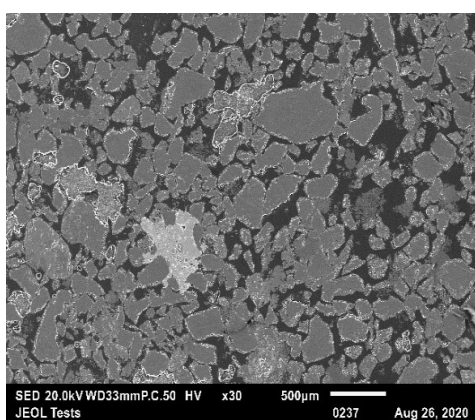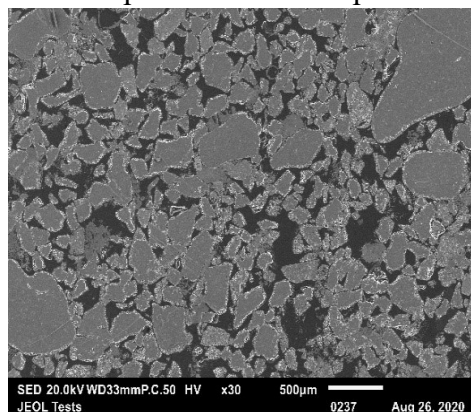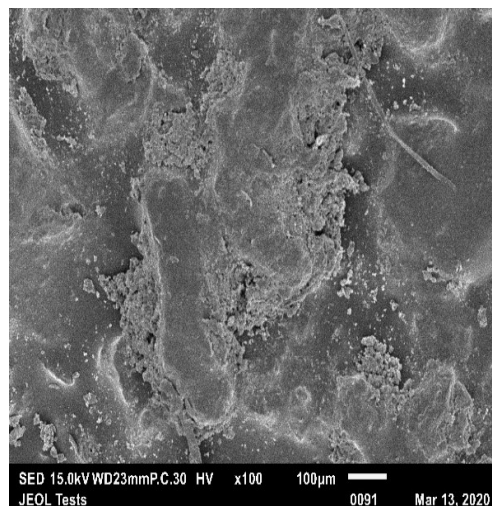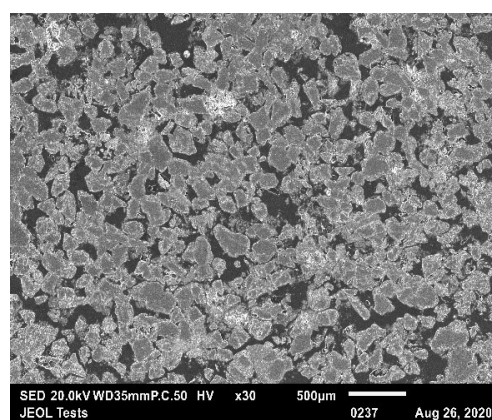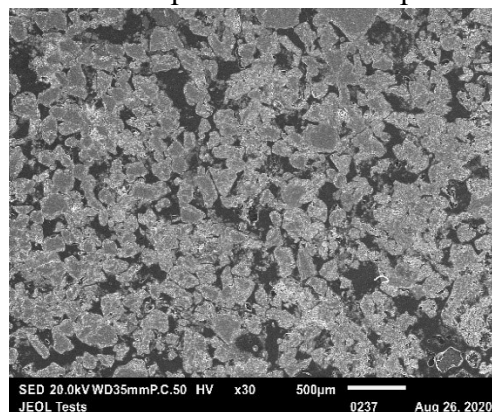
Precompressed gCO$_2$-br sample | Postcompressed gCO$_2$-br sample
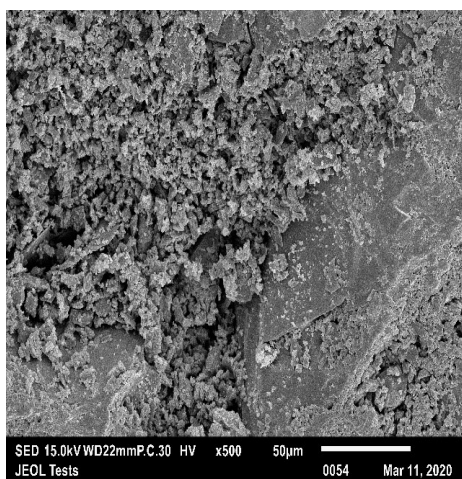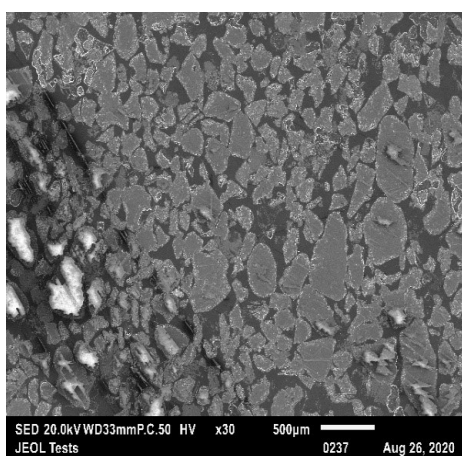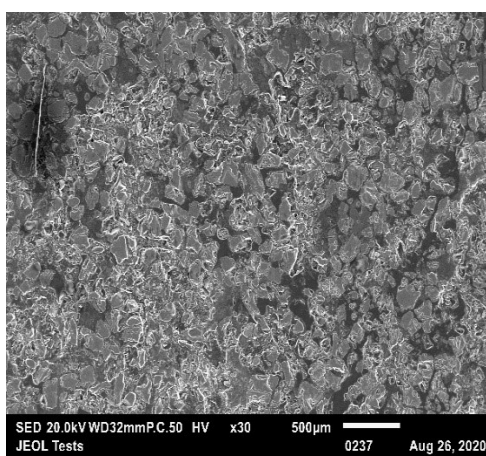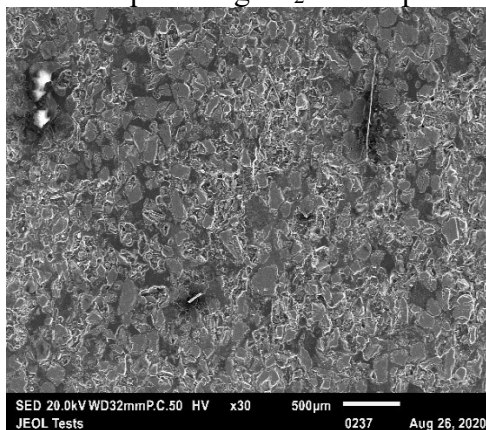
Precompressed scCO$_2$-br sample   Postcompressed scCO$_2$-br sample
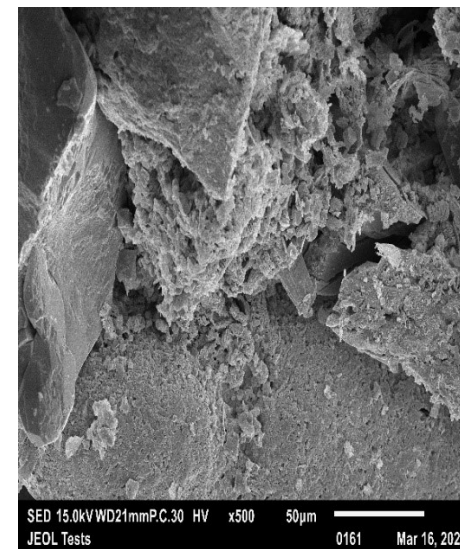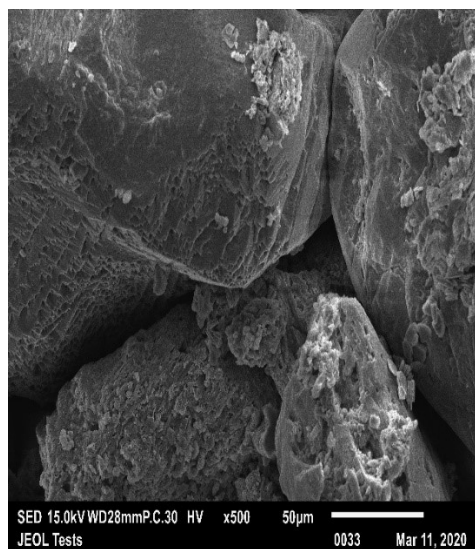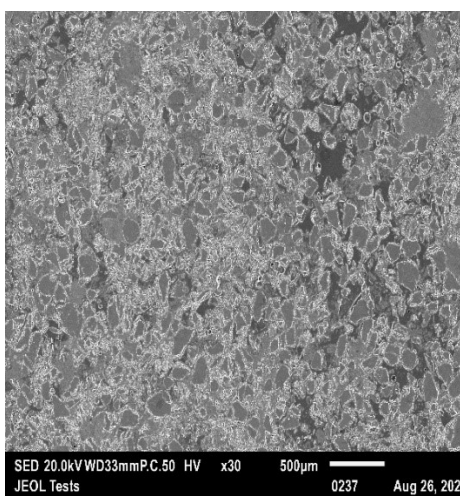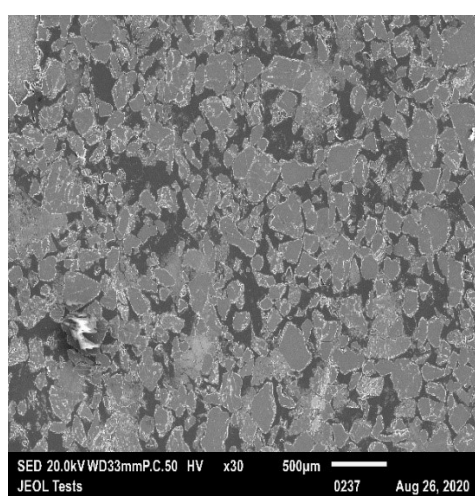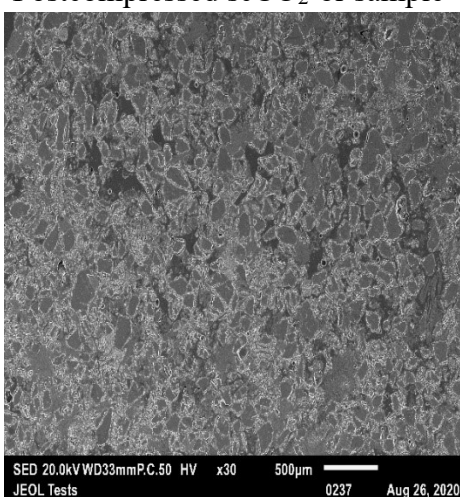
Precompressed gCO₂ sample | Postcompressed gCO₂ sample
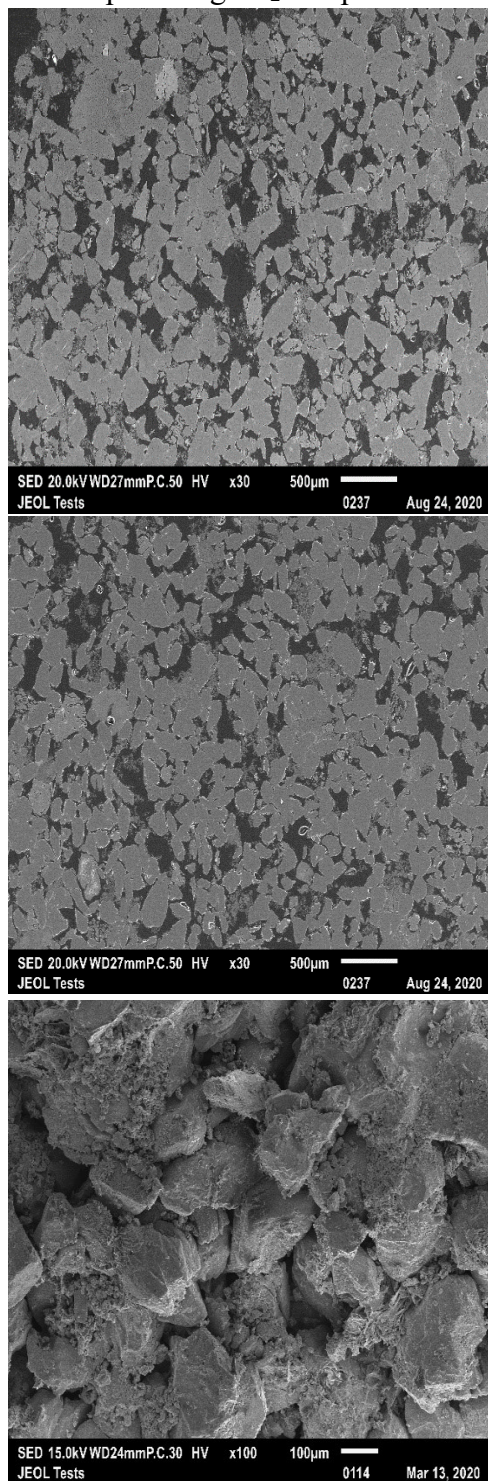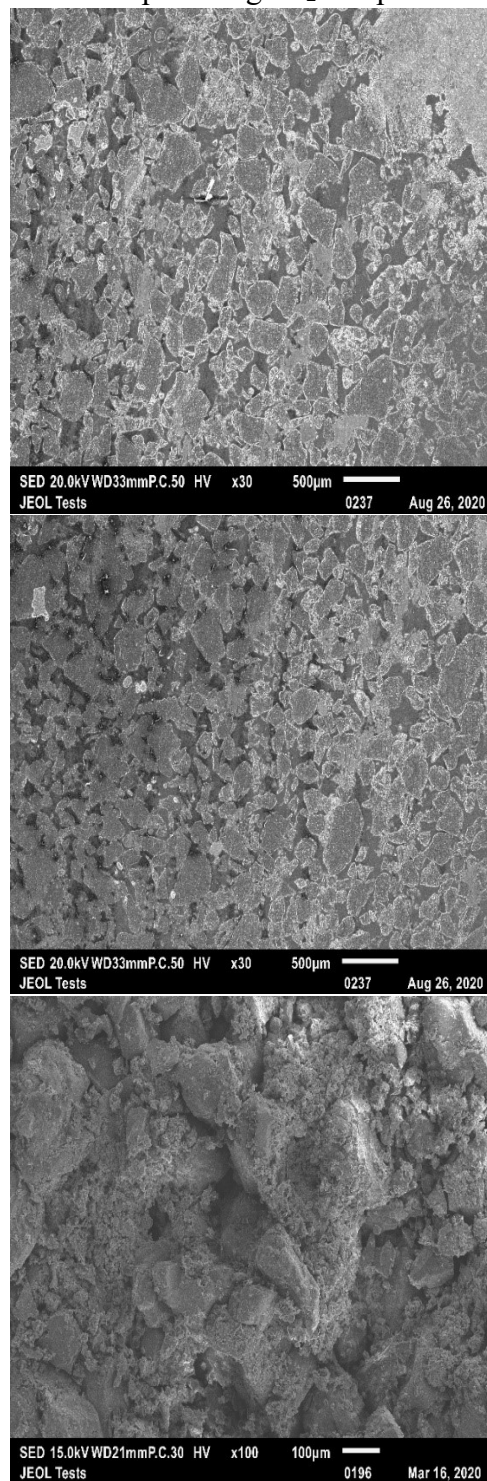
Appendix 3a: Fatigue curves for the dry sample
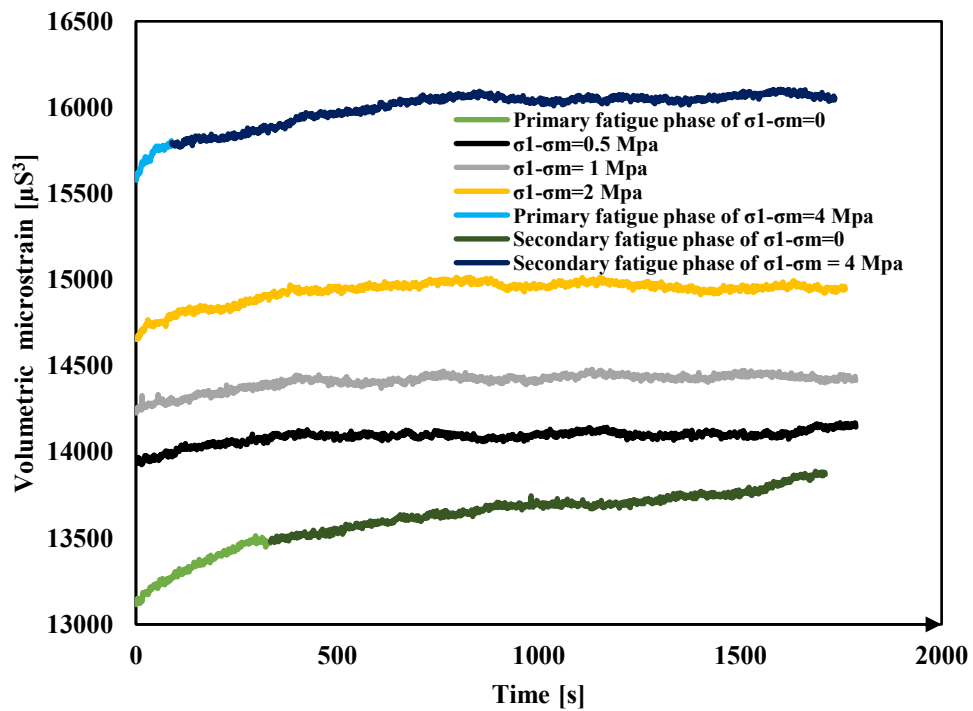
Fatigue curve for the dry sample under different deviatoric stresses
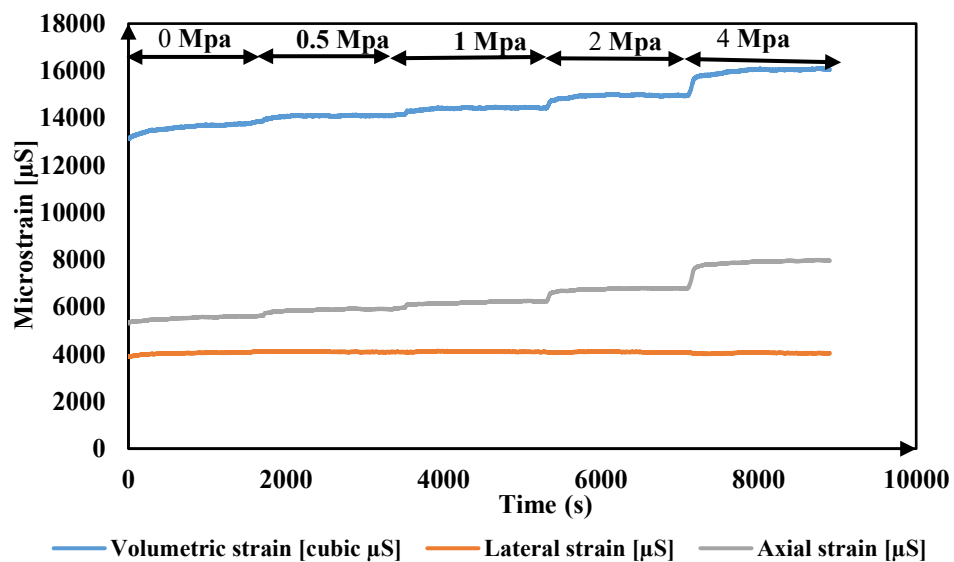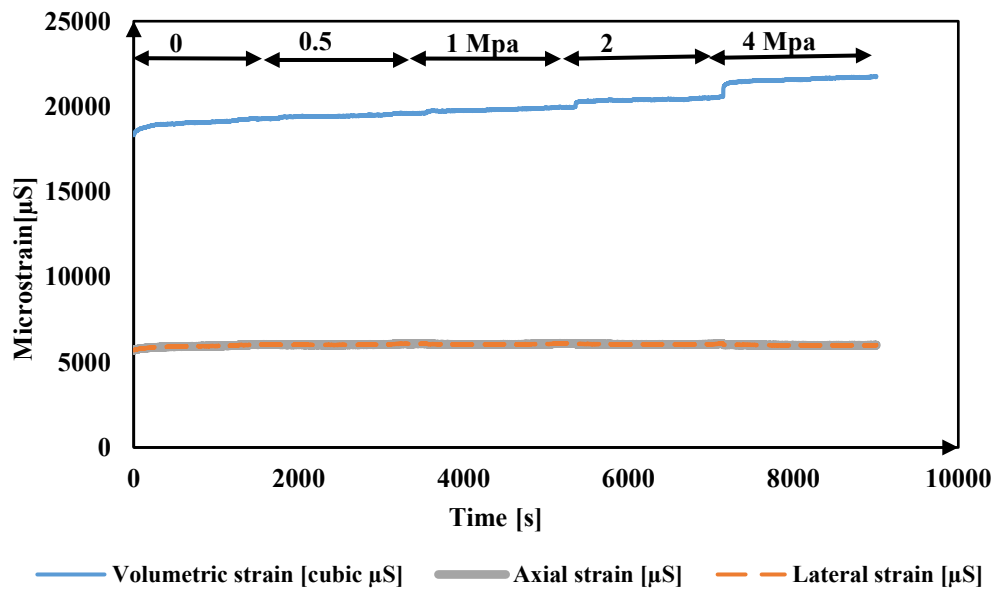

Combined fatigue curves under the different deviatoric stresses from 0 to 4Mpa for the dry sample

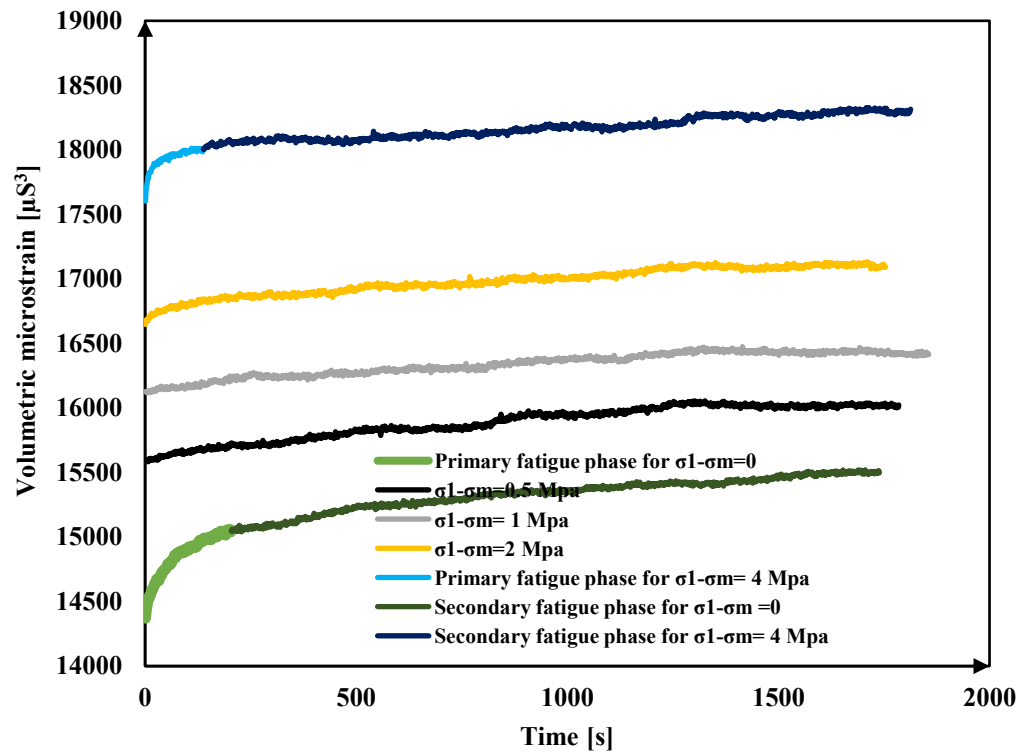**Appendix 3b:** Fatigue curves for the gCO$_2$-br sample
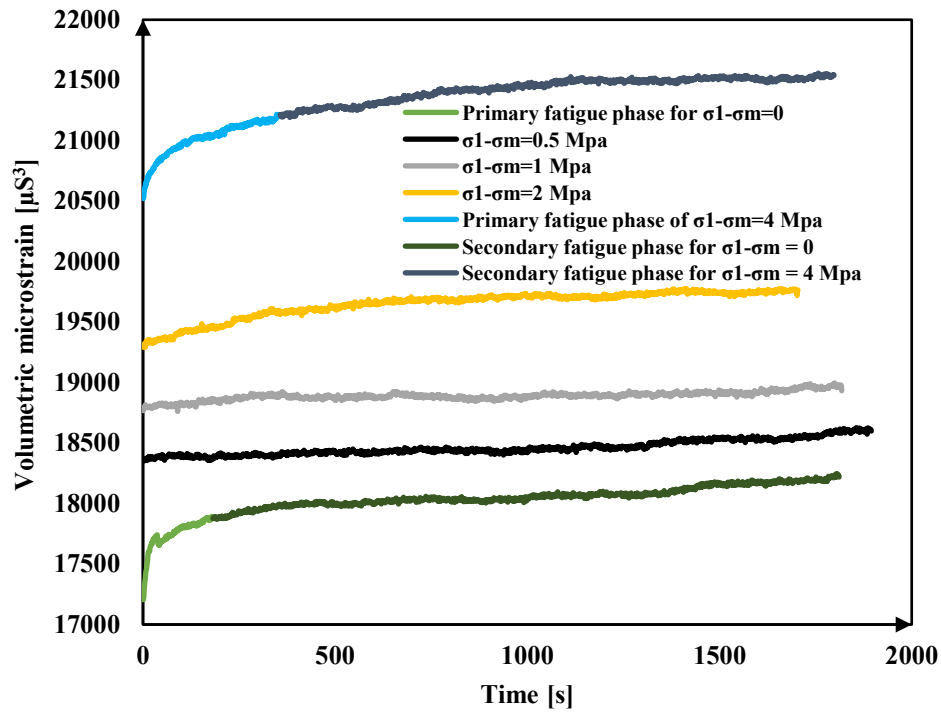
Fatigue curve for the gCO$_2$-br sample for different deviatoric stresses
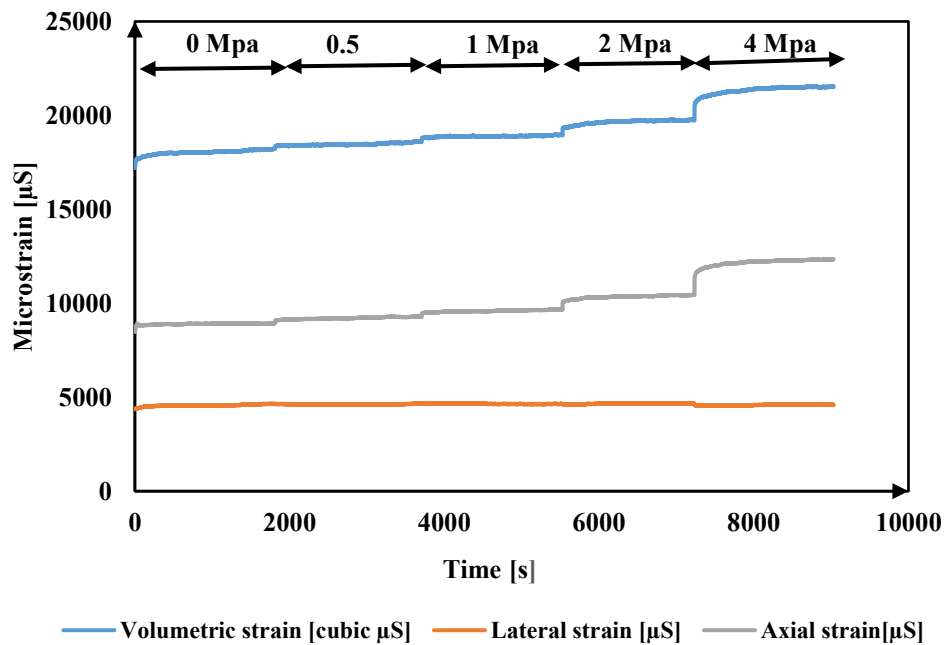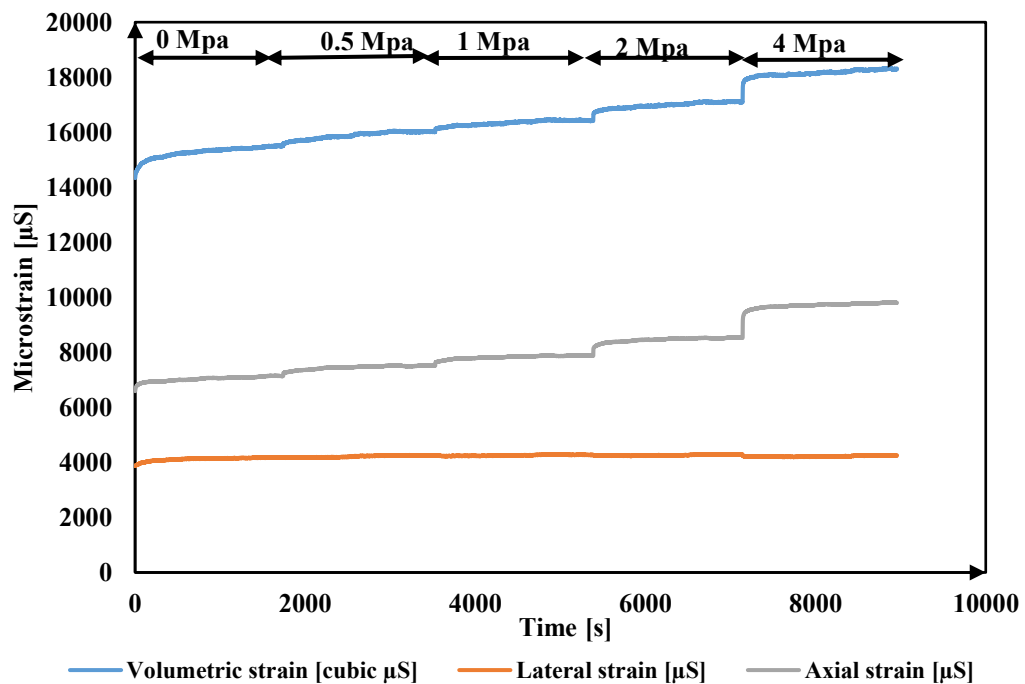

Combined fatigue curves under the different deviatoric stresses from 0 to 4Mpa for the gCO$_2$-br sample.

Appendix 3c: Fatigue curves for the scCO$_2$-br sample
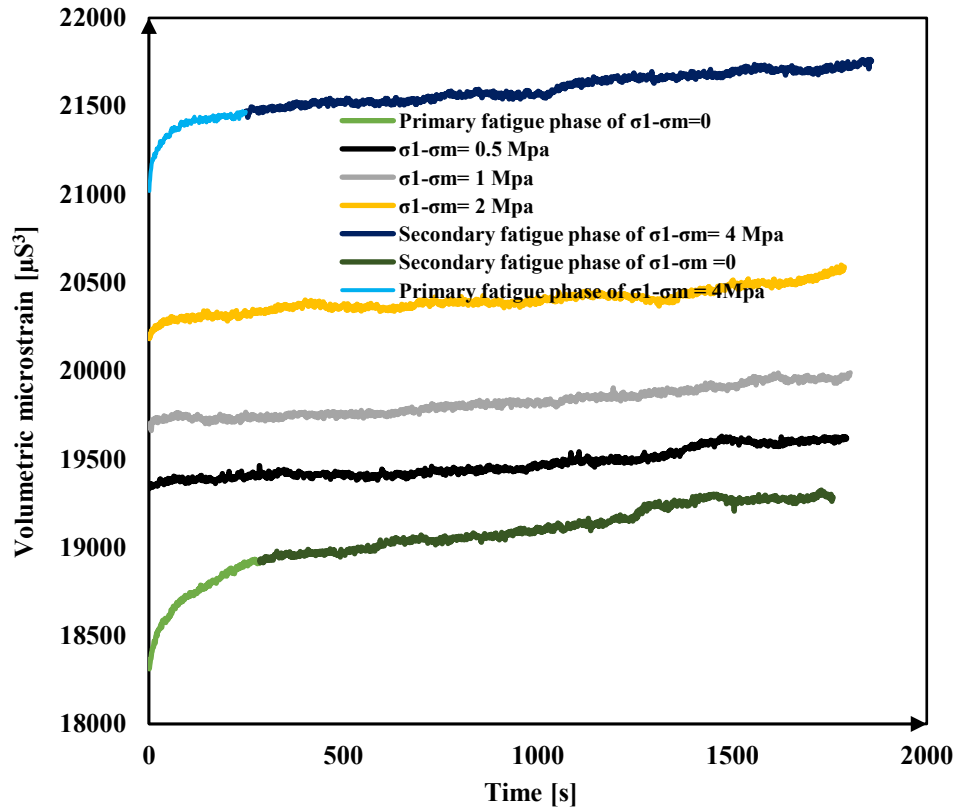
Fatigue curve for the scCO$_2$-br sample for different deviatoric stresses

Combined fatigue curves under the different deviatoric stresses from 0 to 4Mpa for the scCO$_2$-br sample.
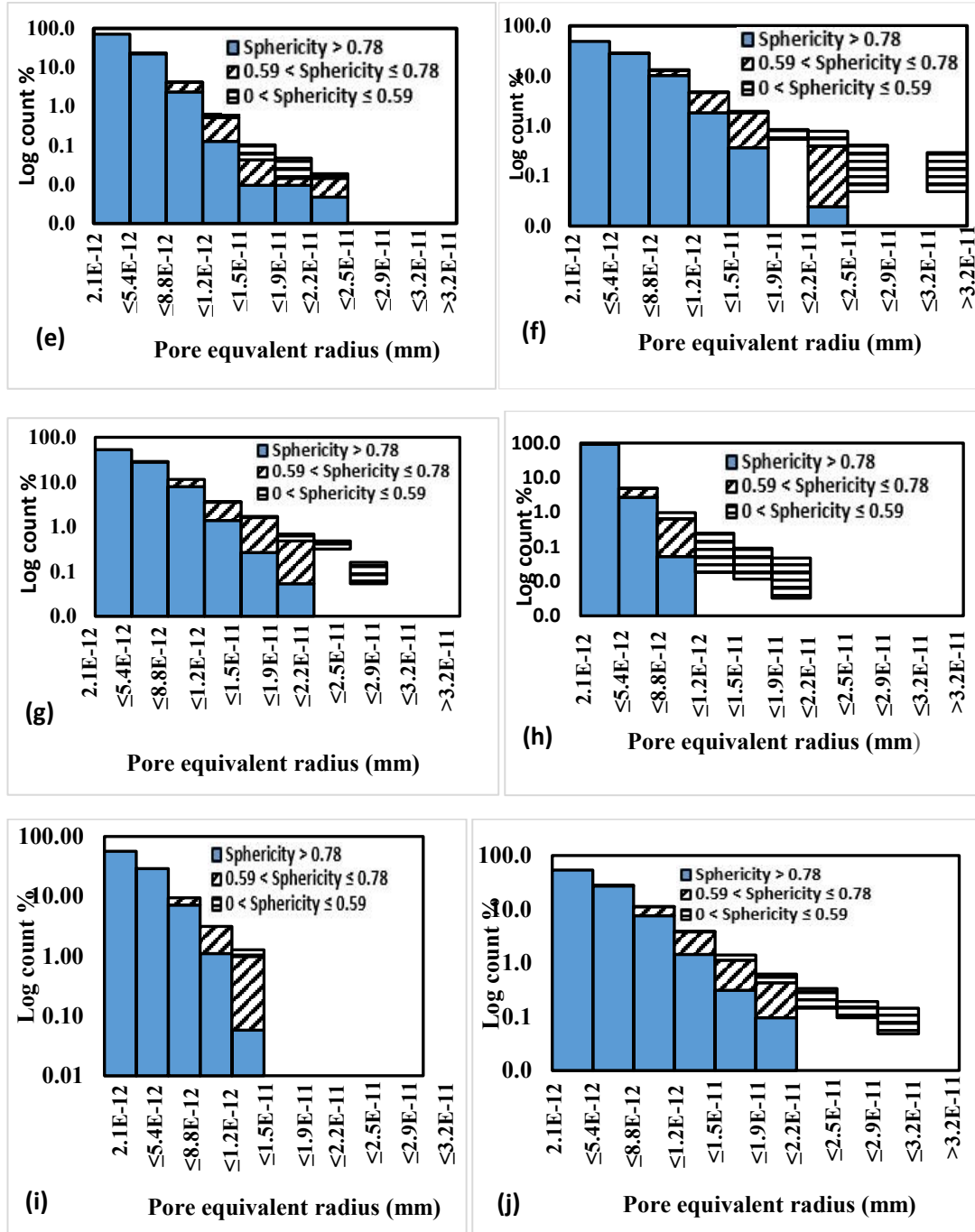
Appendix 3d: Fatigue curves for the gCO₂ sample

Fatigue curve for the gCO₂ sample for different deviatoric stresses

Combined fatigue curves under the different deviatoric stresses from 0 to4Mpa for the gCO₂ sample.

227

Appendix 4: Distribution of equivalent radius and sphericity of pores in the different samples

Distribution of equivalent pore radius and sphericity for (e) Dry sample at pre-compression (f) Dry sample at post-compression (g) scCO$_2$-br sample at pre-compression (h) scCO$_2$-br sample at post-compression (i) gCO$_2$ sample at pre-copmression (j) gCO$_2$ sample at post-compression.

Appendix 5: Distribution of roundness and solidity of grains and pores in the samples

(a) Percentage distribution of classes of grain roundness

Roundness Index	br		gCO$_2$		gCO$_2$-br		ScCO -br	
	a	b	a	b	a	b	a	b
0.21	1	1	0	0	1	0	2	0
0.3	4	2	2	3	3	3	2	1
0.39	7	5	5	7	9	7	9	7
0.48	9	7	6	8	8	7	10	7
0.57	16	14	18	14	18	13	15	18
0.66	13	16	14	14	13	14	15	11
0.75	16	16	17	15	14	19	15	16
0.84	10	15	12	12	9	14	9	10
0.93	6	13	6	9	6	9	8	6
1.00	18	11	20	18	19	14	15	24

(b) Percentage distribution of classes of grain solidity

Solidity index	br		gCO$_2$		gCO$_2$-br		ScCO$_2$-br	
	a	b	a	b	a	b	a	b
0.47	0	0	0	0	0	0	0	0
0.53	0	0	0	0	1	0	1	0
0.59	1	2	1	2	1	1	1	1
0.65	3	1	2	2	3	1	2	1
0.71	4	2	5	5	7	4	6	5
0.77	8	4	7	9	9	6	10	6
0.83	11	13	15	13	14	15	14	12
0.89	29	30	26	26	25	30	27	26
0.95	21	35	18	23	15	27	21	17
1.00	23	13	26	20	25	16	18	32

c) Percentage distribution of classes of pore roundness

Roundness index	br		gCO$_2$		gCO$_2$-br		scCO$_2$-br	
	a	b	a	b	a	b	a	b
0.21	2	1	0	1	2	1	2	1
0.3	6	5	3	5	5	4	5	3
0.39	11	9	8	9	11	10	11	9
0.48	12	11	10	11	12	11	11	11
0.57	15	15	17	16	18	16	16	15
0.66	15	15	15	16	14	14	15	15
0.75	14	16	17	15	13	16	15	17
0.84	10	13	12	12	8	13	10	10
0.93	7	9	6	6	5	9	6	8
1.00	8	6	12	9	12	6	9	11

d) Percentage distribution of classes of pore solidity

Solidity index	br		gCO$_2$		gCO$_2$-br		scCO$_2$-br	
	a	b	a	b	a	b	a	b
0.47	2	1	1	25	2	1	3	1
0.53	3	2	1	11	2	1	1	1
0.59	3	2	1	9	2	2	3	2
0.65	3	3	4	11	4	2	2	3
0.71	7	4	8	11	7	5	5	6
0.77	8	7	8	9	9	7	9	8
0.83	16	13	17	8	17	14	16	14
0.89	29	30	30	5	26	32	30	30
0.95	18	31	15	3	13	29	20	20
1.00	11	7	15	8	18	7	11	15

*a= pre-compression, b=post-compression

Appendix 6: Digital rock model for the different samples

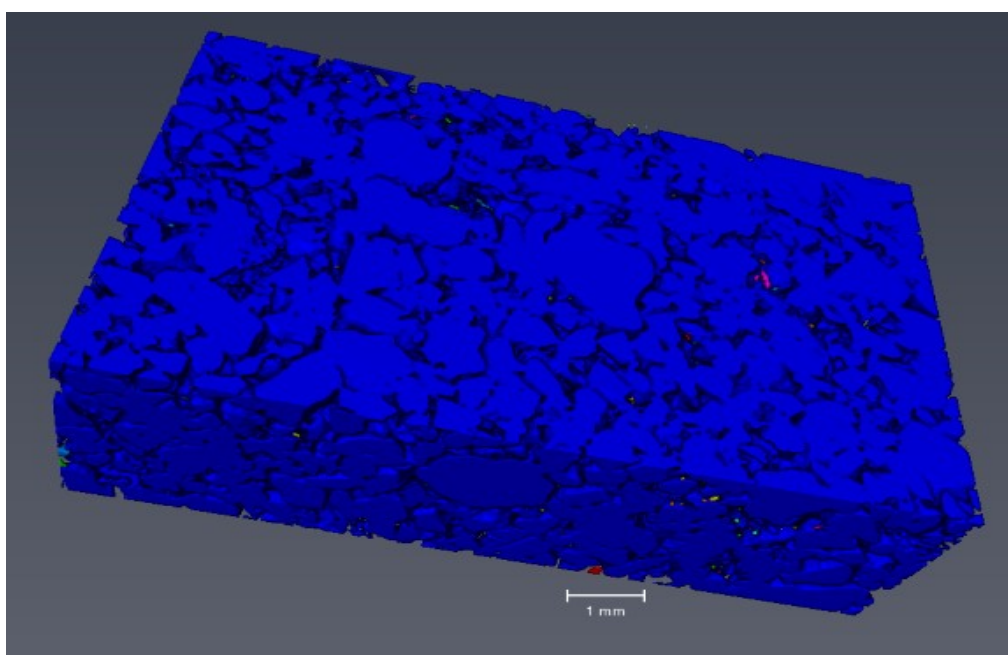Pre-compression digital rock model for the brine saturated sample

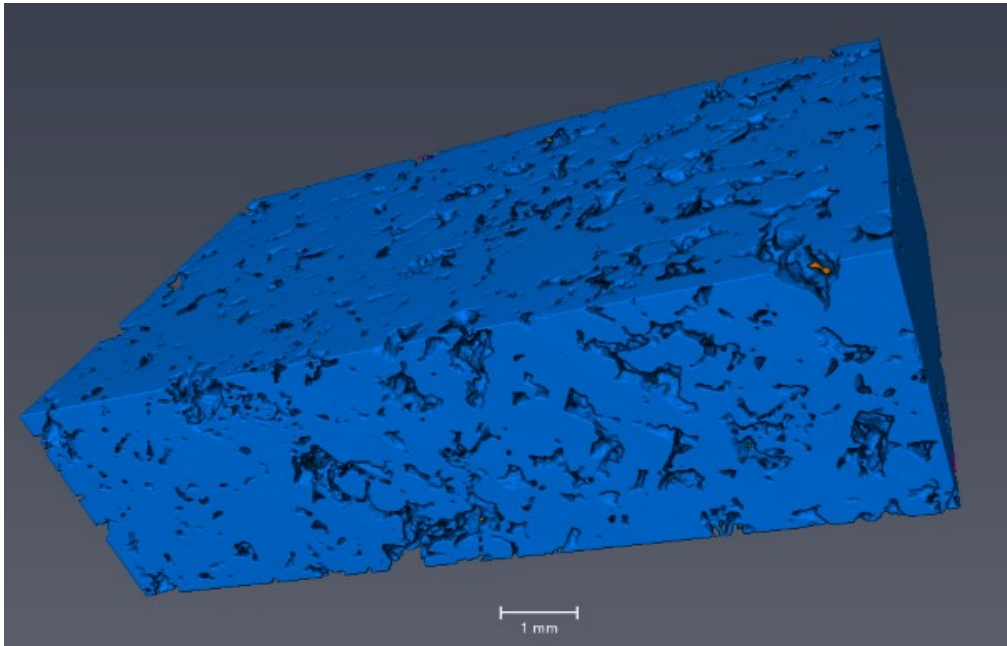Post-compression digital rock model for the brine saturated sample

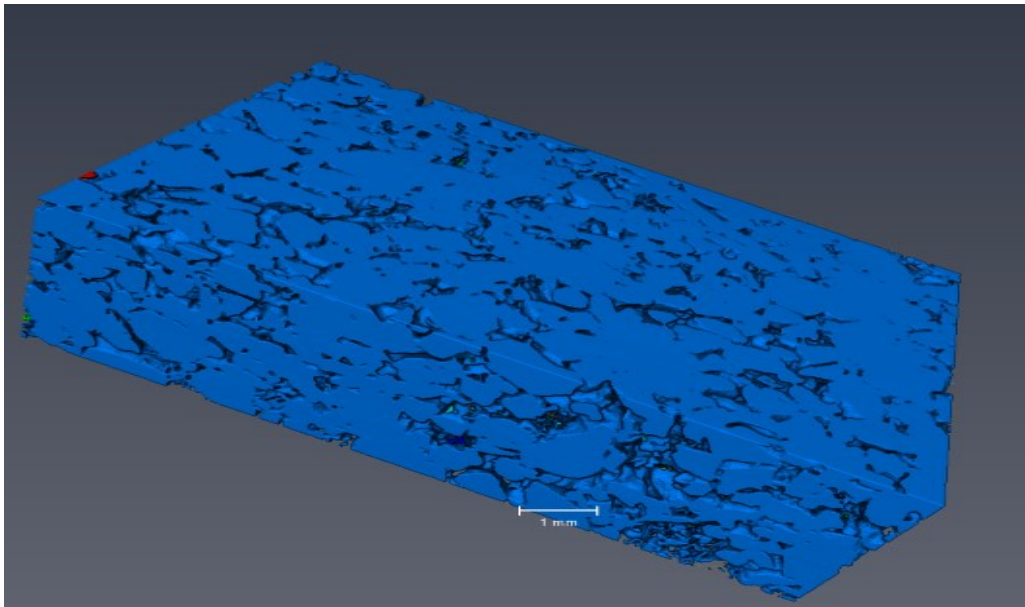Pre-compression digital rock model for the gCO$_2$-br saturated sample

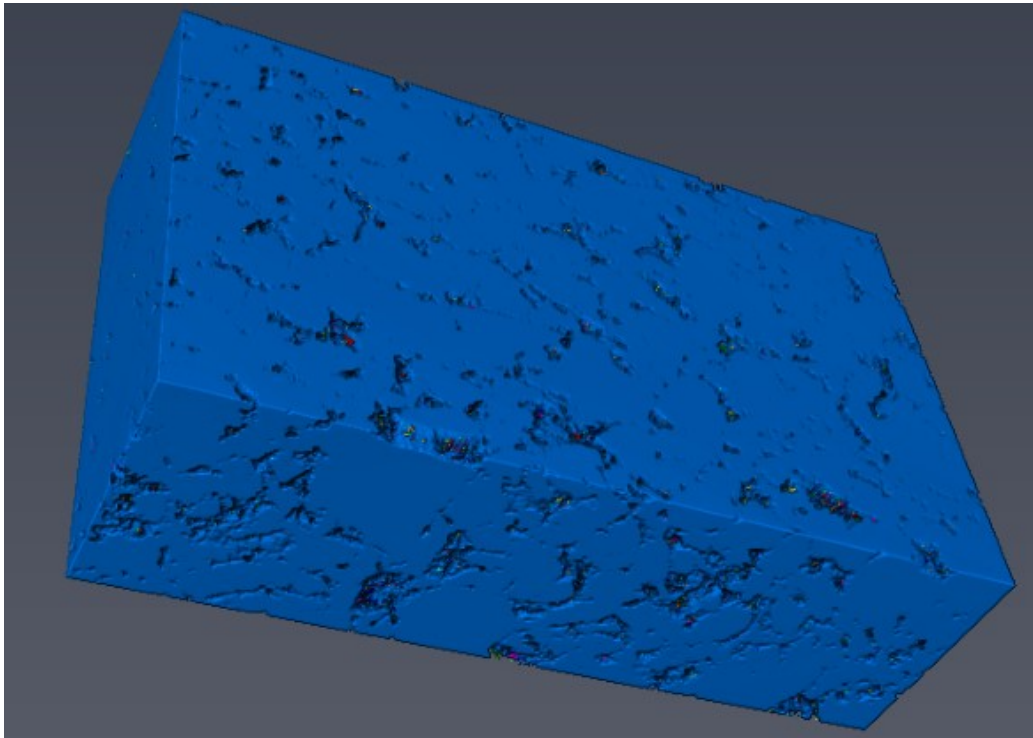Post-compression digital rock model for the gCO$_2$-br saturated sample

 Pre-compression digital rock model for the gCO$_2$ saturated sample

Post-compression digital rock model for the gCO$_2$ saturated sample

Pre-compression digital rock model for the scCO$_2$-br saturated sample

Post-compression digital rock model for the scCO$_2$-br saturated sample